

UC Riverside

UC Riverside Electronic Theses and Dissertations

Title

Development and Applications of the Transport Model for Soil Water Stable Isotopes Considering Fractionation

Permalink

<https://escholarship.org/uc/item/9fw392n5>

Author

Zhou, Tiantian

Publication Date

2022

Peer reviewed|Thesis/dissertation

UNIVERSITY OF CALIFORNIA
RIVERSIDE

Development and Applications of the Transport Model for Soil Water Stable Isotopes
Considering Fractionation

A Dissertation submitted in partial satisfaction
of the requirements for the degree of

Doctor of Philosophy

in

Environmental Sciences

by

Tiantian Zhou

December 2022

Dissertation Committee:

Dr. Jirka Šimůnek, Chairperson

Dr. Hoori Ajami

Dr. Amir Haghverdi

Copyright by
Tiantian Zhou
2022

The Dissertation of Tiantian Zhou is approved:

Committee Chairperson

University of California, Riverside

Acknowledgments

I want to start by thanking my supervisor, Dr. Jirka Šimůnek. I could not have successfully finished my PhD study without his guidance and support. He always responds to my questions patiently and timely. He encourages me to collaborate with others to establish my networks. He recommends me when I apply for scholarships and postdoc positions. I cannot thank him enough for everything he has done for me. He is not only a giant in scientific research, but also a strong man in life. He seems to be good at everything that he loves. He is always a role model in my career and life, constantly inspiring me to become a well-rounded person and do everything to perfection. I would also like to thank all my dissertation committee and qualifying exam committee members, Dr. Hoori Ajami, Dr. Amir Haghverdi, Dr. James Sickman, Dr. Laosheng Wu, and Dr. Nicolas Barth for their invaluable comments and advice throughout my PhD study.

Thanks to my brilliant collaborators for their mentorship in writing the journal papers, including Dr. Isabelle Braud (code, methodology, and editing in Chapter 2 and 3), Dr. Giuseppe Brunetti (code, methodology, and editing in Chapter 3 and 4), Dr. Paolo Nasta (conceptualization, code, and editing in Chapter 3 and 4), Dr. Yi Liu (code and editing in Chapter 3), Dr. Marcel Gaj (methodology and editing in Chapter 4), and Dr. Christoph Neukum (data and editing in Chapter 4), Dr. Vincent Post (data and editing in Chapter 4). Thanks to Šimůnek lab members and visiting scholars for their

friendship in the past four years, including Dr. Lin Chen, Dr. Paulo Gubiani, Dr. Salini Sasidharan, Dr. Ji'an Shi, Dr. Mika Turunen, Dr. Xiaojun Shen, Dr. Everton Pinheiro, Dr. Jing Liang, Dr. Sarah Helalia, Dr. Kun Tu, Dr. Tingzhang Zhou, Dr. Ce Zheng, Dr. Lin Chen, Dr. Anooja Thomas, Dr. Meixiang Xie, Dr. Kun Liu, Dr. Shuai Chen, Dr. Jinsong Ti, and all other friends, professors, and advisors in the Department of Environmental Sciences at UCR.

Thanks to my father, my mother, my sister, my brother-in-law, my brother, and my sister-in-law, who have always respected my choices and stood behind me through tough times. I would like to thank my boyfriend, Jiabin Gao, for his constant support and encouragement.

This research was mainly supported by the Multistate W4188 program funded by NIFA (grant no. CA-R-ENS-5047-RR). Additional research funding came from UCR Dean's Distinguished Fellowship Award, UCR Dissertation Year Program Award, ENSC outstanding research award (graduate students), and Hilda and George Liebig ENSC Summer Fellowship. Travel grants for conferences were also provided by the UCR GSA travel grants, ENSC Mini-GSA travel grants, and SSSA Robert Luxmoore Student Travel Award.

Copyright Acknowledgments

The text in Chapter 2 of this dissertation, in full, is a reprint of the material as it appears in “Adapting HYDRUS-1D to simulate the transport of soil water isotopes with evaporation fractionation,” published in *Environmental Modelling and Software*, 143 (2021), pp. 105118, co-authored by Jirka Šimůnek, and Isabelle Braud.

The text in Chapter 3 of this dissertation, in full, is a reprint of the material as it appears in “The impact of evaporation fractionation on the inverse estimation of soil hydraulic and isotope transport parameters,” published in *Journal of Hydrology*, 612 (2022), pp. 128100, co-authored by Jirka Šimůnek, Isabelle Braud, Paolo Nasta, Giuseppe Brunetti, and Yi Liu.

ABSTRACT OF THE DISSERTATION

Development and Applications of the Transport Model for Soil Water Stable Isotopes
Considering Fractionation

by

Tiantian Zhou

Doctor of Philosophy, Graduate Program in Environmental Sciences
University of California, Riverside, December 2022
Dr. Jirka Šimůnek, Chairperson

Stable isotope tracing is widely used to track water movement in the Groundwater-Soil-Plant-Atmosphere Continuum system. Physics-based modeling of soil water flow and stable isotope transport has the potential for providing continuous and real-time isotopic information. However, the evaporation fractionation effect is often ignored in current models, or they still implement only a simple treatment of evaporation fractionation. The lack of these considerations will result in simulation errors that may be propagated into practical applications.

To solve these problems, we first adapted and tested the HYDRUS-1D model, a numerical model widely used to simulate variably-saturated water flow and solute transport in porous media, by including an option to simulate isotope fate and transport

while accounting for evaporation fractionation. The numerical results obtained by the adapted model are in excellent agreement with existing analytical solutions. Additional plausibility tests and field evaluation further demonstrate the adapted model's accuracy.

We then investigated the impact of considering evaporation fractionation on model performance and practical applications (travel times and evaporation estimation). The global sensitivity analysis using the Morris and Sobol' methods and the parameter estimation using the Particle Swarm Optimization algorithm show that the Kling-Gupta efficiency (KGE) index for isotope data can increase by 0.09 and 1.49 for the humid and arid datasets, respectively, when selecting suitable fractionation scenarios. Considering evaporation fractionation using the Craig-Gordon (CG) and Gonfiantini models is likely to result in older water ages than the no-fractionation scenario estimates for the humid dataset. The direct use of simulated isotopic compositions in the no-fractionation scenario may result in large biases in practical applications in the arid zone.

We further explored the impact of considering soil tension control on model performance and practical applications (spatial-temporal origin of RWU). The results show that considering soil tension control (the TC_Frac scenario) leads to a depleted surface isotopic composition compared with only considering temperature control (CG_Frac). The contribution ratios of all soil layers in the TC_Frac scenario are always between the no fractionation (Non_Frac) and CG_Frac scenarios. The order of both drainage and root zone (RZ) travel times is: Non_Frac > TC_Frac > CG_Frac. All

methods can reflect the overall vertical trends of contribution ratios of different soil layers to RWU, and temporal trends of drainage and RZ travel times, although absolute differences between different methods always exist. Overall, the impact of the soil temperature fractionation effect is much more important for model performance and practical applications than the impact of the soil tension fractionation effect.

Table of Contents

Acknowledgments.....	iv
Copyright Acknowledgments	vi
ABSTRACT OF THE DISSERTATION	vii
List of Figures	xiii
List of Tables	xxii
Chapter 1 Introduction	1
1.1 Backgrounds	1
1.2 Literature Review.....	2
1.3 Unresolved Scientific Questions.....	5
1.3.1 How to Develop a User-Friendly Isotope Transport Model With Evaporation Fractionation?.....	5
1.3.2 How Will Evaporation Fractionation Affect the Model Performance and Practical Applications?	5
1.3.3 How Will Tension Control Affect the Model Performance and Practical Applications?	6
1.4 Research Objectives.....	7
References.....	8
Chapter 2 Adapting HYDRUS-1D to Simulate the Transport of Soil Water Isotopes With Evaporation Fractionation.....	14
2.1 Introduction.....	15
2.2 Definition of the Isotope Concentrations	22
2.3 Craig-Gordon Model (1965).....	23
2.4 Numerical Models.....	29
2.4.1 Evaporation Fractionation in a System That Neglects Vapor Flow	29
2.4.2 Evaporation Fractionation in a System That Considers Vapor Flow	31
2.4.3 Particle Tracking Module (PTM).....	36
2.5 Numerical Implementations	40
2.6 Model Verification and Evaluation.....	43
2.6.1 Verification of the Numerical Solutions	43
2.6.2 Evaluation Against the Experiment Data.....	62
2.7 Summary and Conclusions	69
References.....	71
Supplementary Material.....	81
Appendix A.....	81
Tables.....	82
Figures.....	85
Method S2.1. Estimation of the Atmospheric Isotope Ratio <i>R_a</i>	88
Chapter 3 The Impact of Evaporation Fractionation on the Inverse Estimation of Soil Hydraulic and Isotope Transport Parameters.....	92

3.1 Introduction.....	94
3.2 Materials and Methods.....	98
3.2.1 Site Description and Data Availability	100
3.2.2 Model Setup	103
3.2.3 Global Sensitivity Analysis.....	107
3.2.4 Parameter Optimization	111
3.2.5 First Practical Application: Calculation of Drainage Travel Times and RWU Temporal Origin	112
3.2.6 Second Practical Application: Calculation of Evaporation Flux	114
3.3 Results.....	116
3.3.1 Stumpp et al. (2012) Dataset Analysis.....	116
3.3.2 Braud et al. (2009a) Dataset Analysis.....	124
3.4 Discussion	127
3.4.1 Impacts of Evaporation Fractionation on Parameter Estimation and Model Performance	127
3.4.2 Impacts of Evaporation Fractionation on Practical Applications	130
3.4.3 Comparison of Different Climate Conditions and Implications for Future Studies.....	133
3.5 Summary and Conclusions	135
References.....	137
Supplementary Material.....	144
Tables.....	144
Figures.....	150
Method S3.1: Evaporation Fractionation Models.....	160
Method S3.2: Global Sensitivity Analysis Methods.....	161
Results S3.1: Global Sensitivity Analysis and Monte-Carlo Filtering for the Stumpp et al. (2012) Dataset.....	164
Results S3.2: Global Sensitivity Analysis and Monte-Carlo Filtering for the Braud et al. (2009a) Dataset.....	170
Chapter 4 The Impact of Soil Tension on Isotope Fractionation, Transport and Spatial-Temporal Origin of Root Water Uptake.....	173
Abstract:	173
4.1 Introduction.....	175
4.2 Materials and Methods.....	181
4.2.1 Study Area and Data Collection	181
4.2.2 HYDRUS-1D Model Setup	182
4.2.3 Practical Applications	187
4.3 Results.....	191
4.3.1 Performance of the Isotope Transport Model	191
4.3.2 Spatial Origin of RWU	192

4.3.3 Temporal Origin of RWU	195
4.3.4 Isotope Mass Balance	200
4.4 Discussion	201
4.4.1 Impacts of the Model Setup on Model Performance	201
4.4.2 Impacts of the Model Setup on the Spatial Origin of RWU	202
4.4.3 Impacts of the Model Setup on the Temporal Origin of RWU.....	204
4.4.4 Comparison of the Water Flow and Isotope Transport-Based Methods...	205
4.4.5 Implications for the Langeoog Island Groundwater Recharge	208
4.4.6 Model Limitations and Future Work	209
4.5 Summary and Conclusions	211
References	214
Supplementary Materials	220
Figures.....	220
Tables.....	226
Result S4.1 Mann-Kendall Trend Tests.....	227
Chapter 5 Summary and Conclusions.....	229

List of Figures

Figure 1.1. Schematic diagram of some critical research topics in the agricultural GSPAC system.....	2
Figure 2.1. The Craig–Gordon model of isotopic fractionation during evaporation (modified from Gat, 2010).....	24
Figure 2.2. Schematic diagram of the water flow-based particle tracking module.	39
Figure 2.3. Comparison of analytical and numerical solutions for profiles of (a) the ^2H isotopic composition and (b) the ^{18}O isotopic composition, (c) the dual-isotope plot of simulated values, and (d) the LC-excess profile for isothermal saturated soil under steady evaporation.	49
Figure 2.4. Comparison of the results of analytical and numerical solutions for nonisothermal unsaturated soils under steady evaporation. Vertical profiles of (a) the soil water content, (b) the matric potential, (c) the soil temperature, (d) the water fluxes (liquid, q_l , vapor, q_v , and total, q ; negative values represent evaporation), (e) the ^2H isotopic composition, (f) the ^{18}O isotopic composition, (g) the dual-isotope plot of the simulated values and (h) the LC-excess profile. “VDZ” and “LDZ” represent the vapor and liquid-dominant zones, respectively.	55

Figure 2.5. Vertical profiles of (a) the soil water content, (b) the water fluxes (liquid, q_l , vapor, q_v , and total, q ; negative values represent evaporation), (c) the ^2H isotopic composition, and (d) the ^{18}O isotopic composition in plausibility tests 1-6 at 250 d.61

Figure 2.6. Simulated $\delta^{18}\text{O}$ in the seepage water at the bottom of the lysimeter when equilibrium fractionation was (i.e., $\alpha_i^* = \alpha_i^*$; $nk = 0$) or was not (i.e., $\alpha_i^* = 1$; $nk = 0$) considered for the Stumpp et al. (2012) dataset using the Gonfiantini and Craig-Gordon evaporation fractionation models.66

Figure 2.7. Precipitation (a), spatial-temporal distribution of particles (b), and mean particle velocity (c) (simulated by the Particle Tracking Module) for the Stumpp et al. (2012) dataset. “W” and “D” represent wet and dry seasons, respectively.69

Figure S2.1. The node distribution versus depth (a) and spatial steps versus the node number (b) for the coarse, medium, and fine spatial discretizations. ‘C’, ‘M’, and ‘F’ refer to ‘coarse,’ ‘medium,’ and ‘fine’, respectively.85

Figure S2.2. Comparison of analytical and numerical solutions (bottom axis) and their differences (top axis) for (a) ^2H and (b) ^{18}O isotopic composition profiles using the coarse, medium, and fine spatial discretizations for isothermal saturated soil under steady evaporation. ‘C’, ‘M’, and ‘F’ refers to ‘coarse’, ‘medium’, and ‘fine’, respectively.85

Figure S2.3. Comparison of analytical and numerical solutions (left) and their differences (right) for ^2H (top) and ^{18}O (bottom) isotopic composition profiles using the coarse, medium, and fine spatial discretizations for nonisothermal unsaturated soil under steady evaporation. ‘C’, ‘M’, and ‘F’ refer to ‘coarse’, ‘medium’, and ‘fine’, respectively. Results are presented for the top 30 cm only.	86
Figure S2.4. The ^2H - ^{18}O isotope plots for Plausibility Tests 3-6 (a-d) at 250 d obtained using fine spatial discretization.	87
Figure S2.5. LC-excess profiles for Plausibility Tests 3-6 at 250 d obtained using fine spatial discretization.	87
Figure 3.1. Schematic outline of methods used.	99
Figure 3.2. The temporal distribution of precipitation (P) (a), potential evapotranspiration (ET_0) (b), soil surface temperature (T_s) (c), air relative humidity (RH) (d), and leaf area index (LAI) (e) during the simulation period for the Stumpp et al. (2012) dataset (adapted from Stumpp et al., 2012)..	101
Figure 3.3. Time series of the evaporation flux (E) (a) isotopic composition of the evaporation flux (δE) (b), outlet air temperature (T_{air}) (c), outlet air relative humidity (RH) (d), during the simulation period for the Braud et al. (2009a) dataset (adapted from Braud et al., 2009a).	103

Figure 3.4. Model setup for the Stumpp et al. (2012) dataset. Note that "W," "H," and "I" represent water flow, heat transport, and isotope transport, respectively. 105

Figure 3.5. Model setup for the Braud et al. (2009a) dataset. Note that "W," "H," and "I" represent water flow, heat transport, and isotope transport, respectively. 107

Figure 3.6. Measured (symbols) and simulated discharge ^{18}O isotopic compositions for different fractionation scenarios (for the Stumpp et al. (2012) dataset). 118

Figure 3.7. The residence time distributions (*RTDs*) for different fractionation scenarios (Non_Frac – top, CG_Frac – middle, and Gon_Frac – bottom). Note that the dashed red line represents the rooting depth. 122

Figure 3.8. The temporal origin of root water uptake (RWU) for different fractionation scenarios (Non_Frac – top, CG_Frac – middle, and Gon_Frac – bottom). The upper panels show the monthly transpiration sums (in different colors); the lower panels show fractional contributions of water of a certain age/origin (by month) to the monthly transpiration sums. 123

Figure 3.9. Measured (symbols) and simulated (lines) $\delta^{18}\text{O}$ isotopic compositions across the soil profile for different fractionation (Non_Frac, CG_Frac,

Gon_Frac, and Meas_Frac) scenarios (for the Braud et al. (2009a) dataset).	126
Figure S3.1. The μ_j^* and $\mu_j^* \sim \sigma_j$ plots for the Morris sensitivity analysis for the bottom water flux (subscript <i>bf</i> , top left), soil water content (subscript <i>wc</i> , top right), isotopic composition of the discharge (subscript <i>wi</i> , middle left), water retention curve (subscript <i>rc</i> , middle right), and the average of them (subscript <i>avg</i> , bottom left) for the Stumpp et al. (2012) dataset.	150
Figure S3.2. Scatter plots for pair relations θ_{s1} -KGE, α_1 -KGE, n_1 -KGE, and K_{s1} -KGE for the average performance for the Stumpp et al. (2012) dataset.	151
Figure S3.3. Scatter plots for pair relations θ_{s2} -KGE, α_2 -KGE, n_2 -KGE, and K_{s2} -KGE for the average performance for the Stumpp et al. (2012) dataset.	152
Figure S3.4. Scatter plots for pair relations θ_{s3} -KGE, α_3 -KGE, n_3 -KGE, and K_{s3} -KGE for the average performance for the Stumpp et al. (2012) dataset.	153
Figure S3.5. Bivariate KDE plots (below diagonal), univariate KDE plots (diagonal), and correlation plots (above diagonal) for the parameters of the first soil layer (0-30 cm) (for the Stumpp et al. (2012) dataset).	154

Figure S3.6. Bivariate KDE plots (below diagonal), univariate KDE plots (diagonal), and correlation plots (above diagonal) for the parameters of the second soil layer (30-90 cm) (for the Stumpp et al. (2012) dataset)..... 155

Figure S3.7. Bivariate KDE plots (below diagonal), univariate KDE plots (diagonal), and correlation plots (above diagonal) for the parameters of the third soil layer (90-150 cm) (for the Stumpp et al. (2012) dataset). 156

Figure S3.8. The soil water retention (left) and hydraulic conductivity (right) curves for different layers (first layer - top, second layer - middle, and third layer - bottom) and different fractionation scenarios for the Stumpp et al. (2012) dataset..... 157

Figure S3.9. The particles trajectories simulated using the soil hydraulic parameters estimated assuming different fractionation scenarios (Non_Frac – top, CG_Frac – middle, and Gon_Frac – bottom). 158

Figure S3.10. The probability density distribution of water travel times calculated using the soil hydraulic parameters estimated assuming different fractionation scenarios (Non_Frac – left, CG_Frac – middle, and Gon_Frac – right)..... 158

Figure S3.11. The μ_j^* and $\mu_j^* \sim \sigma_j$ plots for the Morris sensitivity analysis for the soil water content (subscript wc , top left), isotopic composition (subscript

<p><i>w_i</i>, top right), and average (subscript <i>avg</i>, bottom) for the Braud et al. (2009a) dataset.</p>	159
<p>Figure S3.12. The soil water retention (left) and hydraulic conductivity (right) curves for different fractionation scenarios for the Braud et al. (2009a) dataset.</p>	159
<p>Figure S3.13. Precipitation contributions to different water balance components in the Non_Frac scenario for the Stumpp et al. (2012) dataset.....</p>	160
<p>Figure 4.1. Schematic outline of methods used.</p>	180
<p>Figure 4.2. HYDRUS-1D model setup. W, H, and I represent water flow, heat transport, and isotope transport, respectively, while Non_Frac, CG_Frac, and TC_Frac indicate no fractionation, fractionation described by the Craig-Gordon equation, and fractionation according to the modified Craig-Gordon equation. BC denotes boundary condition. Note that the description of the variables in this figure is shown in Table S4.1 in the Supplementary Materials.</p>	184
<p>Figure 4.3. Measured (blue circles) and simulated (a) $\delta^{2}\text{H}$ and (b) $\delta^{18}\text{O}$ profiles under three fractionation scenarios (Non_Frac, CG_Frac, and TC_Frac).</p>	192
<p>Figure 4.4. The contribution ratios of different soil layers (Layer 1, Layer 2, Layer 3, and Layer 4) to RWU calculated using the water balance (WB) method.</p>	194

Figure 4.5. The contribution ratios of different soil layers (a - Layer 1, b - Layer 2, c - Layer 3, and d - Layer 4) to RWU for different fractionation scenarios (Non_Frac, CG_Frac, and TC_Frac) using the SIAR model..... 194

Figure 4.6. The spatial distribution of residence times plotted versus time (a), the temporal origin of monthly RWU (b), and relative frequency distributions of drainage (c) and RWU (d) travel times from the particle tracking. Note that only the travel times from the last 250 days are displayed in the graphs of relative frequency distributions. For the temporal origin, the upper panel shows the monthly transpiration sums (in different colors), and the lower panel shows fractional contributions of water of a certain age/origin (by month) to the monthly transpiration sums. 196

Figure 4.7. Precipitation (contributing to drainage) (a), surface soil tension (b), soil profile water storage (c), drainage travel times (d), and their relative frequency distributions (e~g) for different fractionation scenarios (Non_Frac, CG_Frac, and TC_Frac)..... 198

Figure 4.8. Precipitation (contributing to RWU) (a), surface soil tension (b), root zone water storage (c), root zone travel times (d), and their relative frequency distributions (e~g) for different fractionation scenarios (Non_Frac, CG_Frac, and TC_Frac). Note that the different background colors (blue, green, violet) represent the early (between about 2018/10/18~2019/03/09), middle

(between about 2019/03/10~2019/05/18), and final (between about 2019/05/19~2019/06/25) stages, respectively, separated by vertical red dashed lines.....	199
Figure 4.9. The relationship between α_{vw} (a~b) and contribution of soil tension control (c~d) vs. soil temperature and tension for ^2H (left) and ^{18}O (right) isotopes.	211
Figure S4.1. The root density profile.	220
Figure S4.2. The temporal distribution of precipitation (a), the isotopic composition of precipitation (b), soil surface temperature (Ts) (c), and leaf area index (LAI) (d) during the simulation period.....	221
Figure S4.3. Simulated $\delta^2\text{H}$ (top graph) and $\delta^{18}\text{O}$ (bottom graph) of different soil layers (a, b, c, and d for Layer 1, 2, 3, and 4, respectively) and RWU (e) for different fractionation scenarios (Non_Frac, CG_Frac, and TC_Frac).	223
Figure S4.4. Particle trajectories (with root water uptake).	224
Figure S4.5. The particle trajectories (a), spatial distribution of residence times plotted versus time (b), and relative frequency distributions of drainage travel times (c) when there is no root water uptake. Note that only the travel times from the last 250 days are displayed in the graphs of relative frequency distributions.....	225

List of Tables

Table 2.1. History of the development of physics-based transport models for soil water stable isotopes.	22
Table 2.2. Basic soil hydraulic, thermal, and solute transport parameters.	45
Table 2.3. Values of all variables used in the analytical solution of <i>Zimmermann et al.</i> (1967).....	48
Table 2.4. Values of all variables used in the analytical solution of <i>Barnes and Allison</i> (1984).....	53
Table 2.5. Values of all variables used in the plausibility tests.	60
Table 2.6. Plausibility tests' conditions.	61
Table 2.7. Statistics of the model performance.....	66
Table S2.1. Equations used in this study to calculate the kinetic fractionation coefficient (nk).	82
Table S2.2. Optimized soil hydraulic and solute transport parameters from <i>Stumpp et al.</i> (2012).....	82
Table S2.3. Estimated flow parameters for each particle during the simulation period.	83
Table S2.4. Comparison of the water storage in the soil profile when the particle leaves the transport domain at its bottom with the net water input into the soil profile during particle's presence in the profile.	84

Table 3.1. Optimized parameters and Kling-Gupta efficiency (KGE) indices (bf, wc, wi, and avg refer to the bottom flux, water content, water isotopic composition, and average, respectively) for different fractionation scenarios (Non_Frac, CG_Frac, and Gon_Frac) (for the Stumpp et al. (2012) dataset).	118
Table 3.2. Estimated mean travel times of drainage (t_0 *) and mean water fluxes (v_0 *) for different fractionation scenarios (Non_Frac, CG_Frac, and Gon_Frac) using different methods (peak displacement and particle tracking).	119
Table 3.3. Optimized parameters and Kling-Gupta efficiency (KGE) indices (wc, wi, and avg refer to the water content, water isotopic composition, and average, respectively) for different fractionation scenarios (Non_Frac, CG_Frac, Gon_Frac, and Meas_Frac) (for the Braud et al. (2009a) dataset).	125
Table 3.4. Cumulative evaporation measured using different experimental methods and calculated considering different fractionation scenarios.	127
Table S3.1. Summary of the observed data in the Stumpp et al. (2012) dataset.	144
Table S3.2. Initial and reduced ranges of parameters used in the Morris analysis of the Stumpp et al. (2012) dataset.	145

Table S3.3. Sobol' sensitivity analysis indices for the Stumpp et al. (2012) dataset.

$S1_{bf}$, $S1_{wc}$, $S1_{wi}$, $S1_{rc}$, $S1_{avg}$, ST_{bf} , ST_{wc} , ST_{wi} , ST_{rc} , and ST_{avg} represent the first-order (subscript 1) and total variances (subscript T) for the bottom flux time series (subscript bf), soil water content time series (subscript wc) at different depths, the bottom water isotopic composition time series (subscript wi), the water retention curves (subscript rc), and the average of them (subscript avg), respectively. 146

Table S3.4. Initial and reduced ranges of parameters used in the Morris analysis of the Braud et al. (2009a) dataset. 148

Table S3.5. Sobol' sensitivity analysis indices for the Braud et al. (2009a) dataset for the isotopic composition of soil water. $S1_{wc}$, $S1_{wi}$, $S1_{avg}$, ST_{wc} , ST_{wi} , and ST_{avg} represent the first-order (subscript 1) and total variances (subscript T) for the final soil water content profile (subscript wc), the water isotopic composition profile (subscript wi), and the average of them (subscript avg), respectively. 149

Table 4.1. Root mean square error (RMSE) indices (wi , and avg refer to the water isotopic composition, and average, respectively) for different fractionation scenarios (Non_Frac, CG_Frac, and TC_Frac). 192

Table 4.2. The average contribution ratios of different soil layers to RWU for different fractionation scenarios (Non_Frac, CG_Frac, and TC_Frac) based on the water balance (WB) and SIAR methods.	195
Table 4.3. The mean drainage and RZ travel times (TT) for different fractionation scenarios (Non_Frac, CG_Frac, and TC_Frac) based on particle tracking (PT) and virtual tracer experiment (VTE) methods.	200
Table 4.4. The isotope mass balance components for different fractionation scenarios; <i>cvTop</i> , <i>cvRoot</i> , <i>cvBot</i> , and <i>cvTotChange</i> indicate actual isotope fluxes across the soil surface, across roots, across the bottom of the soil profile, and the total isotope removal, respectively. Note that the unit is ‰ ·cm/d. For the convenience of comparison, the Non_Frac scenario is taken as a reference and its value is set to 0 (by shifting). The values of other fractionation scenarios are also shifted correspondingly.	201
Table S4.1. Descriptions of variables in Fig. 4.2.	226

Chapter 1 Introduction

1.1 Backgrounds

Climate change is expected to increase fluctuations in precipitation and thus affect the water demand by agriculture (Liu et al., 2021; Waisman et al., 2019). At the same time, agriculture in many areas will also face increasing competition from non-agricultural users, such as domestic and industrial sectors. Besides, the available water in many regions is polluted due to increased pollution activities, making the water shortage situation even worse (Evans et al., 2019). Water resource shortages have caused challenges to food security, but globally in both irrigated and rain-fed agriculture, only about 10-30% of the available water (in the form of rainfall, surface water, or groundwater) is used by plant transpiration (Wallace, 2000). **Improving agricultural water use efficiency under combined continued changes has become an essential scientific issue** (Hatfield and Dold, 2019).

Scientific understanding of water transformation mechanisms in the groundwater, soil, plant, and air continuum (GSPAC) (Philip, 1966) should provide a theoretical basis for realizing the efficient utilization of regional agricultural water resources (Fig. 1.1). The core issue is the sourcing and quantification of water fluxes at the GSPAC interfaces (Liu, 2014), including **the accurate partitioning of evapotranspiration, and the identification of spatial-temporal origins of root water**

uptake. Integrated use of experiments with isotope tracers and model simulations

is needed to solve the above-discussed issues.

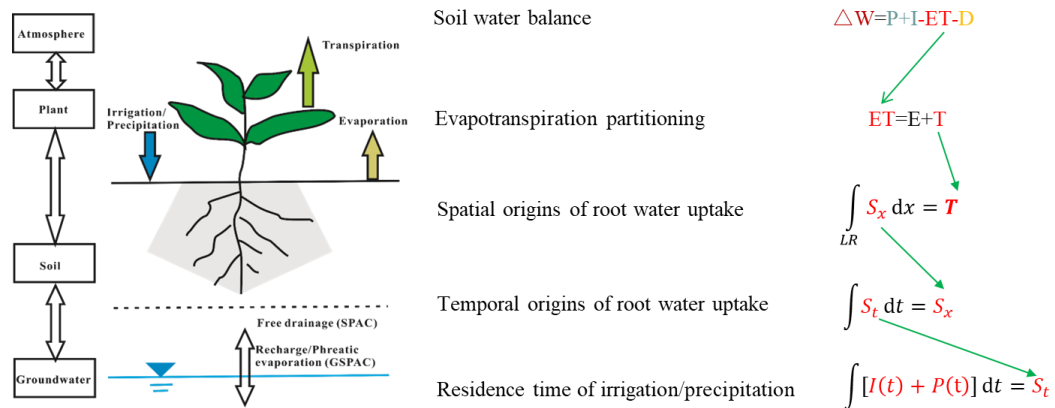


Figure 1.1. Schematic diagram of some critical research topics in the agricultural GSPAC system.

1.2 Literature Review

The water balance method is a conventional method to study water transformation in the GSPAC system by observing and estimating various water balance components. To ensure the accuracy of the determination of each component (especially crop evapotranspiration and groundwater recharge), precise and expensive instruments or methods such as lysimeters, Bowen ratio apparatuses, or eddy covariance methods are needed. In addition, the water balance method makes it difficult to reveal specific details and mechanisms of water transformation. Numerical simulations are important tools for studying water movement within the GSPAC system. Many numerical models have been developed in the literature (see, for example, (Pruess, 1991; Van Dam et al., 1997; Verburg, 1996). Among them, HYDRUS (Šimůnek et al., 2008; Šimůnek et al., 2016) is one of the most widely used models to simulate water

movement under different soil, crop, water management, and climate change conditions. However, numerical models are often affected by the equifinality problem, which means that the different sets of parameters may result in the same or similar model performance (Beven, 2006).

The isotopic composition of hydrogen and oxygen stable isotopes varies due to fractionation and mixing effects in the process of water transformation. Isotope tracers are thus good indicators that can be used to reveal many hydrological processes (Gazis and Feng, 2004; Gehrels et al., 1998; Hsieh et al., 1998; Robertson and Gazis, 2006). Because of significant differences in the water vapor isotope ratio during evaporation and transpiration, evapotranspiration can be partitioned using the isotope tracer technique (Kool et al., 2014; Wang and Yakir, 2000; Xiao et al., 2018). The spatial origin of root water uptake (RWU) are generally determined graphically by comparing the isotopic characteristics of stem/xylem water, soil water at different depths, and groundwater, or estimated by statistical models such as the IsoSource and Bayesian mixing models (SIAR, MixSIR, and MixSIAR) (e.g., (Corneo et al., 2018; Ma and Song, 2016; Wang et al., 2019; Zhang et al., 2022).

Despite the advantages discussed above, long-term field monitoring and water isotope measurements are time-consuming and expensive. Numerical modeling of soil water flow and isotope transport can integrate the benefits of field monitoring, stable isotope tracing, and numerical modeling methods. It is essential

for providing continuous and real-time isotopic information, while constraining the numerical modeling errors (Beyer and Penna, 2021; Stumpp et al., 2018).

However, the current isotope transport models are not widely used. Some of them are no longer maintained (e.g., Mathieu and Bariac, 1996; Melayah et al., 1996), quite complex to deploy (e.g., Braud et al., 2005; Haverd and Cuntz, 2010), or still only implement a simple treatment of evaporation fractionation (e.g. (Shurbaji and Phillips, 1995; Stumpp et al., 2012). These may be some of the reasons why these models are not commonly used.

On the other hand, compared with the spatial origin, research on the temporal origin of water for RWU has been limited to a few studies (Brinkmann et al., 2018; Miguez-Macho and Fan, 2021). Research on how long it will take for the precipitation/irrigation water to reach a certain depth (i.e., the residence time of precipitation/irrigation) and to identify which precipitation/ irrigation event is the water source for the crop roots on a particular day (i.e., temporal origins of crop water uptake) should be enhanced to develop better irrigation strategies (Sprenger et al., 2019).

1.3 Unresolved Scientific Questions

1.3.1 How to Develop a User-Friendly Isotope Transport Model With Evaporation Fractionation?

Since there are some limitations in current isotope transport models, a new isotope transport model based on the HYDRUS-1D code should be welcome, which will enable many existing HYDRUS users to efficiently operate the new model while using the various functions of the HYDRUS software (Šimůnek et al., 2016).

Since the particle tracking algorithm (e.g., Šimůnek, 1991) can be technically based solely on water balance calculations without requiring isotopic measurements, such algorithms can thus have broad applicability and can act as an excellent supplement to the traditional isotope transport-based methods (e.g., peak displacement, flux tracking by virtual tracer) for calculating transit times.

1.3.2 How Will Evaporation Fractionation Affect the Model Performance and Practical Applications?

The new isotope transport model will be able to simulate continuous dynamic space-time concentrations of soil water. However, since evaporation fractionation will affect the isotope concentration in the soil, how this impacts isotope concentration and transit time estimation is little understood and remains to be further studied. How much different will the soil hydraulic and solute transport parameters be when they are estimated from field data while considering, or not, evaporation fractionation? How

will this parameter difference propagate into practical applications? These questions have to be answered to avoid errors in applications in GSPAC systems (Penna et al., 2018).

1.3.3 How Will Tension Control Affect the Model Performance and Practical Applications?

Recent research shows that equilibrium fractionation is also influenced by the interactions between water films on soil particle surfaces and water vapor. For example, soil tension increases the energy required to remove water from the soil matrix and induces the water vapor pressure deficit. As a result, the surface of soil particles preferentially attracts lighter isotopes and increases soil water vapor diffusion toward the atmosphere (Gaj and McDonnell, 2019). How this impacts isotope concentration and transit time of soil water is little understood and remains to be further studied. These questions must be clarified before isotope transport models can be used in applications such as partitioning of recharge and discharge sources and plant water source analysis (Rothfuss and Javaux, 2017).

1.4 Research Objectives

This project aims to develop a comprehensive set of modeling tools for the quantification, sourcing, and timing of water fluxes in the agricultural GSPAC systems.

Here are three specific objectives:

(1) To adapt the current HYDRUS-1D model to simulate water flow and isotope transport while considering multiple types of evaporation fractionation situations and soil conditions (e.g., with and without vapor flow) (Chapter 2);

(2) To conduct global sensitivity analysis (using Morris and Sobol methods) and parameter optimization (using the particle swarm algorithm) for the new proposed model using field and laboratory datasets in different climate conditions and evaluate the impacts of evaporation fractionation on parameter estimation, model performance, and practical applications (drainage and RWU travel times, evaporation estimation) (Chapter 3);

(3) To evaluate the impacts of tension control on model performance and practical applications (spatial-temporal origin of RWU) of the new proposed model using field datasets and compare the reliability of water flow (water balance, particle tracking) and isotope transport-based (SIAR, seasonal origin index, virtual tracer) methods (Chapter 4).

References

- Beven, K., (2006), A manifesto for the equifinality thesis. *Journal of Hydrology*, 320(1-2), pp. 18-36, doi:10.1016/j.jhydrol.2005.07.007
- Beyer, M., and Penna, D., (2021), On the Spatio-Temporal Under-Representation of Isotopic Data in Ecohydrological Studies. *Front. Water*, 3, pp. 9, doi:10.3389/frwa.2021.643013
- Bouhleb, M.A., Bartoli, N., Otsmane, A., and Morlier, J., (2016), Improving kriging surrogates of high-dimensional design models by Partial Least Squares dimension reduction. *Struct. Multidiscip. Optim.*, 53(5), pp. 935-952, doi:10.1007/s00158-015-1395-9
- Braud, I., Bariac, T., Gaudet, J.P., and Vauclin, M., (2005), SiSPAT-Isotope, a coupled heat, water and stable isotope (HDO and H₂¹⁸O) transport model for bare soil. Part I. Model description and first verifications. *Journal of Hydrology*, 309(1-4), pp. 277-300, doi:10.1016/j.jhydrol.2004.12.013
- Brinkmann, N., Seeger, S., Weiler, M., Buchmann, N., Eugster, W., and Kahmen, A., (2018), Employing stable isotopes to determine the residence times of soil water and the temporal origin of water taken up by *Fagus sylvatica* and *Picea abies* in a temperate forest. *New Phytologist*, 219(4), pp. 1300-1313, doi:10.1111/nph.15255
- Brunetti, G., Simunek, J., Turco, M., and Piro, P., (2017), On the use of surrogate-based modeling for the numerical analysis of Low Impact Development techniques. *Journal of Hydrology*, 548, pp. 263-277, doi:10.1016/j.jhydrol.2017.03.013
- Corneo, P.E., Kertesz, M.A., Bakhshandeh, S., Tahaei, H., Barbour, M.M., and Dijkstra, F.A., (2018), Studying root water uptake of wheat genotypes in different soils using water delta O-18 stable isotopes. *Agriculture Ecosystems & Environment*, 264, pp. 119-129, doi:10.1016/j.agee.2018.05.007
- Evans, A.E.V., Mateo-Sagasta, J., Qadir, M., Boelee, E., and Ippolito, A., (2019), Agricultural water pollution: key knowledge gaps and research needs. *Current Opinion in Environmental Sustainability*, 36, pp. 20-27, doi:10.1016/j.cosust.2018.10.003

- Gaj, M., and McDonnell, J.J., (2019), Possible soil tension controls on the isotopic equilibrium fractionation factor for evaporation from soil. *Hydrological Processes*, 33(11), pp. 1629-1634, doi:10.1002/hyp.13418
- Gazis, C., and Feng, X.H., (2004), A stable isotope study of soil water: evidence for mixing and preferential flow paths. *Geoderma*, 119(1-2), pp. 97-111, doi:10.1016/s0016-7061(03)00243-x
- Gehrels, J.C., Peeters, J.E.M., De Vries, J.J., and Dekkers, M., (1998), The mechanism of soil water movement as inferred from O-18 stable isotope studies. *Hydrological Sciences Journal*, 43(4), pp. 579-594, doi:10.1080/02626669809492154
- Hatfield, J.L., and Dold, C., (2019), Water-use efficiency: Advances and challenges in a changing climate. *Frontiers in Plant Science*, 10, doi:10.3389/fpls.2019.00103
- Haverd, V., and Cuntz, M., (2010), Soil-Litter-Iso: A one-dimensional model for coupled transport of heat, water and stable isotopes in soil with a litter layer and root extraction. *Journal of Hydrology*, 388(3-4), pp. 438-455, doi:10.1016/j.jhydrol.2010.05.029
- Herman, J., and Usher, W., (2017), SALib: an open-source Python library for sensitivity analysis. *Journal of Open Source Software*, 2(9), pp. 97,
- Hsieh, J.C.C., Chadwick, O.A., Kelly, E.F., and Savin, S.M., (1998), Oxygen isotopic composition of soil water: Quantifying evaporation and transpiration. *Geoderma*, 82(1-3), pp. 269-293, doi:10.1016/s0016-7061(97)00105-5
- Kool, D., Agam, N., Lazarovitch, N., Heitman, J.L., Sauer, T.J., and Ben-Gal, A., (2014), A review of approaches for evapotranspiration partitioning. *Agricultural and Forest Meteorology*, 184, pp. 56-70, doi:10.1016/j.agrformet.2013.09.003
- Liu, C.M., (2014), Agricultural water problems in China: Some research priorities and discussions. *Chinese Journal of Eco-Agriculture*, 22(8), pp. 875-879, doi:10.13930/j.cnki.cjea.140649

- Liu, Z., Herman, J.D., Huang, G.B., Kadir, T., and Dahlke, H.E., (2021), Identifying climate change impacts on surface water supply in the southern Central Valley, California. *Science of the Total Environment*, 759, pp. 14, doi:10.1016/j.scitotenv.2020.143429
- Ma, Y., and Song, X.F., (2016), Using stable isotopes to determine seasonal variations in water uptake of summer maize under different fertilization treatments. *Science of the Total Environment*, 550, pp. 471-483, doi:10.1016/j.scitotenv.2016.01.148
- Mathieu, R., and Bariac, T., (1996), A numerical model for the simulation of stable isotope profiles in drying soils. *Journal of Geophysical Research-Atmospheres*, 101(D7), pp. 12685-12696, doi:10.1029/96jd00223
- Melayah, A., Bruckler, L., and Bariac, T., (1996), Modeling the transport of water stable isotopes in unsaturated soils under natural conditions .2. Comparison with field experiments. *Water Resources Research*, 32(7), pp. 2055-2065, doi:10.1029/96wr00673
- Miguez-Macho, G., and Fan, Y., (2021), Spatiotemporal origin of soil water taken up by vegetation. *Nature*, 598(7882), pp. 624-+, doi:10.1038/s41586-021-03958-6
- Penna, D., Hopp, L., Scandellari, F., Allen, S.T., Benettin, P., Beyer, M., Geris, J., Klaus, J., Marshall, J.D., Schwendenmann, L., Volkmann, T.H.M., von Freyberg, J., Amin, A., Ceperley, N., Engel, M., Frentress, J., Giambastiani, Y., McDonnell, J.J., Zuecco, G., Llorens, P., Siegwolf, R.T.W., Dawson, T.E., and Kirchner, J.W., (2018), Ideas and perspectives: Tracing terrestrial ecosystem water fluxes using hydrogen and oxygen stable isotopes - challenges and opportunities from an interdisciplinary perspective. *Biogeosciences*, 15(21), pp. 6399-6415, doi:10.5194/bg-15-6399-2018
- Philip, J.R., (1966), Plant water relations: Some physical aspects. *Annual Review of Plant Physiology*, 17, pp. 245-268, doi:10.1146/annurev.pp.17.060166.001333
- Pruess, K., (1991), TOUGH2-A general-purpose numerical simulator for multiphase fluid and heat flow.

- Razavi, S., Jakeman, A., Saltelli, A., Prieur, C., Iooss, B., Borgonovo, E., Plischke, E., Lo Piano, S., Iwanaga, T., Becker, W., Tarantola, S., Guillaume, J.H.A., Jakeman, J., Gupta, H., Melillo, N., Rabitti, G., Chabridon, V., Duan, Q.Y., Sun, X.F., Smith, S., Sheikholeslami, R., Hosseini, N., Asadzadeh, M., Puy, A., Kucherenko, S., and Maier, H.R., (2021), The Future of Sensitivity Analysis: An essential discipline for systems modeling and policy support. *Environ. Modell. Softw.*, 137, pp. 22, doi:10.1016/j.envsoft.2020.104954
- Robertson, J.A., and Gazis, C.A., (2006), An oxygen isotope study of seasonal trends in soil water fluxes at two sites along a climate gradient in Washington state (USA). *Journal of Hydrology*, 328(1-2), pp. 375-387, doi:10.1016/j.jhydrol.2005.12.031
- Rothfuss, Y., and Javaux, M., (2017), Reviews and syntheses: Isotopic approaches to quantify root water uptake: a review and comparison of methods. *Biogeosciences*, 14(8), pp. 2199-2224, doi:10.5194/bg-14-2199-2017
- Sheikholeslami, R., Razavi, S., and Haghnegandar, A., (2019), What should we do when a model crashes? Recommendations for global sensitivity analysis of Earth and environmental systems models. *Geosci. Model Dev.*, 12(10), pp. 4275-4296, doi:10.5194/gmd-12-4275-2019
- Shurbaji, A.R.M., and Phillips, F.M., (1995), A numerical model for the movement of H₂O, H₂¹⁸O, and 2HHO in the unsaturated zone. *Journal of Hydrology*, 171(1-2), pp. 125-142, doi:10.1016/0022-1694(94)02604-a
- Šimůnek, J., (1991), Numerical simulation of the transport processes in soil. *Vodohospodarsky Casopis (CSFR)*,
- Šimůnek, J., Sejna, M., Saito, H., Sakai, M., and van Genuchten, M.T., The HYDRUS-1D Software Package for Simulating the One-Dimensional Movement of Water, Heat, and Multiple Solutes in Variably Saturated Media, Version 4.0, *HYDRUS Software Series 3*, Department of Environmental Sciences, University of California Riverside, Riverside, California, USA, pp., 2008.
- Šimůnek, J., van Genuchten, M.T., and Sejna, M., (2016), Recent developments and applications of the HYDRUS computer software packages. *Vadose Zone Journal*, 15(7), pp. 25, doi:10.2136/vzj2016.04.0033

- Sprenger, M., Stumpp, C., Weiler, M., Aeschbach, W., Allen, S.T., Benettin, P., Dubbert, M., Hartmann, A., Hrachowitz, M., Kirchner, J.W., McDonnell, J.J., Orłowski, N., Penna, D., Pfahl, S., Rinderer, M., Rodriguez, N., Schmidt, M., and Werner, C., (2019), The Demographics of Water: A Review of Water Ages in the Critical Zone. *Reviews of Geophysics*, 57(3), pp. 800-834, doi:10.1029/2018rg000633
- Stumpp, C., Bruggemann, N., and Wingate, L., (2018), Stable isotope approaches in vadose zone research. *Vadose Zone Journal*, 17(1), doi:10.2136/vzj2018.05.0096
- Stumpp, C., Stichler, W., Kandolf, M., and Šimůnek, J., (2012), Effects of land cover and fertilization method on water flow and solute transport in five lysimeters: A long-term study using stable water isotopes. *Vadose Zone Journal*, 11(1), pp. 14, doi:10.2136/vzj2011.0075
- Van Dam, J.C., Huygen, J., Wesseling, J., Feddes, R., Kabat, P., Van Walsum, P., Groenendijk, P., and Van Diepen, C., 1997. Theory of SWAP version 2.0; Simulation of water flow, solute transport and plant growth in the soil-water-atmosphere-plant environment, DLO Winand Staring Centre.
- Verburg, K., SWIMv2. 1 user manual, CSIRO, Australia, Division of Soils, pp., 1996.
- Waisman, H., De Coninck, H., and Rogelj, J., (2019), Key technological enablers for ambitious climate goals: insights from the IPCC special report on global warming of 1.5 degrees C. *Environmental Research Letters*, 14(11), doi:10.1088/1748-9326/ab4c0b
- Wallace, J.S., (2000), Increasing agricultural water use efficiency to meet future food production. *Agriculture Ecosystems & Environment*, 82(1-3), pp. 105-119, doi:10.1016/s0167-8809(00)00220-6
- Wang, J., Lu, N., and Fu, B.J., (2019), Inter-comparison of stable isotope mixing models for determining plant water source partitioning. *Science of the Total Environment*, 666, pp. 685-693, doi:10.1016/j.scitotenv.2019.02.262
- Wang, X.F., and Yakir, D., (2000), Using stable isotopes of water in evapotranspiration studies. *Hydrological Processes*, 14(8), pp. 1407-1421, doi:10.1002/1099-1085(20000615)14:8<1407::aid-hyp992>3.0.co;2-k

- Xiao, W., Wei, Z.W., and Wen, X.F., (2018), Evapotranspiration partitioning at the ecosystem scale using the stable isotope method-A review. *Agricultural and Forest Meteorology*, 263, pp. 346-361, doi:10.1016/j.agrformet.2018.09.005
- Zhang, Y.Y., Wu, S.X., Kang, W.R., and Tian, Z.H., (2022), Multiple sources characteristics of root water uptake of crop under oasis farmlands in hyper-arid regions. *Agricultural Water Management*, 271, pp. 8, doi:10.1016/j.agwat.2022.107814

Chapter 2 Adapting HYDRUS-1D to Simulate the Transport of Soil Water Isotopes With Evaporation Fractionation

Abstract: Ecohydrological processes are often evaluated by studying the fate of stable water isotopes. However, isotopic fractionation during evaporation is often ignored or simplified in current models, resulting in simulation errors that may be propagated into practical applications of stable isotope tracing. In this study, we adapted and tested the HYDRUS-1D model, a numerical model widely used to simulate variably-saturated water flow and solute transport in porous media, by including an option to simulate isotope fate and transport while accounting for evaporation fractionation. The numerical results obtained by the adapted model were in excellent agreement with existing analytical solutions. Additional plausibility tests and field evaluation further demonstrated the adapted model's accuracy. A simple particle tracking algorithm was also implemented to calculate soil water's transit times and further validate the modified model's results. Transit times calculated by the particle tracking module (PTM) were similar to those estimated by the isotope peak displacement method, validating the applicability of the PTM. The developed model represents a comprehensive tool to numerically investigate many important research problems involving isotope transport processes in the critical zone.

2.1 Introduction

Evaporation fractionation is characterized by the retainment of heavier isotopes in the liquid phase and the preferential affinity of lighter isotopes in the vapor phase (e.g., *Gonfiantini et al.*, 2018). Due to evaporation fractionation's unique characteristics, stable water isotopes (^2H and ^{18}O) are good indicators for studying many ecohydrological processes in the critical zone (*Gehrels et al.*, 1998; *Sprenger et al.*, 2016a), such as partitioning evapotranspiration (*Kool et al.*, 2014; *Xiao et al.*, 2018) and identifying the sources of crop water uptake (i.e., sourcing) (e.g., *Corneo et al.*, 2018; *Ma and Song*, 2016; *Wang et al.*, 2019) at the soil-vegetation-atmosphere interface. Models that can accurately simulate the transport and fractionation of isotopes are necessary to properly interpret isotopic data in the critical zone.

The concept of water transit or travel time (TT), defined as the time elapsed between water entering and leaving a reservoir, provides a useful insight into many ecohydrological issues, such as partitioning recharge and discharge sources, evaluating the role of mobile and immobile waters, and inferring temporal origins of root water uptake (e.g., *Allen et al.*, 2019; *Brinkmann et al.*, 2018; *McDonnell*, 2014; *Sprenger et al.*, 2016b). The traditional isotope-based method for estimating TTs is by inversely estimating lumped isotope transport parameters assuming time-invariant TT distributions (TTDs) (e.g., *Maloszewski et al.*, 2006; *Stumpp and Maloszewski*, 2010; *Timbe et al.*, 2014) or StorAge Selection (SAS) functions (*Rinaldo et al.*, 2015).

However, the lumped models overgeneralize the isotope transport mechanisms. Some of them cannot truly describe the isotope transport or TTDs under transient conditions, while others can account for the time-variance of TTDs but can only describe the mixing and partitioning of isotopes (*Jury et al.*, 1986; *Sprenger et al.*, 2016a). Physics-based isotope transport models are needed to fully describe the spatial-temporal evolution of isotope concentrations under field conditions (*Kim et al.*, 2016). Such flow and transport models usually rely on the Richards and convection-dispersion equations, respectively.

When evaporation fractionation can be neglected, one can simulate the fate and transport of isotopes in soils as standard solutes. For example, *Stumpp et al.* (2012) used the modified HYDRUS-1D model with isotopic information to analyze the effects of the vegetation cover and fertilization measures on water flow and solute transport in lysimeters. This modified model is available at <https://www.pc-progress.com/en/Default.aspx?h1d-lib-isotope>. *Sprenger et al.* (2016b) used this modified model to infer soil water residence times at different depths. *Brinkmann et al.* (2018) applied the same model to estimate the residence time distribution of soil water and identify the temporal origin of water taken up by *Picea abies* and *Fagus sylvatica*.

This modified version of the HYDRUS-1D model by *Stumpp et al.* (2012) allows isotopes to leave the soil profile at the soil surface without considering the fractionation effect during evaporation. This is implemented by assuming that the

isotope concentration of the evaporation flux is the same as that of soil water at the soil surface. However, ignoring the evaporative enrichment, as done in this modified HYDRUS-1D, leads to underestimating ^2H and ^{18}O concentrations in the topsoil, which may be more significant in regions with higher evaporative losses (*Sprenger et al.*, 2018). Additionally, transit times calculations as done in these studies (e.g., *Sprenger et al.*, 2016b; *Brinkmann et al.*, 2018) are based on isotope transport simulations and require labor-intensive and time-consuming high precision isotope measurements to calibrate the model. The inaccurate sampling or modeling of soil water isotopes, especially in case of physical-nonequilibrium (i.e., immobile water content, dual-porosity/permeability type solute transport), can easily lead to large errors in transit time calculations (e.g., *Sprenger et al.*, 2018; *Tetzlaff et al.*, 2014).

The temporal evolution of evaporation fractionation was first studied and modeled for the free water surface (*Craig and Gordon*, 1965). The Craig-Gordon model has been the cornerstone of isotope hydrology since it was proposed in 1965. After that, *Zimmermann et al.* (1967) applied this model to saturated soil under steady-state evaporation conditions. *Barnes and Allison* (1983) extended this work to isothermal steady-state evaporation conditions in unsaturated soils. *Barnes and Allison* (1984) further extended this work to the nonisothermal steady-state conditions in unsaturated soils with a defined soil temperature profile. *Barnes and Allison* (1983, 1984) also provided analytical solutions for the transport of isotopes with evaporation fractionation

under steady-state conditions. However, to describe and predict the spatial and temporal evolution of isotope concentrations under field evaporation conditions, a model capable of describing transient conditions is required.

Shurbaji and Phillips (1995) proposed the first numerical model (ODWISH) that considered evaporation fractionation. This model coupled heat transport and water flow equations in the soil proposed by *Philip and De Vries* (1957) and introduced a transition factor into the isotope transport equation. This transition factor combines the influence of hydrology and isotope parameters. It changes slowly with depth except for quick changes in the evaporative zone, which is conducive to obtaining a unique isotope profile shape. However, the upper boundary condition must be determined by measuring temperatures and humidities at the soil surface and the evaporation front. The evaporation front is located at a depth above which the water vapor flux becomes dominant compared to the liquid flux. Generally, it corresponds to the peak in the isotope concentration profile (*Braud et al.*, 2005a). Since such data are rarely available, a model that interacts with the atmosphere is needed to address the surface energy budget. *Mathieu and Bariac* (1996) proposed a simplified model (MOISE) for constant potential evaporation and a predefined soil temperature profile. This model still lacked the option of evaluating the surface energy budget (*Soderberg et al.*, 2013).

Melayah et al. (1996a) fully coupled the transport of heat, water, and isotopes with surface energy budget calculations. The results showed that the model was very

sensitive to the initial isotope profile and small changes in liquid water convective transport. Better knowledge of isotope transport coefficients in porous media (e.g., mobile/immobile phases) should improve its prediction ability (*Melayah et al.*, 1996b). *Braud et al.* (2005a) corrected some inconsistencies in the derivations of *Melayah et al.* (1996a) and several isotope transport models, such as SiSPAT-Isotope (*Braud et al.*, 2005a) and Soil-Litter-Iso (*Haverd and Cuntz*, 2010) have been developed based on this modified theory. The Soil-Litter-Iso model was based on Ross' explicit numerical solution of the Richards equation (*Ross*, 2003), resulting in significantly improved computational efficiency compared with the SiSPAT-Isotope model. This allowed isotope calculations to be performed for soil profiles with vegetation using coarser spatial discretization and larger time steps (*Haverd and Cuntz*, 2010). However, these models did not consider the impacts of physical nonequilibrium flow (e.g., immobile water or preferential flow) on isotope transport and concentrations. *Muller et al.* (2014) and *Sprenger et al.* (2018) used the SWIS model (Soil Water Isotope Simulator) to model stable isotopes for uniform and nonequilibrium (mobile and bulk) soil water flow in the vadose zone, respectively. This model considered evaporation fractionation but neglected vapor flow.

Despite the successes of isotope transport modeling with evaporation fractionation, the current isotope transport models (Table 2.1) are not widely used. Some of them are no longer maintained (e.g., *Mathieu and Bariac*, 1996; *Melayah et*

al., 1996), are quite complex to deploy (e.g., *Braud et al.*, 2005a; *Haverd and Cuntz*, 2010), or still only implement a simple treatment of evaporation fractionation (e.g., *Shurbaji and Phillips*, 1995; *Stumpp et al.*, 2012), which may be some of the reasons why they are not commonly used.

The standard version of HYDRUS-1D can simulate volatile solutes' transport in soils by allowing solute transport by convection and dispersion in the liquid phase and diffusion in the soil air. Thus, the model is quite widely used to simulate transport processes of many emerging organic chemicals such as pesticides and fumigants (e.g., *Spurlock et al.*, 2013ab; *Brown et al.*, 2019). The governing equations for volatile solute transport (see Eqs. (6.55) and (6.56) in *Radcliffe and Šimůnek*, 2018) are similar to those for the isotope transport by *Braud et al.* (2005a). The relationship between the liquid and vapor solute concentrations is described in HYDRUS-1D by Henry's law, assuming an instantaneous distribution of a solute between the liquid and air phases. This volatile solute transport model in HYDRUS-1D can be adapted to simulate the transport of stable isotopes by modifying the upper boundary condition (considering fractionation) and reinterpreting Henry's coefficient in the governing solute transport equation.

Particle tracking algorithms represent an alternative and more straightforward way of calculating TTDs (e.g., *Šimůnek*, 1991; *Asadollahi et al.*, 2020) while still considering transient water flow. Since the particle tracking algorithm (e.g., *Šimůnek*,

1991) can be technically based solely on water balance calculations without requiring isotopic measurements, it needs much less input information than the stable water isotope transport models. Such algorithms can thus have broad applicability and can act as an excellent supplement to the traditional isotope transport-based methods for calculating transit times. However, it is still highly recommended to observe isotopic data, identifying accurate model parameters and travel times (e.g., *Groh et al.*, 2018; *Mattei et al.*, 2020; *Sprenger et al.*, 2015), and verifying model-determined TTs.

The objectives of this study thus are: 1) to adapt the current HYDRUS-1D model to simulate water flow and transport of stable water isotopes while considering multiple types of evaporation fractionation situations and soil conditions (i.e., isothermal/non-isothermal conditions, equilibrium and nonequilibrium flow, with and without vapor flow), 2) to verify the new model using analytical solutions and plausibility tests, 3) to implement a simple water-flow based particle tracking algorithm, and 4) to evaluate the capability of the new isotope transport and particle tracking modules using a field dataset. The new isotope transport and particle tracking modules provide HYDRUS-1D users with a comprehensive tool for assessing transit times, simulating continuous dynamic changes in soil water isotope concentrations, and numerically investigating many fundamental research problems involving sourcing and timing of soil water.

Table 2.1. History of the development of physics-based transport models for soil water stable isotopes.

Model name	Reference	Description
HYDRUS isotope module	<i>Stumpp et al. (2012)</i>	Without fractionation
ODWISH	<i>Shurbaji and Phillips (1995)</i>	With fractionation, no surface energy budget
MOISE	<i>Mathieu and Bariac (1996); Melayah et al. (1996)</i>	With fractionation, no surface energy budget
SiSPAT-Isotope	<i>Braud et al. (2005a, 2005b)</i>	With fractionation and surface energy budget, but no physical nonequilibrium flow, numerically inefficient
Soil-Litter-Iso	<i>Haverd and Cuntz (2010)</i>	With fractionation and surface energy budget, but no physical nonequilibrium flow
SWIS	<i>Muller et al. (2014); Sprenger et al. (2018)</i>	With fractionation but without vapor flow

2.2 Definition of the Isotope Concentrations

Following *Braud et al. (2005a)*, the concentration C_i (kg m⁻³) of the isotope i , can be defined as:

$$C_i = \frac{m_i}{V} = \frac{m_i}{m_T} \frac{m_T}{V} = \frac{N_i M_i}{N_i M_i + N_w M_w} \frac{N_i M_i + N_w M_w}{V} \approx \frac{M_i}{M_w} R_i \rho \quad (2.1)$$

where m_i (kg) is the mass of the isotope i , either in the liquid or vapor phase, V (m³) is the volume of water, m_T (kg) is the total mass of water, M_i and M_w are the molar masses of water including the isotope i and ordinary water (kg/mol), respectively, N_i and N_w (mol) are the numbers of moles of water including the isotope i and ordinary water, respectively, R_i [-] is the isotope ratio of the isotope i (i.e., $\frac{N_i}{N_w}$), and ρ (kg/m³)

is the density of water either in the liquid (ρ_w) or vapor (ρ_v) phases (see Appendix A).

In this equation, we assumed that $N_i M_i \ll N_w M_w$ to get the last term.

The relationship between the isotope ratio R and isotopic composition δ is:

$$\delta_i(\text{‰}) = \frac{R_i - R_{std}}{R_{std}} 1000\text{‰} \quad (2.2)$$

where R_i and $R_{standard}$ are the isotope ratios in the water sample and the standard sample (the Vienna Standard Mean Ocean Water (VSMOW, 0‰), $R_{std} = 155.76 \times 10^{-6}$ for HDO and $R_{standard} = 2005.2 \times 10^{-6}$ for H_2^{18}O , according to *Gonfiantini* (1978)). R_i refers to the $^{18}\text{O}/^{16}\text{O}$ or $^2\text{H}/^1\text{H}$ ratios [-] that can be deduced from Eq. (2.1) as follows:

$$R_i = \frac{M_w C_i}{M_i \rho} \quad (2.3)$$

Note that in this study, the term isotope ratio refers to R [-], isotopic composition refers to δ (‰), and isotope concentration to C (kg m^{-3}). The results will be presented throughout the manuscript in δ -notation, even though numerical computations may be performed using the C , R , or δ notations.

2.3 Craig-Gordon Model (1965)

The separation of heavy and light isotopes between reservoirs (or reactants and products) is called isotopic fractionation (*Gat*, 2010; *Kendall and McDonnell*, 2012). Isotopic fractionation can be divided into equilibrium fractionation (chemical thermodynamic fractionation) and kinetic fractionation (physical diffusion fractionation) according to the processes that cause this change. Equilibrium

fractionation occurs during chemical reactions at equilibrium (exchange reactions); the heavy isotopes are concentrated in substances with the highest bond force constants (i.e., the preferential affinity of the lighter isotope for the vapor phase) (Fry, 2006). Kinetic fractionation is caused by the differences in the diffusion rates of water molecules through the air (i.e., preferential diffusion of the lighter isotope) (Gat, 2010). Evaporation fractionation between the soil and free atmosphere includes both equilibrium and kinetic fractionations (Craig, 1961). Craig and Gordon (1965) calculated the isotope evaporation flux at the liquid-vapor interface based on these two types of fractionations (Fig. 2.1).

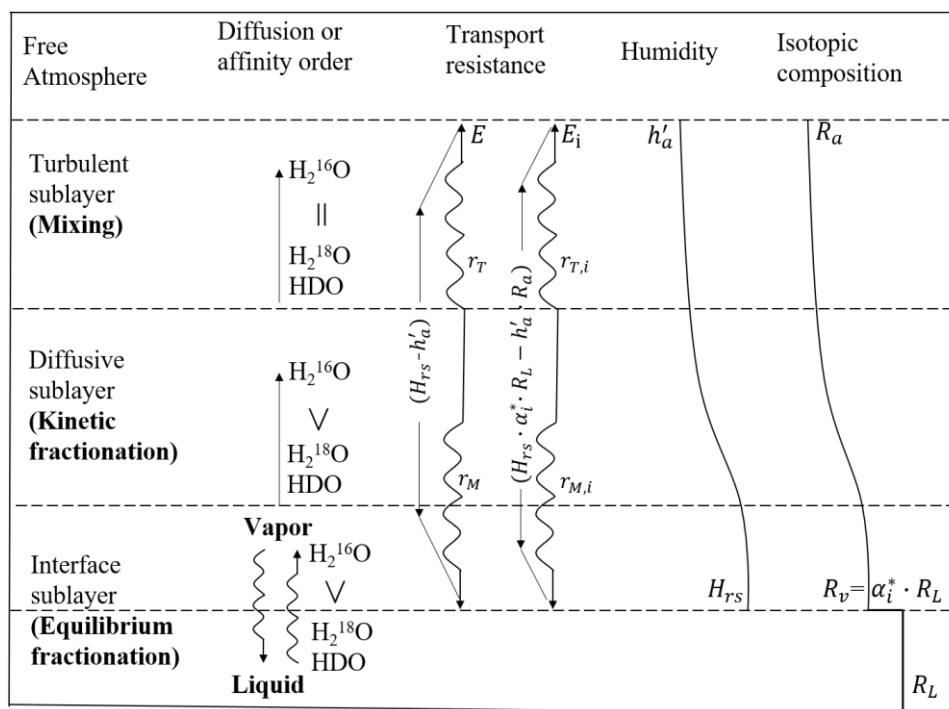


Figure 2.1. The Craig–Gordon model of isotopic fractionation during evaporation (modified from Gat, 2010).

This model considers three layers (Fig. 2.1): (a) a liquid-vapor interface where condensation, evaporation, and equilibrium fractionation occur, (b) a diffusive sublayer where molecular diffusion dominates and thus kinetic fractionation occurs, and (c) a turbulently mixed sublayer where mixing dominates, and thus no fractionation occurs (Gat, 2010; Horita *et al.*, 2008). The water vapor and isotope evaporation fluxes between the water surface and the bottom of the free atmosphere are described by Ohm's Law (or Fick's law) as an analog of the concentration gradient and transport resistance (Braud *et al.*, 2005a; Braud *et al.*, 2009; Gat, 2010)

The evaporation flux for water vapor E (kg/m²/s) is:

$$E = \frac{\rho_{sat}^v(T_s)(H_{rs} - h_a')}{r_a} \quad (2.4)$$

where r_a (s/m) is the sum of the resistances (r_M+r_T) of water vapor to diffusive flow in the diffusive (r_M) and turbulent (r_T) sublayers, ρ_{sat}^v is the density of the saturated water vapor (kg/m³) (see Appendix A), H_{rs} [-] is the relative humidity of the soil air phase at the surface, and h_a' [-] is the relative humidity of the atmosphere at the air temperature T_a (K) normalized to the relative humidity of the atmosphere (h_a [-]) at the interface temperature T_s (K). H_{rs} and h_a' can be calculated as follows:

$$H_{rs} = \exp\left(\frac{Mgh_s}{R_u T_s}\right) \quad (2.5)$$

$$h_a' = h_a \frac{\rho_{sat}^v(T_a)}{\rho_{sat}^v(T_s)} \quad (2.6)$$

where g is the gravitational acceleration [LT⁻²], M is the molecular weight of water (kg/mol) (0.018015), R_u is the universal gas constant (J/mol/K) (8.314), h_s is the

matic potential at the soil surface [L], and T_s and T_a are the temperatures of the soil surface and atmosphere (K), respectively.

The corresponding evaporation flux for water isotopes E_i (kg/m²/s) is:

$$E_i = \frac{(C_{is}^v - C_{ia}^v)}{r_i} = \frac{(C_{is}^v - C_{ia}^v)}{\alpha_i^k \cdot r_a} = \frac{\rho_{sat}^v(T_s)}{\alpha_i^k r_a} \frac{M_i}{M_w} (H_{rs} \cdot \alpha_i^* \cdot R_L - h_a' \cdot R_a) \quad (2.7)$$

$$= \frac{E}{\alpha_i^k} \frac{M_i}{M_w} \frac{(H_{rs} \cdot \alpha_i^* \cdot R_L - h_a' \cdot R_a)}{H_{rs} - h_a'}$$

The isotope ratio of the evaporation flux R_E is:

$$R_E = E_i/E = [H_{rs} \cdot \alpha_i^* \cdot R_L - h_a' \cdot R_a] / [(H_{rs} - h_a') \cdot \alpha_i^k] \cdot \frac{M_i}{M_w} \quad (2.8)$$

where C_{is}^v and C_{ia}^v are the isotope concentrations of the surface water vapor and atmosphere (kg m⁻³), r_i (s/m) is the sum of the resistances ($r_{Mi} + r_{Ti}$) of water isotopes to diffusive flow in the diffusive (r_{Mi}) and turbulent (r_{Ti}) sublayers, $R_v(R_L)$ are the isotope ratios of the water vapor and remaining liquid water at the soil surface [-], respectively, R_a is the isotope ratio of the atmosphere [-], α_i^* is the equilibrium fractionation factor [-], and α_i^k is the kinetic fractionation factor [-]. Note that α_i^* is defined here as the ratio of vapor to liquid phase isotope ratios, and it is thus smaller than 1.

The equations used to compute α_i^* for ²H and ¹⁸O isotopes as a function of temperature T (K) can be found in *Majoube* (1971) and *Horita and Wesolowski* (1994).

The equations by *Majoube* (1971) were used in this study:

$$\alpha_i^* \left(\frac{^{18}\text{O}}{^{16}\text{O}} \right) = \exp \left(2.0667 \cdot 10^{-3} + \frac{0.4156}{T} - \frac{1.137 \cdot 10^3}{T^2} \right) \quad (2.9)$$

$$\alpha_i^* \left(\frac{^2\text{H}}{^1\text{H}} \right) = \exp \left(-52.612 \cdot 10^{-3} + \frac{76.248}{T} - \frac{24.844 \cdot 10^3}{T^2} \right) \quad (2.10)$$

The kinetic fractionation factor α_i^k is calculated as (*Mathieu and Bariac*, 1996):

$$\alpha_i^k = \left(\frac{D^v}{D_i^v} \right)^{n_k} \quad (2.11)$$

where n_k is the kinetic fractionation coefficient [-], and D^v and D_i^v are the molecular diffusion coefficients of light and heavy water (isotopes) in free air [L^2T^{-1}], respectively.

The diffusion ratio D^v/D_i^v can be calculated from Graham's Law of gas diffusion:

$$\frac{D^v}{D_i^v} = \left(\frac{M_i(M_w + 0.029)}{M_w(M_i + 0.029)} \right)^{1/2} \quad (2.12)$$

where the number 0.029 represents the mean molecular weight of air (kg/mol). For ^{18}O , $M_w=0.018$ kg/mol and $M_i=0.020$ kg/mol, and thus $D^v/D_i^v=1.0324$; while for ^2H , $M_w=0.018$ kg/mol and $M_i=0.019$ kg/mol, and thus $D^v/D_i^v=1.0166$, which are the values used in our study. In addition to these theoretical values, much research has been conducted to measure these values. Readers are referred to *Horita et al.* (2008) for more details. For example, *Merlivat* (1978) measured $D^v/D_i^v(^2\text{H})=1.0251$ and $D^v/D_i^v(^{18}\text{O})=1.0285$.

The kinetic fractionation coefficient n_k is associated with considerable uncertainty depending on evaporation conditions. Different equations have been used to calculate this value. Readers can refer to *Braud et al. (2005b)*, *Horita et al. (2008)*, and *Quade et al. (2018)* for more details. Table S2.1 shows the equations used in this study.

The equilibrium fractionation enrichment ε^* (‰), and the kinetic fractionation enrichment ε_k (‰) can be calculated as follows (*Gat, 2010*):

$$\varepsilon^* = 1000 \cdot (1 - \alpha_i^*) \quad (2.13)$$

$$\varepsilon_k = 1000 \cdot (\alpha_i^k - 1) \cdot (H_{rs} - h_a') \quad (2.14)$$

This equation can be further simplified to get the widely used kinetic fractionation enrichment equation (*Horita et al., 2008*):

$$\varepsilon_k = 1000 \cdot \left(\left(\frac{D^v}{D_i^v} \right)^{n_k} - 1 \right) \cdot (H_{rs} - h_a') \quad (2.15)$$

$$\cong 1000 \cdot n_k \cdot \left(\frac{D^v}{D_i^v} - 1 \right) \cdot (H_{rs} - h_a')$$

According to *Gonfiantini (1986)*, the total fractionation factor (α_i^{total}) can be simplified and expressed as follows:

$$\alpha_i^{total} = 1/\alpha_i^* + \frac{\varepsilon_k}{1000} \quad (2.16)$$

The isotope ratio of the evaporation flux (R_E) is then calculated using its linear relationship with the isotope ratio of the liquid phase (R_L):

$$R_E = R_L/\alpha_i^{total} \quad (2.17)$$

2.4 Numerical Models

The current isotope transport models can be generally divided into two groups. The first group includes numerical models for evaporation fractionation without vapor flow. These models can be used in relatively humid areas, where the evaporation front is close to the ground surface, and vapor flow in the soil profile can thus be neglected. There is no fractionation within the soil due to the lack of the vapor phase (or its consideration). The second group includes numerical models for evaporation fractionation with vapor flow. These models are intended for more arid zones, where the evaporation front can occur deeper in the soil profile, and vapor flow in the soil profile should thus be considered. Under such conditions, both equilibrium and kinetic fractionations must be considered within the soils (*Braud et al.*, 2005a; *Mathieu and Bariac*, 1996). For the calculation of relevant water flow and heat transport parameters, the readers are referred to the HYDRUS-1D manual (*Šimůnek et al.*, 2008). Here we only focus on the calculation of isotope-related parameters.

2.4.1 Evaporation Fractionation in a System That Neglects Vapor Flow

When vapor flow can be neglected (e.g., in humid zones), the one-dimensional uniform soil water movement in HYDRUS-1D can be described using the Richards equation, which assumes that the air phase plays a negligible role in water flow and water flow due to thermal gradients can be neglected (*Šimůnek et al.*, 2008).

The governing equation for water flow then is:

$$\frac{\partial \theta_l}{\partial t} = \frac{\partial}{\partial z} \left[K_{Lh} \left(\frac{\partial h}{\partial z} + \cos \gamma \right) \right] - S \quad (2.18)$$

where θ_l is the liquid volumetric water content [L^3L^{-3}], t is time [T], h is the water pressure head [L], z is the spatial coordinate [L] (positive upward), γ is the angle between the flow direction and the vertical axis, K_{Lh} is the isothermal hydraulic conductivity of the liquid phase [LT^{-1}], and S is the sink term [$L^3L^{-3} T^{-1}$].

Since there is no fractionation within the soil, the governing equation for the isotope transport is the same as the classical advection-dispersion equation:

$$\frac{\partial \theta_l C_i^l}{\partial t} = \frac{\partial}{\partial z} \left(D_i^{l*} \frac{\partial C_i^l}{\partial z} \right) - \frac{\partial (q_l C_i^l)}{\partial z} - S C_i^l \quad (2.19)$$

where C_i^l corresponds to isotope concentrations of soil water ($kg\ m^{-3}$), q_l is the liquid water flux [LT^{-1}], and D_i^{l*} is the effective dispersion coefficient of the isotope i in soil water [L^2T^{-1}]. Evaporation fractionation, which does not appear in Eq (2.19), is considered using the upper boundary condition. Since Eq. (2.19) is a linear equation, linear conversions of concentration do not affect the numerical results. Therefore, not only the C notation, but also the R or δ notations can be used to define isotope concentrations in the numerical model.

Compared with traditional solute transport models, which leave all solutes behind in the soil during evaporation, the isotope transport models allow isotopes to leave with evaporation. *Stumpp et al.* (2012) did not consider fractionation and assumed that the isotope concentration of the evaporation flux is the same as that of the soil water

at the soil surface. Here, the isotope ratio of the evaporation flux is instead evaluated using two methods. The first method uses the Craig-Gordon model (Eq. (2.8)), which requires the atmosphere's relative humidity, temperature, and isotope ratio as additional inputs. The second approach follows the *Gonfiantini* (1986) model (Eqs 2.16~2.17), which requires only the atmosphere's relative humidity as an additional input. The isotope ratio of the evaporation flux is then automatically used in HYDRUS to calculate the isotope evaporation flux at the upper boundary corresponding to the water flux.

2.4.2 Evaporation Fractionation in a System That Considers Vapor Flow

a. Water Flow

Vapor flow in the soil profile should be considered in many arid zones. Nonisothermal liquid and vapor flow in HYDRUS-1D is described as follows (*Saito et al.*, 2006; *Zheng et al.*, 2020):

$$\frac{\partial \theta_T(h)}{\partial t} = \frac{\partial}{\partial z} \left[K_{Lh} \left(\frac{\partial h}{\partial z} + \cos \gamma \right) + K_{LT} \frac{\partial T}{\partial z} + K_{vh} \frac{\partial h}{\partial z} + K_{vT} \frac{\partial T}{\partial z} \right] - S \quad (2.20)$$

$$q_l = -K_{Lh} \left(\frac{\partial h}{\partial z} + \cos \gamma \right) - K_{LT} \frac{\partial T}{\partial z} \quad (2.21)$$

$$q_v = -K_{vh} \frac{\partial h}{\partial z} - K_{vT} \frac{\partial T}{\partial z} \quad (2.22)$$

where θ_T is the total volumetric water content [L^3L^{-3}], being the sum ($\theta_T = \theta_l + \theta_v$) of the volumetric liquid water content (θ_l) and the volumetric water vapor content (θ_v) [L^3L^{-3}] (both expressed in terms of equivalent water contents, i.e., $\theta_v = \rho_v \frac{\theta_s - \theta_l}{\rho_w}$, where θ_s is the saturated water content [L^3L^{-3}]), K_{LT} is the thermal hydraulic conductivity of the liquid phase [$L^2K^{-1}T^{-1}$], K_{vh} is the isothermal vapor hydraulic conductivity [LT^{-1}],

K_{vT} is the thermal vapor hydraulic conductivity [$L^2K^{-1}T^{-1}$], and q_v is the vapor flux [LT^{-1}]. The right-hand side of Eq. (2.20) represents isothermal liquid flow, gravitational liquid flow, thermal liquid flow, isothermal vapor flow, and thermal vapor flow, respectively. Since several terms are a function of temperature, this equation should be solved simultaneously with the heat transport equation to account for temporal and spatial changes in soil temperature properly.

b. Heat Transport

The governing equation for heat transport is (*Šimůnek et al.*, 2008):

$$\begin{aligned}
C_p(\theta_l) \frac{\partial T}{\partial t} + L_0 \frac{\partial \theta_v}{\partial t} \\
= \frac{\partial}{\partial z} \left(\lambda(\theta_l) \frac{\partial T}{\partial z} \right) - C_w q_l \frac{\partial T}{\partial z} - C_v \frac{\partial q_v T}{\partial z} - L_0 \frac{\partial q_v}{\partial z} \\
- C_w S T
\end{aligned} \tag{2.23}$$

where $\lambda(\theta_l)$ is the coefficient of the apparent thermal conductivity of the soil [$MLT^{-3}K^{-1}$] and $C_p(\theta_l)$, C_w , and C_v are the volumetric heat capacities [$ML^{-1}T^{-2}K^{-1}$] of the porous medium, the liquid phase, and vapor phase, respectively. L_0 is the volumetric latent heat of vaporization of liquid water [$ML^{-1}T^{-2}$]. The right-hand side of Eq. (2.23) represents the conduction of sensible heat (the first term), convection of sensible heat by liquid water (the second term) and water vapor (the third term), and convection of latent heat by vapor flow (the fourth term), and energy uptake by plant roots (the fifth term), respectively.

c. Isotope Transport

Following the theory of the SiSPAT-Isotope model (Braud *et al.*, 2005a), the total isotope flux is the sum of isotope fluxes in the liquid phase, q_i^l , and the vapor phase, q_i^v , while both fluxes include convection and diffusion terms. Assuming instantaneous equilibrium between the liquid and vapor phases, the liquid and vapor isotopic ratios can be related by an equilibrium fractionation factor (Mathieu and Bariac, 1996; Melayah *et al.*, 1996a). The governing equations for isotope transport then are:

$$\frac{\partial\{[\theta_l + (n_{soil} - \theta_l)\beta_i^*]C_i^l\}}{\partial t} = -\frac{\partial}{\partial z}[q_i^l + q_i^v] - SC_i^l \quad (2.24)$$

$$\begin{aligned} \frac{\partial\{[\theta_l + (n_{soil} - \theta_l)\beta_i^*]C_i^l\}}{\partial t} &= -\frac{\partial}{\partial z}[C_i^l q_l - D_i^{l*} \frac{\partial C_i^l}{\partial z} + \beta_i^* q_v C_i^l - D_i^{v*} \frac{\partial \beta_i^* C_i^l}{\partial z}] \\ &\quad - SC_i^l \end{aligned} \quad (2.25)$$

$$\begin{aligned} \frac{\partial\{[\theta_l + (n_{soil} - \theta_l)\beta_i^*]C_i^l\}}{\partial t} &= -\frac{\partial}{\partial z}[(q_l + \beta_i^* q_v - D_i^{v*} \frac{\partial \beta_i^*}{\partial z})C_i^l - (D_i^{l*} \\ &\quad + D_i^{v*} \beta_i^*) \frac{\partial C_i^l}{\partial z}] - SC_i^l \end{aligned} \quad (2.26)$$

that is:

$$\frac{\partial[\theta_i C_i^l]}{\partial t} = \frac{\partial}{\partial z}[D_i^{lv*} \frac{\partial C_i^l}{\partial z} - Q_i^{lv*} C_i^l] - SC_i^l \quad (2.27)$$

$$\theta_i = [\theta_l + (n_{soil} - \theta_l)\beta_i^*] \quad (2.28)$$

$$Q_i^{lv*} = (q_l + \beta_i^* q_v - D_i^{v*} \frac{\partial \beta_i^*}{\partial z}) \quad (2.29)$$

$$D_i^{lv*} = D_i^{l*} + D_i^{v*} \beta_i^* \quad (2.30)$$

$$C_i^v = \beta_i^* C_i^l \quad (2.31)$$

$$C_i^v = \frac{M_i}{M_w} R_i^v \rho_v = \frac{M_i}{M_w} \alpha_i^* R_i^l \rho_v = \alpha_i^* \frac{\rho_v}{\rho_w} C_i^l \quad (2.32)$$

where n_{soil} is the soil porosity [L^3L^{-3}], β_i^* is the ratio of the isotope concentration in the vapor phase and the isotope concentration in the liquid phase [-], and C_i^l (R_i^l) and C_i^v (R_i^v) are isotope concentrations (ratios) in soil water (vapor) ($kg\ m^{-3}$) ([-]), respectively. The effective dispersion coefficients of the isotope i in soil water (vapor), D_i^{l*} (D_i^{v*}) [L^2T^{-1}], are given as follows:

$$D_i^{l*} = D_i^{lo} \tau_w \theta_l + \Lambda |q_l| \quad (2.33)$$

$$D_i^{v*} = (n_{soil} - \theta_l) \tau_g D^v \left(\frac{D_i^v}{D^v} \right)^{n_k} \quad (2.34)$$

where τ_w and τ_g are tortuosity coefficients in the liquid and vapor phases [-], respectively, Λ is dispersivity [L], and D_i^{lo} is the molecular diffusion coefficient of the isotope i in free water [L^2T^{-1}] (see Appendix A).

d. Modifications on HYDRUS-1D

This subsection lists all implemented changes into the standard HYDRUS-1D model to simulate the fate and transport of stable water isotopes. To expand the capabilities of the HYDRUS-1D model and to be consistent with previous verification studies with other models (e.g., the plausibility tests and comparisons with the analytical solution of *Barnes and Alison*, 1984), a new upper boundary condition (BC) for water flow was implemented into the atmospheric boundary in HYDRUS-1D to simulate evaporation from bare soils. Actual evaporation E ($kg/m^2/s$) is calculated in this BC as a function of potential evaporation E_p ($kg/m^2/s$) and the difference in relative humidities between the atmosphere and the soil surface, similarly as done in other studies (*Mathieu and Bariac*, 1996; *Melayah et al.*, 1996; *Braud et al.*, 2005a).

This is a more convenient way of estimating actual evaporation at the upper boundary. However, if sufficient information is available, it is better to use the surface energy balance to estimate actual evaporation.

$$E = E_p \frac{H_{rs} - h_a'}{1 - h_a'} \quad (2.35)$$

The standard version of HYDRUS-1D can simulate the transport of volatile solutes by also considering solute transport via diffusion in the vapor phase. The governing equations for volatile solute transport (see Eqs. (6.55) and (6.56) in *Radcliffe and Šimůnek, 2018*) are very similar to those for isotope transport. The solute transport equation solved in HYDRUS-1D considers convective and diffusion-dispersion transport in the liquid phase and diffusion transport in the vapor phase. It does not consider convective transport in the vapor phase. To consider the vapor convection term in solute transport, two additional transport terms ($\beta_i^* q_v$) and $(D_i^{v*} \frac{\partial \beta_i^*}{\partial z})$ in Eq. (2.29) had to be included in the governing solute transport equation of HYDRUS-1D.

HYDRUS-1D considers the relationship between the liquid and vapor solute concentration that assumes instantaneous linear distribution of a solute between the liquid and vapor phases (Henry's law):

$$C_i^v = K_H C_i^l \quad (2.36)$$

where K_H is the Henry coefficient [-], which can be temperature-dependent. HYDRUS-1D assumes that temperature dependency can be expressed using the Arrhenius equation. To model the isotope transport using the current volatile solute

boundary condition in HYDRUS, one can replace the original Henry coefficient (K_H) with the ratio of the isotope concentration in the vapor phase and the isotope concentration in the liquid phase ($\beta_i^* = \frac{\rho_v}{\rho_w} \alpha_i^*$). Since the density of water vapor ρ_v is a function of relative humidity of soil air phase (i.e., the soil matric potential), while equilibrium fractionation factor α_i^* is a function of soil temperature, the Henry coefficient for isotope transport is, in general, a function of both depth z and temperature T .

The standard HYDRUS-1D uses the stagnant boundary layer BC for volatile solutes. This BC considers the convective solute flux with evaporation and the diffusion solute flux (by gaseous diffusion) through a stagnant boundary layer on the soil surface (Jury *et al.*, 1983). This upper boundary condition was modified to implement the Craig-Gordon model to account for both equilibrium and kinetic fractionations at the interface between the soil surface and the atmosphere (Eq. (2.7)).

2.4.3 Particle Tracking Module (PTM)

To calculate soil water travel times, the particle tracking algorithm from Šimůnek (1991) was implemented into HYDRUS-1D. The algorithm is based on the water balance calculations, with the development of soil water profiles fully described by solving the Richards equation (Fig. 2.2).

The first monitored particle below the soil surface is at depth $z = z_0$ at time $t = t_0$. The amount of water W_0 [L] is between this particle and the soil surface ($z = 0$):

$$W_0 = \int_0^{z_0} \theta(z, t_0) dz \quad (2.37)$$

During the time interval (t_0, t_1) , the amount of water N [L] passes through the soil surface:

$$N = \int_{t_0}^{t_1} [e(t) - i(t)] dt \quad (2.38)$$

where $e(t)$ [LT^{-1}] is actual evaporation and $i(t)$ [LT^{-1}] is actual infiltration from precipitation or irrigation. During the same interval, the layers in the root zone between the soil surface and the monitored particles are depleted by root water uptake S_T [L]:

$$S_T = \int_{t_0}^{t_1} \int_0^{z_p(t)} s(z, t) dz dt \quad (2.39)$$

where $z_p(t)$ is the particle depth at time t [L] and $s(z, t)$ is the sink (extraction) term [$L^3L^{-3} T^{-1}$]. At time t_1 , there is thus between the soil surface and the monitored particle the following quantity of water W_1 [L] (enriched by infiltration and reduced by evaporation and root water uptake):

$$W_1 = W_0 - N - S_T \quad (2.40)$$

The monitored particle is now located at a depth of $z = z_1$.

$$\begin{aligned} \int_0^{z_1} \theta(z, t_1) dz &= \int_0^{z_0} \theta(z, t_0) dz - \int_{t_0}^{t_1} [e(t) - i(t)] dt \\ &\quad - \int_{t_0}^{t_1} \int_0^{z_p(t)} s(z, t) dz dt \end{aligned} \quad (2.41)$$

By repeatedly solving this equation for the time sequence (t_0, t_1, \dots, t_n) , we obtain a sequence of depths (z_0, z_1, \dots, z_n) , i.e., we obtain the trajectory of the observed particle.

The calculation of the location of the second and further particles can be performed analogously. Now, however, the amount of water is balanced between the next two particles located at z_a and z_b . Between these particles, the amount of water W_0 , at time t_0 and the amount of water W_1 at time t_1 are:

$$W_0 = \int_{z_a(t_0)}^{z_b(t_0)} \theta(z, t_0) dz \quad (2.42)$$

$$W_1 = \int_{z_a(t_1)}^{z_b(t_1)} \theta(z, t_1) dz \quad (2.43)$$

During the time interval (t_0, t_1) , the amount of water between the two particles is depleted by the transpiration amount S_T :

$$S_T = \int_{t_0}^{t_1} \int_{z_a(t)}^{z_b(t)} s(z, t) dz dt \quad (2.44)$$

According to Eq. (2.40), the resulting equation now has the form:

$$\int_{z_a(t_1)}^{z_b(t_1)} \theta(z, t_1) dz = \int_{z_a(t_0)}^{z_b(t_0)} \theta(z, t_0) dz - \int_{t_0}^{t_1} \int_{z_a(t)}^{z_b(t)} s(z, t) dz dt \quad (2.45)$$

The algorithm itself proceeds as follows. From the particles' known position at the beginning of the time interval, the pre-solved development of the moisture profile, and the actual values of infiltration, evaporation, and transpiration, the first monitored particle's new position is calculated using Eq. (2.41). New positions of all other particles are then calculated using Eq. (2.45). On the surface and at the bottom of the soil profile,

new particles may be created or may leave the soil profile, depending on the moisture profile's actual development. By calculating particles' trajectories, the movement of inert substances not subject to dispersion can be modeled.

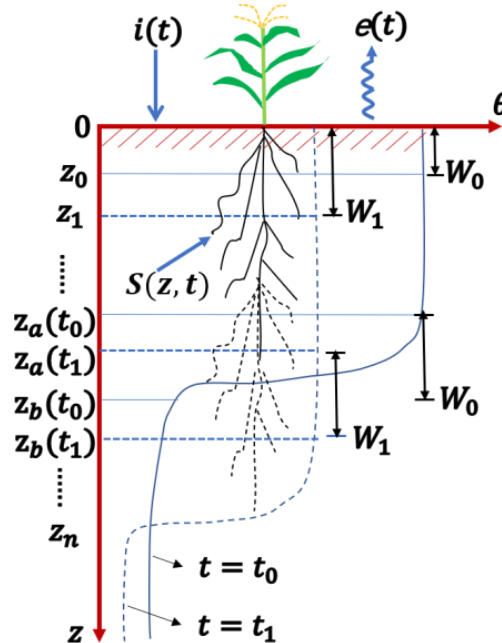


Figure 2.2. Schematic diagram of the water flow-based particle tracking module.

The initial position of particles can be defined geometrically (at specified depths) or based on mass balance calculations (by water storage). Similarly, the release of new particles at the boundary can be defined chronologically (at specified times) or meteorologically (rainfall events or depths). The newly implemented particle tracking module requires two input parameters: w_{Stand} and w_{Prec} . The w_{Stand} parameter represents the water storage, which separates neighboring particles in the soil profile at the beginning of the simulation. Therefore, the particles are not geometrically evenly distributed when the soil profile's initial water content is not uniform. The w_{Prec}

parameter is the amount of water that passes through the soil surface before a new particle is released. This means that particles are released at the soil surface only under wet conditions. Under dry conditions, the surface flux is directed out of the soil profile, and thus, new particles will not be released.

2.5 Numerical Implementations

The same graphical user interface (GUI) used in HYDRUS-1D is used to select and execute the model. The HYDRUS software uses the finite element method for spatial discretization and the finite difference method for temporal discretization. For consistency with the numerical model (the SiSPAT-Isotope model) used for the verification, the Galerkin-type finite element method (FEM) and an implicit finite difference scheme were used to solve the Richards and advection-dispersion equations for water flow and isotope transport in this study. However, the upstream weighting FEM for space weighting and the Crank-Nicholson scheme for time weighting are also available. At each time step, the isotope transport is calculated after the water flow and heat transport equations have been solved first. This provides the isotope transport routine with nodal values of soil temperature, soil matric potential, and water content at both old and new time levels to constitute the storage and transport coefficients for isotope transport in Eqs. (2.27~2.32). Details about the numerical solutions of subsurface water flow and heat and solute transport can be found in the HYDRUS-1D manual (*Šimůnek et al.*, 2008) and *Braud* (2000).

To adequately capture the isotope concentration at the soil surface, similar to the SiSPAT-Isotope model, the isotope transport equation's solution requires a fine resolution of the vertical unsaturated soil profile close to the soil surface. Three discretization schemes (i.e., coarse, medium, and fine) (Fig. S2.1) were selected in the following verification examples to explore the impact of spatial discretization on the modeling results. The first scheme uses 101 nodes uniformly distributed in the soil profile, i.e., with a spatial step of 1 cm. The second scheme uses 288 nodes with spatial steps gradually increasing from the bottom to the top, being twice as large at the bottom (0.46 cm) than the top (0.23 cm). The third scheme follows the same spatial discretization as used by *Braud et al.* (2005a) with 288 nodes (Fig. S2.1). The spatial steps increase from 1 mm at the surface to 1 mm at a depth of about 1 cm and 5 mm at 5 cm. They remain 5 mm between depths of about 5 to 95 cm and then gradually decrease to 1 mm at the bottom. Only the modeling results obtained using the fine spatial discretization are presented in the main text. The results obtained using medium and coarse spatial discretizations can be found in the Supplementary Material.

While the initial time step of 25 s was used in this study, time steps vary during the simulation. They are automatically adjusted by the model depending on the number of iterations required by the water flow scheme to converge (adaptive time discretization). Since the adaptive time discretization was used, the temporal resolution is expected to have only a minor effect on the results and is not discussed in this study.

It must be emphasized that the accuracy of the numerical solution of isotope transport equations is very sensitive to those of water flow and heat transport equations. The water flow iteration process continues until absolute changes in water contents (pressure heads) at all nodes in the unsaturated (saturated) zone between two successive iterations are less than prescribed tolerances. We used 10^{-7} for both water content and pressure head (m) tolerances. When heat transport is also considered, water flow and heat transport equations are solved simultaneously since they affect each other. Two choices are provided in this case, depending on whether the nodal water flux balance smaller than a prescribed tolerance (10^{-16} m/s) is used as a convergence criterion for water flow and heat transport. The former iteration criterion without the nodal water flux balance is more numerical efficient and more applicable for systems that neglect vapor flow. The latter convergence criterion with the nodal water flux balance is more accurate and recommended for a system that considers vapor flow. Note that iterations are not needed in standard HYDRUS-1D for solute transport when the governing solute transport equation is linear. In this study, the difference in the isotope flux at the upper boundary between two successive iterations smaller than a prescribed tolerance (10^{-16} kg/m²/s) was added as a convergence criterion for isotope transport. The above iterative criteria are important prerequisites for obtaining accurate numerical solutions. It is worth mentioning that the new HYDRUS isotope transport model is faster than the

SiSPAT-Isotope model when no heat transport is considered because fewer iterations are required by the water flow scheme to converge.

2.6 Model Verification and Evaluation

2.6.1 Verification of the Numerical Solutions

First, we verified the numerical model that considers evaporation fractionation without vapor flow against the analytical solution of *Zimmermann et al.* (1967) for isothermal saturated soils under steady evaporation. Second, the numerical model that considers evaporation fractionation with vapor flow was then verified against the analytical solution of *Barnes and Allison* (1984) for nonisothermal unsaturated soils under steady evaporation. Third, *Mathieu and Bariac* (1996) designed six plausibility tests for isothermal unsaturated soils to check whether the model produces plausible results as equilibrium and kinetic fractionations were sequentially switched on in the model. *Braud et al.* (2005a) and *Haverd and Cuntz* (2010) used these tests to verify the SiSPAT-Isotope and Soil-Litter-Iso models, respectively. We repeated these tests with the HYDRUS-1D Isotope model to see whether the new model produced expected shapes of isotope profiles.

We considered a one-meter deep soil profile of Yolo Light Clay from *Philip* (1957) in all verification examples. Basic soil hydraulic, thermal, and solute transport parameters are given in *Braud et al.* (2005a) and shown in Table 2.2. For consistency

with previous studies, we combined the van Genuchten (VG) water retention model (*van Genuchten*, 1980) with the *Burdine* (1953) and Brooks and Corey (BC) hydraulic conductivity model (*Brooks and Corey*, 1964):

$$\frac{\theta_l - \theta_r}{\theta_s - \theta_r} = \frac{1}{[1 + |\alpha h|^n]^m} \quad (2.46)$$

$$m = 1 - 2/n \quad (2.47)$$

$$K(\theta) = K_s \left(\frac{\theta_l - \theta_r}{\theta_s - \theta_r} \right)^\eta \quad (2.48)$$

where θ_s and θ_r are saturated and residual water content, respectively, m , n , and α , are the shape parameters of the retention curve, K_s is the saturated hydraulic conductivity, and η is the shape parameter of the conductivity curve.

Equations from *de Vries* (1963) and *Chung and Horton* (1987) (already available in HYDRUS) were used to describe the volumetric heat capacity and thermal conductivity, respectively. The tortuosity coefficients in the liquid and vapor phases (τ_w and τ_g) are evaluated in HYDRUS using the model of *Millington and Quirk* (1991) or *Moldrup et al.* (1997). In all verification examples, τ_w and τ_g were set to 0.67, and Λ was set to 0 to be consistent with previous studies to evaluate our model's accuracy. This choice is justified because convective and hydrodynamic dispersion processes are negligible compared with the diffusion process under evaporation conditions (*Auriault and Adler*, 1995).

Table 2.2. Basic soil hydraulic, thermal, and solute transport parameters.

Parameter	Symbol	Value
Saturated water content	θ_s	0.35 m ³ /m ³
Residual water content	θ_r	0.00 m ³ /m ³
Shape parameter of the retention curve	n	2.22
Shape parameter of the retention curve	m	0.099
Shape parameter of the retention curve	α	5.18 m ⁻¹
Saturated hydraulic conductivity	K_s	1.23×10 ⁻⁷ m/s
Shape parameter of the conductivity curve	η	9.143
Volumetric fraction of the solid phase	θ_n	0.60
Volumetric fraction of organic matter	θ_o	0.01
Empirical parameters	b_i (i=1,2,3)	-0.197, -0.962, 2.521 Wm ⁻¹ K ⁻¹
Volumetric heat capacity of the solid phase	C_n	1920000 Jm ⁻³ K ⁻¹
Volumetric heat capacity of the organic matter	C_o	2510000 Jm ⁻³ K ⁻¹
Volumetric heat capacity of the liquid phase	C_w	4180000 Jm ⁻³ K ⁻¹
Tortuosity coefficient in the liquid and vapor phases	τ_w, τ_g	0.67
Dispersivity	Λ	0

2.6.1.1 Comparison With the Analytical Solution of Zimmermann *et al.* (1967)

Zimmermann *et al.* (1967) conducted experiments and provided an analytical solution for the isotope transport in a homogeneous saturated soil column with the initial isotope ratio (isotopic composition), $R_\infty(\delta_\infty)$, evaporating at a steady rate, E_s , into the atmosphere of constant humidity, h_a , air temperature T_a , and isotope ratio (isotopic composition), $\delta_{ia}^v(R_{ia}^v)$, under isothermal conditions at a soil temperature T_z . Table 2.3 provides all relevant parameter values. Under steady-state conditions, the stable isotope profile can be explained by the balance between the upward convective flux (evaporation) and the downward diffusion flux of the isotope:

$$E_s(R_i^l - R_\infty) = D_i^{l*} dR_i^l/dz \quad (2.49)$$

where R_i^l is the isotope ratio at depth z (z is equal to zero at the soil surface and it is positive downwards).

The above equation can be solved to get:

$$R_i^l = R_\infty + (R_0 - R_\infty) \exp(-z/z_l) \quad (2.50)$$

where R_0 is the isotope ratio at the soil surface, and z_l is the characteristic length given by:

$$z_l = D_i^{l*}/E_s \quad (2.51)$$

If one reports the isotope ratio in Eq. (2.50) in the δ notation (‰) using Eq. (2.2), we can get:

$$\delta_i^l = \delta_\infty + (\delta_0 - \delta_\infty) \exp(-z/z_l) \quad (2.52)$$

where δ_0 (δ_i^l) are isotopic compositions at the soil surface and at depth z , respectively.

The isotopic composition at the soil surface δ_0 can be calculated using a variant of the Craig-Gordon model as follows (*Barnes and Allison, 1983*):

$$\alpha_i^* (1 + \delta_0) - h_a'(1 + \delta_{ia}^v) = (1 - h_a')\alpha_i^k(1 + \delta_\infty) \quad (2.53)$$

The analytical solution for ^{18}O is:

$$\delta^{18}\text{O} (\text{‰}) = 31.9 \exp(-16.949z) \cdot 1000\text{‰} \quad (2.54)$$

and for ^2H is:

$$\delta^{2}\text{H} (\text{‰}) = 67 \exp(-16.667z) \cdot 1000\text{‰} \quad (2.55)$$

In the HYDRUS numerical simulation, transport parameters were the same as those in the analytical solution. Both the upper and lower BCs were set to a constant water pressure head for water flow. The soil water pressure head was assumed to be 1 cm at the surface and 109.15 cm at the bottom. This BC allowed for a permanent water

supply at the bottom of the soil column and kept the soil saturated while maintaining the steady evaporation rate E_s . Both the upper and lower BCs were set to solute flux BCs for isotope transport. The surface solute flux in this example referred to the evaporation flux for water isotopes E_i calculated by the Craig-Gordon model (Eq. (2.7)). The bottom isotope flux was calculated assuming that the isotope ratio (isotopic composition) of supply water was the same as the initial values, $R_\infty(\delta_\infty)$. No heat transport was considered in this example.

Figs. 2.3a and 2.3b show an excellent agreement between the numerical and analytical solutions using a fine spatial discretization. Fig. S2.2 shows a comparison between the analytical and numerical solutions' results using different spatial discretizations. The maximum differences between the analytical and numerical solutions in the ^{18}O isotopic composition profiles were 0.21‰ (coarse), 0.20‰ (medium), and 0.20‰ (fine). The maximum differences between the analytical and numerical solutions in the ^2H isotopic composition profiles were 0.46‰ (coarse), 0.43‰ (medium), and 0.43‰ (fine). We may conclude that the isotope transport module can produce in this example accurate isotope profiles using all considered spatial discretization schemes.

Water that has experienced evaporation fractionation plots below the global/local meteoric water line (GMWL/LMWL) in dual-isotope plots. The occurrence of kinetic fractionation results in an evaporation line with a slope much

smaller than those of GMWL/LMWL (*Sprenger et al.*, 2016a). The “line conditioned excess” (LC-excess) is the difference between the δ^2H from a water sample and a linear transformation of the δ^2H from a given GMWL/LMWL (*Landwehr and Coplen*, 2006). The more negative it is, the stronger the kinetic fractionation is (*Sprenger et al.*, 2017). The dual-isotope plot (Fig. 2.3c) has a slope of about 2.09, which is much smaller than that (8.20) of the global meteoric water line (GMWL). The LC-excess profile (calculated by Eq. (A2.6)) shows the opposite trend to the isotopic composition profiles and is negative in the entire soil profile (Fig. 2.3d). These results suggest that kinetic fractionation also occurs. This is reasonable given the fact that kinetic fractionation factor (α_i^k) is not equal to one (Table 2.3).

Table 2.3. Values of all variables used in the analytical solution of *Zimmermann et al.* (1967).

Parameter	Value	
E_s	$1.003 \times 10^{-5} \text{ kgm}^{-2}\text{s}^{-1}$	
T_a, T_z	303.15 K (30 °C)	
h_a	0.2	
n_k	1	
	for ^{18}O	for ^2H
D_i^{1*}	$5.91 \times 10^{-10} \text{ m}^2/\text{s}$	$6.01 \times 10^{-10} \text{ m}^2/\text{s}$
Z_l	0.059 m	0.060 m
δ_{ia}^v	-14‰	-100‰
R_{ia}^v	0.001977127	0.000140184
δ_∞	0‰	0‰
R_∞	0.0020052	0.00015576
δ_0	31.9‰	67‰
R_0	0.002063684	0.00016733
α_i^*	0.9911	0.9311
α_i^k	1.031885	1.016363

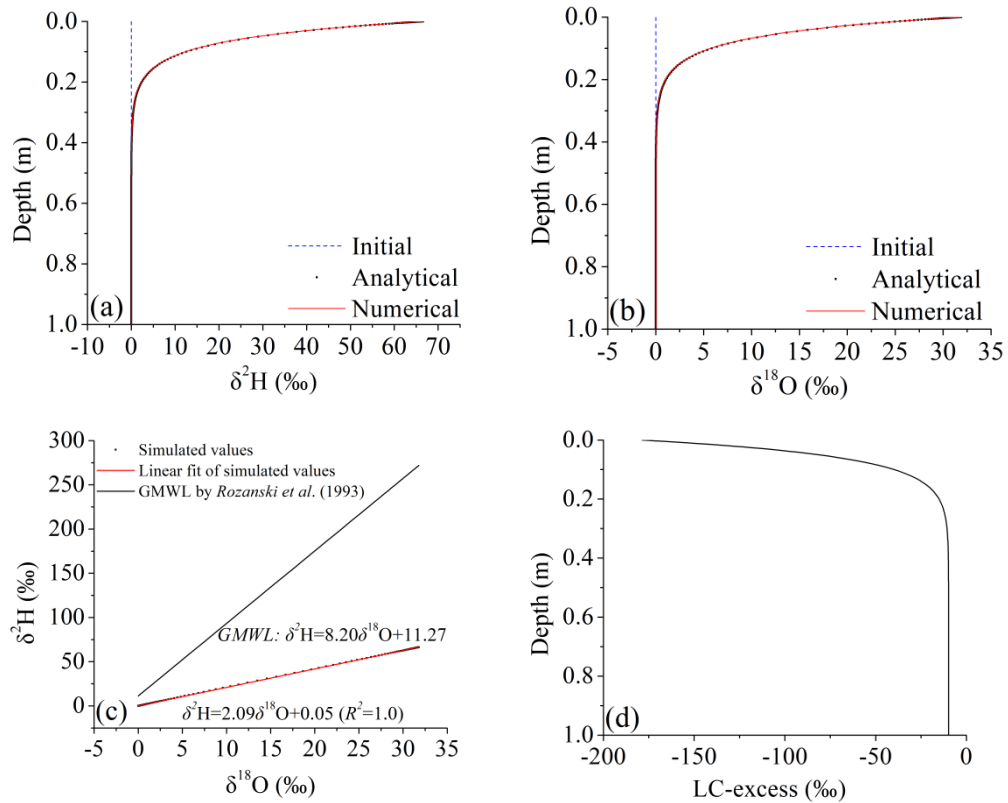


Figure 2.3. Comparison of analytical and numerical solutions for profiles of (a) the ^2H isotopic composition and (b) the ^{18}O isotopic composition, (c) the dual-isotope plot of simulated values, and (d) the LC-excess profile for isothermal saturated soil under steady evaporation.

2.6.1.2 Comparison With the Analytical Solution of Barnes and Allison (1984)

Barnes and Allison (1984) proposed an analytical solution for evaporation from unsaturated soil under steady and nonisothermal conditions. Conditions were the same as for the steady-state saturated case above, except that the initial pressure head was set to 0 in the entire soil profile, nonisothermal conditions were considered, and evaporation occurred at a different rate. Table 2.4 gives the values of all parameters required in this problem. Under steady-state conditions (i.e., at 250 days of the simulation), the stable isotope profile can be explained by the balance between the

upward convective flux (evaporation) and the downward diffusion flux of the isotope both in the liquid and vapor phases:

$$-E_s = \rho_w(q_l + q_v) = \rho_w q_l - D^{v*} \cdot \frac{d(H_r \cdot \rho_{sat}^v)}{dz} \quad (2.56)$$

$$-E_s R_\infty = q_i^l + q_i^v = (\rho_w q_l R_i - \rho_w D_i^{l*} \frac{dR_i^l}{dz}) - D_i^{v*} \frac{d(H_r \cdot \rho_{sat}^v \cdot R_i^v)}{dz} \quad (2.57)$$

where D^{v*} is the effective dispersion coefficient of the light isotope in soil water vapor, E_s is the steady state evaporation rate and H_r is the relative humidity of the soil air phase at a certain depth. H_r can be calculated by Eq. (2.5), while the matric potential h_s and temperature T_s at the soil surface should be replaced by corresponding values at a certain soil depth. If we expand the derivative form of the vapor flux ($-D^{v*} \cdot \frac{d(H_r \cdot \rho_{sat}^v)}{dz}$) in Eq. (2.56), we can easily find that it describes the sum of the isothermal ($K_{vh} \frac{\partial h}{\partial z}$) and nonisothermal ($K_{vT} \frac{\partial T}{\partial z}$) terms in Eq. (2.22). If we expand the derivative form of the isotope diffusion flux in the soil water vapor ($-D_i^{v*} \frac{d(H_r \cdot \rho_{sat}^v \cdot R_i^v)}{dz}$) in Eq. (2.57), we can easily find out that it describes the sum of the convection ($\beta_i^* q_v C_i^l$) and diffusion ($-D_i^{v*} \frac{\partial \beta_i^* C_i^l}{\partial z}$) terms in Eq. (2.25). That is to say, vapor convection within the soil is also a diffusive process (Haverd *et al.*, 2010).

If we define characteristic lengths z_l and z_v as follows:

$$z_l = \rho_w D^{l*} / E_s \quad (2.58)$$

$$z_v = \frac{D^{v*} \rho_{sat}^v}{E_s} \quad (2.59)$$

We can then get:

$$(\rho_w q_v)/E_s = -D^{v*} \frac{d(H_r \cdot \rho_{sat}^v)}{dz} / E_s = -H_r z_v \frac{d[\ln(H_r \cdot \rho_{sat}^v)]}{dz} \quad (2.60)$$

$$\begin{aligned} q_i^v / E_s &= -D_i^{v*} \frac{d(H_r \cdot \rho_{sat}^v R_i^v)}{dz} / E_s \\ &= -H_r z_v R_i^l \alpha_i^* / \alpha_i^k \frac{d[\ln(H_r \rho_{sat}^v \alpha_i^* R_i^l)]}{dz} \end{aligned} \quad (2.61)$$

$$\begin{aligned} q_i^l / E_s &= (\rho_w q_l R_i^l - \rho_w D_i^{l*} \frac{dR_i^l}{dz}) / E_s \\ &= \rho_w q_l R_i^l / E_s - z_l \sigma_i R_i^l \frac{d[\ln(R_i^l)]}{dz} \end{aligned} \quad (2.62)$$

Combining these equations gives:

$$\begin{aligned} H_r z_v R_i^l \left\{ (1 - \alpha_i^* / \alpha_i^k) \frac{d[\ln(H_r \rho_{sat}^v)]}{dz} - \alpha_i^* / \alpha_i^k \frac{d[\ln(\alpha_i^* R_i^l)]}{dz} \right\} \\ = R_i^l - R_\infty + z_l \sigma_i \frac{dR_i^l}{dz} \end{aligned} \quad (2.63)$$

where D^{l*} is the effective dispersion coefficient of the light isotope in soil water, and σ_i is a constant depending on the isotope species (see Appendix A).

According to the relationship between R and δ values shown in Eq. (2.2), the analytical solution can be further simplified and given by the differential equation as follows:

$$\begin{aligned} \frac{d\delta_i^l}{dz} + (z_l + H_r z_v)^{-1} (\delta_i^l - \delta_\infty) \\ = H_r z_v (z_l + H_r z_v)^{-1} (\alpha_i^k \\ - \alpha_i^*) \times \frac{d}{dz} [\ln(H_r \rho_{sat}^v (\alpha_i^k - \alpha_i^*))] \end{aligned} \quad (2.64)$$

This is a semi-analytical solution. It can only be solved once we prescribe the isotopic composition of soil water at the surface and solve the water flow and heat transport equations, which will provide soil temperatures, pressure heads, and water contents. In the HYDRUS numerical simulation, transport parameters were the same as

those in the analytical solution. The constant pressure head (equal to 0) was adopted in the numerical simulation as the lower BC for soil water flow. The new water flow BC, which calculates actual evaporation as a function of potential evaporation (E_p) and the difference in humidities between the air and the soil surface (Eq. (2.35)) was used at the upper atmospheric boundary. The solute flux was used as the lower BC for isotope transport (automatically calculated from its isotopic composition equal to δ_∞ and the bottom water flux). The stagnant BC for volatile solutes was used at the upper boundary for isotope transport. The surface solute flux referred to the evaporation flux for water isotopes E_i calculated by the Craig-Gordon model (Eq. (2.7)). The temperature BC was used for heat transport at both boundaries.

Figs. 2.4e and 2.4f show an excellent agreement between the analytical and numerical solutions using a fine spatial discretization, despite a slight overestimation of the peak isotopic composition by HYDRUS-1D. Fig. S2.3 compares the analytical and numerical solutions obtained using different spatial discretizations. The maximum differences (at the evaporation front) between the analytical and numerical solutions in the ^{18}O isotopic composition profiles were 24.88‰ (coarse discretization), 3.74‰ (medium), and 0.88‰ (fine). The maximum differences between the analytical and numerical solutions in the ^2H isotopic composition profiles were 34.68‰ (coarse), 8.40‰ (medium), and 3.67‰ (fine). This means that in this example, the isotope transport module can produce relatively well isotope profiles as long as an appropriate spatial

discretization is used. The isotopic composition profiles have maximum values at a depth of 2 cm, which corresponds with the water content/matric potential/temperature profiles inflection points (Figs. 2.4a, 2.4b, and 2.4c). This is also the evaporation front location, where the upward soil water flux changes from the liquid to vapor flux (Fig. 2.4d).

The dual-isotope plots (Fig. 2.4g) have slopes of about 2.66 and 1.62 in the vapor and liquid dominant zones (VDZ, LDZ), respectively, which are far smaller than those of the GMWL. The LC-excess profile shows the opposite trend to the isotopic composition profiles and is negative in the entire soil profile (Fig. 2.4h). These results suggest that kinetic fractionation also occurs. This is reasonable since the kinetic fractionation factor (α_i^k) is not equal to one when n_k is one (Table 2.4).

Table 2.4. Values of all variables used in the analytical solution of *Barnes and Allison* (1984).

Parameter	Value
E_p	$2.0 \times 10^{-4} \text{ kgm}^{-2}\text{s}^{-1}$
E_s	$1.043 \times 10^{-5} \text{ kgm}^{-2}\text{s}^{-1}$
T_a	313.15 K (40 °C)
T_z	$T_z = 20(1 + \exp(-20z)) + 273.15 \text{ K}$
h_a	0.2
δ_{ia}^v	-14‰ for ^{18}O and -100‰ for ^2H
δ_∞	0‰ for ^{18}O and 0‰ for ^2H
n_k	1

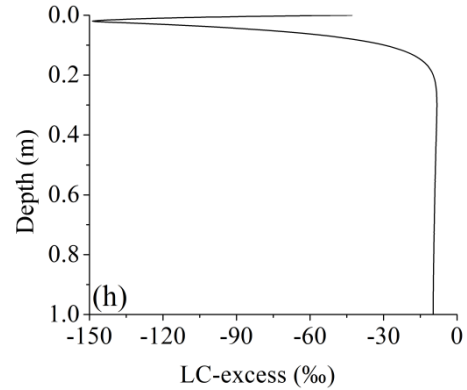
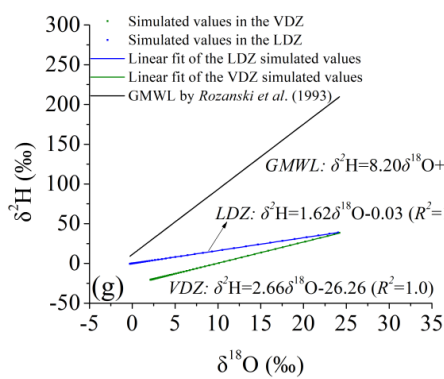
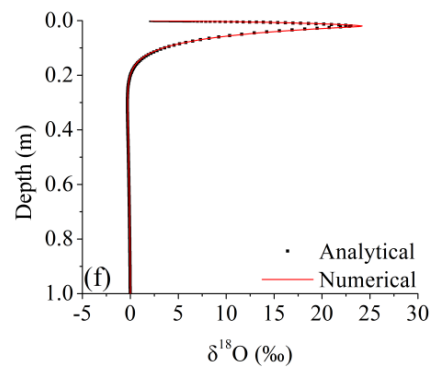
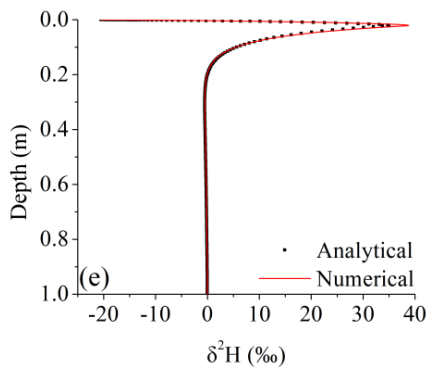
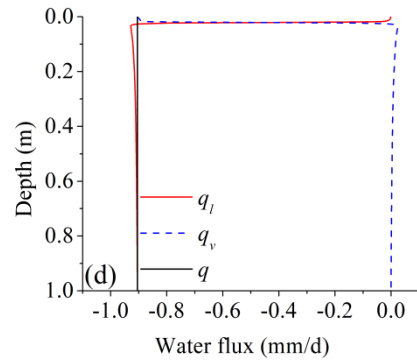
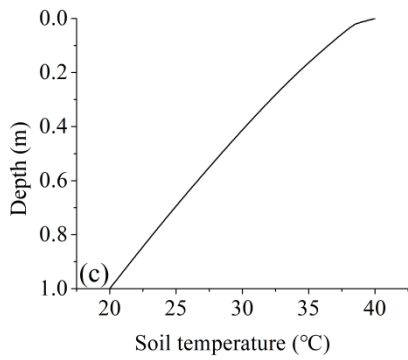
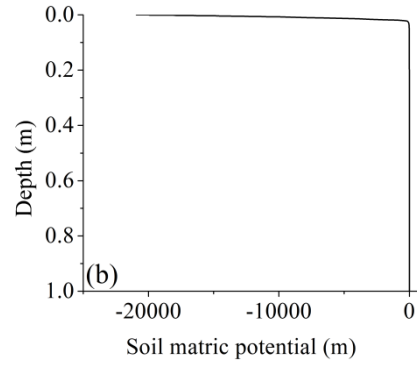
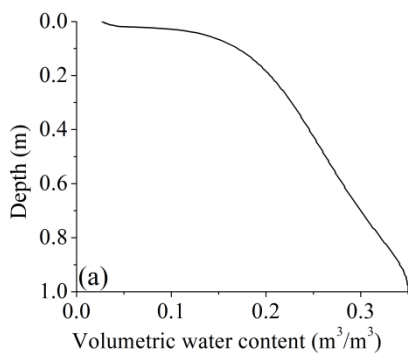


Figure 2.4. Comparison of the results of analytical and numerical solutions for nonisothermal unsaturated soils under steady evaporation. Vertical profiles of (a) the soil water content, (b) the matric potential, (c) the soil temperature, (d) the water fluxes (liquid, q_l , vapor, q_v , and total, q ; negative values represent evaporation), (e) the ^2H isotopic composition, (f) the ^{18}O isotopic composition, (g) the dual-isotope plot of the simulated values and (h) the LC-excess profile. “VDZ” and “LDZ” represent the vapor and liquid-dominant zones, respectively.

2.6.1.3 Plausibility Tests

The soil was initially saturated and under hydrostatic conditions (the soil water pressure head was equal to -0.01 m at the top and linearly increased to 0.99 m at the bottom). The initial isotopic composition, δ_{∞} , and soil temperature, T_z , in the soil column were uniform (i.e., the same at all depths). Water was evaporating from the soil column into an atmosphere with temperature, T_a , relative humidity, h_a , and isotopic composition, δ_{ia}^v . All relevant parameters are summarized in Table 2.5 (Mathieu and Bariac, 1996; Melayah et al., 1996; Braud et al., 2005a). In the HYDRUS numerical simulation, zero water and isotope fluxes were adopted as the lower BCs. The new water flow BC, which calculates actual evaporation as a function of potential evaporation (E_p) and the difference in humidities between the air and the soil surface (Eq. (2.35)) was used at the upper atmospheric boundary. The stagnant BC for volatile solutes was used at the upper boundary for isotope transport. The surface solute flux referred to the evaporation flux for water isotopes E_i calculated by the Craig-Gordon model (Eq. (2.7)). No heat transport was considered in this example.

The plausibility test conditions are listed in Table 2.6. The impacts of four parameters on isotopic composition profiles were considered, including the equilibrium fractionation factor, α_i^* , the kinetic fractionation factor, α_i^k , which affects the molecular diffusion coefficient of the isotope i in free air, D_i^v , the molecular diffusion coefficient of the isotope i in free water, D_i^l , and the isotopic composition of

atmospheric vapor, δ_{ia}^v . Equations from *Majoube* (1971) and *Mathieu and Bariac* (1996) were used to calculate the equilibrium α_i^* and kinetic fractionation factor α_i^k , respectively, for tests in which they were not equal to 1. The molecular diffusion coefficients of the isotope i in free water (air) D_i^{lo} (D_i^v) [L^2T^{-1}] were calculated by Eqs. (A2.3~A2.5). These values were then used to calculate the effective dispersion coefficients for the isotope i in soil water (vapor), D_i^{l*} (D_i^{v*}), based on Eqs. (2.33~2.34). The steady vertical isotopic composition profiles at the end of the 250-day simulation are shown in Fig. 2.5.

Test 1: Equilibrium and kinetic fractionation factors (α_i^* , α_i^k) are set to one, and molecular diffusion coefficient of the isotope i in free water (D_i^{lo}) is set to zero. In other words, evaporation fractionation and diffusion in the liquid phase are neglected. The isotopic composition of the atmospheric water vapor is set equal to that of the initial soil water δ_∞ . This results in uniform isotopic compositions in soil water throughout the soil profile (equal to δ_∞) as expected.

Test 2: Test 2 is the same as Test 1, except that the isotopic composition of the atmospheric water vapor is set to a low value δ_{ia}^v . Isotope diffusion in soil water vapor due to the concentration gradient between the free atmosphere and soil results in increased isotopic compositions of liquid and vapor phases within the soil as depth increases, given the linear relationship between them (Eq. (2.32)). The isotopic

composition of surface soil water is close to that of the atmospheric water vapor δ_{ia}^v and increases gradually with depth to its initial value δ_∞ .

Test 3: Test 3 is the same as Test 1, except that equilibrium isotopic fractionation is turned on (i.e., α_i^* is not equal to one). Equilibrium fractionation between soil water and soil water vapor moves lighter water molecules from the liquid phase into the vapor phase, which causes isotopic enrichment of the remaining soil water. However, this enrichment rate is different between regions above and below 5 cm (i.e., the evaporation front, as seen in Figs. 2.5a and 2.5b) due to different vapor fluxes. Above 5 cm, the vapor flux is approximately constant with depth, and thus the effect of equilibrium fractionation does not differ too much with depth. This results in a slow transition from the isotopic composition of soil water towards the surface value. Below 5 cm, the isotopic composition of soil water increases rapidly towards the 5-cm depth due to the increased upward vapor flux (Fig. 2.5b).

Test 4: Test 4 is the same as Test 3, except that the isotopic composition of the atmospheric water vapor is reset to a low value δ_{ia}^v . This shifts the isotopic composition of surface soil water close to δ_{ia}^v , similarly as in Test 2. This surface effect, combined with increasing enrichment from the soil bottom towards the soil surface (as discussed in Test 3), leads to the simulated maximum of the isotopic composition profile.

Test 5: Test 5 is the same as Test 4, except that diffusion in the liquid phase is turned on (i.e., D_i^{l0} is not equal to zero). Since diffusion in the liquid phase causes

spreading or dispersion of the solute front (*Radcliffe and Šimůnek, 2018*), this test produces a smaller peak of the isotopic composition profile.

Test 6: Test 6 is the same as Test 5, except that the kinetic fractionation at the surface is turned on (i.e., α_i^k is not equal to one), and the molecular diffusion coefficient of the isotope i in free air is set to its real value D_i^v (smaller than D^v as seen in Eq. (2.12)). The smaller molecular diffusion coefficient in free air results in increased kinetic fractionation, by decreasing the removal of heavy isotopes through the vapor flux. This increases isotopic enrichment in the remaining soil water, leading to a larger peak of the isotopic composition profile than in Test 5.

As for dual-isotope plots, Test 6 has slopes far smaller than that of the global meteoric water line (GMWL) in both liquid- (LDZ) and vapor-dominant (VDZ) zones (Fig. S2.4d). The line conditioned excess (LC-excess) profile shows the opposite trends to the isotopic composition profiles and is always negative (Fig. S2.5). These suggest that kinetic fractionation also occurs. This is reasonable given the fact that the kinetic fractionation factor (α_i^k) is not equal to one in Test 6 (Table 2.6). For Tests 3~5, the dual-isotope plots of both the LDZ and VDZ (Figs. S2.4a, S2.4b, and S2.4c) have slopes of about 6.55~7.80, which are much closer to that of the GMWL. This is reasonable since the kinetic fractionation factor is equal to one in Tests 3~5 (Table 2.6), and thus only equilibrium fractionation occurs. These slopes are not exactly equal to that of GMWL, especially for the VDZ, where the exchange with the atmosphere is more

significant. However, the LC-excess values in Tests 3~5 are almost a constant low value (about -10‰) throughout the soil profile, compared to much more negative values in Test 6 (Fig. S2.5). This again verifies that only equilibrium fractionation occurs in Tests 3~5.

Overall, the slopes of dual-isotope plots with kinetic fractionation are much smaller than those without consideration (Fig. 2.3c, Fig. 2.4g, and Fig. S2.4). The LC-excesses at the surface layer (about 0~50 cm) are much more negative than in other depths (Fig. 2.3d, Fig. 2.4h, and Fig. S2.5). This indicates that the fractionation at the surface layer is more significant. These conclusions are also consistent with those in *Sprenger et al.* (2016a). Therefore, the isotope transport module is accurate also from the perspectives of dual-isotope plots and LC-excess values.

Table 2.5. Values of all variables used in the plausibility tests.

Parameter	Value	
E_p	$1.005 \times 10^{-4} \text{ kg/m}^2/\text{s}$	
E_s	$2.568 \times 10^{-6} \text{ kg/m}^2/\text{s}$	
T_a, T_z	303.15 K (30 °C)	
h_a	0.2	
	for ^{18}O	for ^2H
δ_{ia}^v	-15‰	-112‰
δ_∞	-8‰	-65‰
D_i^{lo}	$2.520 \times 10^{-9} \text{ m}^2/\text{s}$	$2.562 \times 10^{-9} \text{ m}^2/\text{s}$
D_i^v	$2.529 \times 10^{-5} \text{ m}^2/\text{s}$	$2.568 \times 10^{-5} \text{ m}^2/\text{s}$

Table 2.6. Plausibility tests' conditions.

Test	α_i^*	α_i^k	D_i^v	D_i^{lo}	δ_{ia}^v
1	1	1	D^v	0	δ_∞
2	1	1	D^v	0	δ_{ia}^v
3	α_i^*	1	D^v	0	δ_∞
4	α_i^*	1	D^v	0	δ_{ia}^v
5	α_i^*	1	D^v	D_i^{lo}	δ_{ia}^v
6	α_i^*	α_i^k	D_i^v	D_i^{lo}	δ_{ia}^v

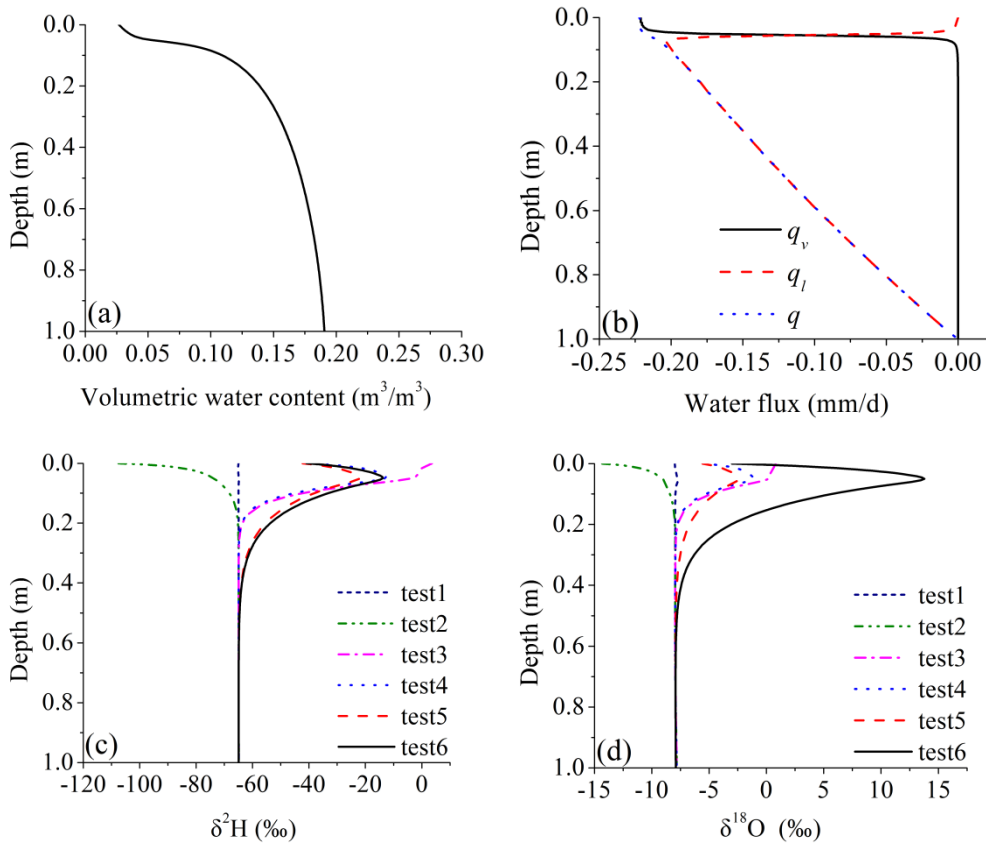


Figure 2.5. Vertical profiles of (a) the soil water content, (b) the water fluxes (liquid, q_l , vapor, q_v , and total, q ; negative values represent evaporation), (c) the ^2H isotopic composition, and (d) the ^{18}O isotopic composition in plausibility tests 1-6 at 250 d.

2.6.2 Evaluation Against the Experiment Data

2.6.2.1 Transport of Isotopes

The dataset is from *Stumpp et al.* (2012) (available <https://www.pc-progress.com/en/Default.aspx?h1d-lib-isotope>). The field experiment was conducted in a humid region located at the research area of the HBLFA Raumberg-Gumpenstein in Gumpenstein, Austria, with a mean annual temperature of 6.9 °C and mean annual precipitation of 1035 mm. The cylindrical lysimeter (with a depth of 1.5 m and a surface area of 1 m²) was embedded in a rainfed agricultural field planted with winter wheat and fertilized with liquid cattle slurry (the lysimeter 3 in *Stumpp et al.* (2012)). The isotopic composition of precipitation and lysimeter seepage water were measured on the event and weekly intervals, respectively, from May 2002 to February 2007 (1736 days in total). More details about other data collection and measurements can be found in *Stumpp et al.* (2012).

The final optimized soil hydraulic and solute transport parameters reported in *Stumpp et al.* (2012) (Table S2.2) were used in the numerical simulations reported below. The atmospheric (with a surface layer) and seepage face boundary conditions were used for water flow at the upper and lower boundaries, respectively. The temperature BC was used for heat transport at both boundaries. The solute flux and zero concentration gradient BCs were used for isotope transport at the upper and lower boundaries, respectively. The isotope ratio of the evaporation flux was automatically

used in HYDRUS to calculate the isotope evaporation flux at the upper boundary corresponding to the water flux. To investigate the sensitivity of the simulation results to the upper boundary conditions for isotope transport, the relevant parameters (R_E , R_a) of different evaporation fractionation models (*Stumpp et al.*, 2012; the Craig-Gordon model, and the Gonfiantini model) were adjusted and implemented. Their impacts on the simulation results under different assumptions (with and without fractionation) were discussed. Since kinetic fractionation can be neglected in humid zones (*Horita et al.*, 2008), only equilibrium fractionation was considered in this example (i.e., $n_k = 0$). Fig. 2.6 shows the comparison between ^{18}O isotopic compositions of the lysimeter seepage water simulated by *Stumpp et al.* (2012) and using the Gonfiantini and Craig-Gordon models for a system that neglects vapor flow. The Nash-Sutcliffe efficiency (NSE) and determination coefficient (R^2) are shown in Table 2.7.

The water samples from the lysimeter seepage water plot on the LMWL (Fig. 5 of *Stumpp et al.*, 2012), indicating negligible fractionation. Therefore, the measured data are closest to the simulations that do not consider fractionation, as *Stumpp et al.* (2012) did. In this model, the isotope ratio of the evaporation flux (R_E) is the same as that of the surface soil water (R_L) (i.e., $R_E = R_L$).

In the Gonfiantini model, R_E is α_i^* times of R_L . As can be seen in Fig. 2.6, the measured values are close to the values simulated by the Gonfiantini model in case of no fractionation (i.e., $\alpha_i^* = 1$; $n_k = 0$; $R_E = R_L$, which produces the same results

as *Stumpp et al.*, 2012) for most of the simulation period. In the end, during about 1150~1500 days, the measured values are close to those simulated considering equilibrium fractionation (i.e., $\alpha_i^* = \alpha_i^*$; $n_k = 0$; $R_E = \alpha_i^* R_L$).

To obtain a better agreement between the simulation results and measurements using the Craig-Gordon model, the early atmospheric isotope ratio R_a should correspond to Eq. S2.9 (i.e., $R_a = \frac{(\alpha_i^*-1+h_a) \cdot R_L}{h_a}$), while the late R_a should correspond to Eq. S2.7 (i.e., $R_a = \alpha_i^* \cdot R_L$). Therefore, in the Craig-Gordon model method, an approximate estimate of R_a using Eq. (S2.10) was used for the entire simulation period to calculate R_E under equilibrium fractionation assumption (i.e., $\alpha_i^* = \alpha_i^*$; $n_k = 0$; $R_a = \frac{(\alpha_i^*-1+h_a+h_a \cdot \alpha_i^*) \cdot R_L}{2h_a}$). More details can be found in the Supplementary Material.

The Craig-Gordon model has obtained relatively satisfactory simulation results (NSE=0.19; $R^2=0.30$) compared to the Gonfiantini model (NSE=-0.52; $R^2=0.25$) in the case of equilibrium fractionation. The significant differences between the values simulated by the Gonfiantini and Craig-Gordon models emphasize the considerable impact of R_a on the simulation results due to its effect on R_E . However, the model performance is worse than when fractionation is neglected (NSE=0.24; $R^2=0.37$). This also indirectly validates the assumption of *Stumpp et al.* (2012) not to consider evaporation fractionation in their analysis of data from this humid zone. However, this does not rule out errors due to an inaccurate estimation of R_a used in the simulation. We note that the final optimized soil hydraulic and solute transport parameters reported

in *Stumpp et al.* (2012) were used in the numerical simulations. This parameter set was estimated based on the assumption that there was no fractionation, which may not be optimal when fractionation is present. This may also explain the best agreement of the *Stumpp et al.* (2012) simulation with the measurements. However, even under the no-fractionation assumption, this agreement is not very good, likely due to some uncontrollable factors in the field experiments.

The isotopic compositions and overall temporal variation trends simulated using the Gonfiantini or Craig-Gordon models considering fractionation are consistent with measured data and the *Stumpp et al.* (2012) simulation without considering fractionation. This is because evaporation fractionation will not change isotopic composition trends when evaporation is much smaller than the sum of precipitation and soil water storage, and the equilibrium fractionation factor is close to 1. However, the selection of the atmospheric isotope ratio R_a can affect the fluctuation amplitude of the isotope time series by affecting R_E . The isotopic composition of discharge simulated by all models remains the same during the first 150 days because only water initially in the profile (and thus not affected by the upper BC treatment) reaches the bottom during this time. Water infiltrating at the beginning of the simulation starts arriving at the bottom after about 150 days when isotopic compositions simulated by different models with different assumptions start deviating. From this point forward,

differences in simulated discharge isotopic compositions reflect different treatments of the upper BC.

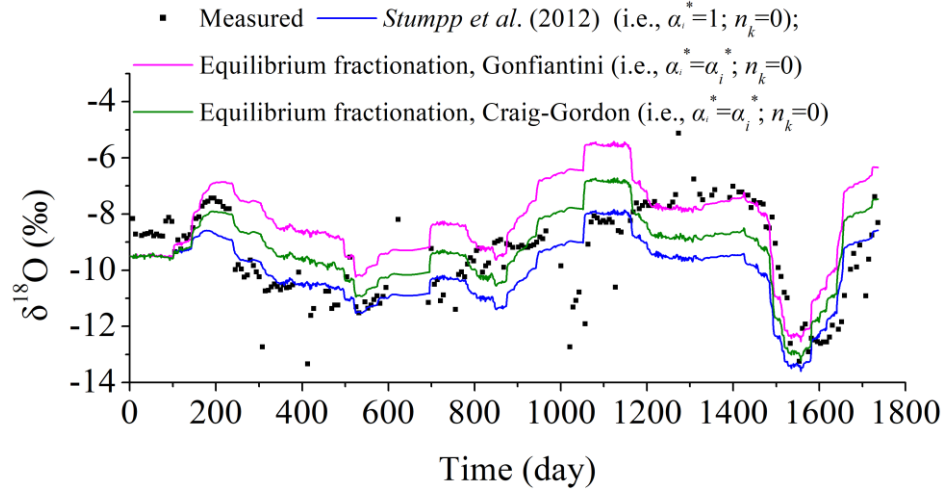


Figure 2.6. Simulated $\delta^{18}\text{O}$ in the seepage water at the bottom of the lysimeter when equilibrium fractionation was (i.e., $\alpha_i^* = \alpha_i^*$; $n_k = 0$) or was not (i.e., $\alpha_i^* = 1$; $n_k = 0$) considered for the Stumpp et al. (2012) dataset using the Gonfiantini and Craig-Gordon evaporation fractionation models.

Table 2.7. Statistics of the model performance.

Indicator	no fractionation, <i>Stumpp et al.</i> (2012) (i.e., $\alpha_i^* = 1$; $n_k = 0$)	Equilibrium	Equilibrium fractionation,
		fractionation, the Gonfiantini model (i.e., $\alpha_i^* = \alpha_i^*$; $n_k = 0$)	the Craig-Gordon model (i.e., $\alpha_i^* = \alpha_i^*$; $n_k = 0$)
NSE	0.24	-0.52	0.19
R^2	0.37	0.25	0.30

2.6.2.2 Particle Tracking

The input parameters, w_{Stand} and w_{Prec} (discussed in Section 2.4.3), of the particle tracking module (PTM) were set equal to 2 and 10 cm, respectively. Fig. 2.7 shows the spatial-temporal distribution of particles during the 5-year simulation. There are 48 particles in total, among which 18 particles (P1-P18) were initially in the soil profile, while the next 26 particles (P19~P44) were released at the soil surface, passed

through the lysimeter, and left at the bottom. Finally, the last 4 particles (P45-P48) were released at the soil surface and remained in the soil profile at the end of the simulation.

The particle trajectories suddenly drop during periods with many rainfall events and slowly decrease or even rise during periods with limited rainfall (Fig. 2.7). Particles move downward faster during wet seasons and slow down during dry seasons. Particles move down sharply after heavy rainfalls, reflecting piston flow's typical characteristics. Particles released right before the wet season move down faster than those released right before the dry season.

The transit times of these particles, and corresponding velocities, were calculated (given in Table S2.4. and shown in Fig. 2.7c). The mean recharge transit time and velocity are 276.1 days and 6.0 mm/day, respectively. These values are slightly different from those calculated by *Stumpp et al.* (2012) using the peak displacement method. The mean recharge transit time (250 days) and velocity (6.0 mm/day) of soil water were estimated by *Stumpp et al.* (2012) by comparing the convective shift in the isotope peaks of the input (precipitation during 2005~2006) and output (lysimeter discharge) and considering dispersion effects. This difference may also be due to different rainfall events selected for these calculations. *Stumpp et al.* (2012) selected precipitation events from 2005~2006 since, only during this period, there was pronounced and distinct correspondence between the isotopic peaks in precipitation and lysimeter discharge. Since particles move faster during the period with

many precipitation events, the peak displacement method is likely to overestimate the flow velocity compared to particle tracking. Overall, the two approaches' results are similar, which shows the particle tracking model's applicability.

However, the peak displacement method is not applicable when there are no pronounced peaks or a distinct correspondence between the input and output peaks. The particle tracking module can be used under such circumstances and overcome this shortcoming of the peak-displacement method, thus expanding the possibility of calculating transit times.

To verify the new particle tracking module, we conducted simple mass balance calculations based on the results of the numerical solution of the Richards equation in HYDRUS-1D. The amount of water in the soil profile when the particle leaves the transport domain (W_{t_final}) should be equal to the amount of water applied at the soil surface (infiltration) since its release, reduced by evaporation and root water uptake from the soil between the particle and the soil surface:

$$W_{t_final} = \int_{t_{init}}^{t_{final}} \left(i(t) - e(t) - \int_0^{z_p(t)} s(z, t) dz \right) dt \quad (2.65)$$

where t_{init} and t_{final} are times when the particle is released at the soil surface and when it leaves at the soil profile bottom, respectively. The mass balance calculations carried out according to (65) are given in Table S2.4, indicating an almost perfect match and validating the particle tracking module.

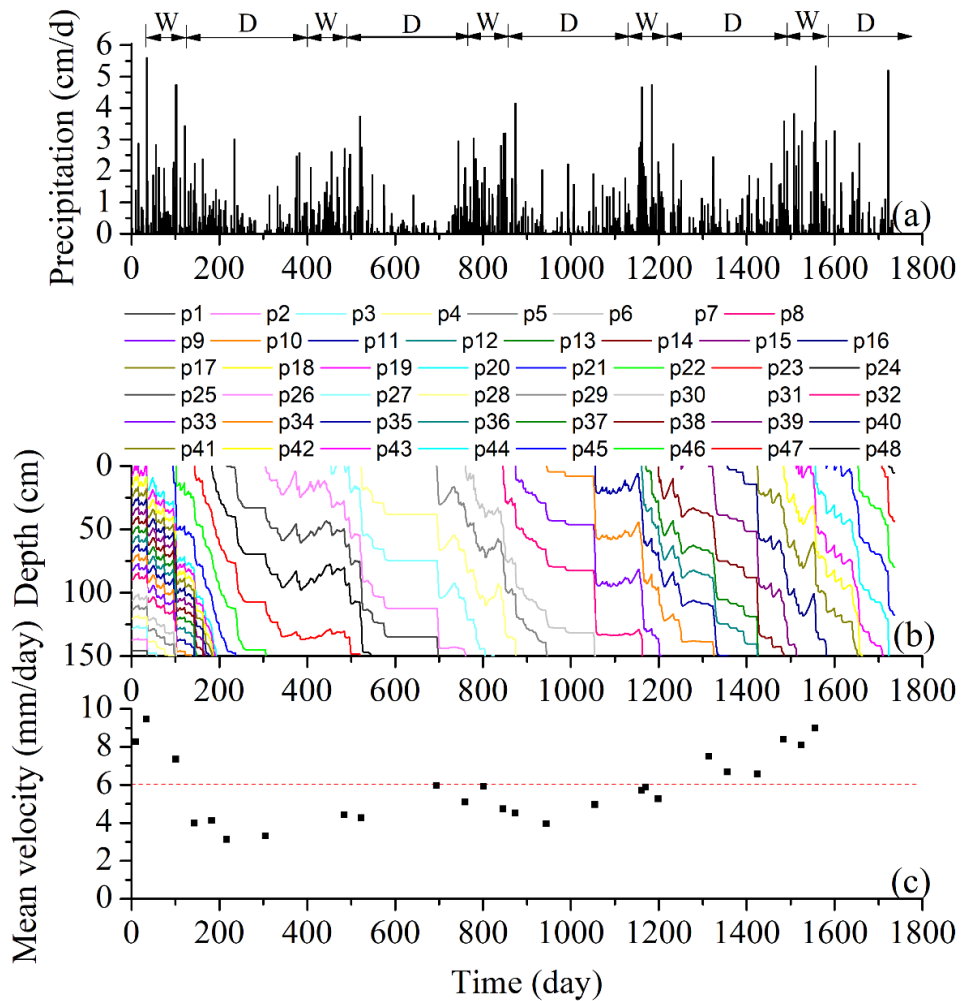


Figure 2.7. Precipitation (a), spatial-temporal distribution of particles (b), and mean particle velocity (c) (simulated by the Particle Tracking Module) for the Stumpp et al. (2012) dataset. “W” and “D” represent wet and dry seasons, respectively.

2.7 Summary and Conclusions

This study presents a model, which can simultaneously solve the coupled equations describing the movement of water, heat, and stable isotopes. It is based on the HYDRUS-1D model, to which the isotope transport and particle tracking modules were added. The comparisons with analytical solutions, plausibility tests under saturated/unsaturated and isothermal/nonisothermal conditions, and field validation

demonstrate the model's accuracy and robustness. Transit times calculated by the particle tracking module (PTM) are similar to those evaluated by the peak displacement method, which validates the use of the water flow-based PTM as an alternative tool to isotope transport-based methods.

As compared with existing isotope models, our approach enables many thousands of current HYDRUS users to efficiently operate the new model while using various advanced HYDRUS software features, including flexible dynamic boundary conditions, equilibrium and nonequilibrium water flow, parameter optimization routines, and the well-designed user-friendly GUI (*Šimůnek et al.*, 2016), while also providing higher computational efficiency. For example, the SiSPAT model always calculates both water flow and heat transport, even when the soil system is isothermal. Our model simulates only water flow for isothermal systems, improving numerical efficiency. The new particle tracking module provides the HYDRUS-1D users with an additional tool for assessing transit times. The developed model represents a comprehensive tool to numerically investigate many important research problems involving isotope transport processes and establishes a more solid foundation for applying stable isotope tracing in the critical zone.

References

- Araguas-Araguas, L., K. Froehlich, and K. Rozanski, Deuterium and oxygen-18 isotope composition of precipitation and atmospheric moisture, *Hydrological Processes*, 14(8), pp. 1341-1355, doi:10.1002/1099-1085(20000615)14:8<1341::aid-hyp983>3.0.co;2-z, 2000.
- Benettin, P., T.H.M. Volkmann, J. von Freyberg, J. Frentress, D. Penna, T.E. Dawson, and J. Kirchner, Effects of climatic seasonality on the isotopic composition of evaporating soil waters, *Hydrology and Earth System Sciences*, 22(5), pp. 2881-2890, doi:10.5194/hess-22-2881-2018, 2018.
- Crawford, J., C.S. Azcurra, C.E. Hughes, J.J. Gibson, and S.D. Parkes, Comparison of atmospheric water vapour delta O-18 and delta H-2 estimated using evaporation pan, rainfall equilibrium and continuous measurements, *Journal of Hydrology*, 576, pp. 551-560, doi:10.1016/j.jhydrol.2019.06.056, 2019.
- Gibson, J.J., S.J. Birks, and T.W.D. Edwards, Global prediction of delta(A) and delta H-2-delta O-18 evaporation slopes for lakes and soil water accounting for seasonality, *Glob. Biogeochem. Cycle*, 22(2), pp. 12, doi:10.1029/2007gb002997, 2008.
- Skrzypek, G., A. Mydlowski, S. Dogramaci, P. Hedley, J.J. Gibson, and P.F. Grierson, Estimation of evaporative loss based on the stable isotope composition of water using Hydrocalculator, *Journal of Hydrology*, 523, pp. 781-789, doi:10.1016/j.jhydrol.2015.02.010, 2015.
- Allen, S.T., J.W. Kirchner, S. Braun, R.T.W. Siegwolf, and G.R. Goldsmith, Seasonal origins of soil water used by trees, *Hydrology and Earth System Sciences*, 23(2), pp. 1199-1210, doi:10.5194/hess-23-1199-2019, 2019. Asadollahi, M., C. Stumpp, A. Rinaldo, and P. Benettin, Transport and water age dynamics in soils: a comparative study of spatially integrated and spatially explicit models, *Water Resources Research*, 56(3), pp. 17, doi:10.1029/2019wr025539, 2020.
- Auriault, J.L., and P.M. Adler, Taylor dispersion in porous media: Analysis by multiple scale expansions, *Advances in Water Resources*, 18(4), pp. 217-226, doi:10.1016/0309-1708(95)00011-7, 1995.

- Barbeta, A., S.P. Jones, L. Clave, L. Wingate, T.E. Gimeno, B. Frejaville, S. Wohl, and J. Ogee, Unexplained hydrogen isotope offsets complicate the identification and quantification of tree water sources in a riparian forest, *Hydrology and Earth System Sciences*, 23(4), pp. 2129-2146, doi:10.5194/hess-23-2129-2019, 2019.
- Barnes, C.J., and G.B. Allison, The distribution of deuterium and ^{18}O in dry soils: 1. Theory, *Journal of Hydrology*, 60(1-4), pp. 141-156, doi:10.1016/0022-1694(83)90018-5, 1983.
- Barnes, C.J., and G.B. Allison, The distribution of deuterium and ^{18}O in dry soils: 3. Theory for non-isothermal water movement, *Journal of Hydrology*, 74(1-2), pp. 119-135, doi:10.1016/0022-1694(84)90144-6, 1984.
- Braud, I., SiSPAT User's Manual Version 3.0. Laboratoire d'Étude des Transferts en Hydrologie et Environnement, Grenoble, France, pp. 106, 2000.
- Braud, I., SiSPAT User's Manual Update, Version 4.0, pp. 13, 2002.
- Braud, I., T. Bariac, J.P. Gaudet, and M. Vauclin, SiSPAT-Isotope, a coupled heat, water and stable isotope (HDO and H_2^{18}O) transport model for bare soil. Part I. Model description and first verifications, *Journal of Hydrology*, 309(1-4), pp. 277-300, doi:10.1016/j.jhydrol.2004.12.013, 2005a.
- Braud, I., T. Bariac, M. Vauclin, Z. Boujamlaoui, J.P. Gaudet, P. Biron, and P. Richard, SiSPAT-Isotope, a coupled heat, water and stable isotope (HDO and H_2^{18}O) transport model for bare soil. Part II. Evaluation and sensitivity tests using two laboratory data sets, *Journal of Hydrology*, 309(1-4), pp. 301-320, doi:10.1016/j.jhydrol.2004.12.012, 2005b.
- Braud, I., P. Biron, T. Bariac, P. Richard, L. Canale, J.P. Gaudet, and M. Vauclin, Isotopic composition of bare soil evaporated water vapor. Part I: RUBIC IV experimental setup and results, *Journal of Hydrology*, 369(1-2), pp. 1-16, doi:10.1016/j.jhydrol.2009.01.034, 2009.
- Braud, I., A.C. Dantasantonino, M. Vauclin, J.L. Thony, and P. Ruelle, A simple soil-plant-atmosphere transfer model(SiSPAT) development and field verification, *Journal of Hydrology*, 166(3-4), pp. 213-250, doi:10.1016/0022-1694(94)05085-c, 1995.

- Brinkmann, N., S. Seeger, M. Weiler, N. Buchmann, W. Eugster, and A. Kahmen, Employing stable isotopes to determine the residence times of soil water and the temporal origin of water taken up by *Fagus sylvatica* and *Picea abies* in a temperate forest, *New Phytologist*, 219(4), pp. 1300-1313, doi:10.1111/nph.15255, 2018.
- Brooks, R., and A. Corey, Hydraulic properties of porous media, *Hydrology Papers*, No. 3. Colorado State University, Fort Collins, Colo., 1964.
- Brown, C.R., M. Kandelous, F. Sartori, C. Collins, and F. Spurlock, Modeling variation in 1,3-dichloropropene emissions due to soil conditions and applicator practices, *Science of the Total Environment*, 678, pp. 768-779, doi:10.1016/j.scitotenv.2019.04.414, 2019.
- Burdine, N.T., Relative permeability calculations from pore size distribution data, *Transactions of the American Institute of Mining and Metallurgical Engineers*, 198, pp. 71-78, 1953.
- Chen, G., K. Auerswald, and H. Schnyder, H-2 and O-18 depletion of water close to organic surfaces, *Biogeosciences*, 13(10), pp. 3175-3186, doi:10.5194/bg-13-3175-2016, 2016.
- Corneo, P.E., Kertesz, M.A., Bakhshandeh, S., Tahaei, H., Barbour, M.M., Dijkstra, F.A., 2018. Studying root water uptake of wheat genotypes in different soils using water delta 18O stable isotopes. *Agriculture Ecosystems & Environment*, 264: 119-129. doi:10.1016/j.agee.2018.05.007.
- Chung, S.O., and R. Horton, Soil heat and water-flow with a partial surface mulch, *Water Resources Research*, 23(12), pp. 2175-2186, doi:10.1029/WR023i012p02175, 1987.
- Craig, H., Isotopic variations in meteoric waters, *Science*, 133(346), pp. 1702-1703, doi:10.1126/science.133.3465.1702, 1961.
- Craig, H., and L. Gordon, Deuterium and oxygen 18 variations in the ocean and the marine atmosphere, Stable Isotopes in Oceanographic Studies and Paleotemperatures E, *Proceedings of the Third Spoleto Conference*, Spoleto, Italy, pp. 9-130, 1965.

- De Vries, D.A., Thermal properties of soils, In *Physics of Plant Environment*, Wijk, R.W.v. (Ed.), North Holland, Amsterdam, pp. 210-235, 1963.
- Figueroa-Johnson, M.A., J.A. Tindall, and M. Friedel, A comparison of O-18 delta composition of water extracted from suction lysimeters, centrifugation, and azeotropic distillation, *Water Air Soil Pollut.*, 184(1-4), pp. 63-75, doi:10.1007/s11270-007-9399-8, 2007.
- Fry, B., *Stable Isotope Ecology*, 521, Springer, New York, NY, pp., 2006.
- Gaj, M., and J.J. McDonnell, Possible soil tension controls on the isotopic equilibrium fractionation factor for evaporation from soil, *Hydrological Processes*, 33(11), pp. 1629-1634, doi:10.1002/hyp.13418, 2019.
- Gat, J., *Isotope Hydrology: A Study of the Water Cycle*, 6, World Scientific, pp., 2010.
- Gehrels, J.C., J.E.M. Peeters, J.J. De Vries, and M. Dekkers, The mechanism of soil water movement as inferred from O-18 stable isotope studies, *Hydrological Sciences Journal*, 43(4), pp. 579-594, doi:10.1080/02626669809492154, 1998.
- Geris, J., D. Tetzlaff, J. McDonnell, J. Anderson, G. Paton, and C. Soulsby, Ecohydrological separation in wet, low energy northern environments? A preliminary assessment using different soil water extraction techniques, *Hydrological Processes*, 29(25), pp. 5139-5152, doi:10.1002/hyp.10603, 2015.
- Gonfiantini, R., Standards for stable isotope measurements in natural compounds, *Nature*, 271(5645), pp. 534-536, doi:10.1038/271534a0, 1978.
- Gonfiantini, R., Environmental isotopes in lake studies, *Handbook of environmental isotope geochemistry*, 2, pp. 113-168, 1986.
- Gonfiantini, R., L.I. Wassenaar, L. Araguas-Araguas, and P.K. Aggarwal, A unified Craig-Gordon isotope model of stable hydrogen and oxygen isotope fractionation during fresh or saltwater evaporation, *Geochimica Et Cosmochimica Acta*, 235, pp. 224-236, doi:10.1016/j.gca.2018.05.020, 2018.
- Haverd, V., and M. Cuntz, Soil-Litter-Iso: A one-dimensional model for coupled transport of heat, water and stable isotopes in soil with a litter layer and root extraction, *Journal of Hydrology*, 388(3-4), pp. 438-455, doi:10.1016/j.jhydrol.2010.05.029, 2010.

- Horita, J., K. Rozanski, and S. Cohen, Isotope effects in the evaporation of water: a status report of the Craig-Gordon model, *Isotopes in Environmental and Health Studies*, 44(1), pp. 23-49, doi:10.1080/10256010801887174, 2008.
- Horita, J., and D.J. Wesolowski, Liquid-vapor fractionation of oxygen and hydrogen isotopes of water from the freezing to the critical temperature, *Geochimica Et Cosmochimica Acta*, 58(16), pp. 3425-3437, doi:10.1016/0016-7037(94)90096-5, 1994.
- Jury, W.A., W.F. Spencer, and W.J. Farmer, Behavior assessment model for trace organics in soil, 1. Model description, *Journal of Environment Quality*, 12(4), pp. 558-564, doi:10.2134/jeq1983.00472425001200040025x, 1983.
- Jury, W.A., G. Sposito, and R.E. White, A transfer-function model of solute transport through soil.1. Fundamental concepts, *Water Resources Research*, 22(2), pp. 243-247, doi:10.1029/WR022i002p00243, 1986.
- Kendall, C., and J.J. McDonnell, *Isotope Tracers in Catchment Hydrology*, Elsevier, pp., 2012.
- Kim, M., L.A. Pangle, C. Cardoso, M. Lora, T.H.M. Volkmann, Y.D. Wang, C.J. Harman, and P.A. Troch, Transit time distributions and StorAge Selection functions in a sloping soil lysimeter with time-varying flow paths: Direct observation of internal and external transport variability, *Water Resources Research*, 52(9), pp. 7105-7129, doi:10.1002/2016wr018620, 2016.
- Kool, D., Agam, N., Lazarovitch, N., Heitman, J.L., Sauer, T.J., Ben-Gal, A., 2014. A review of approaches for evapotranspiration partitioning. *Agricultural and Forest Meteorology*, 184: 56-70. DOI:10.1016/j.agrformet.2013.09.003.
- Landwehr, J., and T. Coplen, Line-conditioned excess: a new method for characterizing stable hydrogen and oxygen isotope ratios in hydrologic systems, *International conference on isotopes in environmental studies*, IAEA Vienna, pp. 132-135, 2006.
- Ma, Y., Song, X.F., 2016. Using stable isotopes to determine seasonal variations in water uptake of summer maize under different fertilization treatments. *Science of the Total Environment*, 550: 471-483. DOI:10.1016/j.scitotenv.2016.01.148.

- Majoube, M., Oxygen-18 and deuterium fractionation between water and steam, *Journal De Chimie Physique Et De Physico-Chimie Biologique*, 68(10), pp. 1423-1436, doi:10.1051/jcp/1971681423, 1971.
- Maloszewski, P., S. Maciejewski, C. Stumpp, W. Stichler, P. Trimborn, and D. Klotz, Modelling of water flow through typical Bavarian soils: 2. Environmental deuterium transport, *Hydrological Sciences Journal*, 51(2), pp. 298-313, doi:10.1623/hysj.51.2.298, 2006.
- Mathieu, R., and T. Bariac, A numerical model for the simulation of stable isotope profiles in drying soils, *Journal of Geophysical Research-Atmospheres*, 101(D7), pp. 12685-12696, doi:10.1029/96jd00223, 1996.
- Mattei, A., P. Goblet, F. Barbecot, S. Guillon, Y. Coquet, and S.T. Wang, Can Soil Hydraulic Parameters be Estimated from the Stable Isotopic composition of Pore Water from a Single Soil Profile?, *Water*, 12(2), pp. 19, doi:10.3390/w12020393, 2020.
- Melayah, A., L. Bruckler, and T. Bariac, Modeling the transport of water stable isotopes in unsaturated soils under natural conditions. 1. Theory, *Water Resources Research*, 32(7), pp. 2047-2054, doi:10.1029/96wr00674, 1996a.
- Melayah, A., L. Bruckler, and T. Bariac, Modeling the transport of water stable isotopes in unsaturated soils under natural conditions. 2. Comparison with field experiments, *Water Resources Research*, 32(7), pp. 2055-2065, doi:10.1029/96wr00673, 1996b.
- Merlivat, L., Molecular diffusivities of H₂¹⁶O, HD¹⁶O, and H₂¹⁸O in gases, *Journal of Chemical Physics*, 69(6), pp. 2864-2871, doi:10.1063/1.436884, 1978.
- Millington, R., and J.P. Quirk, Permeability of porous solids, *Transactions of the Faraday Society*, 57(8), pp. 1200-1207, doi:10.1039/tf9615701200, 1961.
- Moldrup, P., T. Olesen, D.E. Rolston, and T. Yamaguchi, Modeling diffusion and reaction in soils .7. Predicting gas and ion diffusivity in undisturbed and sieved soils, *Soil Sci.*, 162(9), pp. 632-640, doi:10.1097/00010694-199709000-00004, 1997.

- Mueller, M.H., A. Alaoui, C. Kuells, H. Leistert, K. Meusburger, C. Stumpp, M. Weiler, and C. Alewell, Tracking water pathways in steep hillslopes by delta ^{18}O depth profiles of soil water, *Journal of Hydrology*, 519, pp. 340-352, doi:10.1016/j.jhydrol.2014.07.031, 2014.
- Philip, J.R., Evaporation, moisture and heat field in the soil, *Journal of Meteorology*, 14(4), pp. 354-366, doi:10.1175/1520-0469(1957)014<0354:eamahf>2.0.co;2, 1957.
- Philip, J., and D. De Vries, Moisture movement in porous materials under temperature gradients, *Eos, Transactions American Geophysical Union*, 38(2), pp. 222-232, doi:10.1029/TR038i002p00222, 1957.
- Quade, M., N. Bruggemann, A. Graf, J. Vanderborght, H. Vereecken, and Y. Rothfuss, Investigation of kinetic isotopic fractionation of water during bare soil evaporation, *Water Resources Research*, 54(9), pp. 6909-6928, doi:10.1029/2018wr023159, 2018.
- Radcliffe, D.E., and J. Šimůnek, Soil Physics with HYDRUS: Modeling and Applications, CRC Press, pp., 2018.
- Rinaldo, A., P. Benettin, C.J. Harman, M. Hrachowitz, K.J. McGuire, Y. van der Velde, E. Bertuzzo, and G. Botter, Storage selection functions: A coherent framework for quantifying how catchments store and release water and solutes, *Water Resources Research*, 51(6), pp. 4840-4847, doi:10.1002/2015wr017273, 2015.
- Ross, P.J., Modeling soil water and solute transport - Fast, simplified numerical solutions, *Agronomy Journal*, 95(6), pp. 1352-1361, doi:10.2134/agronj2003.1352, 2003.
- Rothfuss, Y., and M. Javaux, Reviews and syntheses: Isotopic approaches to quantify root water uptake: a review and comparison of methods, *Biogeosciences*, 14(8), pp. 2199-2224, doi:10.5194/bg-14-2199-2017, 2017.
- Rozanski, K., L. Araguás-Araguás, and R. Gonfiantini, Isotopic patterns in modern global precipitation, *Climate change in continental isotopic records*, 78, pp. 1-36, 1993.

- Saito, H., J. Šimůnek, and B.P. Mohanty, Numerical analysis of coupled water, vapor, and heat transport in the vadose zone, *Vadose Zone Journal*, 5(2), pp. 784-800, doi:10.2136/vzj2006.0007, 2006.
- Shurbaji, A.R.M., and F.M. Phillips, A numerical model for the movement of H₂O, H₂¹⁸O, and ²HHO in the unsaturated zone, *Journal of Hydrology*, 171(1-2), pp. 125-142, doi:10.1016/0022-1694(94)02604-a, 1995.
- Šimůnek, J., Numerical simulation of the transport processes in soil (in Czech, English abstract), *Vodohosp. Čas.*, 39(1), pp. 20-34, 1991.
- Šimůnek, J., M. Sejna, H. Saito, M. Sakai, and M.T. van Genuchten, The HYDRUS-1D Software Package for Simulating the One-Dimensional Movement of Water, Heat, and Multiple Solutes in Variably Saturated Media, Version 4.0, *HYDRUS Software Series 3*, Department of Environmental Sciences, University of California Riverside, Riverside, California, USA, pp., 2008.
- Šimůnek, J., M.T. van Genuchten, and M. Sejna, Recent developments and applications of the HYDRUS computer software packages, *Vadose Zone Journal*, 15(7), pp. 25, doi:10.2136/vzj2016.04.0033, 2016.
- Soderberg, K., S.P. Good, L.X. Wang, and K. Caylor, Stable isotopes of water vapor in the vadose zone: a review of measurement and modeling techniques, *Vadose Zone Journal*, 11(3), pp. 14, doi:10.2136/vzj2011.0165, 2012.
- Sprenger, M., H. Leistert, K. Gimbel, and M. Weiler, Illuminating hydrological processes at the soil-vegetation-atmosphere interface with water stable isotopes, *Reviews of Geophysics*, 54(3), pp. 674-704, doi:10.1002/2015rg000515, 2016a.
- Sprenger, M., S. Seeger, T. Blume, and M. Weiler, Travel times in the vadose zone: Variability in space and time, *Water Resources Research*, 52(8), pp. 5727-5754, doi:10.1002/2015wr018077, 2016b.
- Sprenger, M., D. Tetzlaff, and C. Soulsby, Soil water stable isotopes reveal evaporation dynamics at the soil-plant-atmosphere interface of the critical zone, *Hydrology and Earth System Sciences*, 21(7), pp. 3839-3858, doi:10.5194/hess-21-3839-2017, 2017.

- Sprenger, M., D. Tetzlaff, J. Buttle, H. Laudon, H. Leister, C.P.J. Mitchell, J. Snelgrove, M. Weiler, and C. Soulsby, Measuring and modeling stable isotopes of mobile and bulk soil water, *Vadose Zone Journal*, 17(1), pp. 18, doi:10.2136/vzj2017.08.0149, 2018.
- Sprenger, M., T.H.M. Volkmann, T. Blume, and M. Weiler, Estimating flow and transport parameters in the unsaturated zone with pore water stable isotopes, *Hydrology and Earth System Sciences*, 19(6), pp. 2617-2635, doi:10.5194/hess-19-2617-2015, 2015.
- Spurlock, F., B. Johnson, A. Tuli, S.D. Gao, J. Tao, F. Sartori, R.J. Qin, D. Sullivan, M. Stanghellini, and H. Ajwa, Simulation of fumigant transport and volatilization from tarped broadcast applications, *Vadose Zone Journal*, 12(3), pp. 10, doi:10.2136/vzj2013.03.0056, 2013a.
- Spurlock, F., J. Šimůnek, B. Johnson, and A. Tuli, Sensitivity analysis of soil fumigant transport and volatilization to the atmosphere, *Vadose Zone Journal*, 12(2), pp. 12, doi:10.2136/vzj2012.013, 2013b.
- Stumpp, C., and P. Maloszewski, Quantification of preferential flow and flow heterogeneities in an unsaturated soil planted with different crops using the environmental isotope delta O-18, *Journal of Hydrology*, 394(3-4), pp. 407-415, doi:10.1016/j.jhydrol.2010.09.014, 2010.
- Stumpp, C., W. Stichler, M. Kandolf, and J. Šimůnek, Effects of land cover and fertilization method on water flow and solute transport in five lysimeters: A long-term study using stable water isotopes, *Vadose Zone Journal*, 11(1), pp. 14, doi:10.2136/vzj2011.0075, 2012.
- Tetzlaff, D., C. Birkel, J. Dick, J. Geris, and C. Soulsby, Storage dynamics in hydrogeological units control hillslope connectivity, runoff generation, and the evolution of catchment transit time distributions, *Water Resources Research*, 50(2), pp. 969-985, doi:10.1002/2013wr014147, 2014.
- Timbe, E., D. Windhorst, P. Crespo, H.G. Frede, J. Feyen, and L. Breuer, Understanding uncertainties when inferring mean transit times of water through tracer-based lumped-parameter models in Andean tropical montane cloud forest catchments, *Hydrology and Earth System Sciences*, 18(4), pp. 1503-1523, doi:10.5194/hess-18-1503-2014, 2014.

- van Genuchten, M.T., A closed-form equation for predicting the hydraulic conductivity of unsaturated soils, *Soil Science Society of America Journal*, 44(5), pp. 892-898, doi:10.2136/sssaj1980.03615995004400050002x, 1980.
- Vargas, A.I., B. Schaffer, Y.H. Li, and L.D.L. Sternberg, Testing plant use of mobile vs immobile soil water sources using stable isotope experiments, *New Phytologist*, 215(2), pp. 582-594, doi:10.1111/nph.14616, 2017.
- Wang, J., Lu, N., Fu, B.J., 2019. Inter-comparison of stable isotope mixing models for determining plant water source partitioning. *Science of the Total Environment*, 666: 685-693. DOI:10.1016/j.scitotenv.2019.02.262.
- Xiao, W., Wei, Z.W., Wen, X.F., 2018. Evapotranspiration partitioning at the ecosystem scale using the stable isotope method-A review. *Agricultural and Forest Meteorology*, 263: 346-361. DOI:10.1016/j.agrformet.2018.09.005.
- Zhao, P., X.Y. Tang, P. Zhao, and J.L. Tang, Dynamics of water uptake by maize on sloping farmland in a shallow Entisol in Southwest China, *Catena*, 147, pp. 511-521, doi:10.1016/j.catena.2016.08.001, 2016.
- Zheng, C., J. Šimůnek, Y. Lu, X. Liu, C. Shi, and H. Li, Monitoring and modeling the coupled movement of water, vapor, and energy in arid areas, *Journal of Hydrology*, 590, pp. 125528, 2020.
- Zimmermann, U., D. Ehhalt, and K. Münnich, Soil-water movement and evapotranspiration: Changes in the isotopic composition of the water, *Proceedings of the symposium of Isotopes in Hydrology.*, IAEA, Vienna, Austria, pp. 567-584, 1967.

Supplementary Material

Appendix A

The density of the saturated water vapor ρ_{sat}^v (kg/m³) depending on temperature T (K) is calculated as follows:

$$\rho_{sat}^v = 10^{-3} \frac{\exp(31.3716 - \frac{6014.79}{T} - 7.92495 \cdot 10^{-3} \cdot T)}{T} \quad (\text{A2.1})$$

The density of the water vapor ρ_v is the product of the density of the saturated water vapor ρ_{sat}^v (kg/m³) and relative humidity H_r [-]:

$$\rho_v = H_r \cdot \rho_{sat}^v \quad (\text{A2.2})$$

The molecular diffusion coefficient of the isotope i in free water D_i^{lo} [L²T⁻¹] is expressed as a function of temperature T (K):

$$D_i^{lo} = \sigma_i \cdot 10^{-9} \exp\left(-\frac{535400}{T^2} + \frac{1393.3}{T} + 2.1876\right) \quad (\text{A2.3})$$

where σ_i is a constant depending on the isotope species (0.98331 for HDO and 0.96691 for H₂¹⁸O).

The molecular diffusion of the isotope i in free air D_i^v [L²T⁻¹] is expressed as a function of temperature T (K):

$$D_i^v = D^v / b_i \quad (\text{A2.4})$$

$$D^v = 2.12 \cdot 10^{-5} \left(\frac{T}{273.16}\right)^2 \quad (\text{A2.5})$$

where b_i is the ratio of the molecular diffusion coefficients of light and heavy water (isotopes) in free air (1.0166 for HDO and 1.0324 for H₂¹⁸O as discussed in Eq. (12)).

For the verification examples in this study, the GMWL defined by *Rozanski et al.* (1993) was used. The LC-excess was calculated as follows:

$$LC - excess = (\delta^{2H} - 8.2\delta^{18O} - 11.27)/1.15 \quad (A2.6)$$

Tables

Table S2.1. Equations used in this study to calculate the kinetic fractionation coefficient (n_k).

Comment	Formulation	References
Molecular diffusion only	$\alpha_i^k = \frac{D_v}{D_i^v}$, i.e. $n_k=1$	<i>Barnes and Allison</i> (1983, 1984)
The evolution from molecular to turbulent transfer	$\alpha_i^k = \left(\frac{D_v}{D_i^v}\right)^{n_k},$ $n_k = \frac{(\theta_s - \theta_r)n_a + (\theta_{sat} - \theta_s)n_s}{(\theta_{sat} - \theta_r)}$ $n_a = 0.5, n_s = 1,$ $\theta_s, \theta_{sat},$ and θ_r are the volumetric water contents at the soil surface, the saturated water content, and the residual water content, respectively.	<i>Mathieu and Bariac</i> (1996)
Turbulent transfer only	$\alpha_i^k = 1$, i.e. $n_k=0$	<i>Melayah et al.</i> (1996a)

Table S2.2. Optimized soil hydraulic and solute transport parameters from *Stumpp et al.* (2012).

Horizon	Depth	θ_r	θ_s	α	n	K_s	Λ
	cm			cm^{-1}	-	cm/d	cm
Ap	0–30	0	0.30	0.023	1.140	110	4.7
Bv	31–90	0	0.32	0.076	1.070	6000	4.7
Cv	91–150	0	0.32	0.016	1.900	110	4.7

Table S2.3. Estimated flow parameters for each particle during the simulation period.

Particle Number	Initial Release Time (day)	Final Exit Time (day)	Transit Time (day)	Mean velocity (mm/day)
19	9.2955	190.8045	181.51	8.26
20	34.39	193.25	158.86	9.44
21	94.53	237.10	142.57	10.52
22	101.14	305.61	204.47	7.34
23	143.29	519.76	376.47	3.98
24	182.37	547.03	364.66	4.11
25	216.63	697.37	480.74	3.12
26	305.00	759.61	454.61	3.30
27	484.67	825.00	340.33	4.41
28	522.80	874.76	351.96	4.26
29	694.29	946.13	251.84	5.96
30	759.17	1054.13	294.96	5.09
31	801.80	1055.68	253.88	5.91
32	845.46	1162.78	317.32	4.73
33	873.74	1205.40	331.66	4.52
34	944.80	1325.61	380.81	3.94
35	1054.77	1357.25	302.48	4.96
36	1161.38	1423.88	262.50	5.71
37	1170.37	1425.82	255.45	5.87
38	1199.00	1484.65	285.65	5.25
39	1313.80	1514.00	200.20	7.49
40	1356.22	1581.16	224.94	6.67
41	1424.64	1652.80	228.16	6.57
42	1484.35	1663.10	178.75	8.39
43	1525.21	1710.63	185.42	8.09
44	1556.32	1723.48	167.16	8.97
Mean			276.05	6.03

Table S2.4. Comparison of the water storage in the soil profile when the particle leaves the transport domain at its bottom with the net water input into the soil profile during particle's presence in the profile.

Particle number	Final water storage (cm)	Precipitation (cm)	Actual evaporation (cm)	Actual transpiration (cm)	Net water input since particle release (cm)	Absolute error (cm)	Relative error (%)
19	39.42	79.84	34.51	5.91	39.42	0	0
20	39.64	72.56	27.68	5.29	39.59	0.05	0.12
21	40.06	53.49	11.55	1.91	40.03	0.03	0.07
22	40.21	51.65	11.15	0.56	39.94	0.27	0.67
23	41.3	94.64	43.4	10.18	41.07	0.24	0.58
24	39.34	91.03	41.7	10	39.33	0.01	0.03
25	40.94	90.56	41.63	8.14	40.78	0.15	0.37
26	40.44	98.38	54.16	4.07	40.15	0.28	0.7
27	35.89	79.47	35.18	8.64	35.65	0.24	0.67
28	40.67	90.57	38.53	11.78	40.25	0.42	1.03
29	39.72	90.87	40.34	10.86	39.67	0.05	0.13
30	41	76.02	27.84	7.22	40.95	0.04	0.1
31	41.35	59.16	16.24	1.78	41.14	0.21	0.5
32	39.7	76.02	33.27	3.13	39.62	0.07	0.18
33	39.96	88.08	34.21	14.06	39.81	0.15	0.38
34	40.35	97.04	43.01	13.86	40.17	0.18	0.44
35	39.44	93.46	43.01	11.06	39.39	0.05	0.13
36	41.3	66.8	18.98	6.74	41.08	0.22	0.53
37	40.91	60.33	17.65	2.02	40.66	0.24	0.6
38	41.07	66.54	25.71	0.13	40.7	0.37	0.9
39	39.33	59.41	19.27	0.95	39.19	0.14	0.37
40	40.72	83.09	31.14	11.41	40.54	0.17	0.42
41	39.87	90.75	40.08	10.9	39.77	0.1	0.25
42	39.28	75.49	28.17	8.05	39.27	0	0.01
43	39.23	58.81	17.8	1.83	39.18	0.05	0.12
44	40.2	53.87	13.45	0.45	39.97	0.23	0.58

Figures

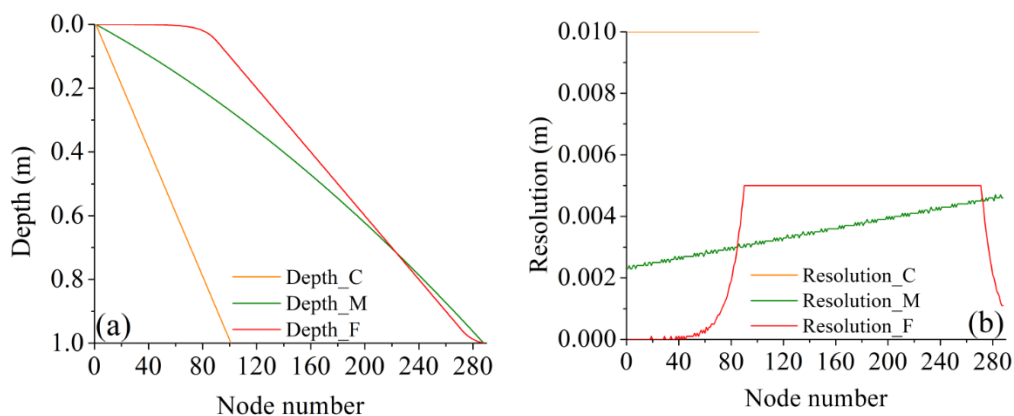


Figure S2.1. The node distribution versus depth (a) and spatial steps versus the node number (b) for the coarse, medium, and fine spatial discretizations. ‘C’, ‘M’, and ‘F’ refer to ‘coarse,’ ‘medium,’ and ‘fine’, respectively.

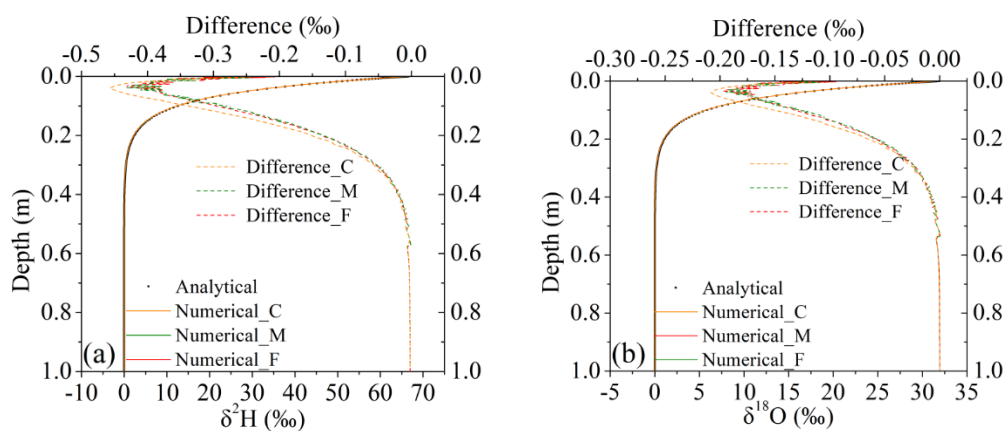


Figure S2.2. Comparison of analytical and numerical solutions (bottom axis) and their differences (top axis) for (a) ^2H and (b) ^{18}O isotopic composition profiles using the coarse, medium, and fine spatial discretizations for isothermal saturated soil under steady evaporation. ‘C’, ‘M’, and ‘F’ refers to ‘coarse’, ‘medium’, and ‘fine’, respectively.

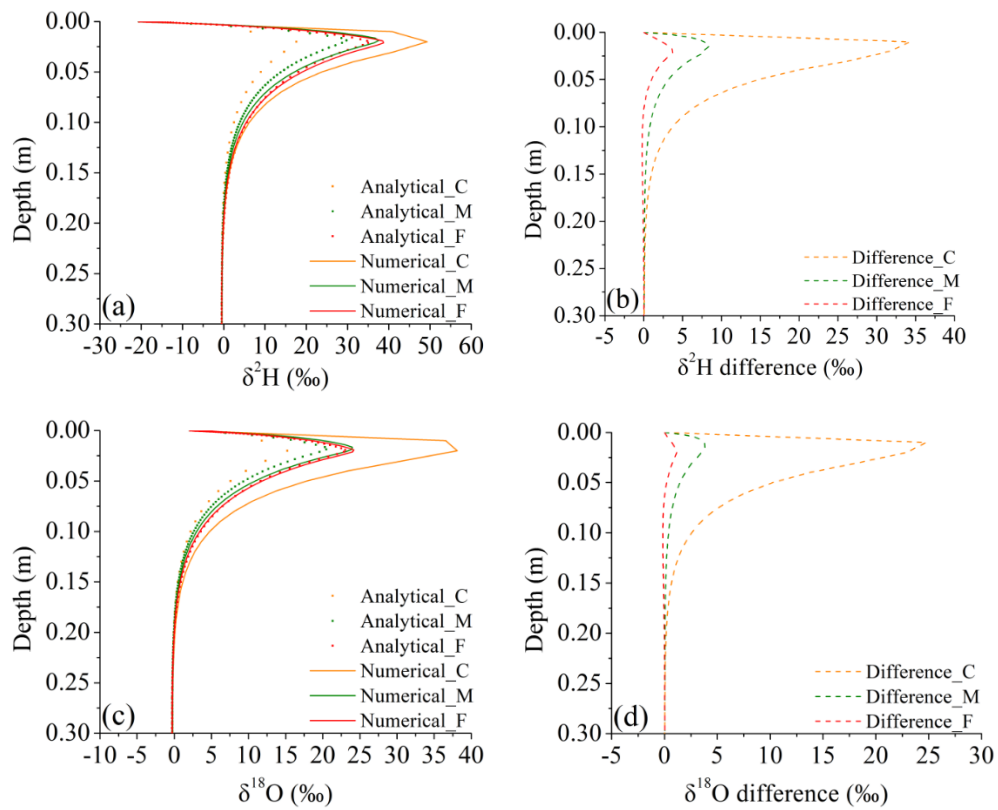


Figure S2.3. Comparison of analytical and numerical solutions (left) and their differences (right) for ^2H (top) and ^{18}O (bottom) isotopic composition profiles using the coarse, medium, and fine spatial discretizations for nonisothermal unsaturated soil under steady evaporation. ‘C’, ‘M’, and ‘F’ refer to ‘coarse’, ‘medium’, and ‘fine’, respectively. Results are presented for the top 30 cm only.

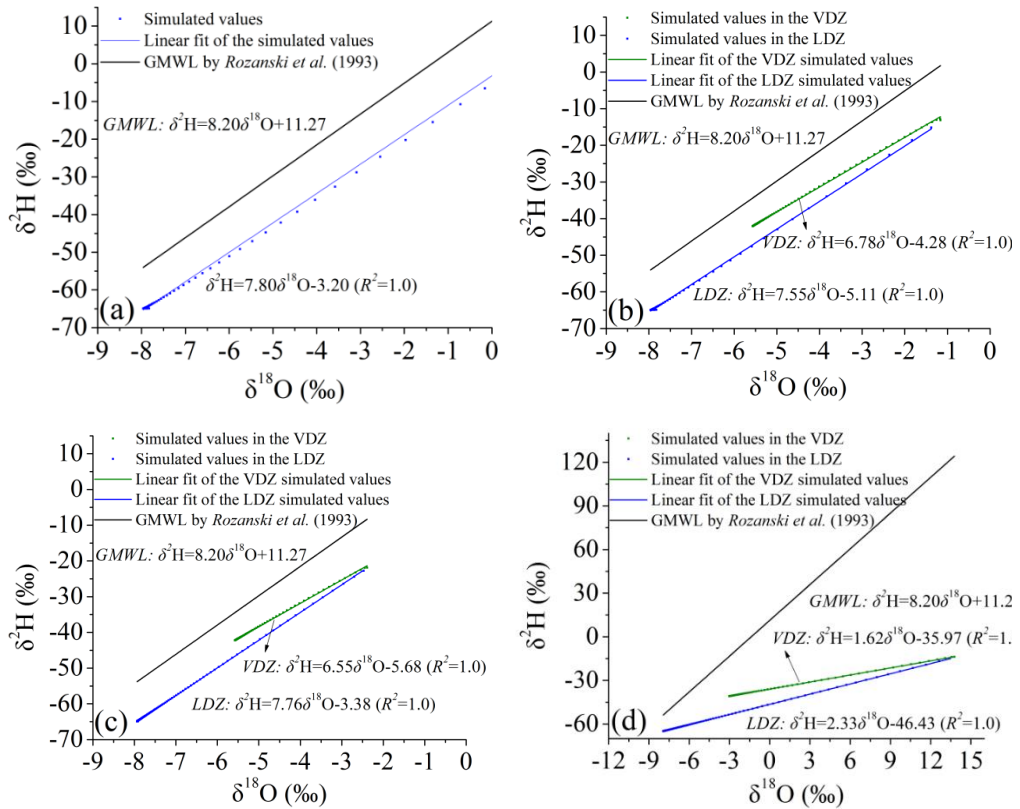


Figure S2.4. The ^2H - ^{18}O isotope plots for Plausibility Tests 3-6 (a-d) at 250 d obtained using fine spatial discretization.

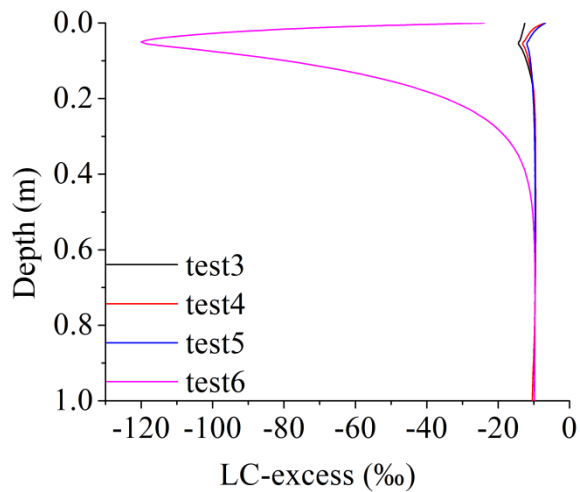


Figure S2.5. LC-excess profiles for Plausibility Tests 3-6 at 250 d obtained using fine spatial discretization.

Method S2.1. Estimation of the Atmospheric Isotope Ratio R_a .

The atmospheric isotope ratio (R_a), an important parameter in the Craig-Gordon model (Eq. 7), is difficult to measure and not always available. It is commonly estimated assuming that its isotopic composition is in equilibrium with that of rainfall (e.g., *Araguás-Araguás et al.*, 2000; *Skrzypek et al.*, 2015; *Benettin et al.*, 2018). However, the equilibrium assumption is mainly used for long-term (e.g., monthly) calculations rather than individual rain events because of various complications on short time scales and local effects. The estimation of R_a from precipitation may not be available for rain-free periods, in arid zones, or areas with significant local or upwind evapotranspiration moisture (*Gibson et al.*, 2008; *Crawford et al.*, 2019). Therefore, the atmospheric isotope ratio was estimated in this study by comparing the measured isotopic compositions with those simulated using the Gonfiantini evaporation fractionation model.

When only equilibrium fractionation is considered (i.e., $\alpha_i^* = \alpha_i^*$; $n_k = 0$), which is very common in humid zones, the isotope ratio of the evaporation flux calculated using the Gonfiantini model (Eq. 17) can be simplified as:

$$R_{E_SWIS} = \frac{R_L}{\alpha_i^{total}} = \alpha_i^* R_L \quad (\text{S2.1})$$

In humid zones, additional simplifying assumptions can be used: the relative humidity of the soil air phase at the surface equals 1 ($H_{rs} = 1$) and the soil surface and atmospheric temperatures are equal ($T_s = T_a$) (*Gat*, 2010; *Gonfiantini*, 1986). When

the R notation is used to define isotope concentrations, the isotope ratio of the evaporation flux calculated using the Craig-Gordon model (Eq. 8) under these conditions can be simplified as follows (Gat, 2010):

$$R_{E_CG} = \frac{\alpha_i^* \cdot R_L - h_a \cdot R_a}{1 - h_a} \quad (\text{S2.2})$$

Since $R_{E_CG} > 0$, we have:

$$R_a < \frac{\alpha_i^* \cdot R_L}{h_a} \quad (\text{S2.3})$$

The difference in the isotope ratio of the evaporation flux evaluated using the Gonfiantini and Craig-Gordon models then is:

$$R_{E_SWIS} - R_{E_CG} = \alpha_i^* R_L - \frac{\alpha_i^* \cdot R_L - h_a \cdot R_a}{1 - h_a} = \frac{h_a \cdot (R_a - \alpha_i^* \cdot R_L)}{1 - h_a} \quad (\text{S2.4})$$

There exist three cases when the Gonfiantini model either overestimates, underestimates, or matches the effects of evaporation fractionation compared to the Craig-Gordon model:

(1) If $R_{E_SWIS} - R_{E_CG} < 0$, then:

$$R_a < \alpha_i^* \cdot R_L \quad (\text{S2.5})$$

(2) If $R_{E_SWIS} - R_{E_CG} > 0$, we get using Eq. (S3):

$$\alpha_i^* \cdot R_L < R_a < \frac{\alpha_i^* \cdot R_L}{h_a} \quad (\text{S2.6})$$

(3) If $R_{E_SWIS} - R_{E_CG} = 0$, then:

$$R_a = \alpha_i^* \cdot R_L \quad (\text{S2.7})$$

This means that only when $R_a = \alpha_i^* \cdot R_L$, we get the same results with both the Gonfiantini or Craig-Gordon models. In the case when fractionation is negligible, the

no-fractionation assumption can be used ($\alpha_i^* = 1$), then $R_a = R_L$, and $R_{E_SWIS} = R_{E_CG} = R_L$.

If we consider evaporation fractionation ($\alpha_i^* \neq 1$) and want the Craig-Gordon model to have the same results as with no fractionation, then we need to have:

$$R_{E_CG} = \frac{\alpha_i^* \cdot R_L - h_a \cdot R_a}{1 - h_a} = R_L \quad (\text{S2.8})$$

Then:

$$R_a = \frac{(\alpha_i^* - 1 + h_a) \cdot R_L}{h_a} \quad (\text{S2.9})$$

In the field evaluation example (Fig. 6), the isotopic composition's measured values are initially close to the values simulated by the Gonfiantini model without considering fractionation. Later on (about 1150~1500 days), they are close to the values simulated considering equilibrium fractionation. To obtain similar simulation results using the Craig-Gordon model, the early atmospheric isotope ratio R_a should correspond to Eq. (S9), while the late R_a should correspond to Eq. (S7). This indicates that the atmospheric isotope ratio R_a in the entire simulation period should be between these two cases. Therefore, an approximate estimate (the average R_a estimated by Eqs. (S7) and (S9)) was used in this study in the Craig-Gordon model implemented into the HYDRUS isotope module, i.e.:

$$R_a = \frac{(\alpha_i^* - 1 + h_a + h_a \cdot \alpha_i^*) \cdot R_L}{2h_a} \quad (\text{S2.10})$$

In theory, the atmospheric isotope ratio R_a is determined by the atmosphere above the soil, and therefore, should be independent of what happens in the soil.

However, the approach described above can provide a relatively reasonable estimate of R_a to be used in the Craig-Gordon model to fit the measurements.

Chapter 3 The Impact of Evaporation Fractionation on the Inverse Estimation of Soil Hydraulic and Isotope Transport Parameters

Abstract: Choosing a suitable process-oriented eco-hydrological model is essential for obtaining reliable simulations of hydrological processes. Determining soil hydraulic and solute transport parameters is another fundamental prerequisite. Research discussing the impact of considering evaporation fractionation on parameter estimation and practical applications of isotope transport models is limited. In this study, we analyzed parameter estimation results for two datasets for humid and arid conditions using the isotope transport model in HYDRUS-1D, in which we either did or did not consider fractionation. The global sensitivity analysis using the Morris and Sobol' methods and the parameter estimation using the Particle Swarm Optimization algorithm highlight the significant impact of considering evaporation fractionation on inverse modeling. The Kling-Gupta efficiency (KGE) index for isotope data can increase by 0.09 and 1.49 for the humid and arid datasets, respectively, when selecting suitable fractionation scenarios. Differences in estimated parameters propagate into the results of two practical applications of stable isotope tracing: i) the assessment of root water uptake (RWU) and drainage travel times (i.e., the time elapsed between water entering the soil profile as precipitation and leaving it as transpiration or drainage) in the lysimeter (humid conditions) and ii) evaporation estimation in a controlled

experimental soil column (arid conditions). The peak displacement method with optimized longitudinal dispersivity provides much lower travel times than those obtained using the particle tracking algorithm in HYDRUS-1D. Considering evaporation fractionation using the Craig-Gordon (CG) and Gonfiantini models is likely to result in estimates of older water ages for RWU than the no fractionation scenario. The isotope mass balance method that uses the isotopic composition profile simulated by HYDRUS-1D while considering fractionation using the CG and Gonfiantini models, or the measured evaporation isotope flux, provides comparable results in evaporation estimation as the HYDRUS-1D water mass balance method and direct laboratory measurements. In contrast, the no fractionation scenario reasonably estimates evaporation only when using the HYDRUS-1D water mass balance method. The direct use of simulated isotopic compositions in the no fractionation scenario may result in large biases in practical applications in the arid zone where evaporation fractionation is more extensive than in humid areas.

3.1 Introduction

Reliable water balance simulations in the vadose zone are important to understand and forecast the impact of anthropogenic disturbances such as global warming and land-use change on soil water storage, groundwater recharge, and evapotranspiration. A detailed mechanistic understanding of water fluxes in the vadose zone could support optimal and efficient management strategies for promoting the long-term sustainability of water resources and associated ecosystem functions (Penna et al., 2018). For example, the exact quantification of evaporation affects water availability for plants (Nelson et al., 2020) and constrains groundwater recharge (Condon et al., 2020). However, the conventional methods (e.g., pan experiments) for estimating evaporation fluxes often require extensive field monitoring of water flow, which is often time-consuming, expensive, labor-demanding, and affected by considerable uncertainty (Skrzypek et al., 2015).

Stable isotopes of hydrogen (^2H) and oxygen (^{18}O) are widely used to trace water fluxes across the critical zone and can be expressed as isotopic ratios, $^2\text{H}/^1\text{H}$ and $^{18}\text{O}/^{16}\text{O}$ by using the δ notation (i.e., $\delta^2\text{H}$ and $\delta^{18}\text{O}$). The isotopic composition of shallow soil water provides insights into evaporation fractionation characteristics. This information can be easily used to calculate corresponding evaporation fluxes. For example, Skrzypek et al. (2015) combined the equations for evaporation estimation based on the revised Craig-Gordon model (Craig and Gordon, 1965) and developed a

software Hydrocalculator. Using this software, they estimated evaporation losses and validated its results using pan measurements. This method has been extended to soil evaporation estimation. For example, Sprenger et al. (2017) estimated that evaporation was about 5 and 10% of infiltrating water in the heath and Scots pine soils, respectively.

While the spatial origin of the water plants use has been widely studied (e.g., Allen et al., 2019), very little is known about its temporal origin (Brinkmann et al., 2018; Miguez-Macho and Fan, 2021). To track water across the critical zone, we need to assess how fast water moves down to the soil profile bottom and when and how much water returns to the atmosphere through root water uptake (RWU). The premise is to accurately estimate travel times (TT) of irrigation/precipitation water (i.e., the time between water entering the soil profile as irrigation/precipitation and leaving it back to the atmosphere as transpiration or at the soil profile bottom as drainage).

The peak displacement method represents the most widespread technique to estimate travel time from the time difference between signals in soil water stable isotope time-series directly measured at specific soil depths (Chesnaux and Stumpp, 2018; Koeniger et al., 2016; Stumpp et al., 2012). However, this method is unfeasible when there is no pronounced peak correspondence between isotopic compositions of precipitation and drainage water samples. Another widely-used isotope-transport-based method is to inversely estimate the parameters for time-invariant TT distributions (TTDs) (e.g., Timbe et al., 2014) or time-variant StorAge Selection (SAS) functions

(Benettin and Bertuzzo, 2018; Harman, 2015; Rinaldo et al., 2015) implemented in lumped hydrological models. Such oversimplified models are based on few soil and vegetation parameters but have limitations in describing transient conditions or simulating isotope transport (Sprenger et al., 2016a).

In contrast, isotope transport can be reliably simulated using the Richards equation-based hydrological models with appropriate soil and vegetation parameters and known boundary and initial conditions. However, direct measurements of soil hydraulic and transport parameters required by such models are time-consuming and labor-demanding. Therefore, such parameters are commonly obtained using inverse modeling by minimizing the errors between easily-measured state variables and fluxes (e.g., soil water contents and pressure heads at different soil depths or leachate water volumes) and corresponding model simulations (Hopmans et al. 2002; Mertens et al., 2006; Vrugt et al., 2008; Wollschläger et al., 2009; Wöhling and Vrugt, 2011).

Nevertheless, it is not always necessary to account for all model parameters in parameter optimization since some can be fixed as they can be either determined experimentally or have a minor impact on the model output. The latter can be determined using the global sensitivity analysis (GSA). The Sobol' and Morris methods are among the two most widespread GSA methods (Liu et al., 2020). The Sobol' method provides the most accurate sensitivity indices, but it requires several model runs and is thus computationally intensive (Gatel et al., 2019). In contrast, the Morris method

cannot yield the order of the most sensitive parameters as accurately as the Sobol' method, but its computational cost is much lower, and it can still pinpoint the most influential parameters (Campolongo et al., 2007; Herman et al., 2013).

Many inverse modeling algorithms can be used for parameter estimation. For example, the Levenberg-Marquardt Optimization (LMO) proved to be very efficient and was, therefore, implemented in HYDRUS (Šimůnek et al., 2008). However, the LMO is sensitive to the initial parameter values provided by the user and often falls into local instead of global minimum (Brunetti et al., 2016). Thus, global optimization algorithms, such as Particle Swarm Optimization (PSO), have become more widespread over the last decades (e.g., Vrugt and Robinson, 2007).

When optimizing isotope transport parameters via inverse modeling, isotopic compositions from multiple soil depths must be included in the objective function and combined with other state variables and fluxes. For example, research shows that the model calibration can be improved by simultaneously considering stable isotopes and soil moisture information (Sprenger et al., 2015; Groh et al., 2018; Mattei et al., 2020). However, the correct model structure is a fundamental prerequisite to obtaining successful simulations. In particular, research discussing the impact of considering evaporation fractionation on parameter estimation and practical applications of isotope transport models is limited (Penna et al., 2018). Therefore, we pose two scientific questions. First, how will the consideration of evaporation fractionation affect the

parameter estimation results of the isotope transport model? Second, how will this effect propagate into practical applications such as water travel times and evaporation estimation?

To answer these questions, we compare the parameter estimation results obtained using the isotope transport model in HYDRUS-1D (Zhou et al., 2021) that does or does not consider evaporation fractionation for two available datasets: 1) a 150-cm-thick layered soil profile in a lysimeter under humid climate where evaporation fractionation is negligible; 2) a 35-cm-thick soil column subject to evaporation where evaporation fractionation process is dominant. The accuracy of the parameterization obtained by the PSO algorithm is assessed based on its ability to reproduce measured water fluxes and isotope transport data. The parameters estimated while considering (or not) evaporation fractionation are then used to calculate travel times and evaporation.

3.2 Materials and Methods

Two experimental datasets are considered in this study. The first dataset is collected using a field lysimeter (150-cm-thick layered soil profile) located in Austria under humid climate conditions (Stumpp et al., 2012) (Section 3.2.1.1). The second dataset is collected using a 35-cm-thick soil column (in France) subject to evaporation to mimic arid climate conditions (Braud et al., 2009a) (Section 3.2.1.2). Numerical simulations of water flow and isotope transport (with and without evaporation fractionation) are implemented in HYDRUS-1D. The modeling setup is briefly

described in Section 3.2.2 and Method S3.1 in the Supplementary Material. The sensitivity analysis based on the Sobol' and Morris methods is performed to evaluate the interactions between soil hydraulic and solute transport parameters and the impact of multiple measured data types (Section 3.2.3, Method S3.3.2, and Results S3.1~S3.2). The accuracy of the parameterization obtained by the PSO algorithm is assessed based on its ability to reproduce the observed data (Sections 3.2.4, 3.3.1.1, and 3.3.2.1). The parameters estimated while considering or not considering evaporation fractionation are then used to calculate travel times and evaporation and quantify the impact of their different estimates (Sections 3.2.5, 3.2.6, 3.3.1.2, and 3.3.2.2). The effects of varying climate conditions and estimation methods are then compared and illuminated (Section 3.4). The schematic outline of the different methods used is shown in Fig. 3.1.

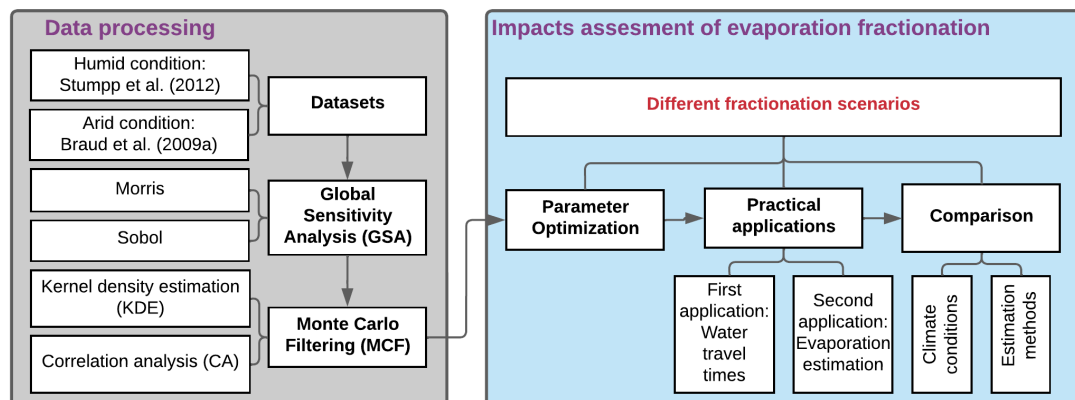


Figure 3.1. Schematic outline of methods used.

3.2.1 Site Description and Data Availability

3.2.1.1 Stumpp et al. (2012) Dataset

The first dataset is taken from the lysimeter 3 of Stumpp et al. (2012) (available at <https://www.pc-progress.com/en/Default.aspx?h1d-lib-isotope>). The field experiment was conducted in a humid region located at the research area of the HBLFA (Höhere Bundeslehr- und Forschungsanstalt für Landwirtschaft) Raumberg-Gumpenstein, in Gumpenstein, Austria. This area has a mean annual temperature of 6.9 °C and average annual precipitation (P) of 1035 mm. The annual potential evapotranspiration (ET_0) (for grass reference) during the experiment period (May 2002 to February 2007) calculated by the Penman-Monteith equation is about 557 mm, and the corresponding aridity index (P/ET_0) is about 1.86, corresponding to a humid climate class (Liang, 1982). The cylindrical lysimeter (with a depth of 150 cm and a surface area of 10000 cm²) was embedded in a rainfed agricultural field (Cambisol) planted with winter rye and fertilized with liquid cattle slurry.

The observation period was from May 2002 to February 2007 (1736 days). Table S3.1 shows the summary of the observed data. The temporal distribution of P , ET_0 , soil surface temperature (T_s), air relative humidity (RH), and leaf area index (LAI) during the simulation period are shown in Fig. 3.2. More details about data acquisition, including meteorological parameters and root water uptake information, can be found in Stumpp et al. (2012).

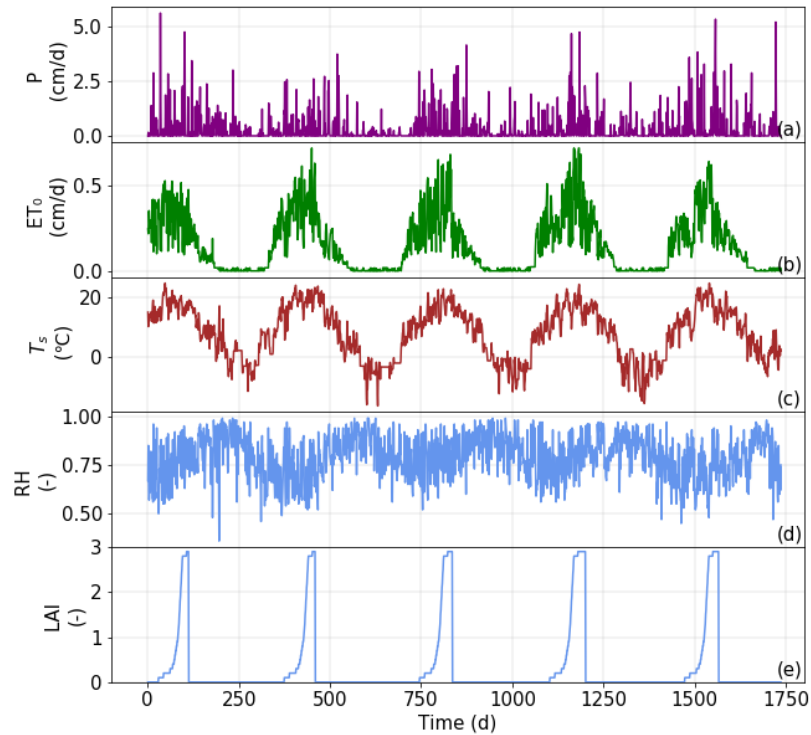


Figure 3.2. The temporal distribution of precipitation (P) (a), potential evapotranspiration (ET_0) (b), soil surface temperature (T_s) (c), air relative humidity (RH) (d), and leaf area index (LAI) (e) during the simulation period for the Stumpp et al. (2012) dataset (adapted from Stumpp et al., 2012).

3.2.1.2 Braud et al. (2009a) Dataset

Braud et al. (2009a) designed a RUBIC IV experiment that started on April 11, 2005, corresponding to Day of the Year (DoY) 101, and lasted 338 days. The experiment consisted of 6 columns, 12 cm in diameter and 35 cm in height. The soil columns were filled with a silt loam collected at the field station of Lusignan, France, and wetted using demineralized water of the known isotopic composition. The bottom was closed by clay marbles. The soil was initially saturated and subject to evaporation only. Dry air was simultaneously injected over all six columns. The isotopic composition of the air changed due to water vapor released by evaporation from soil

columns. The air was finally trapped in a cryoscopic device, which allowed the determination of evaporation fluxes from bare soil columns and the corresponding isotopic composition of the water vapor under non-steady-state conditions. More details about the experimental setup can be found in Figs. 1~2 of Braud et al. (2009a). The data collected in Column 2, ending at DoY 264, were analyzed in this study.

Thirteen variables were measured continuously at a frequency of about 15 minutes to assess the water balance of the soil column. These variables included the room temperature, the atmospheric pressure, the absolute pressure of the dry air before it entered the soil column, air mass flow for the humidity control above the soil column, the mass of the soil column, air temperature and humidity at the outlet of the soil column, the temperatures of the cryoscopic trapping downstream and upstream of the columns, and the air temperature and residual air humidity at the outlets of two cold traps. The vapor was trapped twice a day during the first three months and only once a day after that once evaporation decreased. Soil column 2 was dismantled on September 21, 2005 (DoY 264) to sample liquid water and measure the gravimetric soil water content. More details about data acquisition can be found in Braud et al. (2009a). The temporal distributions of the evaporation flux (E), the isotopic composition of the evaporation flux (δ_E), outlet air temperature (T_{air}), and outlet air relative humidity (RH) during the simulation period are shown in Fig. 3.3.

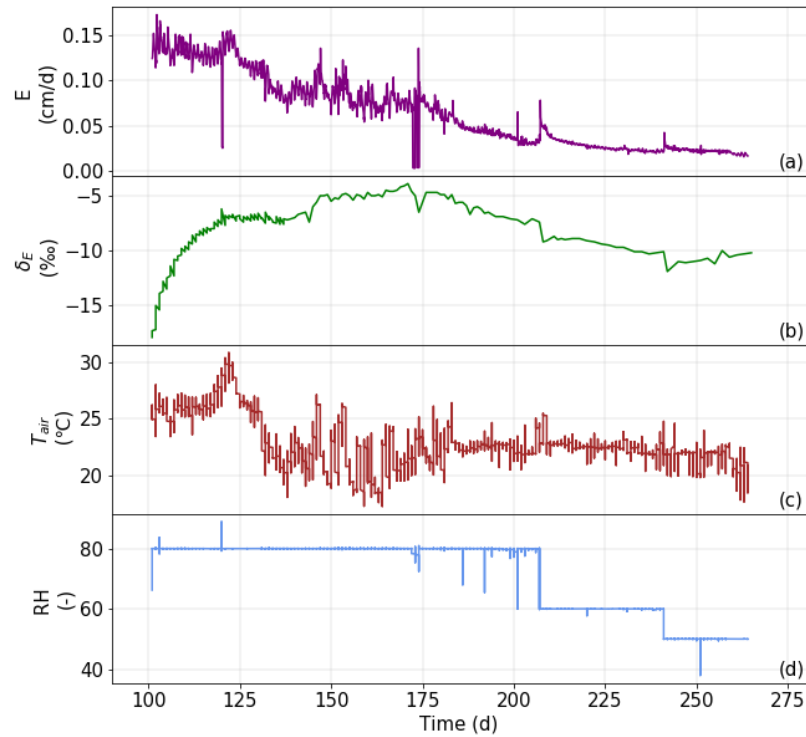


Figure 3.3. Time series of the evaporation flux (E) (a) isotopic composition of the evaporation flux (δ_E) (b), outlet air temperature (T_{air}) (c), outlet air relative humidity (RH) (d), during the simulation period for the Braud et al. (2009a) dataset (adapted from Braud et al., 2009a).

3.2.2 Model Setup

The HYDRUS-1D model modified by Zhou et al. (2021) to simulate the transport of soil water isotopes while considering evaporation fractionation was used in this study. A brief summary of the model setup, including the governing equations (without and with vapor flow for the Stumpp et al. (2012) and Braud et al. (2009a) datasets, respectively), boundary conditions (BCs), and model inputs is shown in Figs. 3.4~3.5. More details can be found in Zhou et al. (2021).

3.2.2.1 *Stumpp et al. (2012) Dataset*

The soil profile was 150 cm deep and was discretized into 151 nodes. It consisted of three different soil horizons (0 ~ 29 cm; 30 ~ 89 cm; 90 ~ 150 cm). The initial pressure head profile was assumed to be at hydrostatic equilibrium with the pressure head $h=-150$ cm at the soil surface. The weighted average $\delta^{18}\text{O}$ of precipitation (-9.5‰) and estimated temperature (20 °C) were used as initial conditions.

The atmospheric (with a surface layer) and seepage face boundary conditions (BC) were used for water flow at the upper and lower boundaries, respectively. The temperature BC was used for heat transport at both boundaries. In this humid condition example, evaporation fractionation was limited to the soil surface due to the lack of the vapor phase within the soil. The solute flux and zero concentration gradient BCs were used for isotope transport at the upper and lower boundaries, respectively. The isotope flux associated with evaporation was calculated either assuming no fractionation or using the Craig-Gordon or Gonfiantini fractionation models (hereafter referred to as Non_Frac, CG_Frac, and Gon_Frac, respectively). The Non_Frac scenario calculated the isotope flux of evaporation by assuming that the isotopic composition of the evaporation flux was the same as that of surface soil water. The isotopic composition of the atmospheric water vapor (δ_A) in the CG_Frac scenario was estimated based on its equilibrium relationship with the isotopic composition of rainfall (Skrzypek et al., 2015). The Gon_Frac scenario was simplified (without the need for the isotopic

composition of the atmospheric water vapor) to consider fractionation (Zhou et al., 2021). A detailed description of the CG and Gonfiantini models can be found in Method S3.1. For simplification, only equilibrium fractionation was considered at the soil surface since kinetic fractionation could be neglected in this example (Zhou et al., 2021). In other words, the kinetic fractionation coefficient (n_k) in Eq. (11) of Zhou et al. (2021) was set to 0, and thus the kinetic fractionation factor at the soil surface (α_i^k) in the CG_Frac and Gon_Frac scenarios (Eqs. S3.2, S3.3) was equal to 1.

Conceptual model	Equations and BCs	Inputs	Abbreviations
<p>humid condition example</p> <p>Note: evaporation fractionation is limited to the soil surface (due to the lack of the vapor phase within soil). For simplicity, only equilibrium fractionation is considered.</p>	<p>➤ Upper BCs:</p> <ul style="list-style-type: none"> • W: Atmospheric BC • H: Temperature BC • I: Non_Frac, Gon_Frac, CG_Frac <p>➤ The governing equations:</p> <ul style="list-style-type: none"> • W $\frac{\partial \theta_l}{\partial t} = \frac{\partial}{\partial z} \left[K_{lh} \left(\frac{\partial h}{\partial z} + \cos \omega \right) \right] - S$ • H $\frac{\partial C_p(\theta_l)T}{\partial t} = \frac{\partial}{\partial z} \left[\lambda(\theta_l) \frac{\partial T}{\partial z} \right] - C_w \frac{\partial q_l T}{\partial z} - C_w S T$ • I $\frac{\partial \theta_l C_i^l}{\partial t} = \frac{\partial}{\partial z} \left(D_i^l \frac{\partial C_i^l}{\partial z} \right) - \frac{\partial (q_l C_i^l)}{\partial z} - S C_i^l$ <p>➤ Lower BCs:</p> <ul style="list-style-type: none"> • W: Seepage face BC • H: Temperature BC • I: Zero concentration gradient 	<p>➤ Upper BCs:</p> <ul style="list-style-type: none"> • W: P, ET_0, LAI, crop growth and RWU parameters. • H: T_s • I: δ_p, RH, δ_A <p>➤ W: VG-M model: $\theta_r, \theta_s, n, \alpha, K_S$ (optimized).</p> <p>➤ H: Chung-Horton model: parameters from Stumpp et al. (2012).</p> <p>➤ I: D_i^{l0} (calculated), λ (optimized).</p> <p>➤ Lower BCs:</p> <ul style="list-style-type: none"> • W: None • H: T_b • I: None 	<p>$C_p(\theta_l), C_w$: volumetric heat capacities of the porous medium, and the liquid phase, respectively</p> <p>C_i^l: isotope concentrations of soil water</p> <p>D_i^l: effective dispersion coefficient of the isotope i in soil water</p> <p>D_i^{l0}: molecular diffusion coefficient of isotope i in free water</p> <p>E: actual evaporation</p> <p>ET_0: potential evapotranspiration</p> <p>h: water pressure head</p> <p>K_{lh}: isothermal hydraulic conductivity of the liquid phase</p> <p>K_S: saturated hydraulic conductivity</p> <p>LAI: leaf area index</p> <p>n, α: shape parameters of the VG model</p> <p>P: precipitation rate</p> <p>Q: drainage or discharge</p> <p>q_l: liquid water flux</p> <p>RH: air relative humidity</p> <p>S: sink term</p> <p>t: time</p> <p>T_b: soil bottom temperature</p> <p>T_s: soil surface temperature</p> <p>z: spatial coordinate (positive upward)</p> <p>ω: angle between the flow direction and the vertical axis</p> <p>δ_A: isotopic composition of the atmospheric water vapor</p> <p>δ_p: isotopic composition of precipitation</p> <p>θ_l: liquid volumetric water content</p> <p>θ_r: residual water content</p> <p>θ_s: saturated water content</p> <p>λ: longitudinal dispersivity</p> <p>$\lambda(\theta_l)$: coefficient of the apparent thermal conductivity of the soil</p>

Figure 3.4. Model setup for the Stumpp et al. (2012) dataset. Note that "W," "H," and "I" represent water flow, heat transport, and isotope transport, respectively.

3.2.2.2 Braud et al. (2009a) Dataset

The simulated soil profile was 35 cm deep and was discretized into 132 nodes following Braud et al. (2009a). The soil column was initially almost fully saturated, with the measured initial pressure head increased linearly from -1 cm at the soil surface to 35 cm at the soil profile bottom. The observed initial soil temperature and $\delta^{18}\text{O}$ were 24.25 °C and -6.34% , respectively.

The temperature BC was used for heat transport at both surface and bottom boundaries, using temperatures measured at 2.5 and 24 cm depths, respectively. The atmospheric and zero flux BCs were used for water flow at the upper and lower boundaries, respectively. The measured evaporation flux, E was used as the upper BC for water flow. In this arid condition example, evaporation fractionation occurred both at the soil surface and within the soil due to the existence of the vapor phase. The stagnant air layer BC (which had been modified to account for evaporation fractionation) and zero flux BC were used for isotope transport at the upper and lower boundaries, respectively. The surface isotope flux associated with evaporation was calculated either assuming no fractionation, using the Craig-Gordon or Gonfiantini fractionation models, or using the measured values (hereafter referred to as Non_Frac, CG_Frac, Gon_Frac, and Meas_Frac, respectively). The Non_Frac scenario calculated the isotope flux of evaporation by assuming that its isotopic composition was the same as that of surface soil water (i.e., no fractionation at the soil surface), and equilibrium and kinetic fractionation factors within the soil (α^+ , α_i^D) were equal to 1 (i.e., no fractionation within the soil). The theory of CG_Frac and Gon_Frac scenarios was explained in Method S3.1. For simplification, the kinetic fractionation coefficient n_k in Eq. (11) of Zhou et al. (2021) was set to 1, and thus the kinetic fractionation factor at the soil surface (α_i^k) in the CG_Frac and Gon_Frac scenarios (Eqs. S3.2, S3.3) was equal to 1.0324. The measured isotopic composition of the outlet water vapor, δ_E , was used in

the Meas_Frac scenario to calculate the surface isotope flux E_i corresponding to the evaporation flux E . More details about how upper boundary fluxes were calculated can be found in Braud et al. (2009a).

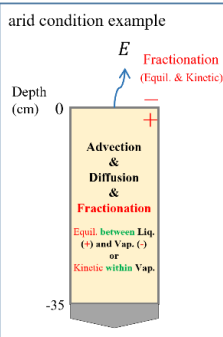
Conceptual model	Equations and BCs	Inputs	Abbreviations
<p>arid condition example</p>  <p>Note: evaporation fractionation happens both at the soil surface and within soil (due to the existence of the vapor phase). Both equilibrium and kinetic fractionation are considered.</p>	<p>> Upper BCs:</p> <ul style="list-style-type: none"> • W: Atmospheric BC • H: Temperature BC • I: Non_Frac, Gon_Frac, CG_Frac, Meas_Frac <p>> Lower BCs:</p> <ul style="list-style-type: none"> • Zero flux BC • Temperature BC • Concentration flux BC <p>> The governing equations:</p> <p>• W</p> $\frac{\partial \theta_r(h)}{\partial t} = \frac{\partial}{\partial z} \left[K_{Lh} \left(\frac{\partial h}{\partial z} + \cos \omega \right) + K_{Lh} \frac{\partial T}{\partial z} + K_{vh} \frac{\partial h}{\partial z} + K_{vT} \frac{\partial T}{\partial z} \right]$ <p>• H</p> $C_p(\theta_r) \frac{\partial T}{\partial t} + L_0 \frac{\partial \theta_e}{\partial t} = \frac{\partial}{\partial z} \left(\lambda(\theta_r) \frac{\partial T}{\partial z} \right) - C_w q \frac{\partial T}{\partial z} - C_v \frac{\partial q_v T}{\partial z} - L_0 \frac{\partial q_e}{\partial z}$ <p>• I</p> $\frac{\partial [\theta_r c_i^l]}{\partial t} = \frac{\partial}{\partial z} [D_i^{lv} \frac{\partial c_i^l}{\partial z} - Q_i^{lv} c_i^l]$ $\theta_r = [\theta_r + (n_{soil} - \theta_r) \beta_i^*]$ $Q_i^{lv} = (q_r + \beta_i^* q_v - D_i^{lv} \frac{\partial \beta_i^*}{\partial z})$ $D_i^{lv} = D_i^* + D_i^{v*} \beta_i^*$ $c_i^v = \beta_i^* c_i^l = \alpha_i^* \frac{\rho_v}{\rho_w} c_i^l$	<p>> Upper BCs:</p> <ul style="list-style-type: none"> • W: E • H: T_s • I: RH, δ_A, δ_E <p>• W: VG-M model: $\theta_r, \theta_s, n, \alpha, K_S$ (optimized).</p> <p>• H: Chung-Horton model: parameters from Braud et al. (2009a).</p> <p>• I: D_i^{lv}, D_i^v (calculated), λ (optimized).</p> <p>> Lower BCs:</p> <ul style="list-style-type: none"> • W: 0 • H: T_b • I: None 	<p>C_i^v: isotope concentrations in soil water (vapor), respectively</p> <p>C_p: volumetric heat capacities of the vapor phase, respectively</p> <p>D_i^{lv}: effective dispersion coefficients of the isotope i in soil water vapor</p> <p>D_i^v: molecular diffusion coefficient of isotope i in free air, respectively</p> <p>K_{Lh}: thermal hydraulic conductivity of the liquid phase</p> <p>K_{vh}: isothermal vapor hydraulic conductivity</p> <p>K_{vT}: thermal vapor hydraulic conductivity</p> <p>L_0: volumetric latent heat of vaporization of liquid water</p> <p>n_{soil}: soil porosity</p> <p>q_r: vapor flux</p> <p>β_i^*: ratio of the isotope concentration in the vapor phase and the isotope concentration in the liquid phase</p> <p>δ_e: isotopic composition of evaporation flux</p> <p>θ_r: total volumetric water content, being the sum ($\theta_r = \theta_l + \theta_v$)</p>

Figure 3.5. Model setup for the Braud et al. (2009a) dataset. Note that "W," "H," and "I" represent water flow, heat transport, and isotope transport, respectively.

3.2.3 Global Sensitivity Analysis

Five soil hydraulic parameters (i.e., θ_r , θ_s , n , α , and K_S) need to be optimized for each layer of the soil profile to simulate water flow using the HYDRUS-1D model. The residual water content θ_r was set to zero to reduce the number of fitting parameters. To simulate isotope transport in the soil, the longitudinal dispersivity λ also needs to be optimized. Since only the isotopic composition of the lysimeter discharge was measured in the Stumpp et al. (2012) dataset, the dispersivity of three individual soil layers cannot be estimated. Therefore, only one longitudinal dispersivity for the entire lysimeter was estimated. Therefore, the total number of parameters p was 13 and 5 for the Stumpp et al. (2012) and Braud et al. (2009a) datasets, respectively.

The global sensitivity analysis (GSA) using both Morris and Sobol' methods was conducted in this study to determine the most influential parameters and their interactions. The detailed description of these two methods is shown in Method S3.2 in the Supplementary Material.

The sensitivity analysis was conducted using Python's Sensitivity Analysis Library (SALib) (Herman and Usher, 2017). The script produces the input parameter space, overwrites the input parameters file, and runs the executable module of HYDRUS-1D. For each simulation of the Stumpp et al. (2012) dataset, five Kling-Gupta efficiency (KGE) indices for different evaluation indicators were calculated, including for the time series of the bottom water flux (KGE_bf), the soil water content at different depths (KGE_wc), the bottom water isotopic composition (KGE_wi), the water retention curves (KGE_rc), and the average of the four KGE values (KGE_avg). For each simulation of the Braud et al. (2009a) dataset, three Kling-Gupta efficiency (KGE) indices for different evaluation indicators were calculated, including the final soil water content profile (KGE_wc), the final water isotopic composition profile (KGE_wi), and the average of the two KGE values (KGE_avg). The KGE index compares the correlation coefficient (r), the ratio of mean values (β), and the ratio of variances (γ) between simulated and observed data. The value of the KGE index is always smaller or equal to 1. The higher the KGE value, the better fit between the

simulated and observed values. The positive and negative KGE values are often considered "good" and "bad" solutions (Knoben et al., 2019).

$$\text{KGE} = 1 - [(1 - r)^2 + (1 - \beta)^2 + (1 - \gamma)^2]^{0.5} \quad (3.1)$$

If a HYDRUS-1D run was not finished within a prescribed time (i.e., 30 s and 60 s for the Stumpp et al. (2012) and Braud et al. (2009a) datasets, respectively) or the length of the modeled hydrograph was shorter than the total simulation period (1736 and 163 days for the Stumpp et al. (2012) and Braud et al. (2009a) datasets, respectively), it was considered non-convergent. The run was then terminated, and a large negative value ($-1\text{E}+7$) was prescribed to the objective function.

Non-convergent runs in GSA are a frequent problem when using nonlinear environmental/hydrological models, and there are no clear indications on how to handle these "unfeasible" points (Razavi et al., 2021). Removing or skipping them alters the sampling trajectory and can result in biased conclusions, especially if non-convergent runs lie in informative regions of the parameter space. Recently, (Sheikholeslami et al., 2019) compared strategies such as median substitution, single nearest-neighbor, or response surface modeling (Brunetti et al., 2017) to fill in for model crashes. Their results show that interpolating non-convergent runs with a radial basis function trained in the vicinity of that point leads to reliable results and outperforms other strategies. We implemented a similar approach in the present work but with important differences. In particular:

1. For each non-convergent point, we calculated its Euclidean distance from all other convergent points in the GSA sample.
2. Convergent points were ordered in ascending order (i.e., from the closest to the farthest).
3. The 100 closest convergent points were used to train a response surface surrogate based on the Kriging Partial Least Squares method (KPLS) (Bouhleb et al., 2016), which outperforms traditional kriging on high-dimensional problems.
4. The trained KPLS surrogate was finally used to interpolate non-convergent runs in the original GSA sample.

The use of multiple localized surrogates allowed for better reconstruction of the topological features of the response surface in the vicinity of the non-convergent points.

In this study, the global sensitivity analysis was combined with the Monte Carlo filtering to identify reduced ranges of parameters with good solutions for subsequent parameter optimization. Potential solutions were filtered into good solutions with $KGE > 0.0$ and bad solutions with $KGE \leq 0.0$. Kernel density estimation (KDE) plots were then used to identify areas with high-density good solutions, while the correlation analysis was conducted to determine interactions between parameters and may help reduce the input factor space. More details can be found in Brunetti et al. (2016). This type of procedure shares multiple similarities with the Generalized Likelihood Uncertainty

Estimation (GLUE) proposed by Beven et al. (2001). The joint use of the GSA sample with the GLUE approach [i.e., GSA-GLUE (Ratto et al., 2001)] allows for obtaining a rough assessment of the parameters uncertainty and successful estimates of soil hydraulic parameters (e.g., Brunetti et al., 2018).

3.2.4 Parameter Optimization

The Particle Swarm Optimization (PSO) algorithm was used in this study for parameter optimization. In the PSO, a swarm of candidate solutions is moved around in the search space according to a few equations. The movement of the particles is guided by the optimal position of themselves and the whole swarm. Once improved positions are discovered, they are used to guide the swarm's movement. This process is repeated until the global optimal position that all particles tend to follow is found (Shi and Eberhart, 1998).

The PSO parameters (cognitive parameter $c_1 = -0.267$; social parameter $c_2 = 3.395$; inertia-weight $w = -0.444$) from Brunetti et al. (2016) were used in this study. The number of particle swarm and iterations are 40 and 200, respectively.

The PySwarm Library in Python was used for the PSO. The process was similar to the GSA, except that reduced ranges of parameters were used. In this way, the number of potential local minima is reduced, and the convergence improves. Only the set of parameters leading to the maximum KGE_avg (i.e., minimum 1-KGE_avg as the objective function) was retained as optimized parameters.

3.2.5 First Practical Application: Calculation of Drainage Travel Times and RWU

Temporal Origin

3.2.5.1 Peak Displacement (Isotope-Transport-Based) Method

The peak displacement method estimates travel times from the time lag between signals in the measured input (rainfall isotopic composition) and output (drainage isotopic composition) isotope time series. In the Stumpp et al. (2012) dataset, a pronounced correspondence was observed between the depleted precipitation peak in the winter (November 18, 2005, to April 14, 2006) and the lysimeter discharge. The mean drainage travel time t_o^* [T], accounting for dispersion effects, can be calculated by the mean peak isotopic composition lag time t_m^* [T] using Eq. 3.2:

$$t_o^* = \frac{t_m^*}{\sqrt{1 + (3\frac{\lambda}{L})^2 - 3\frac{\lambda}{L}}} \quad (3.2)$$

where L is the lysimeter length [L]. More details can be found in Stumpp et al. (2012). In this study, t_m^* from Stumpp et al. (2012) and dispersivities λ optimized using HYDRUS-1D assuming different fractionation scenarios were used.

3.2.5.2 Particle Tracking (Water-Flow-Based) Method

The particle tracking algorithm is based on the water mass balance calculation. The initial position of the particles is defined using the initial water content distribution. Depending on the precipitation/irrigation inputs, the particles may be released at the soil surface and leave at the soil profile bottom. In this study, the input parameters w_{Stand}

(the initial distribution) and w_{Prec} (the upper BC distribution) for the particle tracking algorithm were set to 10 cm and a negative number (which triggers the option of releasing particles with each rain event), respectively. More details about the particle tracking algorithm can be found in Šimůnek (1991) or Zhou et al. (2021).

When knowing the positions of the particles at different times, the residence time (RT) and locations of water from all precipitation/irrigation events can be obtained, i.e., the residence time distribution (RTD). Note that the particle travel time (TT) is the sum of the particle age (i.e., residence time) and life expectancy (i.e., time to reach the destination). The former is the time elapsed since the particle release, while the latter is the remaining time before the particle reaches the outlet (Benettin et al., 2015). Therefore, when the particles leave the lysimeter bottom or as root water uptake (RWU), their residence times can be called drainage or RWU travel times, respectively. The particle tracking module additionally assesses RWU between two neighboring particles as a function of time. When particles are released for each precipitation event, we can precisely evaluate the contribution of each precipitation event to RWU at different times. We can then infer the temporal origin of RWU by synthesizing this information. Different fractionation scenarios with the soil hydraulic parameters optimized using HYDRUS-1D were used to run the particle tracking module to calculate drainage and RWU travel times.

3.2.6 Second Practical Application: Calculation of Evaporation Flux

3.2.6.1 Water-Flow-Based Method

Braud et al. (2009a) calculated evaporation using three methods. The first method determines the evaporation rate by continuously measuring the vapor flux and humidity at the outlet of the soil column. The second method obtains the evaporation rate by repeatedly weighing the soil column. Finally, the third method determines the evaporation rate by weighting the mass of the frozen water trapped at the outlet of the soil column. These three methods are hereafter referred to as direct measurement, column weighting, and trapped volume, respectively. This study presents these results also as the reference for other methods. More details can be found in Braud et al. (2009a). Another water-flow-based method used in this study to calculate water flux components was to analyze the water mass balance simulated in HYDRUS-1D (e.g., Sutanto et al., 2012).

3.2.6.2 Isotope-Transport-Based Method

For an isolated water volume with an initial isotopic composition, δ_0 (‰) evaporating into the atmosphere, the isotopic composition of the residual liquid water δ_s (‰) can be calculated as (Benettin et al., 2018):

$$\delta_s = (\delta_0 - \delta^*)(1 - F_E)^{xm} + \delta^* \quad (3.3)$$

where δ^* (‰) is the limiting isotopic composition that would be approached when water is drying up, xm is the temporal enrichment slope (–), and F_E is described below.

Eq. (3.3) is based on the isotope mass balance equations of Gonfiantini (1986) and the isotopic composition of the evaporation flux estimated by the Craig–Gordon model (Craig and Gordon, 1965). More details about the derivations can be found in Gonfiantini (1986). This equation implies that the isotopic composition of soil water only changes due to evaporation fractionation. The ratio of the evaporation loss to the initial water storage (F_E) can be then estimated as (Sprenger et al., 2017):

$$F_E = 1 - \left[\frac{(\delta_s - \delta^*)}{(\delta_0 - \delta^*)} \right]^{\frac{1}{xm}} \quad (3.4)$$

The two variables δ^* and xm can be calculated as (Benettin et al., 2018):

$$\delta^* = \frac{(RH \cdot \delta_A + \varepsilon_k + \varepsilon^+ / \alpha^+)}{(RH - 10^{-3}(\varepsilon_k + \varepsilon^+ / \alpha^+))} \quad (3.5)$$

$$xm = \frac{(RH - 10^{-3}(\varepsilon_k + \varepsilon^+ / \alpha^+))}{(1 - RH + 10^{-3}\varepsilon_k)} \quad (3.6)$$

where δ_A (‰) is the isotopic composition of the atmospheric water vapor, RH is the air relative humidity, α^+ (–) is the dimensionless equilibrium fractionation factor, while ε^+ (‰) and ε_k (‰) are equilibrium and kinetic fractionation enrichments, respectively. Details about the calculation procedure for these parameters (α^+ , ε^+ , ε_k) can be found in Benettin et al. (2018) or Zhou et al. (2021). The equivalent kinetic fractionation factor within the soil (α_i^D) used to calculate ε_k was optimized manually to get the best match of F_E with those from water-flow-based methods in Section 3.2.6.1.

The fraction of water that evaporated before the end of the Braud et al. (2009a) experiment was calculated in this study. Average measured values of RH , T_{air} , T_s , and

δ_0 during the experiment, and the final isotope profile simulated using HYDRUS-1D were used in the above equations.

3.3 Results

3.3.1 Stumpp et al. (2012) Dataset Analysis

3.3.1.1 Parameter Optimization and Model Performance

The global sensitivity analysis and Monte-Carlo filtering results for the Stumpp et al. (2012) dataset are shown in the Results S3.1 section of the Supplementary material. Overall, soil hydraulic parameters of different layers had comparable impacts on the model outputs. The order of sensitive parameters is: shape parameters of the water retention function, namely n , and α , saturated water content θ_s , saturated hydraulic conductivity K_s , and dispersivity λ . The final optimized soil hydraulic and solute transport parameters and corresponding KGEs are shown in Table 3.1. Considering evaporation fractionation impacted parameter estimation significantly, especially in the optimization of the soil saturated hydraulic conductivity, K_s , and shape parameter, α . Overall, the water retention and soil hydraulic conductivity curves (Fig. S3.8) differed greatly between different fractionation scenarios in the third layer, but were relatively similar in the first and second layers. The water retention curve in the Gon_Frac scenario best matched the measured one, but did not outperform those from the CG_Frac and Non_Frac scenarios, as seen from the KGE_rc values in Table 3.1.

Compared with the CG_Frac and Gon_Frac scenarios, the water retention curve in the Non_Frac scenario had a steeper decline and a lower saturated water content in the third layer, while it became more gradual with higher saturated water contents in the first and second layers. However, the Non_Frac scenario always produced higher hydraulic conductivities than the CG_Frac and Gon_Frac scenarios (Note that the Non_Frac scenario also had higher hydraulic conductivities in the third layer because of relatively higher matric potentials).

The fits for different fractionation scenarios are shown in Fig. 3.6. The isotopic composition of the lysimeter discharge remained the same for different fractionation scenarios during about the first 150 days and started deviating after this time, but the trends were still similar except for some vertical shifts. Different fractionation scenarios resulted in a similar average fitting performance (KGE_avg) (within 0.03). The Non_Frac scenario had the highest KGE_wi (i.e., for water isotopic composition), followed by the CG_Frac scenario, while the Gon_Frac scenario performed the worst. The difference between KGE_wi indices for different fractionation scenarios was within 0.09.

Table 3.1. Optimized parameters and Kling-Gupta efficiency (KGE) indices (bf, wc, wi, and avg refer to the bottom flux, water content, water isotopic composition, and average, respectively) for different fractionation scenarios (Non_Frac, CG_Frac, and Gon_Frac) (for the Stumpp et al. (2012) dataset).

Fractionation scenario	z	θ_r	θ_s	α	n	K_s	λ	KGE_	KGE	KGE	KGE	KGE
	cm	cm ³ /cm ³	cm ³ /cm ³	cm ⁻¹	-	cm/d	cm	bf	_wc	_wi	_rc	_avg
Non_Frac	0–30	0	0.31	0.010	1.19	83.6						
	31–90	0	0.43	0.293	1.11	1131.71	5.00	0.99	0.47	0.59	0.87	0.73
	91–150	0	0.30	0.009	1.91	85.16						
CG_Frac	0–30	0	0.30	0.020	1.15	220.00						
	31–90	0	0.41	0.300	1.11	287.24	5.00	0.99	0.54	0.58	0.89	0.75
	91–150	0	0.30	0.082	1.10	220.00						
Gon_Frac	0–30	0	0.30	0.026	1.14	220.00						
	31–90	0	0.40	0.298	1.11	191.89	6.02	0.99	0.45	0.50	0.92	0.72
	91–150	0	0.35	0.300	1.12	220.00						

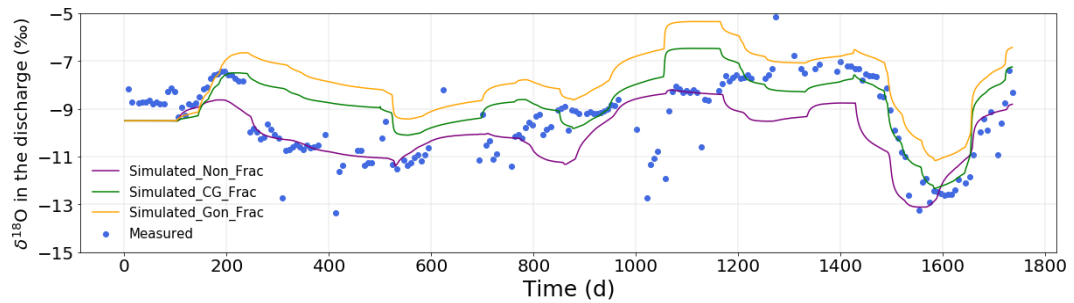


Figure 3.6. Measured (symbols) and simulated discharge ¹⁸O isotopic compositions for different fractionation scenarios (for the Stumpp et al. (2012) dataset).

3.3.1.2 First Practical Application: Drainage Travel Times and RWU Temporal

Origin

The mean travel times (*MTTs*) of drainage (i.e., from the surface to the bottom) estimated by the peak displacement method are shown in Table 3.2. The *MTTs* were 251.9, 251.9, and 257.1 days for the Non_Frac, CG_Frac, and Gon_Frac scenarios, respectively. The consideration of fractionation using the Gonfiantini model slightly

overestimated the travel times compared to the Non_Frac scenario. However, the difference was not very evident (within 6 days) for different fractionation scenarios.

Table 3.2. Estimated mean travel times of drainage (t_0^*) and mean water fluxes (v_0^*) for different fractionation scenarios (Non_Frac, CG_Frac, and Gon_Frac) using different methods (peak displacement and particle tracking).

Method	Fractionation scenario	t_0^* (d)	v_0^* (mm/d)	Ratio of t_0^* compared to t_0^* for Non_Frac
Peak displacement	Non_Frac	251.9	5.95	
	CG_Frac	251.9	5.95	0%
	Gon_Frac	257.1	5.83	2.06%
Particle tracking	Non_Frac	297.5	5.04	
	CG_Frac	356.8	4.20	19.93%
	Gon_Frac	369.9	4.05	24.33%

Fig. S3.9 shows the spatial-temporal distribution of particles simulated using the soil hydraulic parameters estimated considering different fractionation scenarios. The residence time distribution (*RTD*) of soil water is displayed in Fig. 3.7. The mean residence time (*MRT* – the mean of *RTs* averaged over the entire simulation duration) increased with soil depth in all scenarios due to a time lag involved in water transfer. The *MRTs* for the Non_Frac scenario for depths of 30, 70, and 110 cm were 82.1, 138.2, and 203.6 days, respectively. The *MRTs* for the CG_Frac scenario for 30, 70, and 110 cm depths were 69.9, 170.0, and 258.5 days, respectively. Finally, the *MRTs* for the Gon_Frac scenario for 30, 70, and 110 cm depths were 80.6, 174.3, and 270.6 days, respectively. In terms of temporal distribution, *RTs* showed five distinct seasonal cycles. Specifically, they had a trough after every rainy season and a peak after every

dry season, showing a pronounced lag effect. In other words, *RTs* were determined by the trade-off between precipitation input and evapotranspiration removal.

Corresponding travel times of drainage are shown as probability density distribution histograms in Fig. S3.10 and summarized in Table 3.2. The means (and standard deviations) of travel times were 297.5 (79.96), 356.8 (104.29), and 369.9 (101.24) days for the Non_Frac, CG_Frac, and Gon_Frac scenarios, respectively. The particle tracking method produced significantly higher travel times (by about 89 days) than the peak displacement method. Similarly, considering fractionation using the CG_Frac and Gon_Frac scenarios led to longer travel times (*TTs*) than the Non_Frac scenario. In addition, the difference was very evident (reached 78 days) for different scenarios.

To further explore and quantify the *RTD* differences when considering different fractionation models, the temporal origin of RWU is plotted in Fig. 3.8. Fig. 3.8 shows the monthly transpiration sums in the upper panels and fractional contributions of water of a certain age/origin to these monthly transpiration sums in the lower panels. Note that the amount and temporal distribution of transpiration were similar under different fractionation scenarios (54.95, 53.91, and 54.03 cm for Non_Frac, CG_Frac, and Gon_Frac, respectively). Therefore, only the temporal distribution of transpiration in the Non_Frac scenario is displayed. As for the age distribution of RWU, for example, in the Non_Frac scenario, the yellow line in 2002 indicates that about 29% of the water

taken up by roots in August was older than May, while the remaining 71% was from May~August of 2002 (5% from June, 16% from July, and 50% from August). More details about how to read the age distribution of RWU can be found in Fig. 5 of Brinkmann et al. (2018).

The maximum water age for RWU for different fractionation scenarios was almost the same, about 300 d in October 2003, 330 d in September 2004, 270 d in November 2005, and 180 d in February 2006, except for 240 d in December 2004 and 180 d in February of 2005 for the Non_Frac scenario. These results were consistent with water residence times at the maximum rooting depths in Fig. 3.7. However, different fractionation scenarios had relatively large impacts (up to three months) on the minimum water age for RWU. The most obvious example was the 2003 growing season (a relatively dry year with less precipitation, as shown in Fig. 3.2). The minimum water age for RWU in 2003 was within about a month for the Gon_Frac scenario and 120 d (February) for the Non_Frac and CG_Frac scenarios. In addition, the dynamics of fractional monthly contributions to RWU also varied between different scenarios. In general, the water age for RWU was far longer in dry years (2003~2004) than in wet years (2005~2006), suggesting that drought can promote crop uptake of old water. In the same growing season, the water age for RWU was consistently lower in May and June than in July and August, which reflected an increase in the rooting depth.

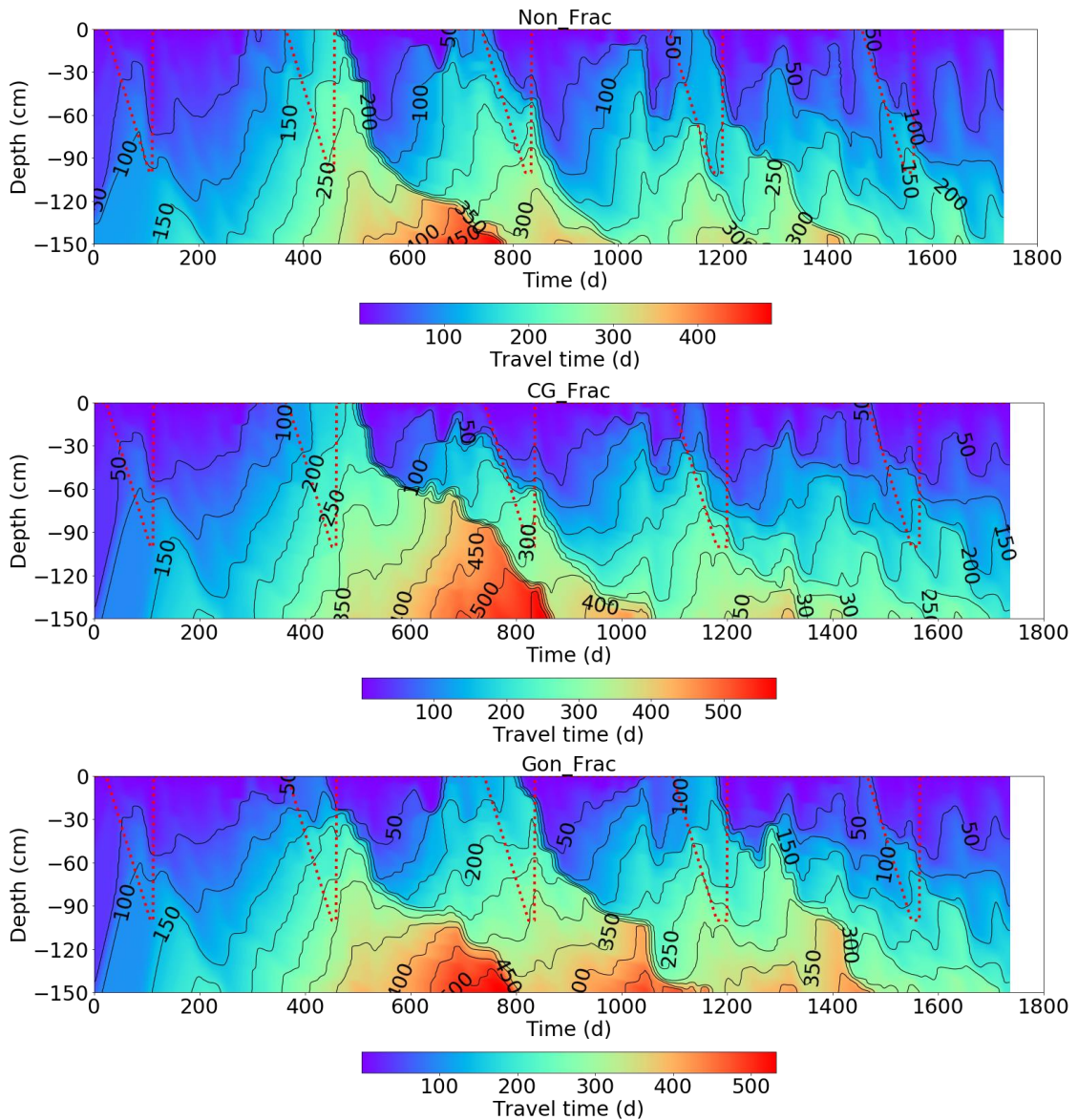


Figure 3.7. The residence time distributions (*RTDs*) for different fractionation scenarios (Non_Frac – top, CG_Frac – middle, and Gon_Frac – bottom). Note that the dashed red line represents the rooting depth.

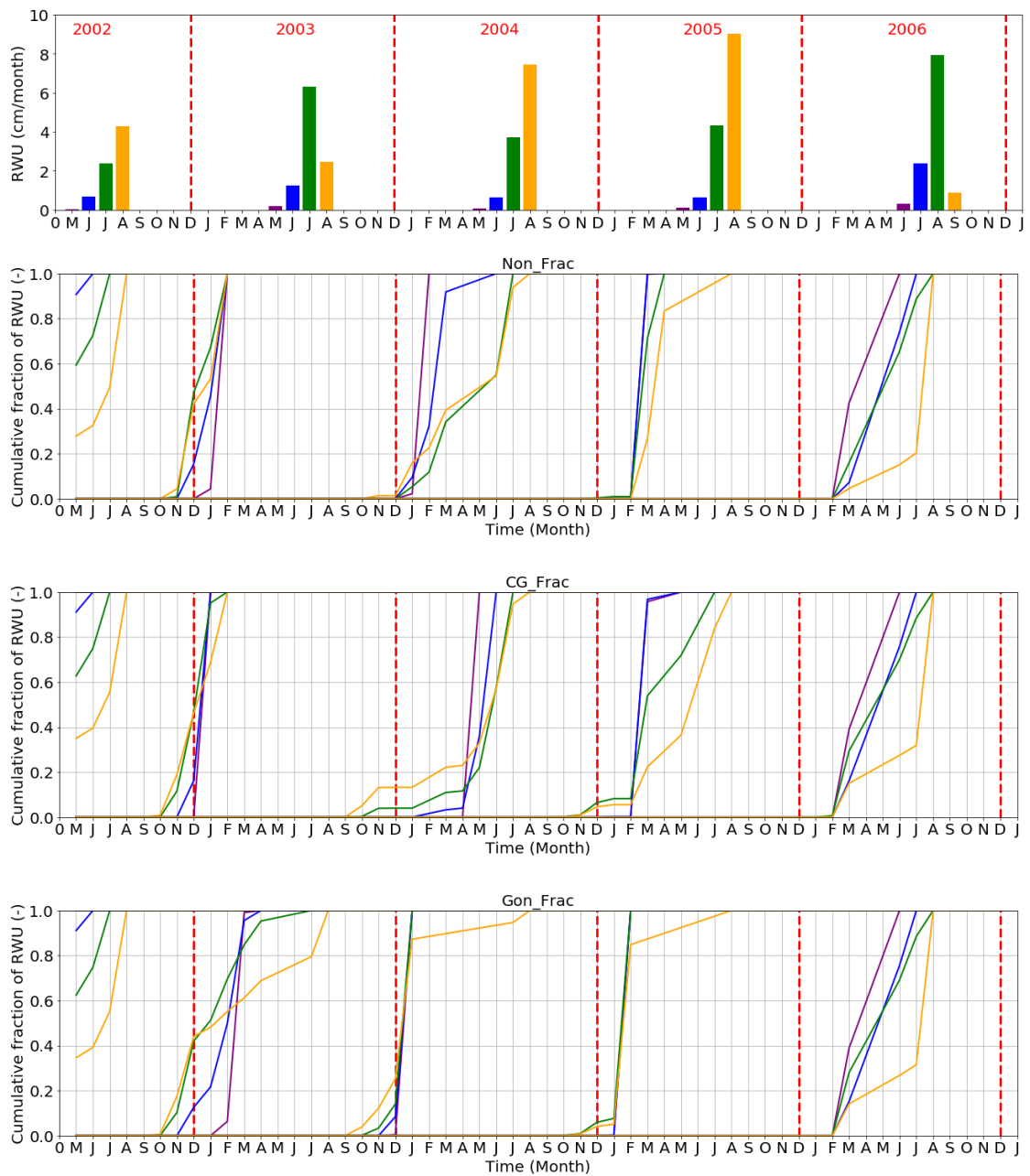


Figure 3.8. The temporal origin of root water uptake (RWU) for different fractionation scenarios (Non_Frac – top, CG_Frac – middle, and Gon_Frac – bottom). The upper panels show the monthly transpiration sums (in different colors); the lower panels show fractional contributions of water of a certain age/origin (by month) to the monthly transpiration sums.

3.3.2 Braud et al. (2009a) Dataset Analysis

3.3.2.1 Parameter Optimization and Model Performance

The global sensitivity analysis and Monte-Carlo filtering results for the Braud et al. (2009a) dataset are shown in the Results S3.2 section of the Supplementary material. The most sensitive parameters were shape parameters n and saturated water contents θ_s . The final optimized soil hydraulic and solute transport parameters and corresponding KGEs are shown in Table 3.3. Considering (or not) evaporation fractionation also impacted parameter estimation significantly. The most significant impacts were on dispersivity, λ , and the shape parameter, α (Table 3.3). The soil water retention curves (Fig. S3.12) showed that the wilting points were almost identical for the Non_Frac and fractionation (CG_Frac, Gon_Frac, Meas_Frac) scenarios. However, the saturated water contents were higher, and water contents started to drop later in the fractionation scenarios than those in the Non_Frac scenario. The soil hydraulic conductivity curves (Fig. S3.12) showed that the saturated hydraulic conductivities were very similar, but the hydraulic conductivities in the fractionation scenarios were a little higher than those in the Non_Frac scenario.

The fits of soil profile isotopic compositions for different fractionation scenarios are shown in Fig. 3.9. The Non_Frac scenario had an almost uniform isotopic composition profile. In this case, the parameter optimization depended mainly on the measured soil water content profile. In fractionation scenarios, the peak value of the

isotopic composition profile in the Meas_Frac scenario was smaller than those in the Gon_Frac and CG_Frac scenarios, while the value of dispersivities was the opposite. Different fractionation scenarios resulted in significantly different average fitting performances (KGE_avg) (reached 0.72). The Meas_Frac scenario had the highest KGE_wi (i.e., for soil water isotopic composition), followed by Gon_Frac and CG_Frac scenarios, while the Non_Frac scenario performed the worst. The difference between KGE_wi indices for different fractionation scenarios reached 1.49.

Table 3.3. Optimized parameters and Kling-Gupta efficiency (KGE) indices (wc, wi, and avg refer to the water content, water isotopic composition, and average, respectively) for different fractionation scenarios (Non_Frac, CG_Frac, Gon_Frac, and Meas_Frac) (for the Braud et al. (2009a) dataset).

Fractionation scenario	θ_r cm ³ / cm ³	θ_s cm ³ / cm ³	α (cm ⁻¹)	n (-)	K_s (cm/d)	λ (cm)	KGE_ wc	KGE _wi	KGE _avg
Non_Frac	0	0.435	0.0103	2.352	0.158	0.166	0.96	-0.55	0.20
CG_Frac	0	0.458	0.0106	2.367	0.139	0.126	0.85	0.37	0.61
Gon_Frac	0	0.441	0.0101	2.352	0.142	0.114	0.96	0.47	0.71
Meas_Frac	0	0.452	0.0082	2.392	0.156	0.932	0.90	0.94	0.92

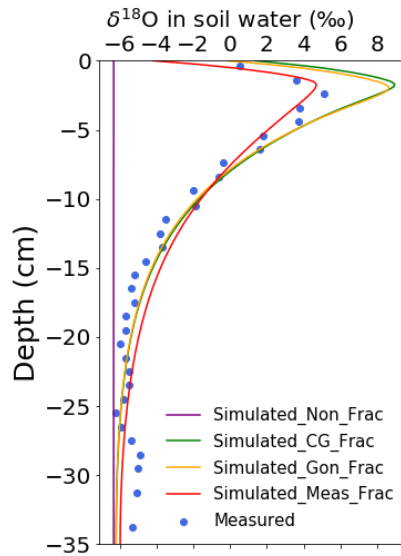


Figure 3.9. Measured (symbols) and simulated (lines) $\delta^{18}\text{O}$ isotopic compositions across the soil profile for different fractionation (Non_Frac, CG_Frac, Gon_Frac, and Meas_Frac) scenarios (for the Braud et al. (2009a) dataset).

3.3.2.2 Second Practical Application: Estimation of Evaporation Flux

Table 3.4 shows cumulative evaporation obtained using different measurements and simulated considering different fractionation scenarios. The average isotopic composition of the whole profile was calculated using soil water contents and the column depth as weights. Cumulative evaporation was estimated to account for about 64.4%, 63.1%, and 65.6% of the initial soil water storage in the CG_Frac, Gon_Frac, and Meas_Frac scenarios, respectively. These values for the CG_Frac, Gon_Frac, and Meas_Frac scenarios were (slightly) lower than but comparable to laboratory measurements and the HYDRUS-1D water balance. Slight differences may have been caused by uncontrollable measurement errors in the isotopic composition of the atmospheric water vapor (δ_a in Eq. 3.5), which is the most sensitive parameter in the isotope mass balance method (Skrzypek et al., 2015). Cumulative evaporation cannot

be estimated using this method in the Non_Frac scenario since no isotopic enrichment occurred (i.e., $\delta_s = \delta_0$ in Eq. 3.4).

Table 3.4. Cumulative evaporation measured using different experimental methods and calculated considering different fractionation scenarios.

Method	Fractionation scenario	Cumulative evaporation (mm)	Initial soil water storage (mm)	F_E (-)
Direct measurement (of airflow and humidity)		105	153	68.7%
Column weighting		103	153	67.1%
Trapped volume		103	153	67.3%
HYDRUS-1D water mass balance	Non_Frac	105	151	69.5%
	CG_Frac	105	159	66.0%
	Gon_Frac	105	153	68.6%
	Meas_Frac	105	157	66.9%
Isotope mass balance	Non_Frac	-	151	-
	CG_Frac	102	159	64.4%
	Gon_Frac	97	153	63.1%
	Meas_Frac	103	157	65.6%

Note that values of cumulative evaporation for the first three laboratory measurement methods are from Braud et al. (2009a).

3.4 Discussion

3.4.1 Impacts of Evaporation Fractionation on Parameter Estimation and Model

Performance

For the Stumpp et al. (2012) dataset, as indicated in Section 3.3.1.1, the fractionation scenarios (CG_Frac and Gon_Frac) had lower hydraulic conductivities than the Non_Frac scenario. This is because fractionation decreases the isotope flux by evaporation compared with a no fractionation scenario (the isotopic composition of the

evaporation flux cannot be greater than that of surface soil water) and thus increases the isotope flux by net infiltration. To get a good fit between simulated and observed isotopic compositions of discharge water, the inverse modeling yields a larger longitudinal dispersivity (to increase the dispersion of isotopes) (Table 3.1) or lower hydraulic conductivities (to decrease downward convection of isotopes) (Fig. S3.8).

The simulated isotopic composition of the lysimeter discharge remained the same for different fractionation scenarios during about the first 150 d and started deviating after this time (Fig. 3.6). This suggests that it takes about 150 d before the impact of different treatments of the upper BC for isotope transport propagates to the soil profile bottom and affects the isotopic composition in drainage water (Zhou et al., 2021). This time interval (i.e., about 150 d) is much smaller than the travel time of the first particle (released at the soil surface) as calculated by the particle tracking method (Fig. S3.9). This is because the particle tracking algorithm considers only piston flow, while dispersion accelerates the arrival of isotopes to the soil profile bottom. However, the trends are still similar, except for some vertical shifts.

Since KGE_{wi} values did not differ much for different fractionation scenarios (within 0.09) (Fig. 3.6 and Table 3.1), considering (or not) evaporation fractionation does not significantly impact the isotopic composition in discharge water in this example (humid conditions). The Non_Frac scenario had a slightly higher KGE_{wi}, indicating that it can fit isotopic data better, followed by CG_Frac, while Gon_Frac

performed the worst. This is understandable since evaporation fractionation could be neglected in this example, as seen from the dual-isotope plots (Fig. 5 of Stumpp et al., 2012).

For the Braud et al. (2009a) dataset, as indicated in Section 3.3.2.1, the hydraulic conductivities in the fractionation (CG_Frac, Gon_Frac, Meas_Frac) scenarios were a little higher than those in the Non_Frac scenario. This is because fractionation decreases the isotope flux by evaporation compared with a no fractionation scenario. A higher hydraulic conductivity in the fractionation scenarios promotes upward evaporation and fractionation. This increases the isotopic composition of remaining soil water and thus produces a better fit between simulated and observed isotope profiles.

When evaporation fractionation was not considered, the isotopic composition of evaporation remained the same as the initial isotopic composition. This resulted in a uniform isotopic composition (equal to the initial value) distribution of soil water throughout the profile in the Non_Frac scenario (Fig. 3.9). In fractionation scenarios, the peak value of the isotopic composition profile was inversely proportional to the dispersivity value (Fig. 3.9 and Table 3.3), which is consistent with the conclusions from Braud et al. (2009b).

The isotopic composition profiles and the KGE_wi values differed dramatically (reached 1.48) between different fractionation scenarios (Fig. 3.9 and Table 3.3). This implies that considering evaporation fractionation significantly impacts the isotopic

composition profile in this example (arid conditions). The Meas_Frac scenario had the highest KGE_wi (i.e., for the water isotopic composition), followed by the Gon_Frac, and then CG_Frac, while the Non_Frac scenario performed the worst. This is understandable since evaporation fractionation could not be neglected, and the measured evaporation isotope flux is the most accurate for this example (Braud et al. 2009b).

3.4.2 Impacts of Evaporation Fractionation on Practical Applications

3.4.2.1 Estimation of Drainage Travel Times and RWU Temporal Origin

Differences in water travel times were not evident among different fractionation scenarios (Table 3.4), since the numerator in Eq. 3.2 is much larger than the denominator in the peak displacement method. As a result, water travel times were similar for different fractionation scenarios despite a very different dispersivity. However, for the particle tracking method based on water flow calculations, differences in water travel times were evident among different fractionation scenarios (Table 3.2), despite their similar KGE values (Table 3.1). In addition, differences in estimated soil hydraulic parameters may also cause discrepancies in *TTs* of individual precipitation events and the temporal origin of water for RWU (Figs. S3.8 and 3.7~3.8).

Overall, the particle tracking method gave much higher travel times than the peak displacement method (Table 3.2). Different results by these two methods may be associated with different rainfall events selected for these calculations. The peak-

displacement method calculates the travel times during frequent and heavy precipitation events (precipitation events from 2005~2006), while particle tracking assesses the travel times over longer periods (Zhou et al., 2021).

Notably, water travel times in the Non_Frac scenario obtained by the particle tracking method are most consistent with the approximate estimate of 41 weeks provided by previous studies with similar crops and areas (Stumpp et al., 2009). It is worth mentioning that Asadollahi et al. (2020) pointed out that the SAS approach was a good alternative for estimating water travel times when the system was too complicated to be fully described by the HYDRUS-1D model. Our study demonstrates that the water-flow-based particle tracking module in HYDRUS-1D is another promising way of constraining estimation errors in water travel times, especially when there is not enough isotope data to calibrate the lumped or physically based isotope transport models.

In contrast, considering fractionation using either the CG or Gonfiantini models will likely lead to larger water travel time estimates than in the Non_Frac scenario (Table 3.2). This is because fractionation scenarios result in a larger dispersivity (to increase the dispersion of isotopes) or lower hydraulic conductivities (to decrease convection of isotopes), as discussed in Section 3.4.1.

3.4.2.2 Estimation of the Evaporation Flux

For evaporation estimation, the isotope-transport-based methods for different fractionation (CG_Frac, Gon_Frac, and Meas_Frac) scenarios can give comparable results to the water-flow-based methods, including laboratory measurements and the HYDRUS-1D water balance. In contrast, the Non_Frac scenario can produce similar results only when using the water-flow-based method (HYDRUS-1D water balance). However, since the measured evaporation flux was used as the upper boundary condition in this (arid conditions) example, it is not clear whether the similarity between estimated evaporation amounts using the HYDRUS-1D water balance method in the Non_Frac and fractionation (CG_Frac, Gon_Frac, Meas_Frac) scenarios was due to this boundary condition, or because actual soil hydraulic conductivities and water contents were continuously adjusted to actual soil fluxes without ever reaching full saturation. However, it is clear that evaporation fractionation has a significant impact on the isotope transport and isotopic compositions in arid conditions, as shown in Fig. 3.9. Therefore, the direct use of simulated isotopic compositions in the Non_Frac scenario may result in large biases in practical applications in arid conditions, as seen from the evaporation estimation results in Table 3.4.

3.4.3 Comparison of Different Climate Conditions and Implications for Future Studies

The soil saturated hydraulic conductivities (K_s), and the retention curve shape parameter (α) were the parameters most affected by the consideration of evaporation fractionation for the humid condition dataset (Table 3.1). For the arid condition dataset, these were the dispersivity (λ) and the retention curve shape parameter (α) (Table 3.3). This is likely associated with the effects of soil texture on retention curves and soil moisture conditions in different climate zones (Radcliffe and Šimůnek, 2018). Overall, soil water retention and hydraulic conductivity curves (Fig. S3.12) in different fractionation scenarios were more similar for the Braud et al. (2009a) dataset than the Stumpp et al. (2012) dataset (Fig. S3.8). One reason is that the measured evaporation flux was used as the upper BC in the former, which constrains the model flexibility. Another reason is that there was only one soil layer in the Braud et al. (2009a) dataset, while there were three soil layers in the Stumpp et al. (2012) dataset. There is likely a compensation effect between the parameters of different layers, and thus the parameter values can vary more in the Stumpp et al. (2012) dataset.

While evaporation fractionation plays an essential role in parameter estimation in both cases, its impact on model performance is relatively small in the example for humid conditions but more significant in the example for arid conditions, as discussed in Sections 3.4.1 and 3.4.2. This is expected since evaporation plays a more important

role in the water balance of the arid dataset (Table 3.4) than in the humid dataset (Fig. S3.13). These conclusions also indirectly validate the common assumption that evaporation fractionation may be neglected in some humid regions but not in arid areas (Sprenger et al., 2016a).

However, parameter sensitivities and optimization results reflect complex combined effects of climate, soil, and vegetation characteristics. The isotopic composition of soil water is not only affected by evaporation fractionation, but also by the mixing of rainfall with soil water and different flow paths in the soil, leading to its variations with depths and time. The insufficient knowledge of the spatial-temporal isotope distribution (e.g., in shallow and deep depths or during different stages of evaporation) and the lack of such information in the objective function may bias the parameter estimation results. For example, not including isotopes from different soil depths within the soil profile might lead to an underestimation of evaporation fractionation in general, biased estimation of water mixing within the profile, and a similar isotopic signal in the discharge. In this study, we considered either the time series of the isotopic composition of the bottom flux in the Stumpp et al. (2012) dataset or the final isotopic composition profile in the Braud et al. (2009a) dataset. In addition, observation data types and spatial-temporal distributions are different for these two datasets, and this difference may affect the comparison of parameter estimation results between different climate conditions.

The GSA was carried out for the Non_Frac scenario for the Stumpp et al. (2012) dataset and the Meas_Frac scenario for the Braud et al. (2009a) dataset because they were closest to the experimental conditions. This implicitly assumes that sensitivity remains the same for different model structures. However, different model structures may affect GSA and PSO results, which should be further explored. Last but not least, the impacts of possible transpiration fractionation, as observed in multiple studies, should also be included in future analyses (e.g., Barbeta et al., 2019). Therefore, it is difficult to generalize the results of this study or apply them to other specific conditions.

3.5 Summary and Conclusions

In this study, we analyzed parameter estimation results for two datasets collected under humid and arid climate conditions using the isotope transport model, in which we either did or did not consider evaporation fractionation. The global sensitivity analysis using the Morris and Sobol' methods and the parameter estimation using the Particle Swarm Optimization algorithm highlight the significant impacts of considering evaporation fractionation on parameter estimation and model performance. The KGE index for isotope data can increase by 0.09 and 1.49 for the humid and arid datasets, respectively, when selecting suitable fractionation scenarios.

The impact of different parameter values estimated when considering (or not) evaporation fractionation propagates into practical applications of isotope transport modeling. The isotope-transport-based method (peak displacement) gave much lower

water travel times than the water-flow-based method (particle tracking) for humid conditions. Considering fractionation using the CG and Gonfiantini models will likely lead to larger water travel time estimates and ages for RWU. For arid conditions example, the isotope-transport-based method (isotope mass balance) can provide comparable evaporation estimates for different fractionation (CG_Frac, Gon_Frac, Meas_Frac) scenarios as the water-flow-based methods (HYDRUS-1D water balance and laboratory measurements). In contrast, the Non_Frac scenario can produce reasonable evaporation estimation only when using the water-flow-based method.

The direct use of simulated isotopic compositions in the no fractionation scenario may result in large biases in practical applications in arid regions where evaporation fractionation is more extensive than in humid areas. Integrated use of water-flow and isotope-transport-based methods may provide mutual validation and be an important way to avoid this problem. This research may shed some light on future laboratory and field experimental designs regarding the practical applications of the isotope-transport modeling in different climate zones.

References

- Allen, S.T., Kirchner, J.W., Braun, S., Siegwolf, R.T.W., Goldsmith, G.R., 2019. Seasonal origins of soil water used by trees. *Hydrology and Earth System Sciences*, 23(2): 1199-1210. DOI:10.5194/hess-23-1199-2019.
- Asadollahi, M., Stumpp, C., Rinaldo, A., Benettin, P., 2020. Transport and Water Age Dynamics in Soils: A Comparative Study of Spatially Integrated and Spatially Explicit Models. *Water Resources Research*, 56(3): 17. DOI:10.1029/2019wr025539.
- Barbeta, A., Jones, S. P., Clavé, L., Wingate, L., Gimeno, T. E., Fréjaville, B., Wohl, S., and Ogée, J., 2019. Unexplained hydrogen isotope offsets complicate the identification and quantification of tree water sources in a riparian forest. *Hydrology and Earth System Sciences*, 23(4): 2129-2146. DOI:10.5194/hess-23-2129-2019.
- Benettin, P., Bertuzzo, E., 2018. tran-SAS v1.0: a numerical model to compute catchment-scale hydrologic transport using StorAge Selection functions. *Geosci. Model Dev.*, 11(4): 1627-1639. DOI:10.5194/gmd-11-1627-2018.
- Benettin, P., Rinaldo, A., Botter, G., 2015. Tracking residence times in hydrological systems: forward and backward formulations. *Hydrological Processes*, 29(25): 5203-5213. DOI:10.1002/hyp.10513.
- Benettin, P., Volkmann, T. H. M., von Freyberg, J., Frentress, J., Penna, D., Dawson, T. E., and Kirchner, J. W., 2018. Effects of climatic seasonality on the isotopic composition of evaporating soil waters. *Hydrology and Earth System Sciences*, 22(5): 2881-2890. DOI:10.5194/hess-22-2881-2018.
- Beven, K., Freer, J., 2001. Equifinality, data assimilation, and uncertainty estimation in mechanistic modelling of complex environmental systems using the GLUE methodology. *Journal of Hydrology*, 249(1-4): 11-29. DOI:10.1016/S0022-1694(01)00421-8.
- Bouhleb, M.A., Bartoli, N., Otsmane, A. and Morlier, J., 2016. Improving kriging surrogates of high-dimensional design models by Partial Least Squares dimension reduction, *Struct. Multidiscip. Optim.*, 53(5), pp. 935-952, doi:10.1007/s00158-015-1395-9.

- Braud, I., Bariac, T., Biron, P., Vauclin, M., 2009a. Isotopic composition of bare soil evaporated water vapor. Part II: Modeling of RUBIC IV experimental results. *Journal of Hydrology*, 369(1-2): 17-29. DOI:10.1016/j.jhydrol.2009.01.038.
- Braud, I., Biron, P., Bariac, T., Richard, P., Canale, L., Gaudet, J. P., and Vauclin, M., 2009b. Isotopic composition of bare soil evaporated water vapor. Part I: RUBIC IV experimental setup and results. *Journal of Hydrology*, 369(1-2): 1-16. DOI:10.1016/j.jhydrol.2009.01.034.
- Brinkmann, N., Seeger, S., Weiler, M., Buchmann, N., Eugster, W., and Kahmen, A., 2018. Employing stable isotopes to determine the residence times of soil water and the temporal origin of water taken up by *Fagus sylvatica* and *Picea abies* in a temperate forest. *New Phytologist*, 219(4): 1300-1313. DOI:10.1111/nph.15255.
- Brunetti, G., Šimůnek, J., Piro, P., 2016. A comprehensive numerical analysis of the hydraulic behavior of a permeable pavement. *Journal of Hydrology*, 540: 1146-1161. DOI:10.1016/j.jhydrol.2016.07.030.
- Brunetti, G., Šimůnek, J., Turco, M., Piro, P., 2018. On the use of global sensitivity analysis for the numerical analysis of permeable pavements. *Urban Water J.*, 15(3): 269-275. DOI:10.1080/1573062x.2018.1439975.
- Brunetti, G., Šimůnek, J., Turco, M., Piro, P., 2017. On the use of surrogate-based modeling for the numerical analysis of Low Impact Development techniques, *Journal of Hydrology*, 548, pp. 263-277, doi:10.1016/j.jhydrol.2017.03.013.
- Campolongo, F., Cariboni, J., Saltelli, A., 2007. An effective screening design for sensitivity analysis of large models. *Environ. Modell. Softw.*, 22(10): 1509-1518. DOI:10.1016/j.envsoft.2006.10.004.
- Chesnaux, R., Stumpp, C., 2018. Advantages and challenges of using soil water isotopes to assess groundwater recharge dominated by snowmelt at a field study located in Canada. *Hydrological Sciences Journal*, 63(5): 679-695. DOI:10.1080/02626667.2018.1442577.
- Condon, L.E., Atchley, A.L., Maxwell, R.M., 2020. Evapotranspiration depletes groundwater under warming over the contiguous United States. *Nature Communications*, 11(1): 8. DOI:10.1038/s41467-020-14688-0.

- Craig, H., Gordon, L., 1965. Deuterium and oxygen 18 variations in the ocean and the marine atmosphere, *Stable Isotopes in Oceanographic Studies and Paleotemperatures E*, Proceedings of the Third Spoleto Conference, Spoleto, Italy, pp. 9-130.
- Gatel, L., Lauvernet, C., Carluer, N., Weill, S., Tournebize, J., and Paniconi, C., 2019. Global evaluation and sensitivity analysis of a physically based flow and reactive transport model on a laboratory experiment. *Environ. Modell. Softw.*, 113: 73-83. DOI:10.1016/j.envsoft.2018.12.006.
- Gonfiantini, R., 1986. Environmental isotopes in lake studies. *Handbook of Environmental Isotope Geochemistry*, 2: 113-168.
- Groh, J., Stumpp, C., Lücke, A., Pütz, T., Vanderborght, J., and Vereecken, H., 2018. Inverse Estimation of soil hydraulic and transport parameters of layered soils from water stable isotope and lysimeter data. *Vadose Zone Journal*, 17(1): 19. DOI:10.2136/vzj2017.09.0168.
- Harman, C.J., 2015. Time-variable transit time distributions and transport: Theory and application to storage-dependent transport of chloride in a watershed. *Water Resources Research*, 51(1): 1-30. DOI:10.1002/2014wr015707.
- Herman, J., Usher, W., 2017. SALib: an open-source Python library for sensitivity analysis. *Journal of Open Source Software*, 2(9): 97. DOI:10.21105/joss.00097.
- Herman, J.D., Kollat, J.B., Reed, P.M., Wagener, T., 2013. Technical Note: Method of Morris effectively reduces the computational demands of global sensitivity analysis for distributed watershed models. *Hydrology and Earth System Sciences*, 17(7): 2893-2903. DOI:10.5194/hess-17-2893-2013.
- Hopmans, J.W., Šimůnek, J., Romano, N., Durner, W., 2002. 3.6. 2. Inverse Methods. *Methods of Soil Analysis: Part 4 Physical Methods*, 5: 963-1008.
- Knoben, W.J.M., Freer, J.E., Woods, R.A., 2019. Technical note: Inherent benchmark or not? Comparing Nash-Sutcliffe and Kling-Gupta efficiency scores. *Hydrology and Earth System Sciences*, 23(10): 4323-4331. DOI:10.5194/hess-23-4323-2019.

- Koeniger, P., Gaj, M., Beyer, M., Himmelsbach, T., 2016. Review on soil water isotope-based groundwater recharge estimations. *Hydrological Processes*, 30(16): 2817-2834. DOI:10.1002/hyp.10775.
- Liang, G., 1982. Net radiation, potential and actual evapotranspiration in Austria. *Archives for Meteorology, Geophysics, and Bioclimatology, Series B*, 31(4): 379-390.
- Liu, D., Li, L.Z., Rostami-Hodjegan, A., Bois, F.Y., Jamei, M., 2020. Considerations and caveats when applying global sensitivity analysis methods to physiologically based pharmacokinetic models. *AAPS J.*, 22(5): 13. DOI:10.1208/s12248-020-00480-x.
- Mattei, A., Goblet, P., Barbecot, F., Guillon, S., Coquet, Y., and Wang, S., 2020. Can soil hydraulic parameters be estimated from the stable isotope composition of pore water from a single soil profile? *Water*, 12(2): 19. DOI:10.3390/w12020393.
- Mertens, J., Stenger, R., Barkle, G.F., 2006. Multiobjective inverse modeling for soil parameter estimation and model verification. *Vadose Zone Journal*, 5(3): 917-933. DOI:10.2136/vzj2005.0117.
- Miguez-Macho, G., Fan, Y., 2021. Spatiotemporal origin of soil water taken up by vegetation. *Nature*: 17. DOI:10.1038/s41586-021-03958-6.
- Nelson, J.A., Pérez-Priego, O., Zhou, S., Poyatos, R., Zhang, Y., Blanken, P.D., Gimeno, T.E., Wohlfahrt, G., Desai, A.R., Gioli, B. and Limousin, J.M., 2020. Ecosystem transpiration and evaporation: Insights from three water flux partitioning methods across FLUXNET sites. *Glob. Change Biol.*, 26(12): 6916-6930. DOI:10.1111/gcb.15314.
- Nossent, J., Elsen, P., Bauwens, W., 2011. Sobol' sensitivity analysis of a complex environmental model. *Environ. Modell. Softw.*, 26(12): 1515-1525. DOI:10.1016/j.envsoft.2011.08.010.

- Penna, D., Hopp, L., Scandellari, F., Allen, S.T., Benettin, P., Beyer, M., Geris, J., Klaus, J., Marshall, J.D., Schwendenmann, L. and Volkmann, T.H., 2018. Ideas and perspectives: Tracing terrestrial ecosystem water fluxes using hydrogen and oxygen stable isotopes - challenges and opportunities from an interdisciplinary perspective. *Biogeosciences*, 15(21): 6399-6415. DOI:10.5194/bg-15-6399-2018.
- Radcliffe, D.E., Šimůnek, J., 2018. Soil physics with HYDRUS: Modeling and applications. CRC Press.
- Ratto, M., Tarantola, S., Saltelli, A., 2001. Sensitivity analysis in model calibration: GSA-GLUE approach. *Comput. Phys. Commun.*, 136(3): 212-224. DOI:10.1016/s0010-4655(01)00159-x.
- Razavi, S., A. Jakeman, A. Saltelli, C. Prieur, B. Iooss, E. Borgonovo, E. Plischke, S. Lo Piano, T. Iwanaga, W. Becker, S. Tarantola, J.H.A. Guillaume, J. Jakeman, H. Gupta, N. Melillo, G. Rabitti, V. Chabridon, Q.Y. Duan, X.F. Sun, S. Smith, R. Sheikholeslami, N. Hosseini, M. Asadzadeh, A. Puy, S. Kucherenko, and H.R. Maier, 2021. The future of sensitivity analysis: An essential discipline for systems modeling and policy support, *Environ. Modell. Softw.*, 137, pp. 22, doi:10.1016/j.envsoft.2020.104954.
- Rinaldo, A., Benettin, P., Harman, C.J., Hrachowitz, M., McGuire, K.J., Van Der Velde, Y., Bertuzzo, E. and Botter, G., 2015. Storage selection functions: A coherent framework for quantifying how catchments store and release water and solutes. *Water Resources Research*, 51(6): 4840-4847. DOI:10.1002/2015wr017273.
- Sheikholeslami, R., Razavi, S. and Haghnegahdar, A., 2019. What should we do when a model crashes? Recommendations for global sensitivity analysis of Earth and environmental systems models, *Geosci. Model Dev.*, 12(10), pp. 4275-4296, DOI:10.5194/gmd-12-4275-2019.
- Shi, Y.H., Eberhart, R., 1998. A modified particle swarm optimizer, *IEEE International Conference on Evolutionary Computation*. Ieee, Anchorage, Ak, pp. 69-73. DOI:10.1109/icec.1998.699146.
- Šimůnek, J., 1991. Numerical simulation of the transport processes in soil. *Vodohospodarsky Casopis (CSFR)*.

- Šimůnek, J., Šejna, M., Saito, H., Sakai, M., van Genuchten, M.T., 2008. The HYDRUS-1D Software Package for Simulating the One-Dimensional Movement of Water, Heat, and Multiple Solutes in Variably Saturated Media, Version 4.0. HYDRUS Software Series 3. Department of Environmental Sciences, University of California Riverside, Riverside, California, USA, 315 pp.
- Skrzypek, G., Mydłowski, A., Dogramaci, S., Hedley, P., Gibson, J. J., and Grierson, P. F., 2015. Estimation of evaporative loss based on the stable isotope composition of water using Hydrocalculator. *Journal of Hydrology*, 523: 781-789. DOI:10.1016/j.jhydrol.2015.02.010.
- Sobol, I.M., 2001. Global sensitivity indices for nonlinear mathematical models and their Monte Carlo estimates. *Math. Comput. Simul.*, 55(1-3): 271-280. DOI:10.1016/s0378-4754(00)00270-6.
- Sprenger, M., Leistert, H., Gimbel, K., Weiler, M., 2016a. Illuminating hydrological processes at the soil-vegetation-atmosphere interface with water stable isotopes. *Reviews of Geophysics*, 54(3): 674-704. DOI:10.1002/2015rg000515.
- Sprenger, M., Seeger, S., Blume, T., Weiler, M., 2016b. Travel times in the vadose zone: Variability in space and time. *Water Resources Research*, 52(8): 5727-5754. DOI:10.1002/2015wr018077.
- Sprenger, M., Volkmann, T.H., Blume, T., Weiler, M., 2015. Estimating flow and transport parameters in the unsaturated zone with pore water stable isotopes. *Hydrology and Earth System Sciences*.
- Stumpp, C., Maloszewski, P., Stichler, W., Fank, J., 2009. Environmental isotope ($\delta^{18}\text{O}$) and hydrological data to assess water flow in unsaturated soils planted with different crops: Case study lysimeter station "Wagna" (Austria). *Journal of Hydrology*, 369(1-2): 198-208. DOI:10.1016/j.jhydrol.2009.02.047.
- Stumpp, C., Stichler, W., Kandolf, M., Šimůnek, J., 2012. Effects of land cover and fertilization method on water flow and solute transport in five lysimeters: A long-term study using stable water isotopes. *Vadose Zone Journal*, 11(1): 14. DOI:10.2136/vzj2011.0075.

- Sutanto, S.J., Wenninger, J., Coenders-Gerrits, A.M.J., Uhlenbrook, S., 2012. Partitioning of evaporation into transpiration, soil evaporation and interception: a comparison between isotope measurements and a HYDRUS-1D model. *Hydrology and Earth System Sciences*, 16(8): 2605-2616. DOI:10.5194/hess-16-2605-2012.
- Timbe, E., Windhorst, D., Crespo, P., Frede, H. G., Feyen, J., and Breuer, L., 2014. Understanding uncertainties when inferring mean transit times of water through tracer-based lumped-parameter models in Andean tropical montane cloud forest catchments. *Hydrology and Earth System Sciences*, 18(4): 1503-1523. DOI:10.5194/hess-18-1503-2014.
- Vrugt, J.A., Robinson, B.A., 2007. Improved evolutionary optimization from genetically adaptive multimethod search. *Proc. Natl. Acad. Sci. U. S. A.*, 104(3): 708-711. DOI:10.1073/pnas.0610471104.
- Vrugt, J.A., Stauffer, P.H., Wohling, T., Robinson, B.A., Vesselinov, V.V., 2008. Inverse modeling of subsurface flow and transport properties: A review with new developments. *Vadose Zone Journal*, 7(2): 843-864. DOI: 10.2136/vzj2007.0078.
- Wohling, T., Vrugt, J.A., 2011. Multiresponse multilayer vadose zone model calibration using Markov chain Monte Carlo simulation and field water retention data. *Water Resources Research*, 47: 19. DOI:10.1029/2010wr009265
- Wollschlager, U., Pfaff, T., Roth, K., 2009. Field-scale apparent hydraulic parameterisation obtained from TDR time series and inverse modelling. *Hydrology and Earth System Sciences*, 13(10): 1953-1966. DOI:10.5194/hess-13-1953-2009.
- Zhou, T., Šimůnek, J., Braud, I., 2021. Adapting HYDRUS-1D to simulate the transport of soil water isotopes with evaporation fractionation. *Environ. Modell. Softw.*, 143: 18. DOI:10.1016/j.envsoft.2021.105118.

Supplementary Material

Tables

Table S3.1. Summary of the observed data in the Stumpp et al. (2012) dataset.

Indicators	Depth (cm)	Frequency	Period
Weather	-	Daily	Whole period
Isotopic composition of precipitation	-	Event	Whole period
Soil water content	10, 15, 25, 45, 70, 100, and 130	Daily	Starting in 2004
Soil retention curve	20, 40, and 100	Once, to obtain $\theta(h)$	At the end of the observation period in 2007
Bottom water flux	-	Weekly	Whole period
Isotopic composition of drainage	-	Weekly	Whole period

Note that soil retention curves were measured using laboratory drainage experiments on the 100-cm³ soil samples collected at depths of 20, 40, and 100 cm, while the time series of soil water contents were measured in-situ at depths of 10, 15, 25, 45, 70, 100, and 130 cm.

Table S3.2. Initial and reduced ranges of parameters used in the Morris analysis of the Stumpp et al. (2012) dataset.

Parameter	Initial range	Reduced range
θ_{s1} [-]	0.3-0.6	0.3-0.5
α_1 [1/cm]	0.001-0.3	0.001-0.2
n_1 [-]	1.1-2.0	1.1-1.4
K_{s1} [cm/day]	10-220	10-220
λ [cm]	1.0-20	5.0-20
θ_{s2} [-]	0.3-0.6	0.4-0.6
α_2 [1/cm]	0.001-0.3	0.1-0.3
n_2 [-]	1.1-2.0	1.1-1.4
K_{s2} [cm/day]	10-12000	10-9000
θ_{s3} [-]	0.3-0.6	0.3-0.6
α_3 [1/cm]	0.001-0.3	0.001-0.3
n_3 [-]	1.1-2.0	1.1-2.0
K_{s3} [cm/day]	10-220	10-220

Table S3.3. Sobol' sensitivity analysis indices for the Stumpp et al. (2012) dataset.

S_{1_bf} , S_{1_wc} , S_{1_wi} , S_{1_rc} , S_{1_avg} , S_{T_bf} , S_{T_wc} , S_{T_wi} , S_{T_rc} , and S_{T_avg} represent the first-order (subscript 1) and total variances (subscript T) for the bottom flux time series (subscript bf), soil water content time series (subscript wc) at different depths, the bottom water isotopic composition time series (subscript wi), the water retention curves (subscript rc), and the average of them (subscript avg), respectively.

Parameter	S_{1_bf}	S_{1_bf} (BCI)	S_{T_bf}	S_{T_bf} (BCI)
α_1	0.499	0.028	0.611**	0.031
n_1	0.228	0.022	0.286*	0.013
θ_{s1}	0.111	0.013	0.135	0.006
α_3	0.017	0.010	0.048+	0.003
K_{s1}	0.001	0.005	0.020	0.002
α_2	0.003	0.005	0.018	0.002
K_{s2}	0.002	0.004	0.014	0.002
K_{s3}	0.002	0.004	0.012	0.001
n_2	0.001	0.003	0.005	0.000
θ_{s2}	0.001	0.002	0.004	0.000
θ_{s3}	0.000	0.002	0.002	0.000
n_3	0.000	0.001	0.001	0.000
λ	0.000	0.000	0.000	0.000
Sum	0.865		1.155	
Parameter	S_{1_wc}	S_{1_wc} (BCI)	S_{T_wc}	S_{T_wc} (BCI)
n_2	0.187	0.023	0.350	0.017
n_1	0.059	0.017	0.229	0.013
α_2	0.042	0.018	0.215	0.014
α_3	0.075	0.017	0.185	0.015
n_3	0.019	0.015	0.142	0.011
θ_{s3}	0.035	0.013	0.133	0.008
θ_{s1}	0.009	0.015	0.125	0.007
θ_{s2}	0.017	0.012	0.099	0.006
α_1	0.010	0.012	0.079	0.007
K_{s1}	0.008	0.008	0.045	0.004
K_{s2}	0.011	0.006	0.024	0.004
K_{s3}	0.000	0.005	0.016	0.004
λ	0.000	0.000	0.000	0.000
Sum	0.473		1.643	
Parameter	S_{1_wi}	S_{1_wi} (BCI)	S_{T_wi}	S_{T_wi} (BCI)
n_2	0.122	0.016	0.247	0.018
n_3	0.076	0.017	0.185	0.012
α_2	0.058	0.014	0.169	0.013

λ	0.073	0.017	0.168	0.009
θ_{s3}	0.089	0.014	0.165	0.009
α_1	0.059	0.012	0.137	0.011
n_1	0.061	0.014	0.118	0.007
θ_{s2}	0.033	0.008	0.074	0.005
α_3	0.018	0.009	0.071	0.007
θ_{s1}	0.043	0.012	0.066	0.004
K_{s3}	0.011	0.007	0.032	0.003
K_{s2}	0.008	0.005	0.019	0.003
K_{s1}	0.000	0.004	0.015	0.003
Sum	0.651		1.466	
Parameter	S_{I_rc}	S_{I_rc} (BCI)	S_{T_rc}	S_{T_rc} (BCI)
n_2	0.184	0.022	0.352	0.019
n_3	0.073	0.023	0.293	0.016
n_1	0.112	0.020	0.246	0.012
α_3	0.040	0.020	0.229	0.013
α_2	0.036	0.015	0.189	0.011
α_1	0.009	0.015	0.135	0.009
θ_{s3}	0.000	0.010	0.070	0.003
θ_{s1}	0.001	0.011	0.066	0.005
θ_{s2}	0.005	0.010	0.062	0.004
K_{s1}	-0.002	0.004	0.013	0.004
K_{s3}	0.001	0.002	0.004	0.003
K_{s2}	0.001	0.001	0.002	0.002
λ	0.000	0.000	0.000	0.000
Sum	0.461		1.659	
Parameter	S_{I_avg}	S_{I_avg} (BCI)	S_{T_avg}	S_{T_avg} (BCI)
n_2	0.219	0.025	0.386	0.020
n_1	0.124	0.018	0.267	0.013
n_3	0.037	0.016	0.218	0.012
α_2	0.044	0.017	0.203	0.013
α_3	0.022	0.018	0.178	0.010
α_1	0.015	0.012	0.119	0.009
θ_{s1}	-0.002	0.011	0.079	0.006
θ_{s3}	0.002	0.011	0.078	0.004
θ_{s2}	0.010	0.010	0.072	0.005
K_{s1}	0.000	0.005	0.016	0.004
K_{s3}	0.001	0.003	0.006	0.004
K_{s2}	0.003	0.003	0.005	0.003
λ	0.000	0.001	0.001	0.000

Sum 0.475 1.628

⁺Red fonts indicate the first-order or total indices within 1%~10%;

* Purple fonts indicate the first-order or total indices within 10%~50%;

**Blue fonts indicate the first-order or total indices larger than 50%.

Table S3.4. Initial and reduced ranges of parameters used in the Morris analysis of the Braud et al. (2009a) dataset.

Parameter	Initial range	Reduced range
θ_s [-]	0.38-0.48	0.38-0.48
α [1/cm]	0.008-0.011	0.008-0.011
n [-]	2.2-2.6	2.2-2.6
K_s [cm/day]	0.1296-0.216	0.1296-0.216
λ [cm]	0.1-1	0.1-1

Table S3.5. Sobol' sensitivity analysis indices for the Braud et al. (2009a) dataset for the isotopic composition of soil water. S_{1_wc} , S_{1_wi} , S_{1_avg} , S_{T_wc} , S_{T_wi} , and S_{T_avg} represent the first-order (subscript 1) and total variances (subscript T) for the final soil water content profile (subscript wc), the water isotopic composition profile (subscript wi), and the average of them (subscript avg), respectively.

Parameter	S_{1_wc}	S_{1_wc} (BCI)	S_{T_wc}	S_{T_wc} (BCI)
n	0.379	0.038	0.691**	0.075
θ_s	0.309	0.036	0.596	0.045
λ	-0.006	0.019	0.495*	0.813
α	0.003	0.007	0.080 ⁺	0.063
K_s	0.008	0.007	0.078	0.064
Sum	0.693		1.940	
Parameter	S_{1_wi}	S_{1_wi} (BCI)	S_{T_wi}	S_{T_wi} (BCI)
n	0.379	0.035	0.691	0.065
θ_s	0.309	0.032	0.596	0.041
λ	-0.006	0.016	0.497	0.742
α	0.003	0.008	0.080	0.052
K_s	0.008	0.008	0.079	0.050
Sum	0.693		1.943	
Parameter	S_{1_avg}	S_{1_avg} (BCI)	S_{T_avg}	S_{T_avg} (BCI)
n	0.629	0.038	0.975	0.039
θ_s	0.019	0.025	0.350	0.017
K_s	0.016	0.008	0.060	0.005
α	0.003	0.006	0.025	0.002
λ	0.003	0.004	0.011	0.002
Sum	0.670		1.421	

⁺Red fonts indicate the first-order indices within 1%~10%;

* Purple fonts indicate the total indices within 10%~50%;

**Blue fonts indicate the total indices larger than 50%.

Figures

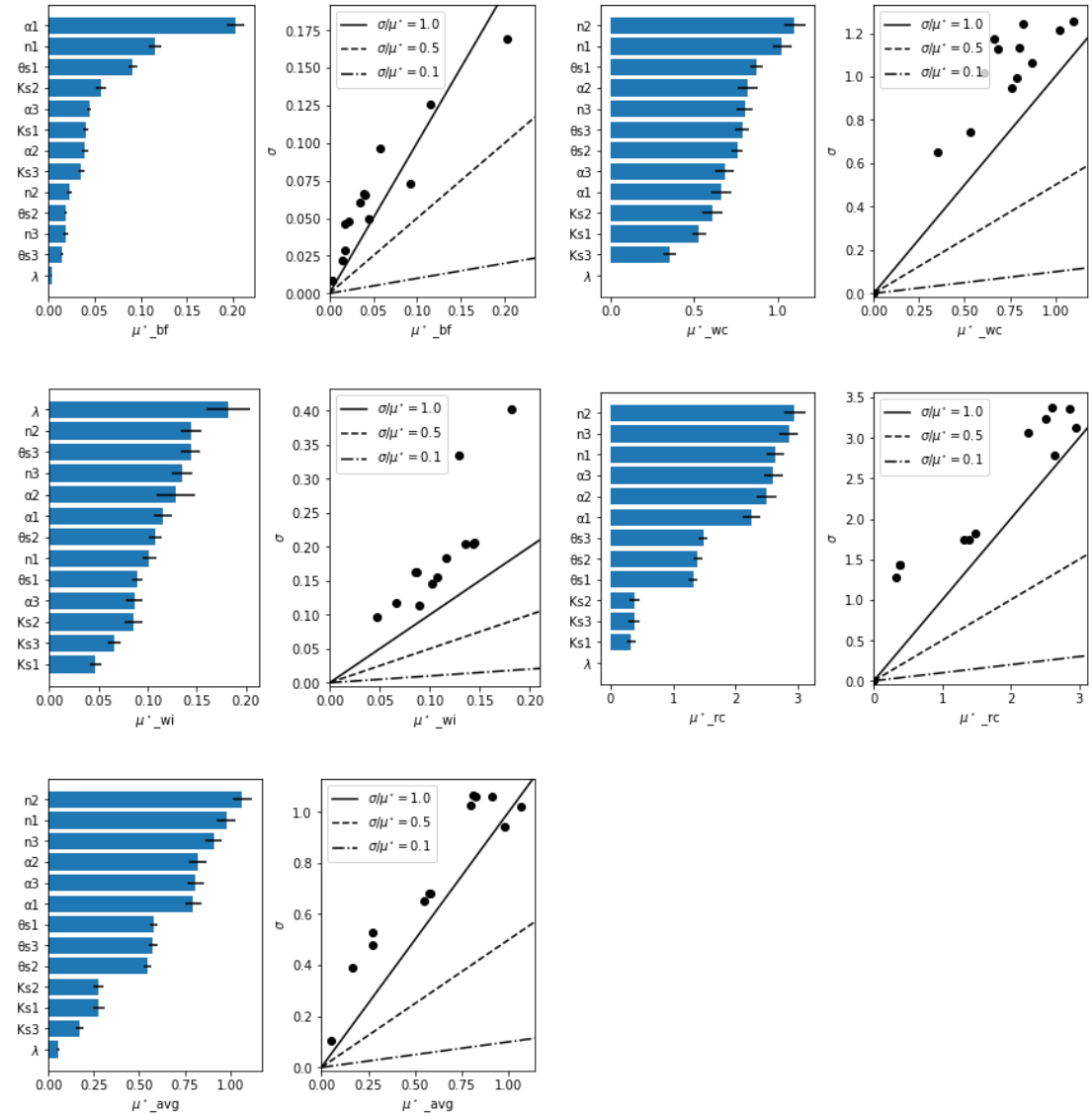


Figure S3.1. The μ_j^* and $\mu_j^* \sim \sigma_j$ plots for the Morris sensitivity analysis for the bottom water flux (subscript *bf*, top left), soil water content (subscript *wc*, top right), isotopic composition of the discharge (subscript *wi*, middle left), water retention curve (subscript *rc*, middle right), and the average of them (subscript *avg*, bottom left) for the Stumpp et al. (2012) dataset.

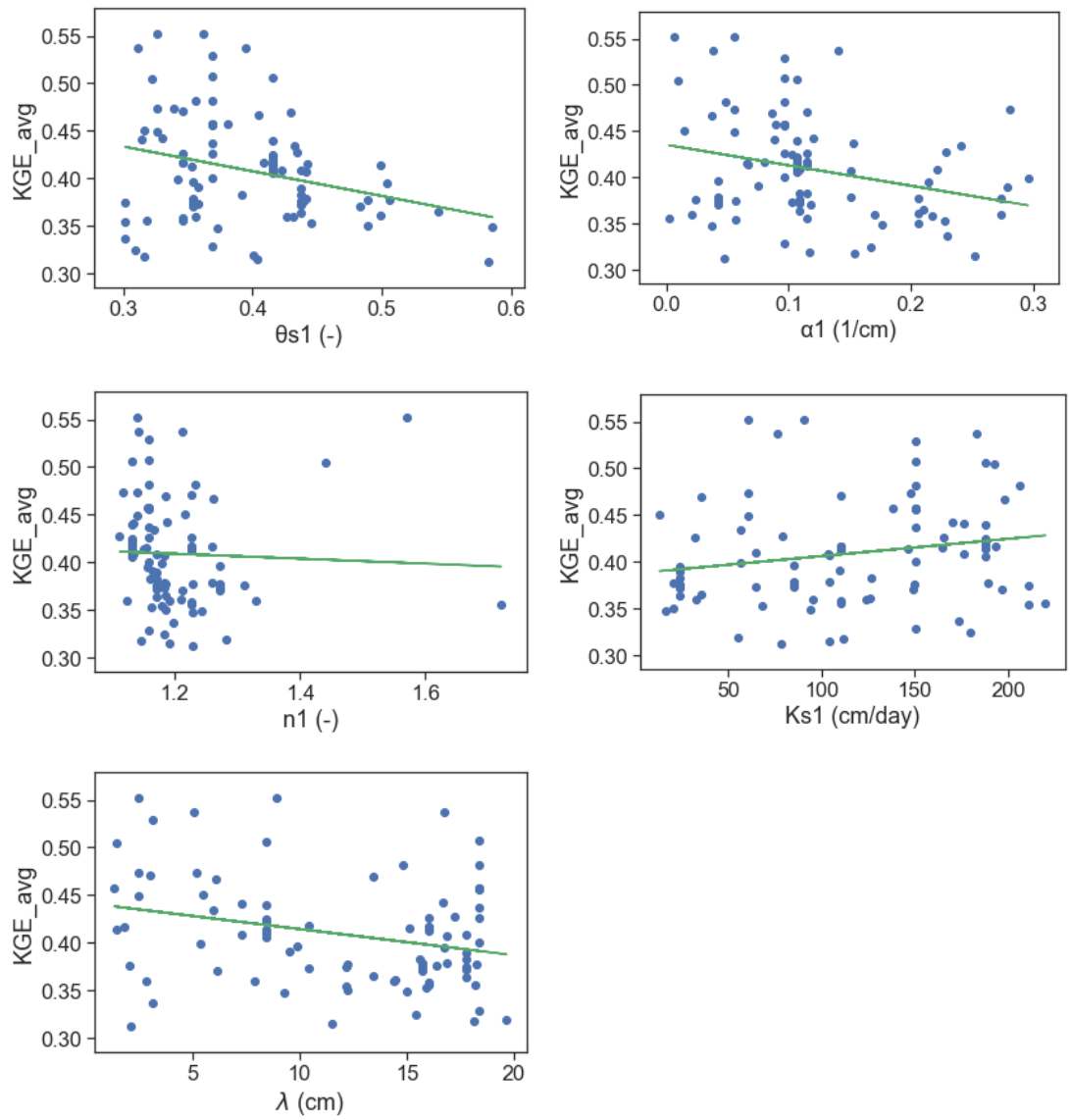


Figure S3.2. Scatter plots for pair relations θ_{s1} -KGE, α_1 -KGE, n_1 -KGE, and K_{s1} -KGE for the average performance for the Stumpp et al. (2012) dataset.

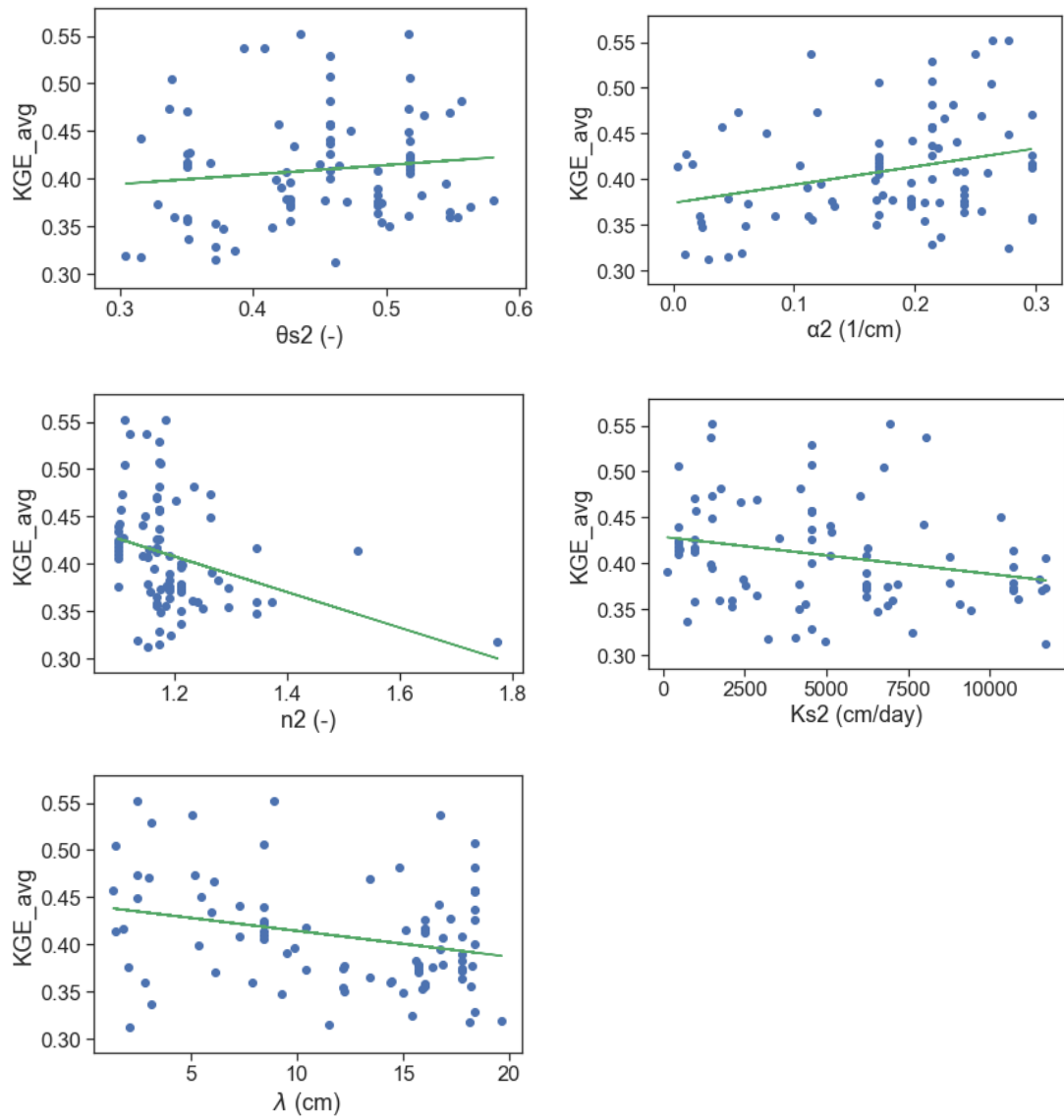


Figure S3.3. Scatter plots for pair relations θ_{s2} -KGE, α_2 -KGE, n_2 -KGE, and K_{s2} -KGE for the average performance for the Stumpp et al. (2012) dataset.

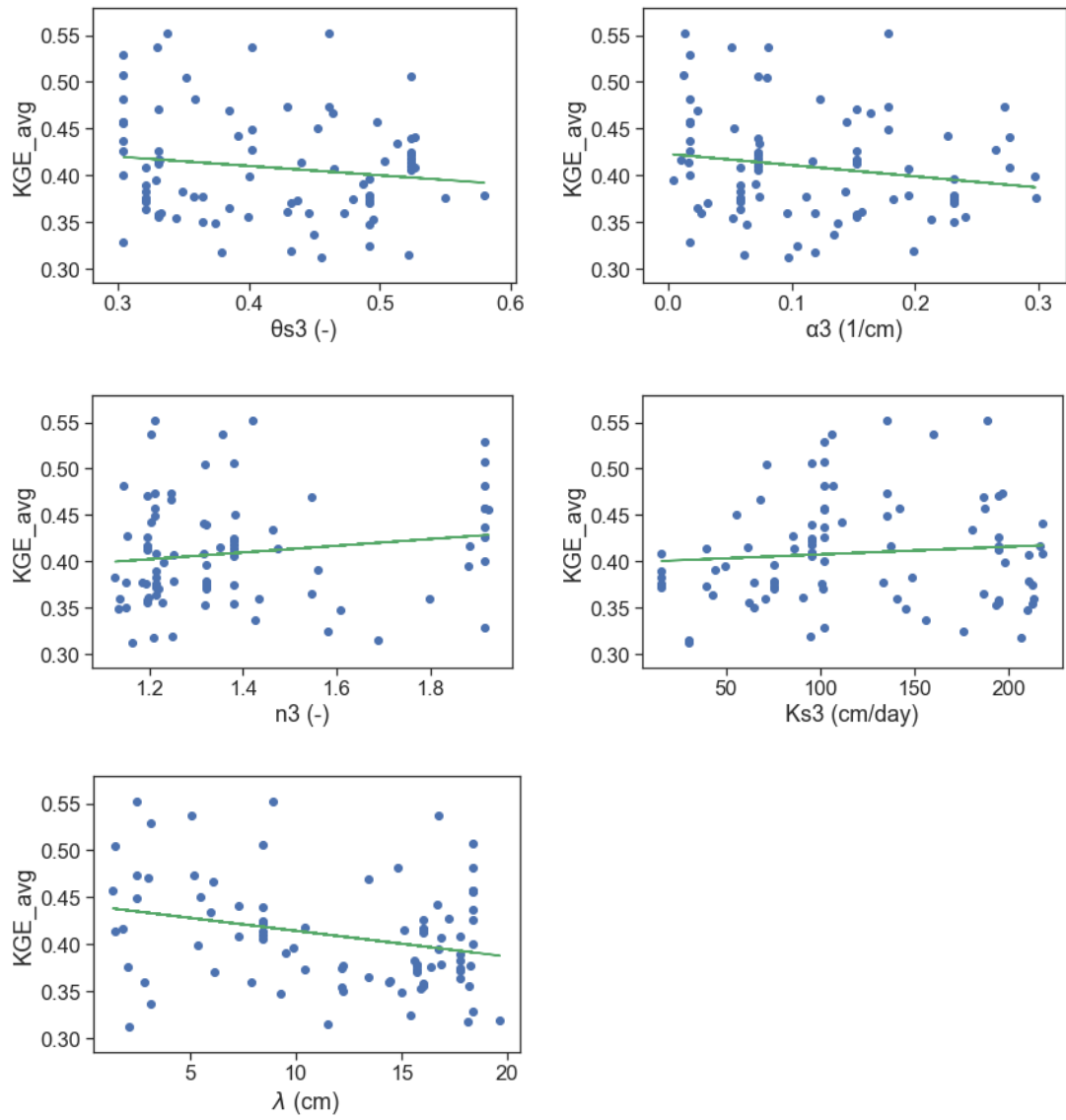


Figure S3.4. Scatter plots for pair relations θ_{s3} -KGE, α_3 -KGE, n_3 -KGE, and K_{s3} -KGE for the average performance for the Stumpp et al. (2012) dataset.

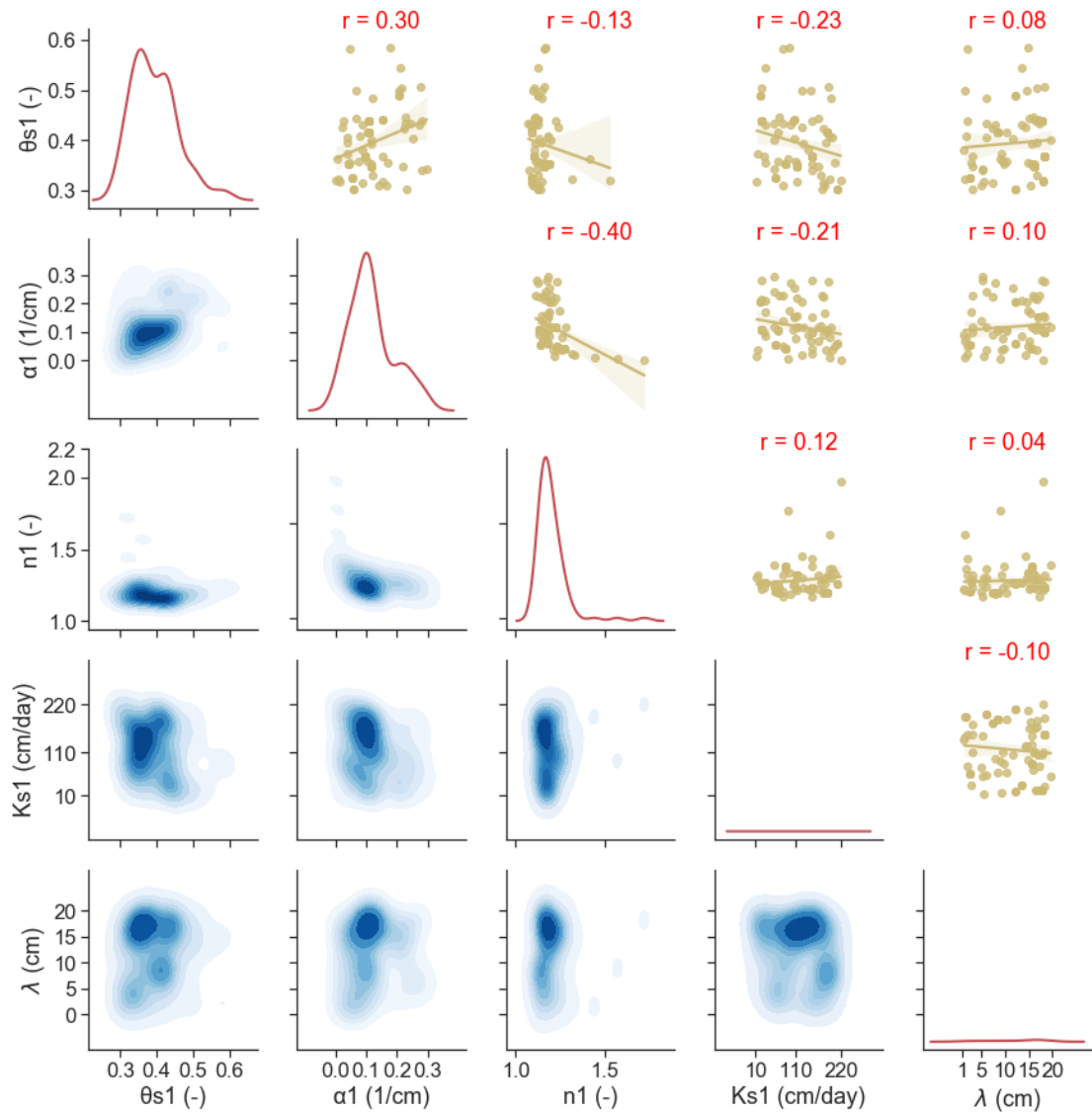


Figure S3.5. Bivariate KDE plots (below diagonal), univariate KDE plots (diagonal), and correlation plots (above diagonal) for the parameters of the first soil layer (0-30 cm) (for the Stumpp et al. (2012) dataset).

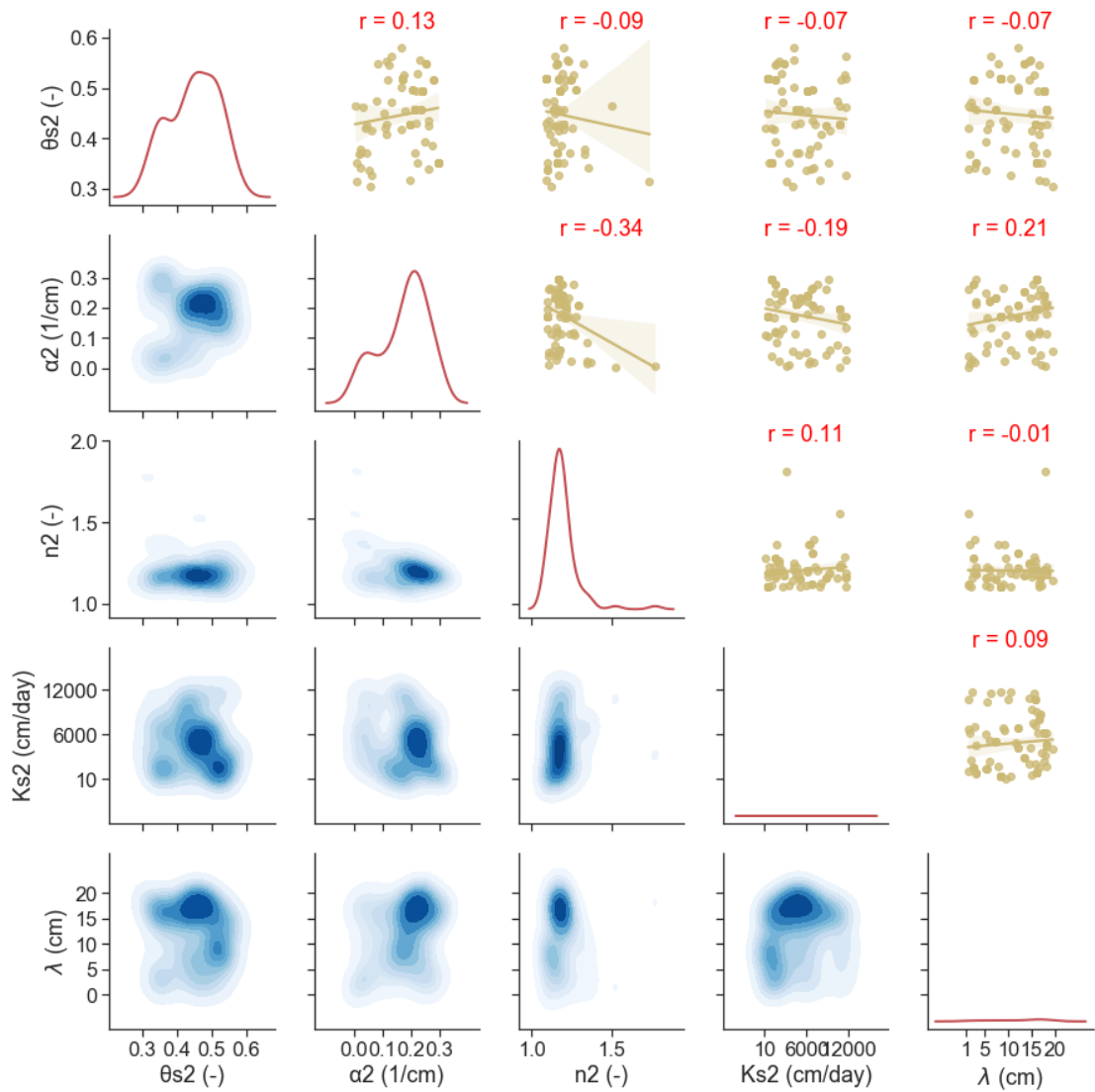


Figure S3.6. Bivariate KDE plots (below diagonal), univariate KDE plots (diagonal), and correlation plots (above diagonal) for the parameters of the second soil layer (30-90 cm) (for the Stumpp et al. (2012) dataset).

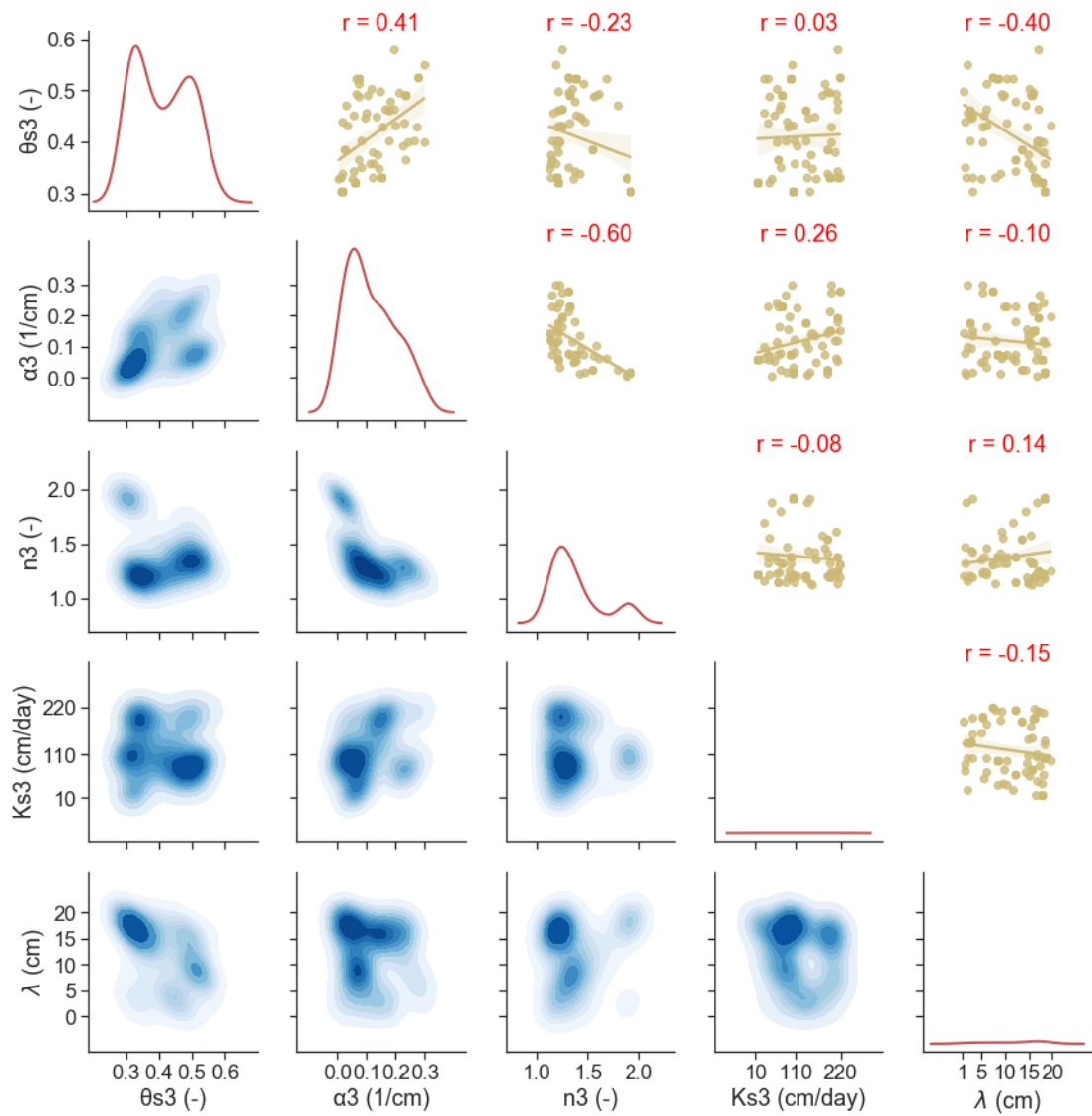


Figure S3.7. Bivariate KDE plots (below diagonal), univariate KDE plots (diagonal), and correlation plots (above diagonal) for the parameters of the third soil layer (90-150 cm) (for the Stump et al. (2012) dataset).

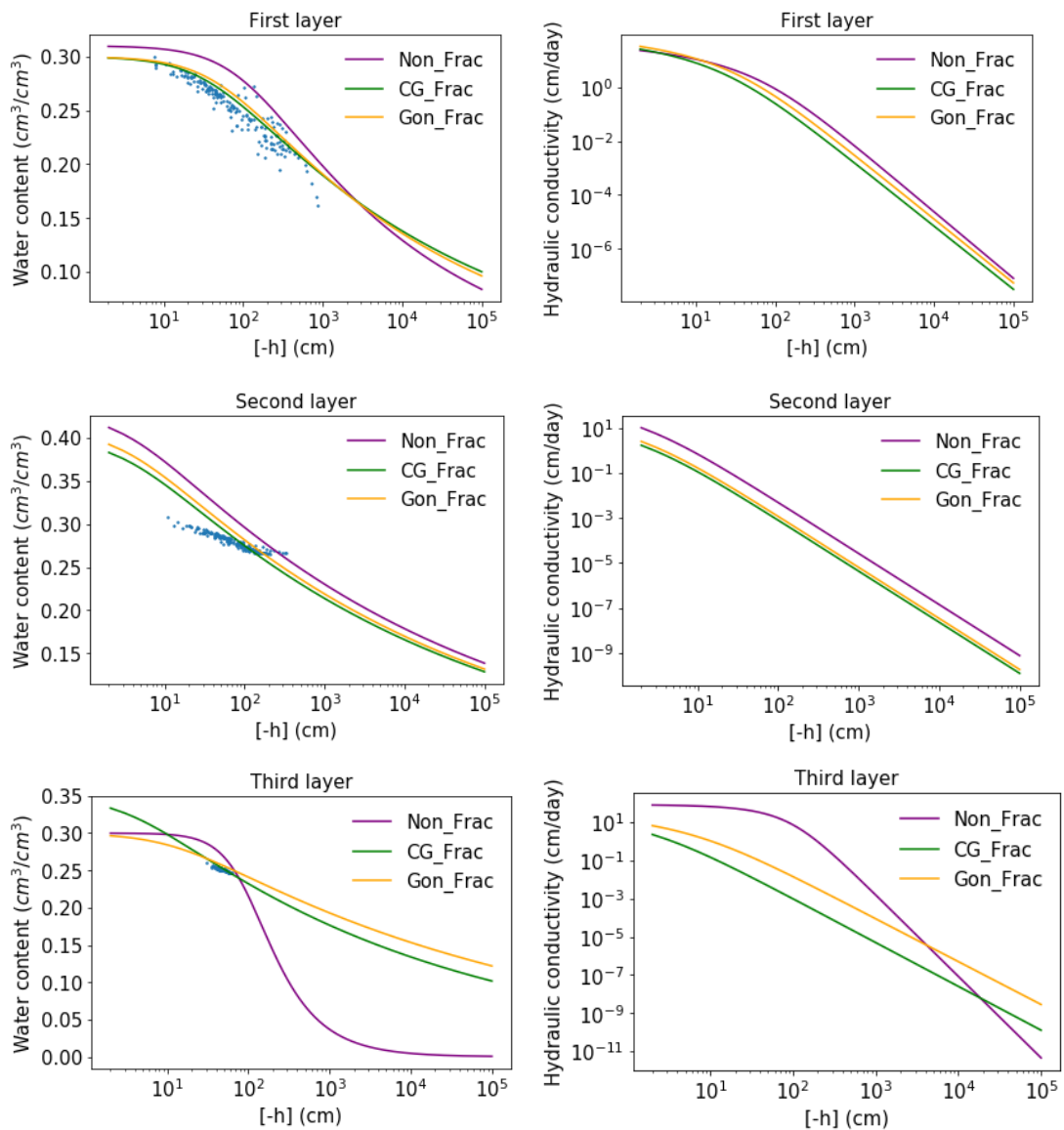


Figure S3.8. The soil water retention (left) and hydraulic conductivity (right) curves for different layers (first layer - top, second layer - middle, and third layer - bottom) and different fractionation scenarios for the Stumpp et al. (2012) dataset.

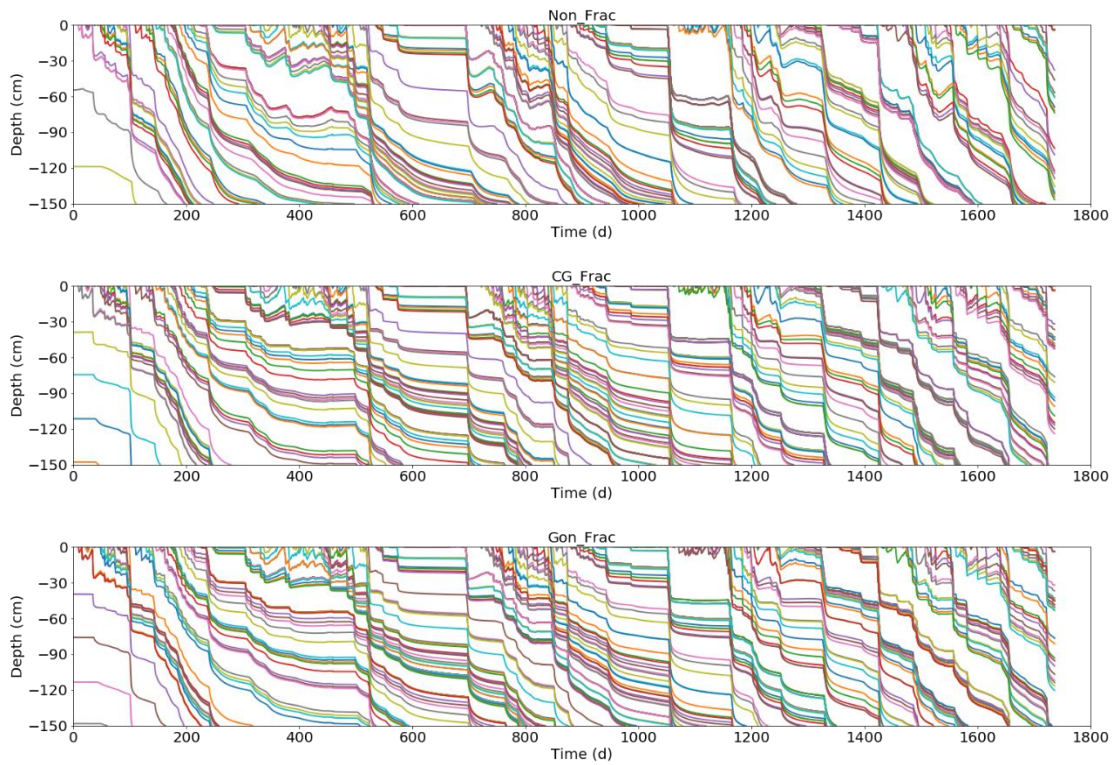


Figure S3.9. The particles trajectories simulated using the soil hydraulic parameters estimated assuming different fractionation scenarios (Non_Frac – top, CG_Frac – middle, and Gon_Frac – bottom).

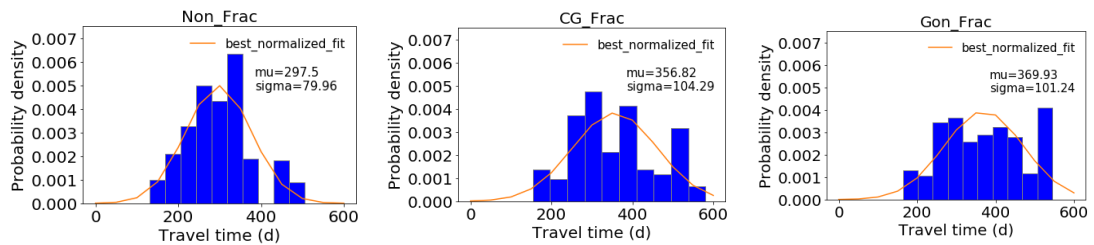


Figure S3.10. The probability density distribution of water travel times calculated using the soil hydraulic parameters estimated assuming different fractionation scenarios (Non_Frac – left, CG_Frac – middle, and Gon_Frac – right).

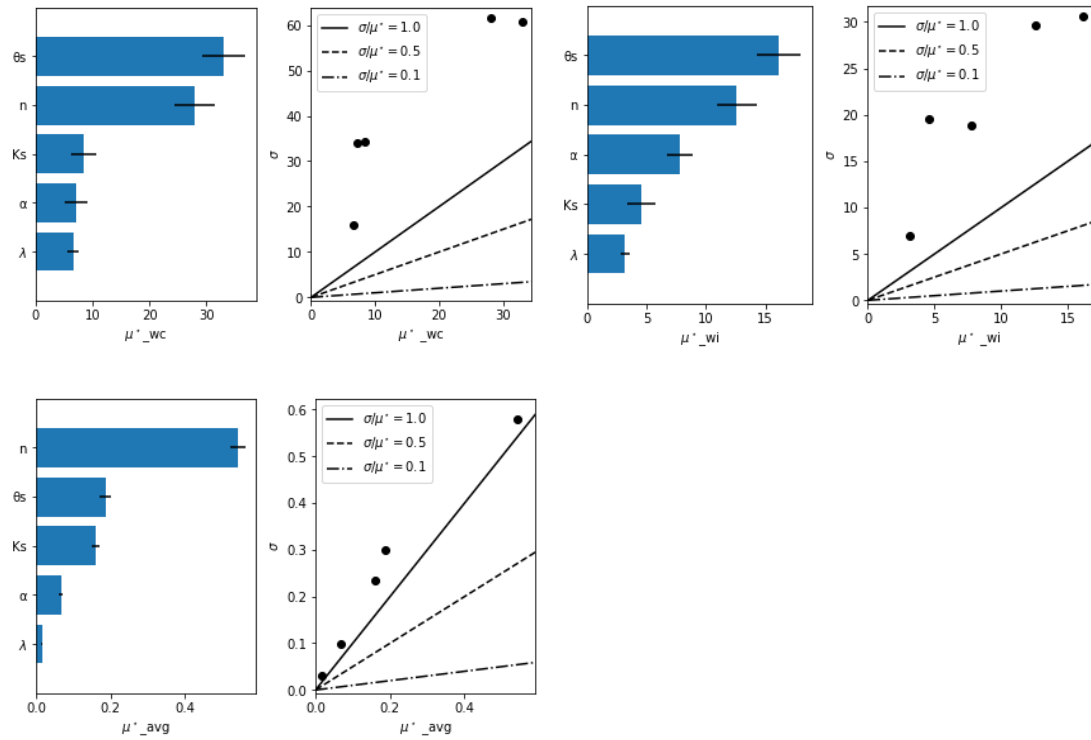


Figure S3.11. The μ_j^* and $\mu_j^* \sim \sigma_j$ plots for the Morris sensitivity analysis for the soil water content (subscript *wc*, top left), isotopic composition (subscript *wi*, top right), and average (subscript *avg*, bottom) for the Braud et al. (2009a) dataset.

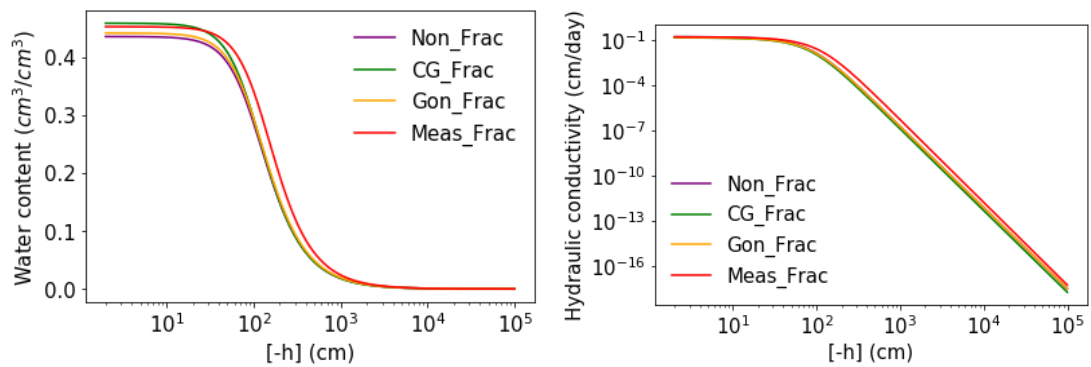


Figure S3.12. The soil water retention (left) and hydraulic conductivity (right) curves for different fractionation scenarios for the Braud et al. (2009a) dataset.

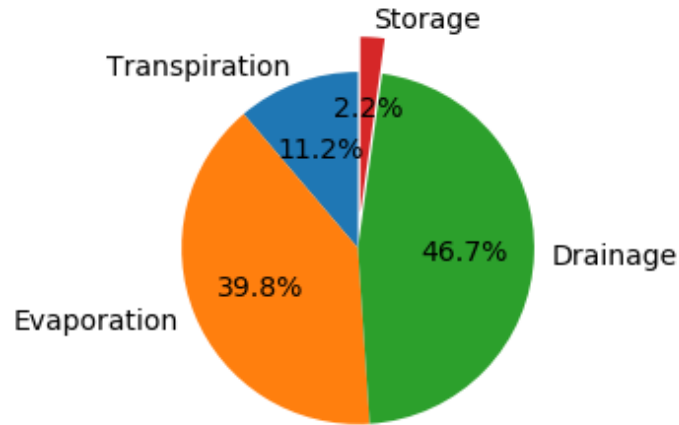


Figure S3.13. Precipitation contributions to different water balance components in the Non_Frac scenario for the Stump et al. (2012) dataset.

Method S3.1: Evaporation Fractionation Models

S1.1 Craig-Gordon Model

The isotope flux of evaporation E_i (kg/m²/s) is:

$$E_i = \frac{E}{\alpha_i^k} \frac{M_i}{M_w} \frac{(H_{rs} \cdot \alpha^+ \cdot R_L - h_a' \cdot R_a)}{H_{rs} - h_a'} \quad (\text{S3.1})$$

The isotope ratio of the evaporation flux R_E (-) is:

$$R_E = E_i/E = [H_{rs} \cdot \alpha^+ \cdot R_L - h_a' \cdot R_a] / [(H_{rs} - h_a') \cdot \alpha_i^k] \cdot \frac{M_i}{M_w} \quad (\text{S3.2})$$

where E is the evaporation flux, H_{rs} [-] is the relative humidity of the surface soil air phase, h_a' [-] is the normalized air relative humidity, R_L is the isotope ratio of the remaining surface liquid water [-], R_a is the isotope ratio of the atmospheric water vapor [-], and α^+ and α_i^k [-] are the equilibrium and kinetic fractionation factors, respectively.

S1.2 Gonfiantini Model

The total fractionation factor (α_i^{total}) can be simplified as (Gonfiantini, 1986):

$$\varepsilon_k = 1000 * (\alpha_i^k - 1) * (H_{rs} - h_a')$$
 (S3.3)

$$\alpha_i^{total} = 1/\alpha_i^* + \frac{\varepsilon_k}{1000}$$
 (S3.4)

The isotope ratio of the evaporation flux (R_E) is then calculated as:

$$R_E = R_L/\alpha_i^{total}$$
 (S3.5)

More details about different fractionation models can be found in Section 3 of Zhou et al. (2021).

Method S3.2: Global Sensitivity Analysis Methods

S3.2.1 Morris Method

The Morris method is a screening-based method that performs a one-at-a-time (OAT) analysis. By randomly selecting the initial X on the grid points and constructing a randomized trajectory in this grid structure, r trajectories can be obtained, which scan the entire input parameter space. Along the trajectory i , each parameter X_j is varied along a size Δe_j to explore its influence on the model output Y . This means that each sample differs by only one coordinate (only one parameter is changed) from the previous sample. This relative variation of the model output for parameter X_j is called the elementary effect E_j^i , which can be calculated as:

$$E_j^i = \frac{Y(X + e_j\Delta) - Y(X)}{e_j\Delta}$$
 (S3.5)

where Y is the model output corresponding to parameter set X , Δ is a value chosen in the range of $\{1/(k-1), \dots, 1-1/k-1\}$, in which k is the number of discretization levels, and e_j is a vector of zeros, but with a unit as its j -th component.

Two indices, μ_j^* and σ_j , are then computed to evaluate the sensitivity order of the input parameters:

$$\mu_j^* = \frac{1}{r} \sum_{i=1}^r |E_j^i| \quad (\text{S3.6})$$

$$\sigma_j = \sqrt{\frac{1}{r} \sum_{i=1}^r (E_j^i - \frac{1}{r} \sum_{i=1}^r E_j^i)^2} \quad (\text{S3.7})$$

where the former estimates the direct effect of the parameter X_j on the model output, and the latter represents the indirect effect or interaction effects with other parameters.

More details can be found in (Campolongo et al., 2007).

In this study, $r = 1000$ was chosen, which is much higher than the recommended (more than 20~30) as suggested by Herman et al. (2013). The model runs were 14000 (i.e., $1000 \cdot (13+1)$) and 6000 (i.e., $1000 \cdot (5+1)$) for the Stumpp et al. (2012) and Braud et al. (2009a) datasets, respectively.

S2.2 Sobol' Method

The Sobol' method is a variance-based method that quantifies the contribution of the change of each parameter to the model output variance. The sensitivity indices (SIs) are expressed as:

$$\text{First-order indices: } S_{1,j} = \frac{V_j}{V} \quad (\text{S3.8})$$

$$\text{Second-order indices: } S_{j,i} = \frac{V_{ji}}{V} \quad (\text{S3.9})$$

$$\text{Total indices: } S_{Tj} = S_{1,j} + \sum_{i \neq j} S_{j,i} \quad (\text{S3.10})$$

where V_j is the variance caused by the j -th parameter, and V is the total variance.

First-order indicators $S_{1,j}$ represent the direct contribution of the variance of an individual parameter X_j to the total unconditional variance (namely the direct effect). The second-order indices $S_{j,i}$ explain the contribution of the interaction between parameters X_j and X_i . The total effect of parameter X_j is denoted by the total index S_{Tj} that includes the direct and indirect effects. More details can be found in Sobol' (2001).

The total number of samples $q = 5000$ as recommended (less than 5000) by Nossent et al. (2011) was chosen in this study. The model runs were 75000 ($5000 * (13 + 2)$) and 35000 (i.e., $5000*(5+2)$) for the Stumpp et al. (2012) and Braud et al. (2009a) datasets, respectively. The bootstrap confidence intervals (BCIs) were also estimated to evaluate the accuracy of the sensitivity indices.

Results S3.1: Global Sensitivity Analysis and Monte-Carlo Filtering for the Stumpp et al. (2012) Dataset

S1.1 Global Sensitivity Analysis

a. Morris Method

Table S3.2 provides the initial ranges of all evaluated parameters. Fig. S3.1 reports the order of parameters sensitive to bottom water fluxes (KGE_bf), soil water contents (KGE_wc), isotopic compositions of the discharge (KGE_wi), the water retention curves (KGE_rc) and the average of them (KGE_avg), respectively. It can be seen from the μ_j^* values for the bottom flux that α_1 and n_1 show the most significant direct effects on the outputs, followed by θ_{s1} and K_{s2} . For the soil water contents, n_2 and n_1 show the most significant direct effects on the outputs, followed by θ_{s1} and α_2 . For the isotopic compositions of discharge, λ and n_2 show the most significant direct effects on the outputs, followed by θ_{s3} and n_3 . For the water retention curves, n_2 and n_3 show the most significant direct effects on the outputs, followed by n_1 and α_3 . For the average performance, n_2 and n_1 show the most significant direct effects on the outputs, followed by n_3 and α_2 .

In general, all parameters with high direct effects (large μ_j^*) often have high indirect effects (large σ_j). The $\mu_j^* \sim \sigma_j$ values plotted around and above the 1:1 line suggest that the indirect effects or interactions between parameters are close to or more significant than the direct effects.

Overall, as seen from μ_j^* and $\mu_j^* \sim \sigma_j$ plots of the KGE_avg, soil hydraulic parameters of different layers have similar impacts on the model outputs. The order of sensitive parameters is: shape parameters n , shape parameter α , saturated water contents θ_s , saturated hydraulic conductivities K_s , and dispersivities λ .

b. Sobol' Method

Table S3.3 reports sensitivity indices for the bottom water flux (KGE_bf), soil water content (KGE_wc), isotopic composition of the bottom flux (KGE_wi), water retention curve (KGE_rc), and the average of them (KGE_avg). For KGE_bf, the α_1 , n_1 , and θ_{s1} parameters show a relatively significant direct effect (50%, 23%, and 11%, respectively). Other parameters have first-order indices less than 10%, indicating that their direct effect on the variance of KGE_bf is relatively smaller. The sum of all first-order indices is less than 1, and about 87% of the variance is caused by the direct effects, suggesting that the interactions between parameters are relatively smaller. To sum up, about 61% of the variance of KGE_bf is caused by α_1 , followed by n_1 (29%) and θ_{s1} (14%), either by the direct effect or interactions with other parameters.

For KGE_wc, the n_2 parameter show a relatively significant direct effect (19%). Other parameters have first-order indices less than 10%, indicating that their direct effect on the variance of KGE_wc is relatively smaller. The sum of all first-order indices is less than 1, and about 47% of the variance is caused by the direct effects, suggesting that the interactions between parameters are very important. To sum up,

about 35% of the variance of KGE_wc is caused by n_2 , followed by n_1 (23%) and α_2 (22%), either by the direct effect or interactions with other parameters.

For KGE_wi, the n_2 parameter show a relatively significant direct effect (12%). Other parameters have first-order indices less than 10%, indicating that their direct effect on the variance of KGE_wc is relatively smaller. The sum of all first-order indices is less than 1, and about 65% of the variance is caused by the direct effects, suggesting that the interactions between parameters are very important. To sum up, about 25% of the variance of KGE_wc is caused by n_2 , followed by n_3 (19%) and α_2 and λ (17%), either by the direct effect or interactions with other parameters.

For KGE_rc, the n_2 and n_1 parameters show a relatively significant direct effect (18% and 11%). Other parameters have first-order indices less than 10%, indicating that their direct effect on the variance of KGE_rc is relatively smaller. The sum of all first-order indices is less than 1, and about 46% of the variance is caused by the direct effects, suggesting that the interactions between parameters are very important. To sum up, about 35% of the variance of KGE_rc is caused by n_2 , followed by n_3 (29%) and n_3 (22%), either by the direct effect or interactions with other parameters.

For KGE_avg, the n_2 and n_1 parameters show a relatively significant direct effect (22% and 12%). Other parameters have first-order indices less than 10%, indicating that their direct effect on the variance of KGE_wc is relatively smaller. The

sum of all first-order indices is less than 1, and about 48% of the variance is caused by the direct effects, suggesting that the interactions between parameters are very important. To sum up, about 39% of the variance of KGE_wc is caused by n_2 , followed by n_1 (27%) and n_3 (22%), either by the direct effect or interactions with other parameters.

The total sensitivity index of all parameters is always greater than zero, which means that none of the parameters can be fixed because they affect the output variance either directly or by their interactions. Overall, seen from the KGE_avg sensitivity analysis results, the order of sensitive parameters is: shape parameters n , shape parameter α , saturated water contents θ_s , saturated hydraulic conductivities K_s , and dispervities λ .

Overall, the qualitative ranking based on the Morris method is in general consistent with quantitative indices obtained by the Sobol' method, which confirms that the sensitivity analysis results are reliable.

S1.2 Monte Carlo Filtering

A Monte Carlo filtering produced a filtered sample of 87 good solutions with KGE_bf, KGE_wc, KGE_wi, KGE_rc, KGE_avg=0 as the threshold value. Scatter plots for the parameters of different soil layers and the convergent solutions for the average model performance (KGE_avg) are displayed in Fig. S3.2, S3.3, and S3.4,

respectively. For the first layer (Fig. S3.2), in general, KGE_avg decreases as θ_{s1} , α_1 , n_1 , and λ , increase, and increases as K_{s1} increases, despite with very different correlation coefficients. More plausible solutions lie in the left part (1.1~1.4) of the scatter plot for the n_1 parameter. For the second layer (Fig. S3.3), in general, KGE_avg decreases as n_2 , K_{s2} , and λ , increase, and increases as θ_{s2} and α_2 increases, despite with very different correlation coefficients. More plausible solutions lie in the left part (1.1~1.4) of the scatter plot for the n_2 parameter. For the third layer (Fig. S3.4), in general, KGE_avg decreases as θ_{s3} , α_3 , and λ , increase, and increases as n_3 and K_{s3} increase, despite with very different correlation coefficients.

The univariate and bivariate plots for different soil layers (Figs. S3.5~S3.7) reveal significant information about reasonable ranges of parameters. Leptokurtic distributions in the univariate KDE plots generally indicate low uncertainty and are often observed for highly sensitive parameters. It means that observations are informative for those parameters, and therefore they can be estimated with good confidence. With this information, we can further compare the bivariate KDE plots and get the parameter ranges of other related variables.

For the first layer (Fig. S3.5), the maximum correlation coefficients (in absolute values) are 0.40 for the α_1 and n_1 parameters and 0.30 for the α_1 and θ_{s1} parameters. The correlation between other parameters is relatively smaller. The univariate KDE for the parameters n_1 and α_1 (the most sensitive parameters for the first layer) exhibit a

leptokurtic distribution, and their good solutions clearly concentrate in 1.1~1.4 and 0.001~0.2, respectively. The bivariate KDE for n_1 - α_1 again highlights a denser region for α_1 in 0.001~0.2. The bivariate KDE for α_1 - θ_{s1} and n_1 - θ_{s1} highlight a denser region for θ_{s1} in 0.3~0.5.

For the second layer (Fig. S3.6), the maximum correlation coefficient (in absolute values) is 0.34 between the α_2 and n_2 parameters. The correlation between other parameters is relatively smaller. The univariate KDE for the parameters n_2 and α_2 (the most sensitive parameters for the first layer) exhibit a leptokurtic distribution, and their good solutions clearly concentrate in 1.1~1.4 and 0.1~0.3, respectively. The bivariate KDE for n_2 - α_2 again highlights a denser region for α_2 in 0.1~0.3. The bivariate KDE for n_2 - λ highlights a denser region for λ in 5~20. The bivariate KDE for α_2 - K_{s2} highlights a denser region for K_{s2} in 10~9000. The bivariate KDE for α_2 - θ_{s2} highlight a denser region for θ_{s1} in 0.4~0.6.

For the third layer (Fig. S3.7), the maximum correlation coefficients (in absolute values) are 0.60 for the α_3 and n_3 parameters, and 0.41 for the α_3 and θ_{s3} parameters. The correlation between other parameters is relatively smaller. No other significant information about the possible ranges of parameters can be found.

The results of the multivariate plot analysis were used to reduce the ranges of parameters for the following optimization process (Table S3.2). The reduction was only applied to parameters that showed well identifiable good solution regions.

Results S3.2: Global Sensitivity Analysis and Monte-Carlo Filtering for the Braud et al. (2009a) Dataset

S2.1 Global Sensitivity Analysis

a. Morris Method

Table S3.4 provides the initial ranges of all evaluated parameters. Fig. S3.10 reports the order of sensitive parameters for the soil water content (KGE_wc), water isotopic composition (KGE_wi), and the average (KGE_avg). It can be seen from the μ_j^* values that the n and θ_s parameters show a significant direct effect on the outputs, followed by the K_s and α parameters, while λ parameter has the smallest direct effect. All parameters with high direct effects (large μ_j^*) also have high indirect effects (large σ_j). The $\mu_j^* \sim \sigma_j$ values plot around or above the 1:1 line, suggesting that the indirect effects or interactions between parameters are close to or more significant than the direct effects.

b. Sobol' Method

Table S3.5 reports sensitivity indices for the isotopic composition of soil water. For KGE_wc and KGE_wi, n , and θ_s , parameters show a relatively significant direct effect (38%, and 31%, respectively). Other parameters have first-order indices less than 10%, indicating that their direct effect on the variance of KGE_bf is relatively smaller. The sum of all first-order indices is less than 1, and about 69% of the variance is caused by the direct effects, suggesting that the interactions between parameters are relatively

smaller. To sum up, about 69% of the variance of KGE_wc is caused by n , followed by θ_s (60%) and λ (14%), either by the direct effect or interactions with other parameters. For KGE_avg, only n parameter show a relatively significant direct effect (63%). Other parameters have first-order indices less than 10%, indicating that their direct effect on the variance of KGE_avg is relatively smaller. The sum of all first-order indices is less than 1, and about 67% of the variance is caused by the direct effects, suggesting that the interactions between parameters are relatively smaller. To sum up, about 98% of the variance of KGE_wc is caused by n , followed by θ_s (35%), either by the direct effect or interactions with other parameters.

The total sensitivity index of all parameters is always greater than zero, which means that none of the parameters can be fixed because they affect the output variance either directly or by their interactions. Overall, seen from the KGE_avg sensitivity analysis results, the most sensitive parameters are shape parameters n and saturated water contents θ_s .

Overall, the qualitative ranking based on the Morris method is in general consistent with quantitative indices obtained by the Sobol' method, which provides additional confirmation that the sensitivity analysis results are reliable.

S2.2 Monte Carlo Filtering

The univariate and bivariate plots do not reveal significant information about reasonable ranges of parameters and thus are not shown here. The reduced ranges of parameters for the following optimization process are shown in Table S3.4.

Chapter 4 The Impact of Soil Tension on Isotope Fractionation, Transport and Spatial-Temporal Origin of Root Water Uptake

Abstract: The new isotope module in HYDRUS-1D can be used to infer the spatial-temporal origin of root water uptake (RWU), a suitable dynamic indicator for agroforestry water management. However, accumulating evidence shows that the equilibrium fractionation between liquid water and water vapor within the soil is affected not only by soil temperature but also by soil tension. How soil tension affects the isotope transport modeling is still unknown. In this study, we evaluated the impact of three fractionation scenarios on model performance for a field dataset from Langeoog Island: *i*) no fractionation (Non_Frac), *ii*) the soil temperature control on equilibrium fractionation as described by the Craig-Gordon model (CG_Frac), and *iii*) CG_Frac plus the soil tension control on equilibrium fractionation (TC_Frac). The model simulations proved that TC_Frac led to more depleted surface isotopic composition than CG_Frac. Concerning the spatial origin of RWU, both water balance and the Bayesian mixing model reflect overall trends of contribution ratios of different soil layers. The contribution ratios of all soil layers in the TC_Frac scenario were always between Non_Frac and CG_Frac. Regarding the temporal origin of RWU, both particle tracking and virtual tracer experiment revealed overall trends in drainage and root zone (RZ) travel times. The order of both drainage and RZ travel times was:

Non_Frac > TC_Frac > CG_Frac. The influencing factors of isotope transport-based methods were more complex than water flow-based methods. The vegetation change from bare soil to grassland increased the travel time for precipitation to recharge groundwater on Langeoog Island.

4.1 Introduction

Equilibrium and kinetic fractionation processes occur between soil water vapor and liquid water or within soil water vapors and induce enrichment of stable isotopes of hydrogen (^2H) and oxygen (^{18}O) in the remaining soil water during evaporation. Kinetic fractionation is influenced by transport resistances from the evaporating surface to the atmosphere and isotope diffusivities. Equilibrium fractionation is usually determined as a function of soil temperature (Majoube, 1971). However, recent research shows that equilibrium fractionation is also influenced by the interactions between water films on soil particle surfaces and water vapor. Therefore, the impact of soil pressure head (or soil tension) on equilibrium fractionation has recently gained attention (Chen et al., 2016; Lin and Horita, 2016; Lin et al., 2018; Oerter et al., 2014; Orłowski and Breuer, 2020). Soil tension increases the energy required to remove water from the soil matrix and induces the water vapor pressure deficit. As a result, the surface of soil particles preferentially attracts lighter isotopes and increases soil water vapor diffusion toward the atmosphere. At very high soil tensions (i.e., dry conditions), tightly-bound soil water (i.e., slow mobile water subject to capillary-driven flow) is thus depleted of heavy isotope species, which induces the enrichment in isotopic signatures of surface soil water vapor (Gaj and McDonnell, 2019).

This is problematic when using this isotopic information to interpret the origin of water fluxes in the soil-plant-atmosphere continuum (SPAC). Considerable attention

has been paid to the spatial-temporal origin of root water uptake (RWU), because it can guide when and how much to irrigate to maximize RWU and reduce deep drainage and groundwater recharge, thus improving agricultural water use efficiency.

The spatial origin of water taken up by roots (RWU) across the soil profile has been i) determined graphically by comparing the isotopic characteristics of xylem water, soil water at different depths, and groundwater, or ii) estimated using statistical models such as the IsoSource and Bayesian mixing models (SIAR, MixSIR, and MixSIAR). Compared with the IsoSource model (Corneo et al., 2018), the Bayesian mixing models can accurately estimate water sources for root uptake in different soil depths while simultaneously considering their uncertainty (e.g., Ma and Song, 2016; Zhang et al., 2022). Multiple Bayesian models (i.e., SIAR, MixSIR, and MixSIAR) were compared by Wang et al. (2019), who reported better performance of SIAR and MixSIAR in identifying water sources.

Compared with the spatial origin, research on the temporal origin of water for RWU has been limited to a few studies (Allen et al., 2019; Brinkmann et al., 2018; Miguez-Macho and Fan, 2021; Zhou et al., 2022). The premise for inferring the temporal origin of water for RWU is an accurate estimate of travel times (TT) of irrigation/precipitation water to different depths in the soil profile (for example, to the bottom of the soil profile as drainage or the root zone as RWU, etc.). As summarized in Sprenger et al. (2019), the three common methods to estimate travel times include

(a) time-invariant TT distributions ($TTDs$), (b) StorAge Selection (SAS) functions, and (c) flux tracking or particle tracking implemented in physically-based hydrological models. The first two methods require the optimization of isotope transport parameters in lumped models (Asadollahi et al., 2020; Benettin et al., 2015; Harman, 2015; Kim and Harman, 2022; Maloszewski et al., 2006; Pangle et al., 2017; Rinaldo et al., 2015; Stumpp and Maloszewski, 2010; Tetzlaff et al., 2014; Tetzlaff et al., 2018; Timbe et al., 2014). However, these lumped models oversimplify the isotope transport mechanisms (Sprenger et al., 2016; Sprenger et al., 2019).

On the other hand, physically-based hydrological models describe water flow and isotope transport using the Richards equation and the advection-dispersion equation, respectively. For example, Brinkmann et al. (2018) employed flux tracking (virtual tracer experiment) using the HYDRUS-1D model by Stumpp et al. (2012) to derive the residence time distribution of precipitation in the soil and the temporal origin of RWU in a temperate forest. They found that 50% of water consumed by trees throughout the year came from precipitation during the growing season (May ~ October), while 40% of it originated from precipitation in the preceding winter (November ~ April) (Brinkmann et al., 2018). Zhou et al. (2022) used particle tracking in HYDRUS-1D and found that considering fractionation using the code by Zhou et al. (2021) was likely to result in longer residence times of precipitation in soil and older water ages of RWU for winter rye in a lysimeter (Zhou et al., 2022).

Physically-based numerical models (e.g., the isotope-enabled module in HYDRUS-1D) has the potential to continuously assess the spatial-temporal origin of water for RWU (Zhou et al., 2021; Zhou et al., 2022), which is often unappreciated in current studies based on graphical and statistical methods (Rothfuss and Javaux, 2017; Seeger and Weiler, 2021). However, reliable model simulations are obtained only when the model setup provides an accurate and realistic description of water flow and isotope transport (Finkenbiner et al., 2022). The factors influencing evaporation fractionation (e.g., soil tension) have often been ignored in isotope transport modeling, introducing the risk of obtaining large isotope mass balance errors.

Langeoog is a sandy barrier island off the coast of northern Germany in a humid zone. The freshwater groundwater lens is the only water source on this island that helps balance water levels between island groundwater and seawater and prevents seawater intrusion. However, this dynamic balance is fragile due to the extensive groundwater pumping over the years resulting from intensive tourism (Post et al., 2022). At the same time, the island is susceptible to seawater erosion, aggravating the groundwater shortage.

Many natural or artificial dunes have been created to protect the coast from erosion (Post and Houben, 2017). Over several years, these dunes have shifted from an almost unvegetated type to a vegetated kind, covered with mosses, grass, and low shrubs (Post et al., 2022). This vegetation change may bring about changes in

groundwater recharge processes due to increased RWU and transpiration. Many studies have been conducted on temporal variations of groundwater recharge in this dune area (Houben et al., 2014; Post et al., 2022). However, characterizing travel times of precipitation to RWU and groundwater recharge is still lacking, while enhancing this understanding is critical for the sustainable development of groundwater resources on this island.

The dune sands are very dry due to evaporation and RWU and its surface soil water is enriched with heavy isotopes due to evaporation fractionation (Post et al., 2022). These conditions make it a good site for studying the impacts of soil tension control on evaporation fractionation.

Therefore, we pose the following three scientific questions:

- 1) To what extent does the consideration of the soil tension and temperature controls on soil water equilibrium fractionation affect the performance of the isotope transport model?
- 2) How will different modeling results (based on different fractionation scenarios) affect the assessment of the spatial-temporal origin of water for RWU on this island?
- 3) Is it better to use water-flow-based or isotope-transport-based methods to determine the spatial-temporal origin of RWU?

To answer these three scientific questions, the main goal of this study are: a) to enhance the HYDRUS-1D ability to simulate the transport of isotopes by implementing the effects of soil temperature and tension on the evaporation fractionation process (Fig.

4.1), b) to use isotope data collected on Langeoog Island (Post et al., 2022) in combination with modified HYDRUS-1D to validate the model and study the influence of temperature and tension controls on the isotope fractionation, c) to evaluate different model setups to determine the spatial-temporal origin of RWU, and d) to compare the impacts of different model setups and methods on model performance and practical applications. Three isotope transport scenarios were evaluated: 1) no evaporation fractionation (Non_Frac); 2) evaporation fractionation with the temperature control as described by the Craig-Gordon law (CG_Frac); 3) evaporation fractionation with the temperature and soil tension controls (TC_Frac). The model performance was assessed based on its ability to reproduce measured soil profile data of soil water contents and isotopic compositions.

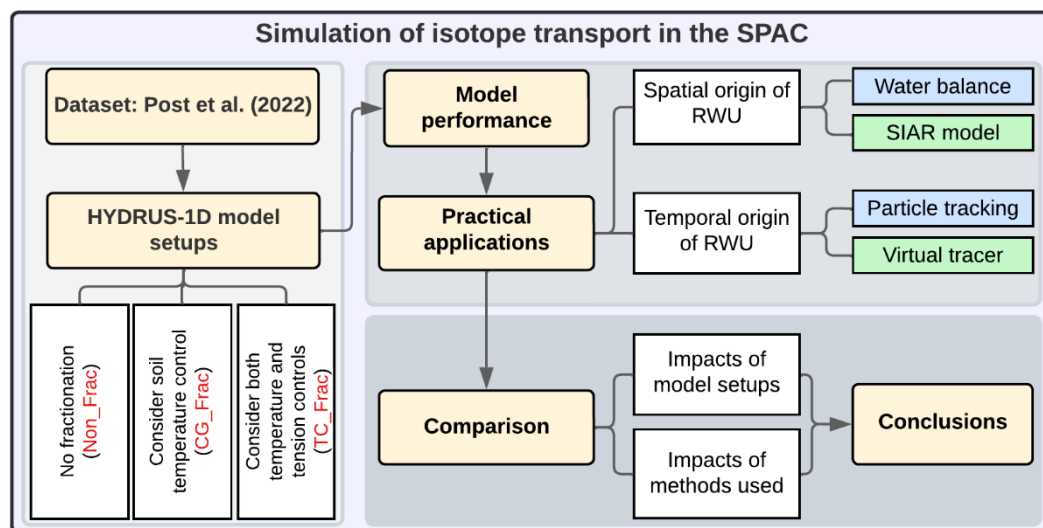


Figure 4.1. Schematic outline of methods used.

4.2 Materials and Methods

4.2.1 Study Area and Data Collection

Langeoog is a sandy barrier island off the coast of northern Germany. The annual precipitation rate on Langeoog island is 777 mm (Houben et al., 2014). In this study, the vegetated dune (Site LB01 in Post et al., 2022, covered by grasses) was selected to analyze the spatial-temporal origin of its vegetation RWU.

The experiment was carried out between July 2012 and June 2019 in a 450-cm-thick soil profile. The meteorological data, including daily precipitation, wind speed, air humidity, mean/maximum/minimum air temperature, and solar radiation, were measured at daily time resolution. Precipitation samples for isotopic compositions were collected fortnightly or monthly. Soil samples were collected on June 25, 2019 (10 to 425 cm below the soil surface, about every 5 or 10 cm) to measure grain size, soil water contents, and soil water isotopic compositions. Soil hydraulic properties were measured on soil cores collected at the nearby site (Fig. 1 of Post et al., 2022) during an earlier project in 2014 using the evaporation method carried out on the HYPROP semi-automatic device (METER Group, Munich, Germany) (Lipovetsky et al., 2020). The temporal distributions of relevant weather and vegetation growth variables are shown in Figs. S4.1 and S4.2. More details about the study area and data collection methods can be found in (Post et al., 2022).

4.2.2 HYDRUS-1D Model Setup

Water flow and isotope transport in the unsaturated zone were simulated using a modified version of the HYDRUS-1D code that considers isotope evaporation fractionation (Zhou et al., 2021). Fig. 4.2 shows a summary of the model setup. The simulation period is 2536 days long (corresponding to about seven years), from July 17, 2012, to June 25, 2019. The 450-cm-thick soil profile is uniform with a single set of soil hydraulic (θ_r , θ_s , α , n , K_s) and isotope transport (λ) parameters.

The actual root water uptake rate of grass, S (the sink term S in the Richards equation in Fig. 4.2), within the root zone depends on the rooting depth and the root density distribution (Fig. S4.1). It is obtained from potential RWU and the stress response function accounting for the root water stress. The latter is modeled using a piecewise linear function depending on the pressure head (Feddes et al., 1978). The maximum rooting depth is set to 40 cm, and the root density decreases exponentially from the soil surface to the maximum rooting depth.

The upper boundary condition is set to the potential water flux across the soil surface (i.e., the difference between daily values of potential evaporation, E_p , and precipitation, P), while the lower boundary condition is set to free drainage (a zero pressure head gradient). Temperature BC is used at upper and lower boundaries for heat transport. Daily isotope concentrations are assigned to their corresponding precipitation events to get the concentration flux for the upper boundary condition, while a zero

concentration gradient (i.e., free drainage) is set as the lower boundary condition. The initial soil water content ($0.046 \text{ cm}^3/\text{cm}^3$), temperature (20°C) and isotopic composition (-110 ‰ for ^2H and -10‰ for ^{18}O) are used throughout the soil profile. Post et al. (2022) provide more details about the model setups.

In our analysis, three fractionation scenarios have been considered, including a) no evaporation fractionation, which is used as a control (the Non_Frac scenario), b) equilibrium evaporation fractionation described by the Craig-Gordon equation, which considers only the soil temperature control (Craig and Gordon, 1965) (the CG_Frac scenario), and c) equilibrium evaporation fractionation according to the modified Craig-Gordon equation, which considers both the soil tension and soil temperature controls (the TC_Frac scenario).

Conceptual model	Equations and BCs	Inputs
<p>Note: evaporation fractionation is limited to the soil surface (due to the lack of the vapor phase within soil).</p>	<p>➤ Upper BCs:</p> <ul style="list-style-type: none"> • W: Atmospheric BC • H: Temperature BC • I: Non_Frac, CG_Frac, TC_Frac <p>➤ Governing equations:</p> <ul style="list-style-type: none"> • W $\frac{\partial \theta_i}{\partial t} = \frac{\partial}{\partial z} \left[K_{Lh} \left(\frac{\partial h}{\partial z} + \cos \omega \right) \right] - S$ • H $\frac{\partial C_p(\theta_i)T}{\partial t} = \frac{\partial}{\partial z} \left[\lambda(\theta_i) \frac{\partial T}{\partial z} \right] - C_w \frac{\partial q_i T}{\partial z} - C_w S T$ • I $\frac{\partial \theta_i C_i^l}{\partial t} = \frac{\partial}{\partial z} \left(D_i^{l*} \frac{\partial C_i^l}{\partial z} \right) - \frac{\partial (q_i C_i^l)}{\partial z} - S C_i^l$ <p>➤ Lower BCs:</p> <ul style="list-style-type: none"> • W: Free drainage BC • H: Temperature BC • I: Zero concentration gradient 	<p>➤ Upper BCs:</p> <ul style="list-style-type: none"> • W: P, ET_0, LAI, crop growth and RWU parameters. • H: T_s • I: $\delta_p, RH, T_{air}, \delta_A$ <p>➤ Soil hydraulic and isotope transport parameters:</p> <ul style="list-style-type: none"> • W: VG-M model: $\theta_r, \theta_s, n, \alpha, K_s$ (from Post et al., 2022). • H: Chung-Horton model: default parameters. • I: D_i^{l0}, λ (from Post et al., 2022). <p>➤ Lower BCs:</p> <ul style="list-style-type: none"> • W: None • H: T_b • I: None

Figure 4.2. HYDRUS-1D model setup. W, H, and I represent water flow, heat transport, and isotope transport, respectively, while Non_Frac, CG_Frac, and TC_Frac indicate no fractionation, fractionation described by the Craig-Gordon equation, and fractionation according to the modified Craig-Gordon equation. BC denotes boundary condition. Note that the description of the variables in this figure is shown in Table S4.1 in the Supplementary Materials.

4.2.2.1 Craig-Gordon Equation

Evaporation fractionation between the soil water and the free atmosphere includes both equilibrium and kinetic fractionation processes (Craig, 1961). Craig and Gordon (1965) calculated the isotope evaporation flux at the soil surface based on these two types of fractionations.

When the isotope concentration is expressed in kg m^{-3} (Eq. 1 in Zhou et al., 2021), the isotope evaporation flux E_i ($\text{kg m}^{-2} \text{s}^{-1}$) is:

$$E_i = E_i^{out} - E_i^{in} = \frac{E_a M_i}{\alpha_i^k M_w} \frac{(RH_s \cdot \alpha_{v/w} \cdot R_L - RH_a' \cdot R_a)}{RH_s - RH_a'} \quad (4.1)$$

The isotope ratio of the evaporation flux R_E (-) is expressed as:

$$R_E = E_i/E_a = [H_{rs} \cdot \alpha_{v/w} \cdot R_L - h_a' \cdot R_a]/[(H_{rs} - h_a') \cdot \alpha_i^k] \cdot \frac{M_i}{M_w} \quad (4.2)$$

where E_a [m/s] is the actual evaporation flux, M_i and M_w (kg/mol) are the molar masses of heavy water and ordinary water, respectively, RH_s [-] is the relative humidity of the surface soil air phase, RH_a' [-] is the normalized air relative humidity, R_L is the isotope ratio of the remaining surface liquid water [-], R_a is the isotope ratio of the atmospheric water vapor [-], and $\alpha_{v/w}$ and α_i^k [-] are the equilibrium and kinetic fractionation factors, respectively. We only show the calculation of $\alpha_{v/w}$ (ranging from 0 to 1) in this study. Calculations of other variables are elaborated in Zhou et al. (2021) and Post et al. (2022).

4.4.2.2 Temperature Control on Evaporation Fractionation

Majoube (1971) computed the equilibrium fractionation factor $\alpha_{v/w}$ as a function of temperature T (K):

$$\alpha_{v/w}({}^2H/{}^1H)_{majoube} = \exp\left(-52.612 \cdot 10^{-3} + \frac{76.248}{T} - \frac{24.844 \cdot 10^3}{T^2}\right) \quad (4.3)$$

$$\alpha_{v/w}({}^{18}O/{}^{16}O)_{majoube} = \exp\left(2.0667 \cdot 10^{-3} + \frac{0.4156}{T} - \frac{1.137 \cdot 10^3}{T^2}\right) \quad (4.4)$$

4.2.2.3 Tension control on Evaporation Fractionation

The equilibrium fractionation factor is affected not only by temperature but also by soil tension when it is above 1260 hPa (about 1284 cm) under dry conditions. The positive correlation between soil tension and the equilibrium fractionation factor is independent of soil texture and is controlled by adhesive and cohesive forces (Gaj and McDonnell, 2019). Gaj and McDonnell (2019) express the equilibrium fractionation factor $\alpha_{v/w}$ as the contribution of $\alpha_{v/w}({}^2H/{}^1H)_{majoube}$ and the effect of soil tension, h (denoted in absolute positive values, cm):

$$\alpha_{v/w}({}^2H/{}^1H) = \alpha_{v/w}({}^2H/{}^1H)_{majoube} + 0.01498 \log_{10}(h) \quad (4.5)$$

$$\alpha_{v/w}({}^{18}O/{}^{16}O) = \alpha_{v/w}({}^{18}O/{}^{16}O)_{majoube} + 0.00607 \log_{10}(h) \quad (4.6)$$

Note that the new isotope transport module used in this study is almost the same as in Zhou et al. (2021). Specifically, both modules require the input of the atmospheric water vapor's relative humidity, temperature, and isotopic composition. No additional input is needed for the newly-implemented soil tension control on equilibrium fractionation.

Various isotope mass balance components are evaluated to understand the reasons behind differences in model performance and practical applications of different fractionation scenarios. These components include actual root isotope uptake ($cvRoot$, positive for mass removal), the soil surface isotope flux in precipitation and actual evaporation ($cvTop$, positive for mass inflow), and the bottom isotope flux in actual

drainage (*cvBot*, negative for mass removal). The total cumulative isotope removal from the SPAC was then quantified using these isotope mass balance components.

4.2.3 Practical Applications

The results of the three modeling scenarios were used to infer the spatial-temporal origin of RWU using both water flow- (water balance, particle tracking) and isotope transport-based (SIAR, virtual tracer experiment) methods. Note that all calculations were conducted on a daily interval.

4.2.3.1 Spatial Origin of RWU

Soil water at different depths of the root zone represents the source of RWU. The root zone was divided into 10-cm-thick sub-layers (0~10 cm, 10~20 cm, 20~30 cm, and 30~40 cm), considered separate water sources (Layer 1, Layer 2, Layer 3, Layer 4, respectively). Capillary rise from groundwater was not considered because of a relatively shallow maximum rooting depth (40 cm) and deep water table (below 450 cm) in this study area. The amount of water taken up by RWU from different soil layers was assessed using two methods.

a. Water Balance (WB)

Root water uptake from different soil layers was calculated using information printed by HYDRUS-1D to the NOD_INF.OUT file.

b. SIAR

The SIAR Bayesian isotope mixing model (Parnell et al., 2010) implemented in the R package was used to identify sources of RWU. In this model, the mean isotopic compositions of different water sources (i.e., different soil layers) and their standard errors are assumed to follow normal distributions. The overall isotopic composition of RWU is the sum of isotopic compositions of different sources multiplied by their corresponding proportional contributions and residual error. The discrimination values in the SIAR model were set to zero for both $\delta^2\text{H}$ and $\delta^{18}\text{O}$ because there is usually no isotope fractionation during RWU (Dawson and Ehleringer, 1991). More details can be found in Cao et al. (2022) and Stock et al. (2018).

In this study, different fractionation scenarios were first simulated using the HYDRUS-1D model to obtain isotopic compositions of RWU ($cvRoot$ from the output file SOLUTE.OUT divided by $vRoot$ from the output file T_LEVEL.OUT) and soil water at different depths (from the output file NOD_INF.OUT). Simulated $\delta^2\text{H}$ and $\delta^{18}\text{O}$ concentrations in RWU and soil water at different depths, and corresponding standard errors were then used as input for the SIAR model.

The Mann-Kendall trend test was used to determine whether there is a trend (indicated by τ values; positive and negative τ values indicate an increasing and decreasing trends, respectively) in the time series of contribution ratios of different water sources obtained by both methods. The null hypothesis is that there is no trend in the data ($\tau=0$). When the p -value of the test is below a certain significance level ($p < 0.01$ was used in this study), it can be concluded that there is a statistically significant trend in the investigated time series.

4.2.3.2 Temporal Origin of RWU

a. Particle Tracking (PT)

Details about the particle tracking algorithm can be found in (Šimůnek, 1991; Zhou et al., 2021; Zhou et al., 2022). The particle tracking algorithm requires two input parameters: w_{Stand} (which defines the initial distribution of particles) and w_{Prec} (which controls the boundary distribution of particles). In this study, the input parameters w_{Stand} and w_{Prec} were set to 10 cm and a negative value, respectively. The latter negative value causes the program to release one particle for each precipitation event so that one can track the movement of each precipitation event separately. The particle tracking algorithm then calculates particles positions based on water mass balance calculations between two neighboring particles (and the soil surface) during a specific time interval. Based on particle positions at different times, one can deduce the residence times of each precipitation event for various soil depths. The difference between the times when

a particle enters and leaves the soil profile (or the root zone) is defined as drainage (or root zone) travel time. The particle tracking module also evaluates the contribution of each particle to RWU at different times, which can be used to infer the temporal origin of RWU.

b. Virtual Tracer Experiment (VTE)

The virtual tracer experiment (VTE) method was used to calculate root zone (RZ) travel times based on simulations of isotope transport using HYDRUS-1D (Nasta et al., 2021). The number of simulations used in this approach equals the number of daily precipitation events n . HYDRUS-1D is run n times, assuming the initially isotope-free soil profile, assigning a known isotope composition to the i th precipitation event, and keeping all remaining rainfall events isotope-free. This technique helps trace isotope composition across the soil profile from every individual rainfall event. The arrival (or exit) time is calculated when the cumulative isotope flux at the soil profile bottom reaches 50% of its final value. The travel time is calculated as a difference between precipitation entry times and arrivals. Different fractionation scenarios were applied to run repeated simulations to calculate drainage and RZ travel times.

4.3 Results

4.3.1 Performance of the Isotope Transport Model

The model performance of each modeling scenario is shown in Fig. 4.3, and the corresponding root mean square errors (*RMSE*) are reported in Table 4.1. The model performance of the CG_Frac and TC_Frac scenarios were quite similar, although very different from the Non_Frac scenario. The Non_Frac scenario produced lower surface isotopic compositions than the CG_Frac and TC_Frac scenarios. On the other hand, the scenario that considered the soil tension control (TC_Frac) predicted the surface isotopic composition to be more depleted (by -3.25‰ for $\delta^2\text{H}$ and -1.25‰ for $\delta^{18}\text{O}$) in this example than the CG_Frac scenario.

The impact of isotope fractionation driven by temperature and tension controls on the model simulations is evaluated as a percentage of a contribution to the *RMSE* for isotope compositions. *RMSEs* are evaluated for different variables (subscripts *wi*, and *avg* refer to the water isotopic composition and average, respectively). As can be seen in Table 4.2, the temperature control almost halved *RMSEs*. Considering both temperature and tension controls halved *RMSEs* as well, thus obtaining similar performance. In other words, adding tension control does not provide substantial benefits and even slightly increased *RMSEs* in this example. The impact of considering the soil temperature control on *RMSE_wi* was 91%, while the impact of considering the

soil tension control on $RMSE_{wi}$ was 9%. The effect of the temperature control played a dominant role in the model performance.

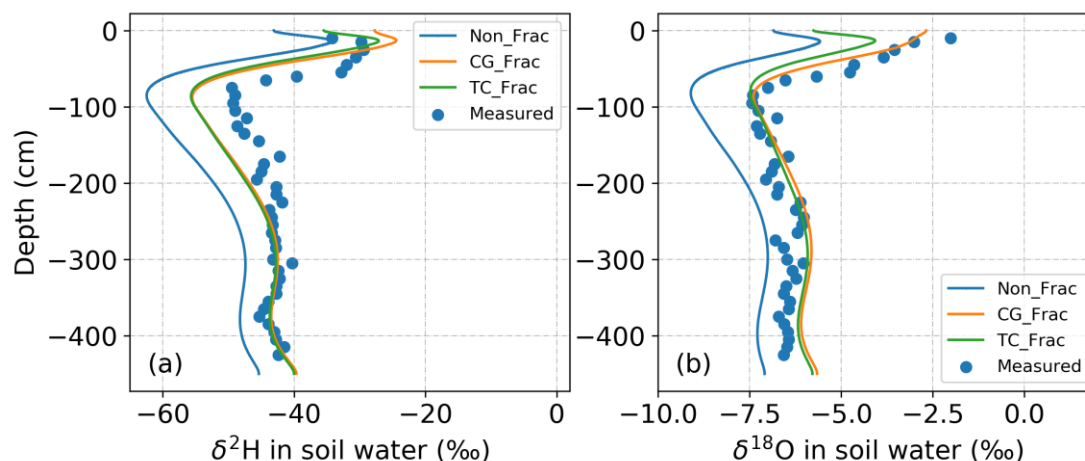


Figure 4.3. Measured (blue circles) and simulated (a) δ^2H and (b) $\delta^{18}O$ profiles under three fractionation scenarios (Non_Frac, CG_Frac, and TC_Frac).

Table 4.1. Root mean square error (RMSE) indices (wi , and avg refer to the water isotopic composition, and average, respectively) for different fractionation scenarios (Non_Frac, CG_Frac, and TC_Frac).

Fractionation scenario	Non_Frac	CG_Frac	TC_Frac	CG_Frac relative to Non_Frac	TC_Frac relative to CG_Frac	TC_Frac relative to Non_Frac	Contribution of temp. control (%)	Contribution of tension control (%)
RMSE _{wi} for δ^2H (‰)	10.058	5.063	5.416	-4.995	0.353	-4.642	93	7
RMSE _{wi} for $\delta^{18}O$ (‰)	1.657	0.563	0.792	-1.094	0.229	-0.865	83	17
RMSE _{avg}	5.858	2.813	3.104	-3.045	0.291	-2.754	91	9

4.3.2 Spatial Origin of RWU

The dynamics of contribution ratios of the four soil layers obtained using the water balance method and the SIAR model are shown in Figs. 4.4~4.5 and Table 4.2 (note that their sum is one). Since the same set of soil hydraulic parameters was used in

all fractionation scenarios, the results of the spatial origin of RWU remained the same when using the water balance method.

According to the Mann-Kendall trend tests (Text S4.1 in the Supplementary Materials), the contribution ratios of the 0~10 cm soil layer showed a decreasing trend (characterized by negative τ values) with the largest fluctuations. The contribution ratios of the other soil layers showed increasing trends (suggested by positive τ values) and were relatively stable. In other words, the contribution of deep soil layers gradually increased but was still lower than the contribution of the first layer (Figs. 4.4~4.5). The mean contribution ratios decreased as soil depths increased from Layer 1 to Layer 4 (Table 4.2).

In general, considering fractionation (CG_Frac, TC_Frac) resulted in a decrease in the simulated contribution ratios of Layer 1 and an increase in ratios for the other soil layers (Table 4.2). Compared with CG_Frac, TC_Frac had higher contribution ratios for Layer 1 and lower contribution ratios for the other soil layers. Overall, the contribution ratios in the TC_Frac scenario were always between Non_Frac and CG_Frac for all soil layers. As seen in Table 4.2 (the last two columns), the effect of the temperature control played a dominant role in the contribution ratios of all soil layers to RWU.

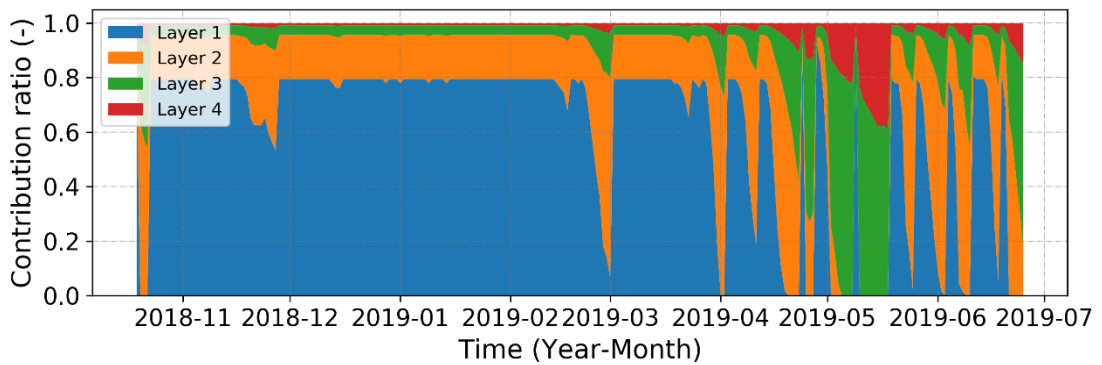


Figure 4.4. The contribution ratios of different soil layers (Layer 1, Layer 2, Layer 3, and Layer 4) to RWU calculated using the water balance (WB) method.

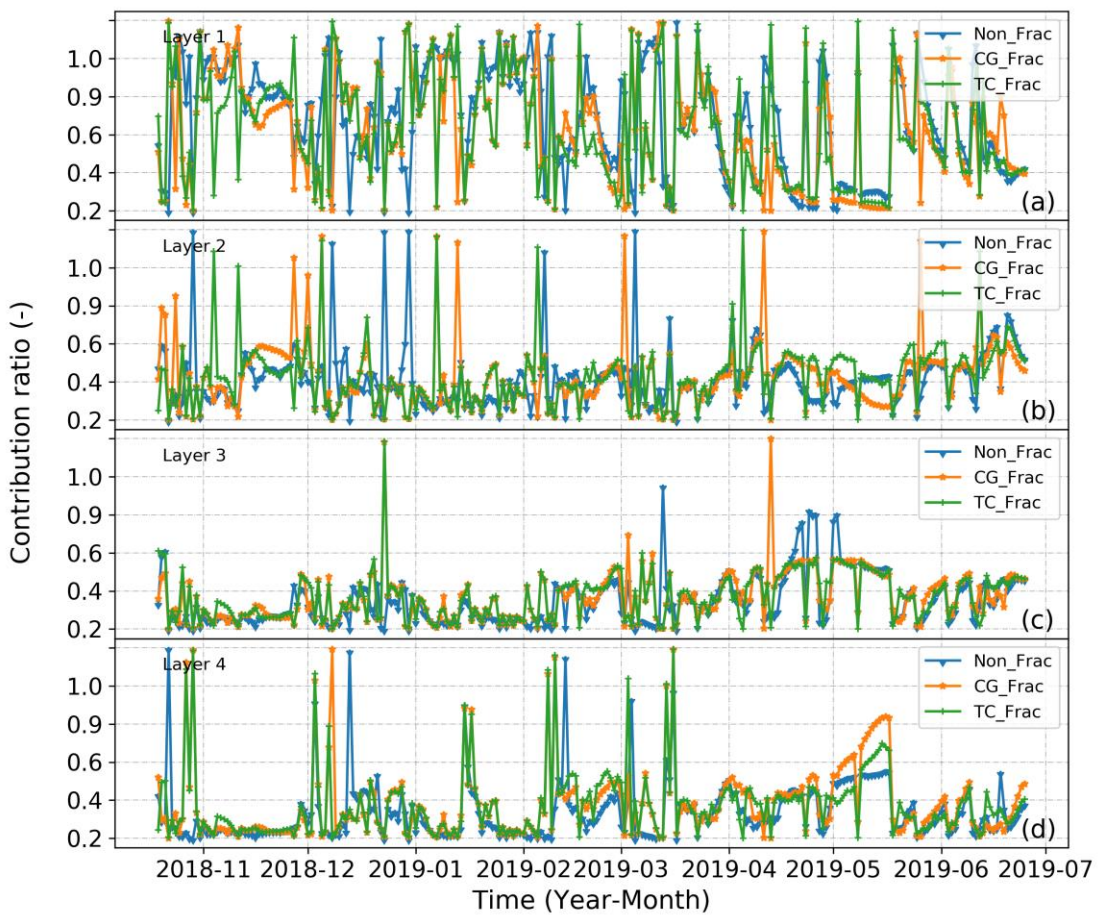


Figure 4.5. The contribution ratios of different soil layers (a - Layer 1, b - Layer 2, c - Layer 3, and d - Layer 4) to RWU for different fractionation scenarios (Non_Frac, CG_Frac, and TC_Frac) using the SIAR model.

Table 4.2. The average contribution ratios of different soil layers to RWU for different fractionation scenarios (Non_Frac, CG_Frac, and TC_Frac) based on the water balance (WB) and SIAR methods.

Method	Source	Non_Frac	CG_Frac	TC_Frac	CG_Frac relative to Non_Frac	TC_Frac relative to CG_Frac	TC_Frac relative to Non_Frac	Contribution of temp. control (%)	Contribution of tension control (%)
WB	Layer 1	0.603							
	Layer 2	0.240							
	Layer 3	0.123							
	Layer 4	0.035							
SIAR	Layer 1	0.493	0.426	0.444	-0.067	0.018	-0.049	79	21
	Layer 2	0.216	0.228	0.216	0.012	-0.012	0	50	50
	Layer 3	0.150	0.165	0.161	0.015	-0.004	0.011	79	21
	Layer 4	0.140	0.180	0.179	0.04	-0.001	0.039	98	2

4.3.3 Temporal Origin of RWU

Particle Tracking

Since the same set of parameters was used in all fractionation scenarios, the results of the temporal origin of RWU remained the same when using the particle tracking method. The residence time distribution of precipitation in soil water and the temporal origin of RWU showed seven cycles in the entire simulation period (Figs. 4.6a and 4.6b). Only the last 250 days (2018/10/18~2019/06/25) of the relative frequency distributions of drainage and RZ travel times (Figs. 4.6c and 4.6d) are displayed to be consistent with the display of the results of the isotope transport-based methods. During this period, the drainage travel times decreased with time (Fig. 4.6a). Water taken up by the roots during about November 2018 ~ April 2019 originated mainly from winter precipitation (November 2018 ~ March 2019) and during May and June of 2019 mainly

Virtual Tracer Experiment

Figs. 4.7~4.8 show that the drainage and RZ travel times (Fig 4.7d, Fig 4.8d) decreased when precipitation and the soil profile (or root zone) water storage (Fig. 4.7a and 4.7c, Fig. 4.8a and 4.8c) increased, and vice versa, despite some time lags. The maximum differences in drainage travel times were larger than in RZ travel times (197 and 18 days, respectively). The trends in drainage and RZ travel times evaluated by the virtual tracer experiment were similar to those obtained by particle tracking. The drainage travel times in general decreased with time (Fig. 4.7d). RZ travel times gradually increased during 2018/10/18~2019/05/18; although they were relatively stable during 2018/10/18~2019/03/09 and then decreased during 2019/05/19~2019/6/25 (Fig. 4.8d). The mean drainage travel times were 185.32, 183.78, and 183.95 days for the Non_Frac, CG_Frac, and TC_Frac scenarios, respectively (Fig. 4.7e~4.7g, Table 4.3). The mean RZ travel times were 3.93, 3.12, and 3.14 days for the Non_Frac, CG_Frac, and TC_Frac scenarios, respectively (Fig. 4.8e~4.8g, Table 4.3). The order of both drainage and RZ travel times was: Non_Frac > TC_Frac > CG_Frac.

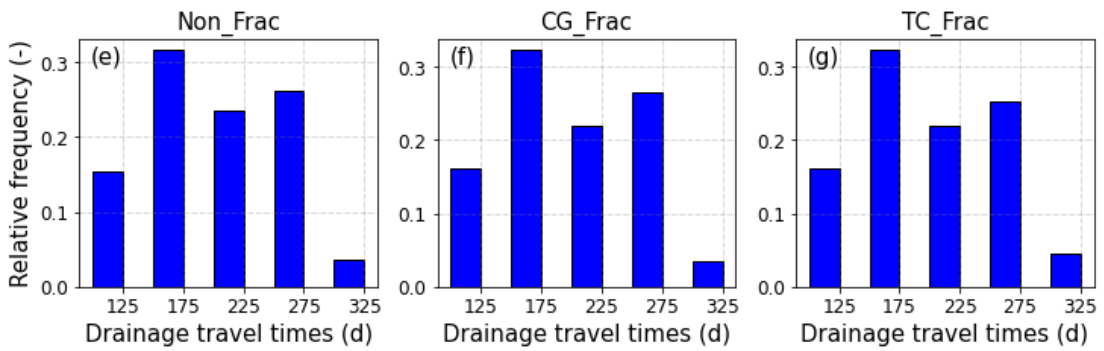
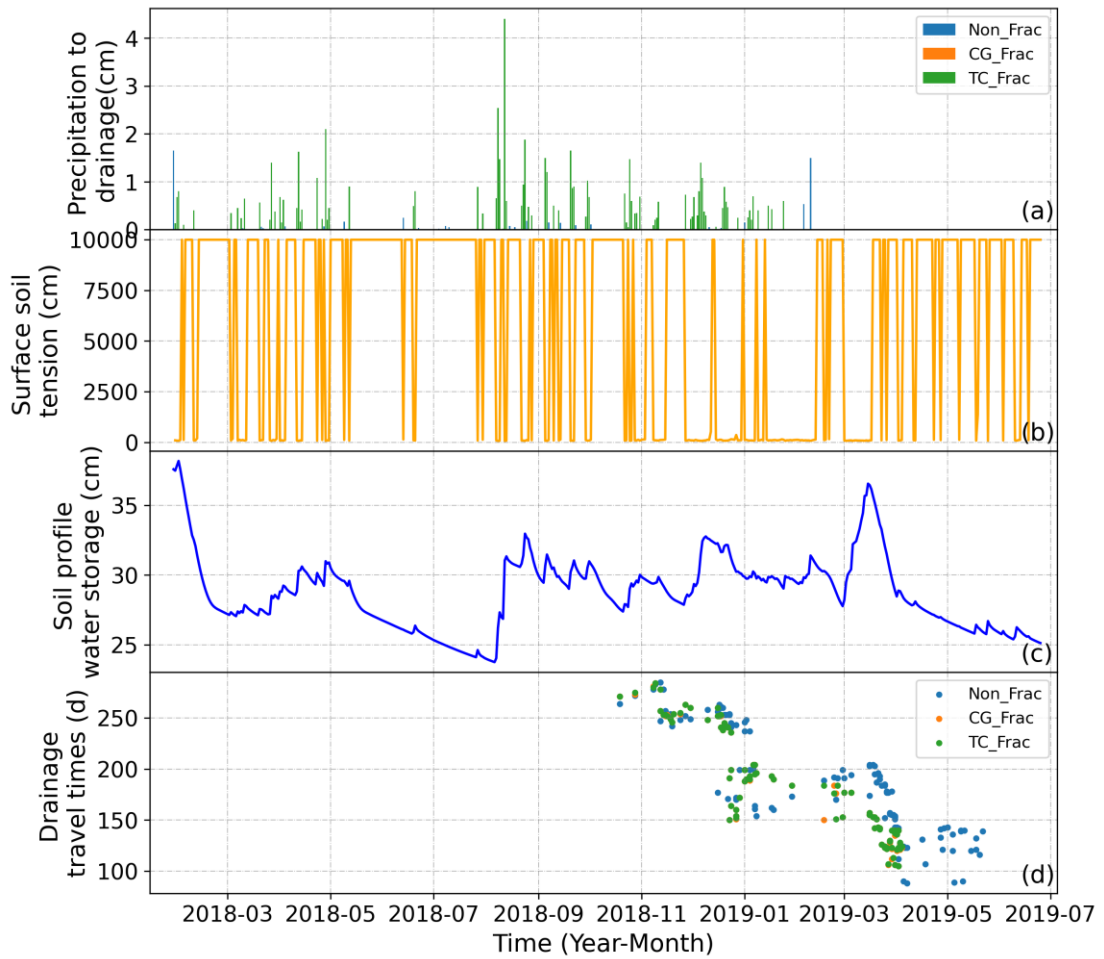


Figure 4.7. Precipitation (contributing to drainage) (a), surface soil tension (b), soil profile water storage (c), drainage travel times (d), and their relative frequency distributions (e~g) for different fractionation scenarios (Non_Frac, CG_Frac, and TC_Frac).

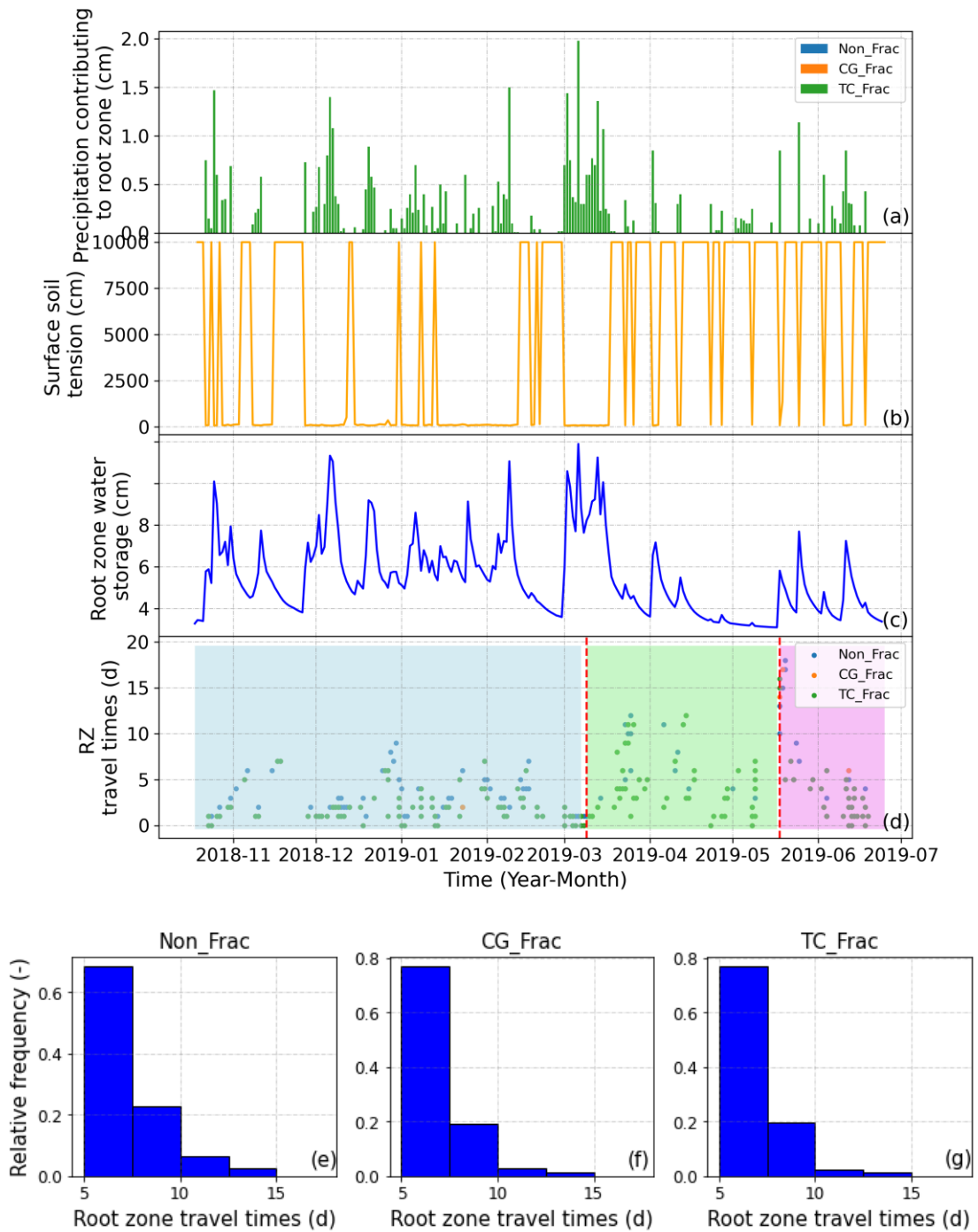


Figure 4.8. Precipitation (contributing to RWU) (a), surface soil tension (b), root zone water storage (c), root zone travel times (d), and their relative frequency distributions (e~g) for different fractionation scenarios (Non_Frac, CG_Frac, and TC_Frac). Note that the different background colors (blue, green, violet) represent the early (between about 2018/10/18~2019/03/09), middle (between about 2019/03/10~2019/05/18), and final (between about 2019/05/19~2019/06/25) stages, respectively, separated by vertical red dashed lines.

Table 4.3. The mean drainage and RZ travel times (TT) for different fractionation scenarios (Non_Frac, CG_Frac, and TC_Frac) based on particle tracking (PT) and virtual tracer experiment (VTE) methods.

Method	Term	Non_Frac	CG_Frac	TC_Frac	CG_Frac relative to Non_Frac	TC_Frac relative to CG_Frac	TC_Frac relative to Non_Frac	Contribution of temp. control (%)	Contribution of tension control (%)
PT	Drainage	193.10							
	TT								
	RZ TT	8.95							
VTE	Drainage	185.32	183.78	183.95	-1.54	0.17	-1.37	90	10
	TT								
	RZ TT	3.93	3.12	3.14	-0.81	0.02	-0.79	98	2

4.3.4 Isotope Mass Balance

Evaporation fractionation influences mostly the actual isotope flux across the soil surface ($cvTop$). The final cumulative value of the surface isotope flux [$cum(cvTop)$] was the lowest in the Non_Frac scenario, which implies that evaporation losses significantly decreased the downward isotope flux. In contrast, the two evaporation fractionation scenarios induced a lower isotope flux with evaporation, resulting in larger downward isotope fluxes across the soil surface. Therefore, evaporation fractionation also influences the isotope mass balance in terms of $cvRoot$ and $cvBot$. In the absence of fractionation (Non_Frac), roots absorbed less isotope mass. On the other hand, lower isotope loss through evaporation increased the isotope mass absorbed by roots ($cvRoot$) in the two fractionation scenarios, especially in CG_Frac. Similarly, the actual bottom isotope flux ($cvBot$) in the Non_Frac scenario was lower than those simulated in the other two fractionation scenarios. The isotope mass balances obtained in the three fractionation scenarios directly impact the assessment of the spatial and

temporal origin of RWU simulated using the SIAR mixing model and the virtual tracer experiment, respectively.

Table 4.4. The isotope mass balance components for different fractionation scenarios; *cvTop*, *cvRoot*, *cvBot*, and *cvTotChange* indicate actual isotope fluxes across the soil surface, across roots, across the bottom of the soil profile, and the total isotope removal, respectively. Note that the unit is ‰ ·cm/d. For the convenience of comparison, the Non_Frac scenario is taken as a reference and its value is set to 0 (by shifting). The values of other fractionation scenarios are also shifted correspondingly.

Terms	Non_Frac	CG_Frac	TC_Frac	CG_Frac	TC_Frac	TC_Frac	Contribution of temp. control (%)	Contribution of tension control (%)
				relative to Non_Frac	relative to CG_Frac	relative to Non_Frac		
Sum(<i>cvTop</i>)	0	2084.0	3331.0	2084.0	1247.0	3331.0	249	-149
Sum(<i>cvRoot</i>)	0	3392.3	1502.6	3392.3	-1889.7	1502.6	64	36
Sum(<i>cvBot</i>)	0	-15363.9	-9806.9	-15363.9	5557.0	-9806.9	73	27
Sum(<i>cvTotChange</i>)	0	-16672.2	-7978.5	-16672.2	8693.7	-7978.5	66	34

4.4 Discussion

4.4.1 Impacts of the Model Setup on Model Performance

The isotopic composition profiles (Fig. 4.3) and the statistical indicators (Table 4.1) show that the results of the CG_Frac and TC_Frac scenarios were quite similar and better than those of the Non_Frac scenario. This is because fractionation cannot be ignored in this example, as the dual-isotope plots show (Fig. 4 of Post et al., 2022).

The soil tension control on fractionation (the TC_Frac scenario) always resulted in a more depleted isotopic composition than the CG_Frac scenario, especially in the surface layer. This is because the total isotope removal in the TC_Frac is between

Non_Frac and CG_Frac (Table 4.4). Therefore, the isotopic composition is also between Non_Frac and TC_Frac scenarios (Fig. 4.3). The CG_Frac scenario fits the data best because the soil hydraulic and isotope transport parameters were optimized based on this scenario in Post et al. (2022).

The impact of considering the soil temperature control on evaporation fractionation and, consequently, on $RMSE_{wi}$ reached 91%, while the impact of considering the soil tension control on $RMSE_{wi}$ was 9% (Table 4.1). This suggests that considering the soil tension control on evaporation fractionation does not significantly impact the model performance, but considering the soil temperature control does.

4.4.2 Impacts of the Model Setup on the Spatial Origin of RWU

The two methods used to assess the spatial origin of RWU proved that the contribution ratios of the surface soil layer (0~10 cm soil depth) to RWU exhibited a decreasing trend with the largest fluctuations. In contrast the contribution ratios of deeper soil layers showed increasing trends and were less important but relatively more stable than those of the surface layer (Table 4.2 and Figs. 4.4~4.5). This is because the functioning of the top layer (0~10 cm) is different from the other layers as it is affected by evaporation fractionation during the dry season and mixing during precipitation (Barnes and Turner, 1998). The deeper soil layers gradually became more important water sources, probably due to the lack of rainfall (Fig. S4.2), which increased the root

water stress in the surface soil and promoted uptake from deeper layers. The contribution ratios decreased from Layer 1 to 4 because the root density decreases as soil depths increases (Fig. S4.1).

As discussed in Section 3.2, considering fractionation (CG_Frac, TC_Frac) likely resulted in a decrease in the contribution ratios of Layer 1 and an increase in the contribution ratios of the other soil layers (Table 4.2). The isotopic composition of surface soil water and RWU was higher in the fractionation scenarios (CG_Frac, TC_Frac) than in the Non_Frac scenario (Fig. S4.3). Therefore, a decrease in the contribution ratio of Layer 1 may suggest that an increased isotopic composition of surface soil water exceeded that of RWU in the fractionation scenarios.

The contribution ratios of all soil layers in the TC_Frac scenario were always between Non_Frac and CG_Frac. This is because the isotopic composition of soil water and RWU within the root zone in the TC_Frac scenario was always between Non_Frac and CG_Frac (Fig. 4.3 and Fig. S4.3). The contribution ratios of the same soil layer in the CG_Frac and TC_Frac scenarios were much more similar than in other combinations of any two scenarios (i.e., Non_Frac and CG_Frac, Non_Frac and TC_Frac). Table 4.2 (the last two columns) shows that the contribution of the temperature fractionation control also plays a dominant role in determining the spatial origin of RWU.

4.4.3 Impacts of the Model Setup on the Temporal Origin of RWU

During the early stage (between 2018/10/18~2019/03/09), the root zone (0~40 cm) water storage remained, on average, relatively high, with a mean of 2.53 cm and large fluctuations reflecting individual precipitation events (Fig. 4.8c). The RZ travel times were relatively stable with time (2.29, 2.02, and 2.01 days on average, with a range of 0~9, 0~7, and 0~7 days for the Non_Frac, CG_Frac, and TC_Frac, respectively) (Fig. 4.8d).

During the middle stage (between about 2019/03/10~2019/05/18), the root zone was drier (with mean water storage of 2.15 cm), increasing the root uptake stress, as discussed in Section 4.2. Therefore, the RZ travel times increased steeply with time (5.96, 4.60, and 4.65 days on average, with a range of 1~13, 0~15, and 0~16 days for the Non_Frac, CG_Frac, and TC_Frac, respectively) compared with the early stage.

During the final stage (between 2019/05/19~2019/6/25), the root zone water storage increased with time (with a mean of 2.11 cm), resulting in reduced RZ travel times (5.53, 3.27, and 2.81 days on average, with a range of 1~18, 0~17, and 0~7 days for the Non_Frac, CG_Frac, and TC_Frac, respectively).

During the first stage, the tension of the soil surface rarely reaches 10,000 cm (Fig. 4.8b), and travel time differences between different fractionation scenarios are relatively small. However, during the second and third stages, the soil surface tension

often reaches 10,000 cm, and somewhat larger differences in travel times occur between different fractionation scenarios.

The order of drainage and RZ travel times obtained using the isotope transport-based method (VTE) was: Non_Frac > TC_Frac > CG_Frac (Table 4.3). This is because the removal of isotopes by evaporation makes it difficult for isotopes to move downwards to the root zone or soil profile bottom and thus increases travel times. Since the isotope removal by evaporation was largest in the Non_Frac scenario, followed by TC_Frac and CG_Frac (Table 4.4), the travel time order was the same.

The drainage and RZ travel times in the CG_Frac and TC_Frac scenarios were much more similar than in any combination of two other scenarios. Table 4.3 (the last two columns) again indicates that the impact of the temperature control of fractionation again prevails over the tension control in identifying the temporal origin of RWU.

4.4.4 Comparison of the Water Flow and Isotope Transport-Based Methods

Regarding the spatial origin, all methods reflected the overall trends in contribution ratios of different soil layers. However, absolute differences always existed among different methods. The mean contribution ratios of the middle layers (Layers 2 and 3) were similar using both methods, while those of the shallow and deep layers (Layers 1 and 4) were quite different (Table 4.2). This is because the isotopic compositions of water sources were assumed to be arithmetic averages within the corresponding soil layers, which may not approximate reality. In addition, the spatial

origin of RWU can be reliably identified only when the isotopic composition profile gradient in the root zone is large and monotonic (Allen and Kirchner, 2022; Couvreur et al., 2020). However, considering the soil tension control resulted in a considerable change in surface isotopic compositions between different fractionation scenarios, and the “monotonic” characteristic of the root zone (0~40 cm) isotopic composition was clearly not fulfilled at least in the Non_Frac and TC_Frac scenarios (Fig. 4.3). This indicates that the appropriate model setup plays a vital role in ensuring the accurate identification of the spatial water origin when using the isotope transport-based methods.

Compared with the traditional in-situ isotopic measurements, the isotopic compositions of soil water and RWU in this study were obtained directly from the model output, alleviating the measurement burden and achieving higher spatial-temporal resolution (Stumpp et al., 2018). This is useful since the isotopic measurements are often compromised by several factors, especially under arid conditions, such as sampling spatial-temporal representativeness, instrument deficiencies, etc. (Beyer and Penna, 2021). On the other hand, in this study, we directly used the isotope composition of root water uptake instead of xylem water. This can avoid the uncertainty of isotopic composition changes during the water movement from the roots to the xylem (Allen and Kirchner, 2022; Barbeta et al., 2020; Chen et al., 2020).

Regarding the temporal origin, all methods revealed the overall variation trends with time and relative differences in drainage and RZ travel times between different fractionation scenarios. However, absolute differences always existed among different methods and were more significant for RWU than drainage travel times (Table 4.3). This is because the impact of hydrodynamic dispersion may affect the virtual tracer experiment, which the particle tracking module neglects. This may lead to apparent differences between the two methods. Larger differences in the RZ travel times compared to the drainage travel times between the particle tracking and virtual tracer experiment methods, was likely due to the longer travel distance for the latter. Therefore, the impact of dispersion is much smaller on RWU. In addition, outside factors make it easier to disturb the dynamic balance between upward evaporation, downward infiltration, and dispersion in the root zone since it is closer to the soil surface.

Overall, the influencing factors and applicable conditions of isotope transport-based methods (SIAR, virtual tracer experiment) are more complex and demanding than water flow-based (water balance, particle tracking) methods. However, in this study, both are based on numerical modeling results characterized by the equifinality problem (Beven, 2006). Therefore, it is hard to judge which one is better. On the one hand, the simultaneous use of the water flow and isotope transport-based methods may be a good way to provide mutual validation. On the other hand, the accuracy of these two methods should be verified by other benchmark methods, such as direct water

balance measurements, artificial labeling tracers (Benettin et al., 2019; Seeger and Weiler, 2021) or tracer-based water balance analysis (Benettin et al., 2021).

4.4.5 Implications for the Langeoog Island Groundwater Recharge

To quantify the impact of vegetation change on groundwater recharge, we also calculated the drainage travel times assuming there were no plants and no RWU (Fig. S4.5). The mean drainage travel time during the last 250 days of the simulation period was 164.7 days (compared to 193.1 days in Table 4.3 when RWU was considered). Groundwater recharge fluxes (assuming them equal to deep drainage) during this period in scenarios with and without RWU were 31.30 and 34.6 cm, respectively. In other words, because of the vegetation change, groundwater recharge decreased by 9.5% (note that a decrease in groundwater recharge caused by RWU was also reported by Post et al. (2022)), while drainage travel times increased by 17.2%.

This phenomenon was also witnessed in many studies in inland areas (Kim and Jackson, 2012; Liu et al., 2022; Oliveira et al., 2017; Scanlon et al., 2005). However, for coastal areas like Langeoog island, decreased groundwater recharge (due to longer travel times of precipitation through the root zone) may increase seawater intrusion risks (Strack et al., 2016). This is more threatening under increased sea level rise (about 1.1 mm/yr) induced by climate change (Behre, 2012; Bungenstock and Schafer, 2009).

4.4.6 Model Limitations and Future Work

Three isotope-enabled transport models are available in HYDRUS-1D: *i*) the original one (Stumpp et al., 2012) is suitable when fractionation is negligible; *ii*) the module introduced by Zhou et al. (2021) considers the soil temperature control on equilibrium fractionation; *iii*) the new module presented in this study considers also the soil tension control on equilibrium fractionation. However, the soil tension control on equilibrium fractionation is described using empirical equations (Eqs. 4.5~4.6). It may be possible to replace it with physically-based equations once discovered in the future.

In this study, we investigated the impact of considering the soil tension control on model performance and practical applications using the field dataset collected in a humid region. To assess the possible impact of the soil tension control on equilibrium fractionation under various temperature and soil tension conditions, we carried out a sensitivity analysis by plotting $\alpha_{v/w}$ vs. soil temperature (from 0°C to 45°C, i.e., from 273.15K to 318.15K) and tension (1,284 cm, 2,500 cm, 5,000 cm, 10,000 cm) in Fig. 4.9a~4.9b. We also calculated the contribution of the tension control to $\alpha_{v/w}$ (Fig. 4.9c~4.9d), or to isotope removal by evaporation if we only consider E_i^{out} (i.e.,

$$\frac{E_a}{\alpha_i^k} \frac{M_i}{M_w} \frac{(RH_s \cdot \alpha_{v/w} \cdot RL)}{RH_s - RH_{a'}}$$
 in Eq. 4.1.

Figs. 4.9c~4.9d show that the contribution of the soil tension control decreases as temperature increases and is always lower than 6.5% and 2.5% for ^2H and ^{18}O , respectively. This is because $\alpha_{v/w} \left(\frac{^2\text{H}}{^1\text{H}} \right)_{majoube}$ increases as temperature

increases (Eqs. 4.3~4.4). Overall, the soil tension control has a higher impact on $\alpha_{v/w}$ of ^2H than ^{18}O .

Figs. 4.9a~4.9b illustrates that $\alpha_{v/w}$ increases up to 1.003 for ^2H and 1.016 for ^{18}O under very dry conditions when the soil temperature is 318.15 K (45 °C) and the soil tension is 10,000 cm. This is 0.060 and 0.024 higher than the temperature control alone (0.943 for ^2H and 0.992 for ^{18}O). However, this small change in $\alpha_{v/w}$ may be significant for evaporation fractionation. Specifically, with only the temperature control, there is only -5.7% (i.e., 0.943-1) and -0.8% (i.e., 0.992-1) less isotope removal than in the Non_Frac scenario for ^2H and ^{18}O , respectively. However, combined with the tension control, there is 0.3% (i.e., 1.003-1) and 1.6% (i.e., 1.016-1) more isotope removal compared with the Non_Frac scenario for ^2H and ^{18}O , respectively.

This change in isotope removal may result in a considerable difference in isotopic composition. For example, in this study, the surface soil tension often reached 10,000 cm (Fig. 4.7b and Fig. 4.8b), the temperature was between 265.65 and 306.65 K (-7.5 to 33.5 °C), and the surface isotopic composition in the TC_Frac changed by -3.25‰ (for ^2H) and -1.25‰ (for ^{18}O) compared to CG_Frac scenario. In addition, as discussed in Sections 4.4.2 and 4.4.3, these isotopic composition differences also propagated into practical applications albeit in limited magnitude. However, the extent of the isotopic composition change and subsequent errors in practical applications

depends on specific experimental conditions and needs further exploration, especially for arid regions (Allen and Kirchner, 2022; Finkenbiner et al., 2022).

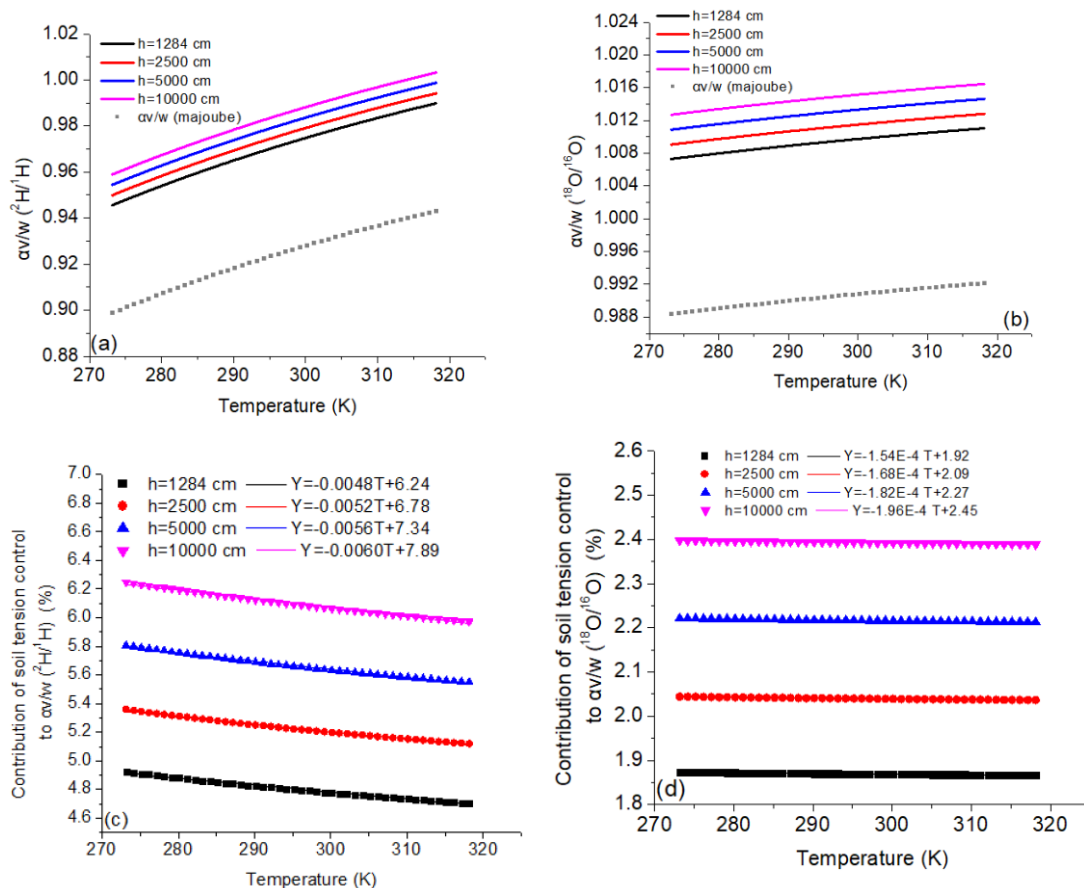


Figure 4.9. The relationship between $\alpha_{v/w}$ (a~b) and contribution of soil tension control (c~d) vs. soil temperature and tension for ^2H (left) and ^{18}O (right) isotopes.

4.5 Summary and Conclusions

In this study, we first quantified the impact of the soil temperature and tension evaporation fractionation on model performance in HYDRUS-1D. The results showed that additional consideration of the soil tension control depletes the surface isotopic composition more than when only the temperature control is considered. The effect of

soil temperature on evaporation fractionation is significantly larger than that of soil tension.

Regarding the spatial origin of root water uptake (RWU), all methods could reflect the overall variation trends of different soil layers. The contribution ratios of all soil layers in the TC_Frac scenarios were always between Non_Frac and CG_Frac. The average contribution ratios of the middle soil layers were similar using both methods, while those of the top and deep layers were quite different.

Regarding the temporal origin of RWU, all methods could reflect the overall variation trends in drainage and root zone (RZ) travel times. The order of both drainage and RZ travel times was: Non_Frac > TC_Frac > CG_Frac. Absolute differences between different methods always existed and were more significant in RWU than drainage travel times.

Overall, considering the soil temperature effect on evaporation fractionation, rather than soil tension, is important in determining the spatial-temporal origin of RWU. The results obtained using the isotope transport-based methods for different fractionation scenarios are very similar. The influencing factors and applicable conditions of isotope transport-based methods (SIAR, virtual tracer experiment) are more complex and demanding than water flow-based methods (water balance, particle tracking). However, the accuracy of these two methods needs to be further verified by other benchmark methods.

This study emphasizes the necessity of selecting a suitable model setup and the simultaneous employment of the water flow and isotope transport-based methods to secure reliable isotopic data interpretation. This study sheds light on future experimental designs regarding the practical applications of isotope transport modeling. However, the impacts of the soil tension control on isotope transport and practical applications should be further explored under arid conditions where soil tension is higher, and thus the impact of the tension control is expected to be more important.

References

- Allen, S.T., J.W. Kirchner, S. Braun, R.T.W. Siegwolf, and G.R. Goldsmith, Seasonal origins of soil water used by trees, *Hydrology and Earth System Sciences*, 23(2), pp. 1199-1210, doi:10.5194/hess-23-1199-2019, 2019.
- Asadollahi, M., C. Stumpp, A. Rinaldo, and P. Benettin, Transport and Water Age Dynamics in Soils: A Comparative Study of Spatially Integrated and Spatially Explicit Models, *Water Resources Research*, 56(3), pp. 17, doi:10.1029/2019wr025539, 2020.
- Barnes, C.J., and J.V. Turner, Isotopic exchange in soil water, *Isotope tracers in catchment hydrology*, pp. 137-163, 1998.
- Behre, K.E., Reconstructing middle to late Holocene sea-level change: A methodological review with particular reference to "A new Holocene sea-level curve for the southern North Sea" presented by K.-E. Behre': *Comments, Boreas*, 41(2), pp. 308-314, doi:10.1111/j.1502-3885.2011.00242.x, 2012.
- Benettin, P., A. Rinaldo, and G. Botter, Tracking residence times in hydrological systems: forward and backward formulations, *Hydrological Processes*, 29(25), pp. 5203-5213, doi:10.1002/hyp.10513, 2015.
- Beven, K., A manifesto for the equifinality thesis, *Journal of Hydrology*, 320(1-2), pp. 18-36, doi:10.1016/j.jhydrol.2005.07.007, 2006.
- Beyer, M., and D. Penna, On the Spatio-Temporal Under-Representation of Isotopic Data in Ecohydrological Studies, *Front. Water*, 3, pp. 9, doi:10.3389/frwa.2021.643013, 2021.
- Brinkmann, N., S. Seeger, M. Weiler, N. Buchmann, W. Eugster, and A. Kahmen, Employing stable isotopes to determine the residence times of soil water and the temporal origin of water taken up by *Fagus sylvatica* and *Picea abies* in a temperate forest, *New Phytologist*, 219(4), pp. 1300-1313, doi:10.1111/nph.15255, 2018.

- Bungenstock, F., and A. Schafer, The Holocene relative sea-level curve for the tidal basin of the barrier island Langeoog, German Bight, Southern North Sea, *Glob. Planet. Change*, 66(1-2), pp. 34-51, doi:10.1016/j.gloplacha.2008.07.007, 2009.
- Chen, G., K. Auerswald, and H. Schnyder, H-2 and O-18 depletion of water close to organic surfaces, *Biogeosciences*, 13(10), pp. 3175-3186, doi:10.5194/bg-13-3175-2016, 2016.
- Corneo, P.E., M.A. Kertesz, S. Bakhshandeh, H. Tahaei, M.M. Barbour, and F.A. Dijkstra, Studying root water uptake of wheat genotypes in different soils using water delta O-18 stable isotopes, *Agriculture Ecosystems & Environment*, 264, pp. 119-129, doi:10.1016/j.agee.2018.05.007, 2018.
- Couvreur, V., Y. Rothfuss, F. Meunier, T. Bariac, P. Biron, J.L. Durand, P. Richard, and M. Javaux, Disentangling temporal and population variability in plant root water uptake from stable isotopic analysis: when rooting depth matters in labeling studies, *Hydrology and Earth System Sciences*, 24(6), pp. 3057-3075, doi:10.5194/hess-24-3057-2020, 2020.
- Craig, H., Isotopic variations in meteoric waters, *Science*, 133(346), pp. 1702-1703, doi:10.1126/science.133.3465.1702, 1961.
- Craig, H., and L. Gordon, Deuterium and oxygen 18 variations in the ocean and the marine atmosphere, *Stable Isotopes in Oceanographic Studies and Paleotemperatures E*, Proceedings of the Third Spoleto Conference, Spoleto, Italy, pp. 9-130, 1965.
- Dawson, T.E., and J.R. Ehleringer, Streamside trees that do not use stream water, *Nature*, 350(6316), pp. 335-337, 1991.
- Gaj, M., and J.J. McDonnell, Possible soil tension controls on the isotopic equilibrium fractionation factor for evaporation from soil, *Hydrological Processes*, 33(11), pp. 1629-1634, doi:10.1002/hyp.13418, 2019.
- Harman, C.J., Time-variable transit time distributions and transport: Theory and application to storage-dependent transport of chloride in a watershed, *Water Resources Research*, 51(1), pp. 1-30, doi:10.1002/2014wr015707, 2015.

- Houben, G.J., P. Koeniger, and J. Sultenfuss, Freshwater lenses as archive of climate, groundwater recharge, and hydrochemical evolution: Insights from depth-specific water isotope analysis and age determination on the island of Langeoog, Germany, *Water Resources Research*, 50(10), pp. 8227-8239, doi:10.1002/2014wr015584, 2014.
- Kim, J.H., and R.B. Jackson, A Global Analysis of Groundwater Recharge for Vegetation, Climate, and Soils, *Vadose Zone Journal*, 11(1), pp. 35, doi:10.2136/vzj2011.0021RA, 2012.
- Knighton, J., S.M. Saia, C.K. Morris, J.A. Archiblad, and M.T. Walter, Ecohydrologic considerations for modeling of stable water isotopes in a small intermittent watershed, *Hydrological Processes*, 31(13), pp. 2438-2452, doi:10.1002/hyp.11194, 2017.
- Lin, Y., and J. Horita, An experimental study on isotope fractionation in a mesoporous silica-water system with implications for vadose-zone hydrology, *Geochimica Et Cosmochimica Acta*, 184, pp. 257-271, doi:10.1016/j.gca.2016.04.029, 2016.
- Lin, Y., J. Horita, and O. Abe, Adsorption isotope effects of water on mesoporous silica and alumina with implications for the land-vegetation-atmosphere system, *Geochimica Et Cosmochimica Acta*, 223, pp. 520-536, doi:10.1016/j.gca.2017.12.021, 2018.
- Lipovetsky, T., L.W. Zhuang, W.G. Teixeira, A. Boyd, E.M. Pontedeiro, L. Moriconi, J.L.D. Alves, P. Couto, and M.T. van Genuchten, HYPROP measurements of the unsaturated hydraulic properties of a carbonate rock sample, *Journal of Hydrology*, 591, pp. 7, doi:10.1016/j.jhydrol.2020.125706, 2020.
- Liu, X.P., Y.H. He, S.S. Sun, T.H. Zhang, Y.Q. Luo, L.M. Zhang, M.M. Wang, L. Cheng, H.J. Hu, and Y.Z. Xu, Restoration of sand-stabilizing vegetation reduces deep percolation of precipitation in semi-arid sandy lands, northern China, *Catena*, 208, pp. 9, doi:10.1016/j.catena.2021.105728, 2022.
- Ma, Y., and X.F. Song, Using stable isotopes to determine seasonal variations in water uptake of summer maize under different fertilization treatments, *Science of the Total Environment*, 550, pp. 471-483, doi:10.1016/j.scitotenv.2016.01.148, 2016.

- Majoube, M., Oxygen-18 and deuterium fractionation between water and steam, *Journal of Chemical Physics*, 68(10), pp. 1423-1436, doi:10.1051/jcp/1971681423, 1971.
- Maloszewski, P., S. Maciejewski, C. Stumpp, W. Stichler, P. Trimborn, and D. Klotz, Modelling of water flow through typical Bavarian soils: 2. Environmental deuterium transport, *Hydrological Sciences Journal*, 51(2), pp. 298-313, doi:10.1623/hysj.51.2.298, 2006.
- Martin-Gomez, P., L. Serrano, and J.P. Ferrio, Short-term dynamics of evaporative enrichment of xylem water in woody stems: implications for ecohydrology, *Tree Physiology*, 37(4), pp. 511-522, doi:10.1093/treephys/tpw115, 2017.
- Miguez-Macho, G., and Y. Fan, Spatiotemporal origin of soil water taken up by vegetation, *Nature*, 598(7882), pp. 624+, doi:10.1038/s41586-021-03958-6, 2021.
- Nasta, P., G. Bonanomi, J. Šimůnek, and N. Romano, Assessing the nitrate vulnerability of shallow aquifers under Mediterranean climate conditions, *Agricultural Water Management*, 258, pp. 12, doi:10.1016/j.agwat.2021.107208, 2021.
- Oerter, E., K. Finstad, J. Schaefer, G.R. Goldsmith, T. Dawson, and R. Amundson, Oxygen isotope fractionation effects in soil water via interaction with cations (Mg, Ca, K, Na) adsorbed to phyllosilicate clay minerals, *Journal of Hydrology*, 515, pp. 1-9, doi:10.1016/j.jhydrol.2014.04.029, 2014.
- Oliveira, P.T.S., M.B. Leite, T. Mattos, M.A. Nearing, R.L. Scott, R.D. Xavier, D.M.D. Matos, and E. Wendland, Groundwater recharge decrease with increased vegetation density in the Brazilian cerrado, *Ecohydrology*, 10(1), pp. 8, doi:10.1002/eco.1759, 2017.
- Parnell, A.C., R. Inger, S. Bearhop, and A.L. Jackson, Source Partitioning Using Stable Isotopes: Coping with Too Much Variation, *Plos One*, 5(3), pp. 5, doi:10.1371/journal.pone.0009672, 2010.
- Post, V.E.A., and G.J. Houben, Density-driven vertical transport of saltwater through the freshwater lens on the island of Baltrum (Germany) following the 1962 storm flood, *Journal of Hydrology*, 551, pp. 689-702, doi:10.1016/j.jhydrol.2017.02.007, 2017.

- Post, V.E.A., T. Zhou, C. Neukum, P. Koeniger, G.J. Houben, A. Lamparter, and J. Šimůnek, Estimation of groundwater recharge rates using soil-water isotope profiles: a case study of two contrasting dune types on Langeoog Island, Germany, *Hydrogeology Journal*, 30(3), pp. 797-812, doi:10.1007/s10040-022-02471-y, 2022.
- Rinaldo, A., P. Benettin, C.J. Harman, M. Hrachowitz, K.J. McGuire, Y. van der Velde, E. Bertuzzo, and G. Botter, Storage selection functions: A coherent framework for quantifying how catchments store and release water and solutes, *Water Resources Research*, 51(6), pp. 4840-4847, doi:10.1002/2015wr017273, 2015.
- Rothfuss, Y., and M. Javaux, Reviews and syntheses: Isotopic approaches to quantify root water uptake: a review and comparison of methods, *Biogeosciences*, 14(8), pp. 2199-2224, doi:10.5194/bg-14-2199-2017, 2017.
- Scanlon, B.R., R.C. Reedy, D.A. Stonestrom, D.E. Prudic, and K.F. Dennehy, Impact of land use and land cover change on groundwater recharge and quality in the southwestern US, *Glob. Change Biol.*, 11(10), pp. 1577-1593, doi:10.1111/j.1365-2486.2005.01026.x, 2005.
- Seeger, S., and M. Weiler, Temporal dynamics of tree xylem water isotopes: in situ monitoring and modeling, *Biogeosciences*, 18(15), pp. 4603-4627, doi:10.5194/bg-18-4603-2021, 2021.
- Šimůnek, J., Numerical simulation of the transport processes in soil (in Czech, English abstract), *Vodohosp. Čas.*, 39(1), pp. 20-34, 1991.
- Sprenger, M., C. Stumpp, M. Weiler, W. Aeschbach, S.T. Allen, P. Benettin, M. Dubbert, A. Hartmann, M. Hrachowitz, J.W. Kirchner, J.J. McDonnell, N. Orłowski, D. Penna, S. Pfahl, M. Rinderer, N. Rodriguez, M. Schmidt, and C. Werner, The Demographics of Water: A Review of Water Ages in the Critical Zone, *Reviews of Geophysics*, 57(3), pp. 800-834, doi:10.1029/2018rg000633, 2019.
- Strack, O.D.L., L. Stoeckl, K. Damm, G. Houben, B.K. Ausk, and W.J. de Lange, Reduction of saltwater intrusion by modifying hydraulic conductivity, *Water Resources Research*, 52(9), pp. 6978-6988, doi:10.1002/2016wr019037, 2016.

- Stumpp, C., N. Bruggemann, and L. Wingate, Stable isotope approaches in vadose zone research, *Vadose Zone Journal*, 17(1), doi:10.2136/vzj2018.05.0096, 2018.
- Stumpp, C., and P. Maloszewski, Quantification of preferential flow and flow heterogeneities in an unsaturated soil planted with different crops using the environmental isotope delta O-18, *Journal of Hydrology*, 394(3-4), pp. 407-415, doi:10.1016/j.jhydrol.2010.09.014, 2010.
- Tetzlaff, D., C. Birkel, J. Dick, J. Geris, and C. Soulsby, Storage dynamics in hydrogeological units control hillslope connectivity, runoff generation, and the evolution of catchment transit time distributions, *Water Resources Research*, 50(2), pp. 969-985, doi:10.1002/2013wr014147, 2014.
- Timbe, E., D. Windhorst, P. Crespo, H.G. Frede, J. Feyen, and L. Breuer, Understanding uncertainties when inferring mean transit times of water through tracer-based lumped-parameter models in Andean tropical montane cloud forest catchments, *Hydrology and Earth System Sciences*, 18(4), pp. 1503-1523, doi:10.5194/hess-18-1503-2014, 2014.
- Zhang, Y.Y., S.X. Wu, W.R. Kang, and Z.H. Tian, Multiple sources characteristics of root water uptake of crop under oasis farmlands in hyper-arid regions, *Agricultural Water Management*, 271, pp. 8, doi:10.1016/j.agwat.2022.107814, 2022.
- Zhou, T., J. Šimůnek, and I. Braud, Adapting HYDRUS-1D to simulate the transport of soil water isotopes with evaporation fractionation, *Environ. Modell. Softw.*, 143, pp. 105118, doi:https://doi.org/10.1016/j.envsoft.2021.105118, 2021.
- Zhou, T., J. Šimůnek, I. Braud, P. Nasta, G. Brunetti, and Y. Liu, The impact of evaporation fractionation on the inverse estimation of soil hydraulic and isotope transport parameters, *Journal of Hydrology*, 612, pp. 128100, doi:https://doi.org/10.1016/j.jhydrol.2022.128100, 2022.

Supplementary Materials

Figures

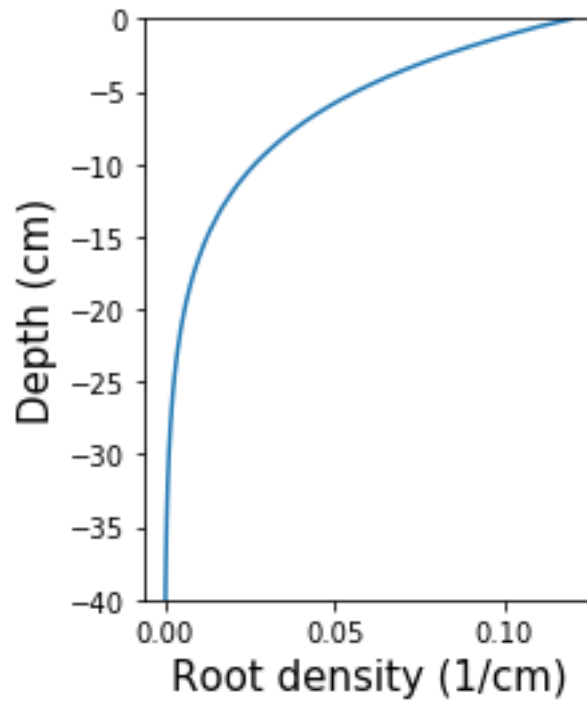


Figure S4.1. The root density profile.

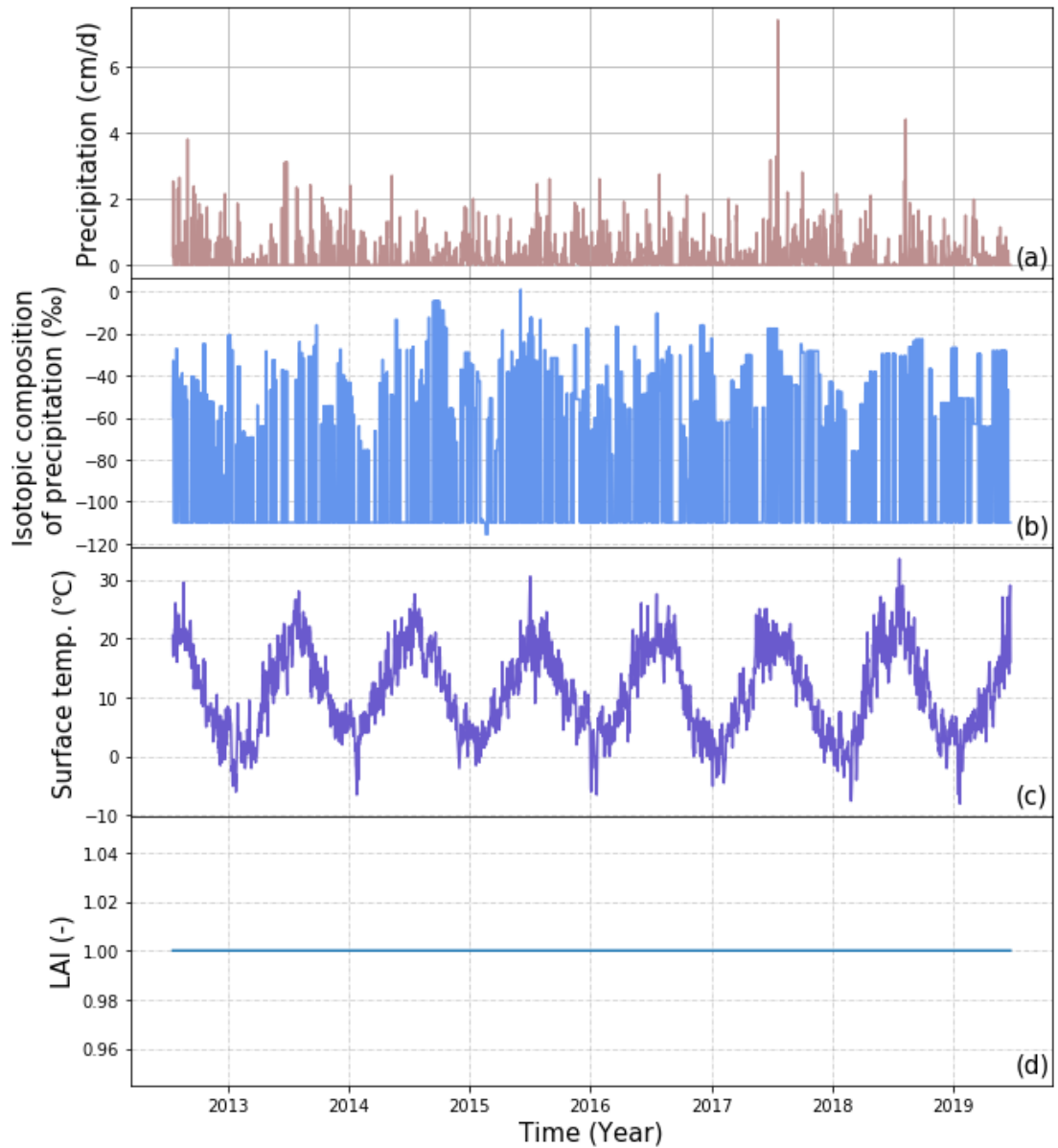
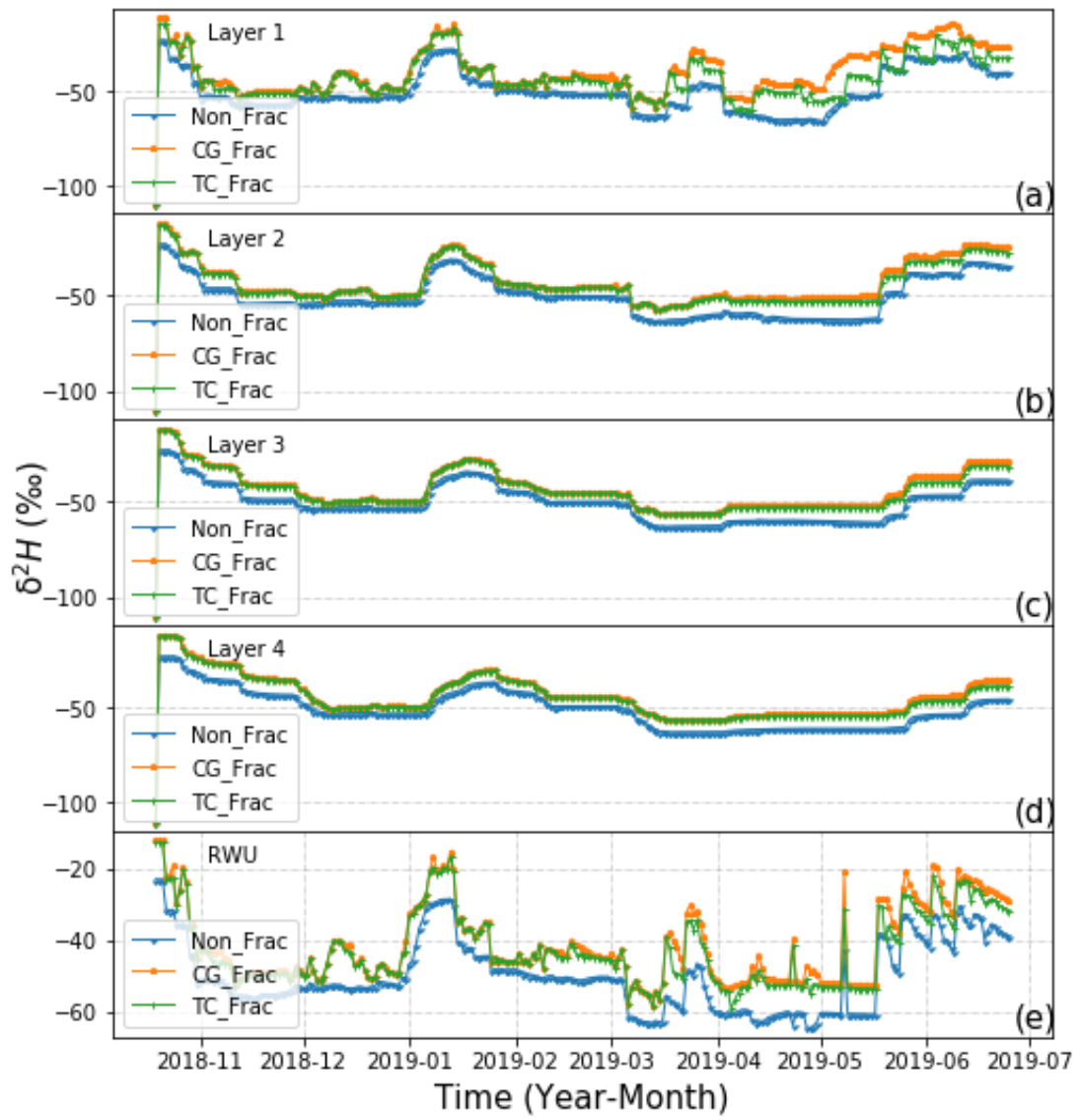


Figure S4.2. The temporal distribution of precipitation (a), the isotopic composition of precipitation (b), soil surface temperature (T_s) (c), and leaf area index (LAI) (d) during the simulation period.



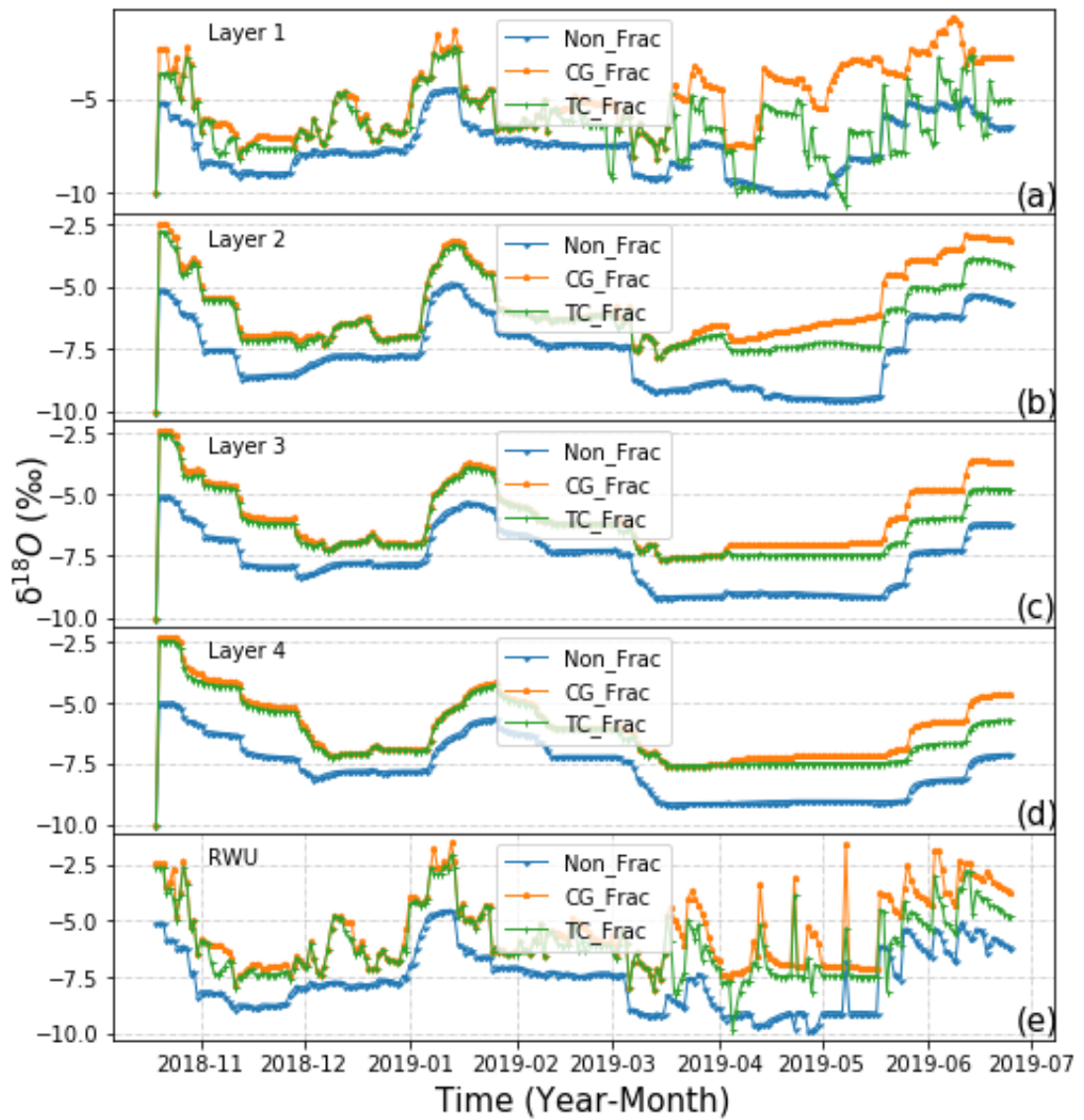


Figure S4.3. Simulated $\delta^2\text{H}$ (top graph) and $\delta^{18}\text{O}$ (bottom graph) of different soil layers (a, b, c, and d for Layer 1, 2, 3, and 4, respectively) and RWU (e) for different fractionation scenarios (Non_Frac, CG_Frac, and TC_Frac).

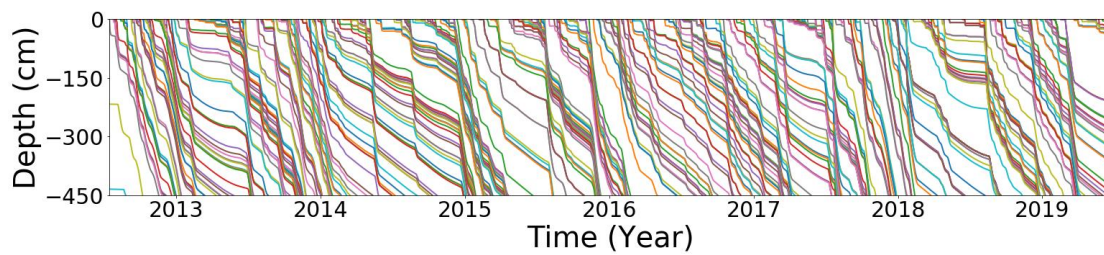


Figure S4.4. Particle trajectories (with root water uptake).

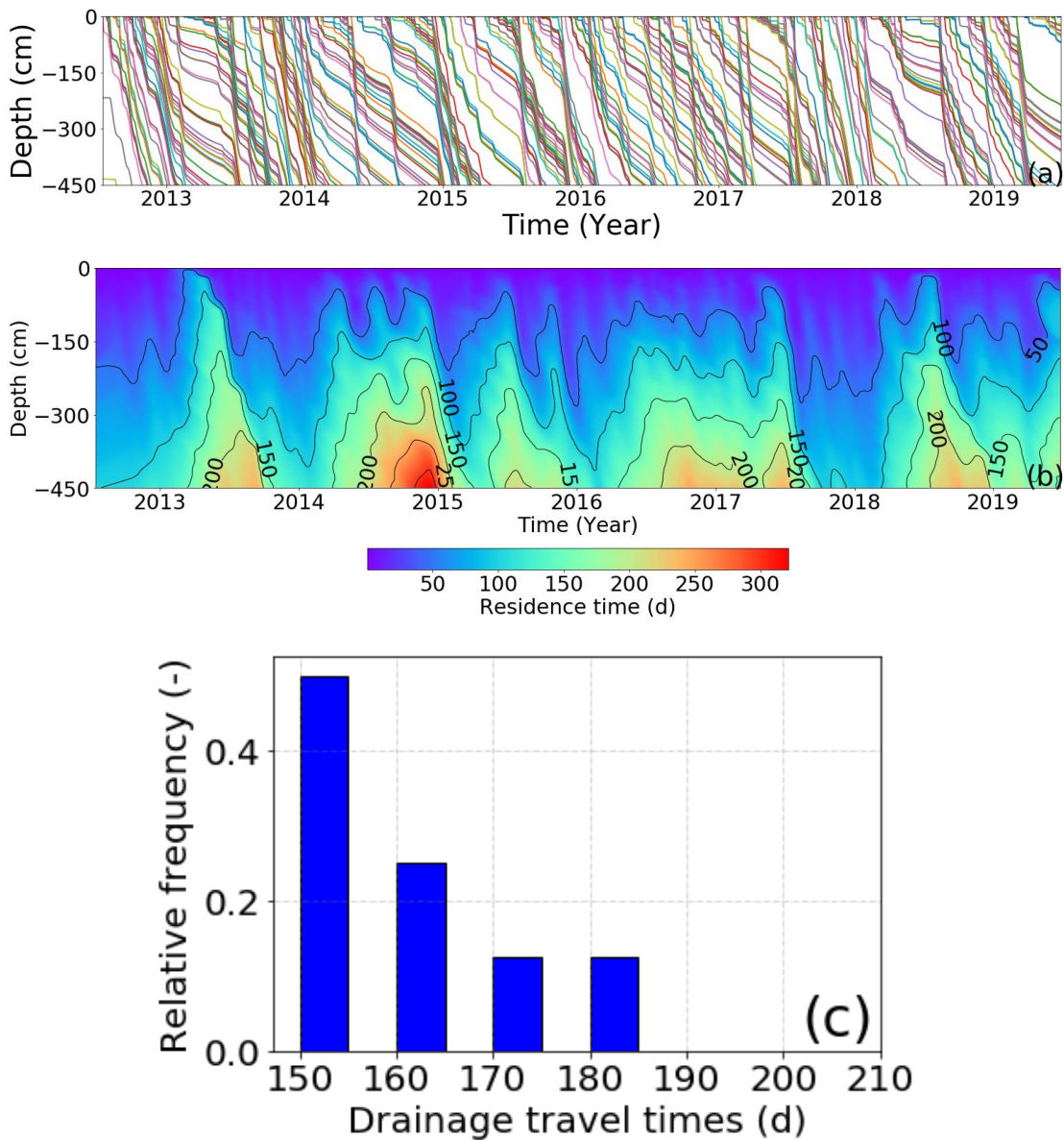


Figure S4.5. The particle trajectories (a), spatial distribution of residence times plotted versus time (b), and relative frequency distributions of drainage travel times (c) when there is no root water uptake. Note that only the travel times from the last 250 days are displayed in the graphs of relative frequency distributions.

Tables

Table S4.1. Descriptions of variables in Fig. 4.2.

Variable	Description
$C_p(\theta_l), C_w$	Volumetric heat capacities of the porous medium and the liquid phase, respectively [$\text{ML}^{-1}\text{T}^{-2}\text{K}^{-1}$]
C_i^l	Isotope concentrations of soil water (kg m^{-3})
D_i^{l*}	Effective dispersion coefficient of the isotope i in soil water [L^2T^{-1}]
D_i^{l0}	Molecular diffusion coefficient of isotope i in free water [L^2T^{-1}]
E_a	Actual evaporation [L/T]
ET_0	Potential evapotranspiration [L/T]
h	Water pressure head [L]
K_{Lh}	Isothermal hydraulic conductivity of the liquid phase [L/T]
K_s	Saturated hydraulic conductivity [L/T]
LAI	Leaf area index [-]
n, α	Shape parameters of the VG model [-]
P	Precipitation rate [L/T]
Q	Drainage or discharge [L/T]
q_l	Liquid water flux [L/T]
RH	Air relative humidity [-]
S	Sink term [L/T]
t	Time [T]
T_{air}	Air temperature ($^{\circ}\text{C}$)
T_b	Soil bottom temperature ($^{\circ}\text{C}$)
T_s	Soil surface temperature ($^{\circ}\text{C}$)
z	Spatial coordinate (positive upward) [L]
ω	Angle between the flow direction and the vertical axis [-]
δ_A	Isotopic composition of the atmospheric water vapor (‰)
δ_P	Isotopic composition of precipitation (‰)
θ_l	Liquid volumetric water content [L^3/L^3]
θ_r	Residual water content [L^3/L^3]
θ_s	Saturated water content [L^3/L^3]
λ	Longitudinal dispersivity [L]
$\lambda(\theta_l)$	Coefficient of the apparent thermal conductivity of the soil [$\text{MLT}^{-3}\text{K}^{-1}$]

Result S4.1 Mann-Kendall Trend Tests

The Mann-Kendall trend test is used to determine whether there is a trend in the time series of contribution ratios of different water sources. When the p -value of the test is below a certain significance level, there is a statistically significant trend in the investigated time series.

Water balance method

Source 1: $\tau=-0.263, p=5.237e-10$

Source 2: $\tau=0.113, p=0.008$

Source 3: $\tau=0.327, p=1.354e-14$

Source 4: $\tau=0.346, p=4.441e-16$

SIAR model

Non_Frac

Source 1: $\tau = -0.213, p = 5.3348e-07$

Source 2: $\tau = 0.127, p = 0.0027856$

Source 3: $\tau = 0.284, p = < 2.22e-16$

Source 4: $\tau = 0.209, p = 8.3447e-07$

CG_Frac

Source 1: $\tau = -0.206, p = 1.1859e-06$

Source 2: $\tau = 0.106, p = 1.258e-02$

Source 3: $\tau = 0.282, p = < 2.22e-16$

Source 4: $\tau = 0.173, p = 4.4465e-05$

TC_Frac

Source 1: $\tau = -0.205, p = 1.4129e-06$

Source 2: $\tau = 0.203, p = 1.7881e-06$

Source 3: $\tau = 0.240, p = < 2.22e-16$

Source 4: $\tau = 0.143, p = 0.00075912$

Chapter 5 Summary and Conclusions

The overall objective of this dissertation was to develop a comprehensive modeling tool for the sourcing and timing of water fluxes in problems involving rainfall/irrigation infiltration, soil moisture change, evaporation, transpiration, and groundwater recharge in the agricultural GSPAC systems.

In chapter 2, the popular HYDRUS-1D model, a numerical model widely used to simulate variably-saturated water flow and solute transport in porous media, was adapted to simulate isotope fate and transport while accounting for evaporation fractionation based on the theory of Craig and Gordon (1965), Melayah et al. (1996a) and Braud et al. (2005a). To verify the model, we compared the numerical solutions obtained by the adapted model against existing analytical solutions under different conditions, including steady evaporation fractionation for isothermal saturated soils (Zimmermann et al., 1967) and steady evaporation fractionation for non-isothermal unsaturated soils (Barnes and Allison, 1984). The results showed that the isotope transport module could produce relatively well isotope profiles as long as an appropriate spatial discretization was used. Additional plausibility tests for isothermal unsaturated soils were conducted to validate that the model could produce plausible results when the equilibrium and kinetic fractionations were sequentially switched on. A simple particle tracking algorithm was also implemented to calculate soil water's transit times and further validate the modified model's results based on a published field

dataset. Transit times calculated by the particle tracking module (PTM) were similar to those estimated by the isotope peak displacement method, validating the applicability of the PTM.

In Chapter 3, we investigated the impacts of considering evaporation fractionation on parameter estimation and practical applications using the new isotope transport model developed in Chapter 2. We designed and conducted simulations considering three fractionation scenarios, including Non_Frac (which does not consider fractionation), CG_Frac (which considers evaporation fractionation as described by the Craig-Gordon model), and Gon_Frac (which considers evaporation fractionation as described by the Gonfiantini model) for a field dataset in humid conditions; and four fractionation scenarios (Non_Frac, CG_Frac, Gon_Frac, and Meas_Frac; note that the first three scenarios were the same as those in the humid conditions, while the last scenario used measured evaporation isotope flux as the upper boundary conditions for isotope transport) for a laboratory dataset under arid conditions. Based on the global sensitivity analysis using the Morris and Sobol' methods, it is shown that the order of sensitive parameters is: shape parameters of the water retention function, namely n , and α , saturated water content θ_s , saturated hydraulic conductivity K_s , and dispersivity λ for the humid dataset, while the most sensitive parameters are shape parameters n and saturated water contents θ_s for the arid dataset. In terms of the parameter estimation using the Particle Swarm Optimization algorithm, the fractionation scenarios (CG_Frac

and Gon_Frac) estimate lower hydraulic conductivities than the Non_Frac scenario for the humid dataset, while the hydraulic conductivities in the fractionation (CG_Frac, Gon_Frac, Meas_Frac) scenarios are a little higher than those in the Non_Frac scenario for the arid dataset. The Kling-Gupta efficiency (KGE) index for isotope data can increase by 0.09 and 1.49 for the humid and arid datasets, respectively, when selecting suitable fractionation scenarios.

The estimated parameters were then applied for two practical applications of stable isotope tracing: i) the assessment of root water uptake (RWU) and drainage travel times (i.e., the time elapsed between water entering the soil profile as precipitation and leaving it as transpiration or drainage) in the lysimeter (humid conditions) and ii) evaporation estimation in a controlled experimental soil column (arid conditions). Considering evaporation fractionation (CG_Frac and Gon_Frac) is likely to result in estimates of older water ages than the no-fractionation scenario. The isotope mass balance method that uses the isotopic composition profile simulated by HYDRUS-1D while considering fractionation (CG_Frac, Gon_Frac, and Meas_Frac), provides comparable results in evaporation estimation as the HYDRUS-1D water mass balance method and direct laboratory measurements. In contrast, the no fractionation scenario reasonably estimates evaporation only when using the HYDRUS-1D water mass balance method. The direct use of simulated isotopic compositions in the no-

fractionation scenario may result in large biases in practical applications in the arid zone where evaporation fractionation is more extensive than in humid areas.

In Chapter 4, we further quantified the impact of the soil tension control on model performance and practical applications using the isotope transport model implemented in HYDRUS-1D. We designed three different fractionation scenarios, including Non_Frac (which does not consider fractionation), CG_Frac (which considers the soil temperature control on equilibrium fractionation as described by the Craig-Gordon model), and TC_Frac (similar to CG_Frac, but considers the soil tension control on equilibrium fractionation as well), and conducted simulations for a field dataset under humid conditions. The results show that TC_Frac leads to a slightly depleted surface isotopic composition compared with CG_Frac. However, the contribution of soil temperature plays a dominant role in evaporation fractionation compared to soil tension.

Using the above simulation results, we determined the spatial-temporal origin of RWU using both water flow (water balance, particle tracking) and isotope transport-based (SIAR, seasonal origin index, virtual tracer) methods. Regarding the spatial origin of RWU, all methods can reflect overall variation trends with depth for contribution ratios of different soil layers. The contribution ratios of all soil layers in the TC_Frac are always between Non_Frac and CG_Frac. The average contribution

ratios of middle soil layers to RWU are similar using both methods, while those of the top and deep soil layers are quite different.

Regarding the temporal origin of RWU, all methods can reflect overall variation trends with time for drainage and root zone (RZ) travel times. The order of both drainage and RZ travel times was: Non_Frac>TC_Frac>CG_Frac. Additionally, absolute differences between different methods always existed and were more significant for RZ than drainage travel times. The results obtained using isotope-transport-based methods are very similar between different fractionation scenarios. Overall, the contribution of soil temperature plays a dominant role in both model performance and identifying the spatial-temporal origin of RWU compared to soil tension.

The innovations of this study lie in:

- (1) This research developed a new isotope transport model, enabling thousands of current HYDRUS users to operate the new model efficiently while using various advanced HYDRUS software features, including flexible dynamic boundary conditions, equilibrium and nonequilibrium water flow, parameter optimization routines, and the well-designed user-friendly GUI.
- (2) This research demonstrated the capability of the new particle tracking module in HYDRUS to assess transit times. This module can further infer

the temporal origin of RWU, a vital but challenging topic in the GSPAC system.

- (3) This research quantified the impact of evaporation fractionation and soil tension control on parameter estimation, model performance, and practical applications of the isotope transport model. This may shed some light on future experimental designs regarding the practical applications of isotope-transport modeling in different climate zones.
- (4) This research compared water-flow and isotope-transport-based methods in identifying the spatial-temporal origin of RWU, which emphasizes the necessity of the integrated employment of multiple methods to secure reliable isotopic data interpretation.

However, more research should be carried out in arid zones to further test the isotope transport model, especially the impacts of soil tension control on isotope transport and practical applications.